MULTIBODY DYNAMICS AND CONTROL OF TETHERED SPACECRAFT SYSTEMS

GANGQIANG LI

A DISSERTATION SUBMITTED TO
THE FACULTY OF GRADUATE STUDIES
IN PARTIAL FULFILLMENT OF THE REQUIREMENTS
FOR THE DEGREE OF

DOCTOR OF PHILOSOPHY

GRADUATE PROGRAM IN
EARTH AND SPACE SCIENCE
YORK UNIVERSITY
TORONTO, ONTARIO

JUNE 2019

Abstract

This doctoral research conducts high-fidelity multiphysics modeling for tethered spacecraft systems, such as electrodynamic tether systems, electric solar wind sail systems, and tether transportation systems with climbers. Two models are developed based on nodal position finite element method. The first model deals with the tethered spacecraft system with fixed length tether, while the second model deals with the tethered spacecraft system with variable tether length using an arbitrary Lagrangian Eulerian description.

First, the nodal position finite element method is applied to model the orbital motion of tethered spacecraft systems with fixed tether length over a prolonged period. A Symplectic integration scheme is employed to attenuate the accumulation of error in numerical analysis due to the long-term integration for tethered spacecraft systems, such as the space debris deorbit by electrodynamic tethers. A high fidelity multiphysics model is developed for electrodynamic tether systems by considering elastic, thermal, and electrical coupling effects of tether. Most importantly, the calculation of electron collection by electrodynamic tether is coupled with the tether libration and flexible deformation, where the orbital motion limited theory for electron collection is discretized simultaneously by the same finite element mesh used for elastodynamic analysis of tether. The model is then used to investigate dynamics and libration stability of bare electrodynamic tethers in

deorbiting end-of-mission spacecraft.

Second, the model of tethered spacecraft system with fixed tether length is extended for the modeling of electric solar wind sail systems. The coupling effect of orbital and self-spinning motions of electric solar wind sail systems is investigated together with the interaction between axial/transverse elastic motion of tether and Coulomb force. A modified throttling control algorithm is implemented in the finite element scheme to control the attitude motion of electric solar wind sail systems through the electric voltage modulation of main tethers.

Third, the model of tethered spacecraft with variable tether length is applied to handle the tether length variation in tether transportation systems. The tether length variation results from the climber moving along tether and deployment and retrieval of tether at end spacecraft. The dynamic behavior of tether transportation systems with single or multiple climbers in characterized and the effectiveness of libration suppression scheme is tested by the high-fidelity model.

Dedication

I dedicate my dissertation work to my family.

Acknowledgements

About five years ago, my life would have taken a completely different path if my supervisor, Professor George Z. H. Zhu, would not have given me an opportunity to visit his Space Engineering Lab at York University as a research assistant. In 2013, I first met professor when he gave a presentation at Shanghai Jiao Tong University. At that time, I was impressed by the professor's good academic background and highly industrial experience. During this visiting time, I was totally attracted by his knowledge, and he always can point out the problem and help me to overcome the problem. In 2015, he gives me an opportunity to pursue a PhD study at York University. Thank him for all these and for everything I have learned from him. Today, I can complete my PhD study because of his unremitting support in my academic as well as personal life and most of all his attitude and dedication towards the research. Thanks for my friend and mentor, Professor George Z. H. Zhu, leading me into the amazing Space Research field. I also would like to thank my supervisor committee members, Dr. Franz Newland, and Dr. Aleksander Czekanski, for their support, instruction, and understanding during the completion of this thesis.

I would also like to thank all the members of Professor Zhu's group for their company and help over the past five years: Dr. Guanghui Sun, Dr. Gangqi Dong, Dr. Peng Li, Mr. Udai Bindra, Mr. Junjie, Kang, Mr. Latheepan Murugathasan, Mr. Chonggang Du, Dr. Huaiping Ding, Dr. Gefei Shi, Dr. Jian Zhang, Dr. Chaofeng LI.

I would like to thank my wife Yanyan and my sons Haiyi and Ben. Especially for my wife, without your support and help, I cannot go through those hard times. I am lucky

to have you in my life.

Finally, I would thank you everyone who give me the support during my PhD study.

Table of Contents

List of Tables

List of Figures

List of Appendices

List of Symbols

a_e	=	Constant of Spindt array, $A \cdot V^{-2}$
$\boldsymbol{a}_p$	=	Vector of additional acceleration term.
A	=	Cross-section area, m^2
$\mathbf{A}$	=	Vector of acceleration of tether.
b_e	=	Constant of Spindt array, $V \cdot m^{-1}$
$\boldsymbol{B}_a$	=	Strain matrix.
$\boldsymbol{B}_{mst}$	=	Vector of Earth magnetic field strength.
c_m	=	Specific heat of tether material, $J \cdot (kg \cdot K)^{-1}$
d	=	Tether diameter, m
$\boldsymbol{D}$	=	Elastic matrix.
e_E	=	Eccentricity of orbit.
$\boldsymbol{e}_t$	=	Unit vector of tether element in tether local frame.
E_k	=	Young's modulus of *k-th* element, $N \cdot m^{-2}$
E_m	=	Motional electric field, $V \cdot m^{-1}$
f	=	External force per unit length, $N \cdot m^{-1}$
$\boldsymbol{F}$	=	Vector of external forces
$\boldsymbol{g}$	=	Vector of gravitational acceleration.
h_t	=	Characteristic transversal length of taped tether, m
H	=	Hamiltonian of tethered spacecraft system, J
H_0	=	Hamiltonian of tethered system in equilibrium configuration, J

i_B, i_C	=	Dimensionless electric currents at points B and C.
i_j	=	Dimensionless electric current at node j = (1∽ n+1).
I	=	Induced electric current along tether, A
I_B, I_C	=	Electric currents at points B and C, A
I_{SC}	=	Short-circuit current of tether, A
I_t	=	Electric current at electron emitter device, A
J	=	Moment of Inertia along the tangent direction.
$\boldsymbol{J}$	=	Inertial tensor of tethered spacecraft system.
$\boldsymbol{K}$	=	Stiffness matrix.
L_a	=	Instant length of tether, m
L_{ao}	=	Unstretched length of tether, m
L_B, L_C	=	Lengths measured from the anode end to points B and C, m
L_*	=	Characteristic length of tether, m
m_e	=	Mass of electron, kg
m_i	=	Mass of ion, kg
m_p	=	Mass of proton, kg
$\boldsymbol{M}_\mathrm{a}$	=	Mass matrix.
$\boldsymbol{M}_\mathrm{e}$	=	Extended mass matrix.
n	=	Number of discretized tether elements.
n_e	=	Solar wind electron density, m^{-3}
n_{orb}	=	Orbital mean motion, $rad{\cdot}s^{-1}$

N_e = Density of electron, m^{-3}

N_t = Number of emitting tips per unit area, m^{-2}

$\boldsymbol{N}_a$ = Shape matrix

$\boldsymbol{N}_e$ = Extended shape matrix

p = Material coordinate, m

q_e = Charge of electron, C

Q = Heat flux, $W{\cdot}m^{-2}$

$\boldsymbol{Q}$ = Transformation matrix.

r = Distance from center of Sun to tether node, m

r_w = Effective radius of charged tether, m

$r_{\oplus}$ = Standard distance is 1, AU

R = Orbital radius of E-sail, m

R_e = Electrical resistance in tether in ohms, Ω

$\boldsymbol{R}$ = Vector of nodal electric current and potential bias

s = Arc-length along tether, m

S_e = Area of emitting board, m^2

t = Thickness of tether, m

T = Instant and initial temperatures in Kelvin, K

T_e = Temperature of electron, eV

T_o = Initial temperatures in Kelvin, K

$\boldsymbol{T}_{f2g}$ = Transformation matrix from Earth-fixed frame to global inertial frame

$\boldsymbol{T}_{l2f}$	=	Transformation matrix from local frame to the Earth-fixed frame
$\boldsymbol{T}_{l2g}$	=	Transformation matrix from local frame to global inertial frame
V	=	Applied voltage of chargeable wire, V
V_{cc}	=	Potential bias at cathodic end C with respect to ambient plasma, V
V_{sw}	=	Solar wind velocity, $\mathrm{m \cdot s^{-1}}$
w	=	Width of tether, m
$\boldsymbol{X}_{\mathrm{a}}$,	=	Vector of nodal coordinate.
$\boldsymbol{X}_{\mathrm{e}}$,	=	Extended vector of nodal coordinate
Z_T	=	Impedance of emitting device in ohms, Ω
$\boldsymbol{Z}$	=	Extended matrix
α	=	Pitch angle of tethered spacecraft system, *rad*
α_p	=	Periodic solution of pitch angle, rad
α_s	=	Sail angle of electric solar wind sail, *rad*
α_{sa}	=	In-plane angle of electric solar wind sail, *rad*
α_{sab}	=	Absorptivity of tether
α_t	=	Linear coefficient of thermal expansion of tether, K^{-1}
β	=	Roll angle of tethered spacecraft system, *rad*
β_c	=	Conning angle of electric solar wind sail, *rad*
β_{sa}	=	Out-of-plane angle of electric solar wind sail, *rad*
ΔT	=	Range of temperate variation experienced by tether in Kelvin, K
ε	=	Emissivity of tether

ε_0	=	Permittivity of vacuum, $F \cdot m^{-1}$
$\boldsymbol{\varepsilon}$	=	Vector of strain of tether
θ	=	North latitude, *rad*
θ'	=	North co-latitude, *rad*
λ	=	East longitude, *rad*
λ_e	=	Two times of Debye length, *m*
μ_g	=	Gravitational constant of Earth, $m^3 \cdot s^{-2}$
μ_s	=	Gravitational constant of the Sun, $m^3 \cdot s^{-2}$
ξ	=	Dimensionless arc-length measured from the anodic end.
ξ_j	=	Dimensionless length of tether element j = (1 ~ n)
ρ_a	=	Atmospheric density, $kg \cdot m^{-3}$
ρ_t	=	Material density of tether, $kg \cdot m^{-3}$
σ	=	Electrical conductivity of tether, $\Omega^{-1} \cdot m^{-1}$
υ	=	True anomaly, *rad*
ϕ_A	=	Dimensionless potential bias at anode end of tether.
ϕ_B	=	Dimensionless potential bias at null potential point of tether.
ϕ_C	=	Dimensionless potential bias at cathodic end of tether.
$\tilde{\phi}_C$	=	Dimensionless potential bias at cathodic end C
ϕ_j	=	Dimensionless potential bias between tether and plasma j = (1~ n+1)
Φ	=	Potential bias between tether and plasma, *V*

Φ_A	=	Potential bias at points A of tether, V
Φ_B	=	Potential bias at points B, V
Φ_{SC}	=	Short-circuit voltage, V
Φ_t	=	Potential bias between tip and gate of Spindt field emit area out, V
ω	=	Spin rate, $deg \cdot s^{-1}$
ω_0	=	Initial spin rate, $deg \cdot s^{-1}$
$\boldsymbol{\omega}_{orb}$	=	Vector of orbital angular velocity in orbital frame, $rad \cdot s^{-1}$
$\boldsymbol{\omega}_{rel}$	=	Relative angular velocity of spacecraft in orbital frame, $rad \cdot s^{-1}$

List of Abbreviations

ALE	=	Arbitrary Lagrangian-Eulerian
ANCF	=	Absolute Nodal Coordinate Formulation
ASDR	=	Active Space Debris Removal
CM	=	Center of Mass
EDT	=	ElectroDynamic Tethers
E-sail	=	Electric solar wind sail
FEA	=	Field Emitter Array
FEM	=	Finite Element Method
IRI	=	International Reference Ionosphere
LEO	=	Low Earth Orbit
NPFEM	=	Nodal Position Finite Element Method
NRLMSISE	=	Naval Research Laboratory Mass Spectrometer Incoherent Scatter Radar Expanded model
OML	=	Orbital-Motion-Limited
TSS	=	Tethered Spacecraft System
TTS	=	Tether Transportation System

Chapter 1 INTRODUCTION AND JUSTIFICATION

1.1 Introduction

1.1.1 Electrodynamic Tether System for Space Debris Removal

After decades of space exploration, Earth orbits, especially in Low Earth Orbit (LEO) region of 600 to 1000 km altitudes [1], have been crowded with debris formed by obsolete or dysfunctional spacecraft and spent rockets. The debris population in the LEO region would rapidly reach a critical point where cascade collision among space debris and spacecraft will become the most dominant debris-generating mechanism if no action is taken soon. To attenuate the risk of potential collision of spacecraft with debris, the Inter-Agency Space Debris Coordination Committee (IADC) was founded in 1993 as an international governmental forum to coordinate worldwide activities for the issue of manufactured and natural debris in space. One of the five typical mitigation scenarios recommended by IADC is to deorbit end-of-mission spacecraft within 25 years or by immediate re-entry. Many active space debris removal (ASDR) concepts have been proposed in the literature, including but not limit to, conventional chemical fuel thrust, electron propulsion, drag sail [2], solar radiation augmentation sail [3], tethered momentum

exchange [4], electrodynamic tether (EDT) [5, 6], laser propulsion, ion-beam shepherd spacecraft and hybrid EDT ion-beam shepherd systems [7]. Among them, the concept of EDT is most appealing due to its advantages of low mass, compact size, propellantless and ease of operation [8]. Particularly, the EDT system can operate independently without working spacecraft. Two types of EDT systems, namely, insulated and bare conductive EDT [9], have been proposed for space tether missions [10]. The bare EDT system in passive mode as a standalone deorbit module appears particularly suitable for the ASDR missions because of its simplicity, high efficiency in electron collection, operational reliability, and flexibility in adaption of different spacecraft [11]. Once the ASDR system captures space debris, for instance by robots, or in case of end-of-mission self-deorbit of spacecraft with a deorbit module, the EDT will be deployed as an anode to collect free electrons from ambient ionosphere for electric current generation. The electrons will be moved to the cathodic end of EDT by an induced motional electromotive force as the EDT across the geomagnetic field of Earth and then ejected back into ionosphere by a dedicated emitter to form an electric circuit. The induced current in the tether generates the Lorentz force, or electrodynamic force, against the orbital motion of the EDT system, leading to a fast orbital decay.

1.1.2 Electric Solar Wind Sail for Deep Space Exploration

Electric Solar Wind Sail (E-sail) is an innovative propulsion technology, which extracts momentum from high-speed plasma stream in solar wind [12]. E-sail consists of a main spacecraft connected with several long and thin conductive tethers called main tethers. The

main tethers are deployed by spinning the main spacecraft and continue to spin around the main spacecraft to maintain a stable umbrella alike shape. The main tethers are positively charged by a solar-powered electron gun on the main spacecraft to form an electrostatic field over a large area [13, 14]. This electrostatic field scatters trajectories of incident protons in the solar wind and transfers the stream-aligned component of protons' momentum to the spacecraft to generate thrust [12, 15]. Each main tether contains a remote unit at its end, which comprises a thruster to control the spin velocity of E-sail [13, 14]. The E-sail design combines the concepts of solar photon sail [16-18] and solar wind magnetic sail that includes traditional magnetic sail [19] and mini-magnetospheric plasmas propulsion sail. The mini-magnetospheric plasmas propulsion sail requires to generate plasma by consuming propellant [20].

The thrust of E-sail decays exponentially over the distance R from the center of the Sun to the center of mass of E-sail system by $1/R^{7/6}$ [13]. It is slower than the solar and magnetic sails ($1/R^2$) [19] but faster than the mini-magnetospheric plasmas propulsion sail ($1/R$). Moreover, the E-sail can easily maneuver into a planetary rendezvous orbit [20] by tilting the sail angle like the solar sail and regulating the magnitude of thrust via varying the electrical field of each main tether like the magnetic sail. This makes the E-sail propulsion a competitive alternative to the solar and magnetic sails, due to its lightweight, propellantless, long operational life [13], easy control of thrust magnitude and orientation, and modest thrust efficiency [21]. Over the years, the E-sail has been proposed for the space exploration for asteroid, cometary, and terrestrial planets [22-24], non-Keplerian

orbits [25, 26], and out-solar system [27].

1.1.3 Tether Transportation System for Payload Orbital Transport

Tether Transportation System (TTS) is an attractive alternative to the classical space elevator due to its ability to long-range mass transport between two spacecraft at low cost [28]. It consists of a main spacecraft, a sub spacecraft, a tether connecting main and sub satellite. and one or multiple climber(s) moving along the tether for orbital transfer of payloads [29]. The mass transfer mechanisms between the two spatial entities using a tether are capable to complete long-range mass exchange missions with low cost. Due to its floating nature, TTS is prone to libration instability as the result of the Coriolis forces acting on the moving climbers.

1.2 Justification of Research

1.2.1 Tethered Spacecraft System

1.2.1.1 Challenges of Modeling of Tethered Spacecraft System

(i) **Mathematical modeling of tether system.** The tether experiences a high-frequency longitudinal oscillation, medium-frequency of transverse libration motion, and low-frequency libration motion around the CM of the system. Thus, a high accurate model for the tethered spacecraft system (TSS) is needed to consider all modes of motion.

(ii) **Modeling of variable-tether length.** The length of tether segment in the mathematical model of TSS may vary due to the movement of climber(s)

along the tether or tether deployment/retrieval at the end spacecraft. Thus, it requires a high-fidelity model that can handle the situations properly while is easy to implement.

(iii) Time integration scheme. The long-term dynamic analysis of TSS requires numerical integration over an extremely prolonged period. It needs an accurate, efficient, stable, and robust numerical integration scheme.

1.2.1.2 Limitation of Existing Treatments

Many tether models have been proposed for the dynamic analysis of TSS in the past for the TSS, for example, dumbbell model [9, 30-32], two-bar tether or double dumbbell model [33], lumped mass model [6, 29], finite difference model [34], and finite element model [31, 35-37]. The dumbbell model simplifies grossly the tether with a pair of force vectors, the lumped mass model or finite difference model are problem specific. Among them, the finite element method (FEM) is the most versatile and adaptive in terms of applicability for various conditions, such as, complex systems with different physical properties along tether and initial/boundary conditions, and easy implementation or integration in general-purpose codes. The challenge arises from the conventional FEM where the current position of a tether is obtained by adding the tether displacement within one-time step to its previous position. The error within each step will accumulate over the time and may eventually lead to erroneous and unstable solutions over an exceedingly prolonged period of numerical integration. This results in the FEM is not widely used in the dynamics analysis of TSS, which it is currently dominated by the dumbbell model, lumped mass model and finite

difference model. No general-purpose codes for TSS that considers full spectrum motion is available.

In addition to the mathematical model of TSS, the FEM, lumped mass and finite difference methods have extremely limited ability in modeling the tether length variation accounted in modeling climber(s) moving along the tether or the tether deployment/retrieval at the end spacecraft. Currently, there are two approaches used to deal with the length variation problem. In the first approach, the total number of degrees of freedom of numerical model is predetermined and fixed. The length of each tether segments in the model is reduced or elongated simultaneously at the same time, which will lead to the extremely long or short tether segments at the end of deployment or retrieval processes. It results in either poor accuracy in case of tether deployment or unnecessary computer effort in case of tether retrieval. Moreover, it lacks the flexibility in modeling cases that involves multiple climbers. The alternative approach is to adopt the variable degrees of freedom of numerical model where new tether segment will be created to accommodate the length increase of tether segment or old tether segments will be merged in case of length decrease of tether segment. Although flexible in modeling tether length variation, it does not enforce the conservation of mass in the process and is not easy to implement numerically.

Finally, all modeling approaches results in nonlinear numerical equations that must be solved by numerical integration. Currently, the widely adopted time integration schemes in the field are classical explicit Runge-Kutta, Newmark and Generalized-α methods. Although effective in transient or short-time period analysis, they prone to numerical

stability in extremely prolonged period of analysis, which is common for TSS. Their stability is sensitive to the size of time integration step and the conservation of energy of numerical models is not guaranteed due to the geometrical nonlinearity of TSS and errors accumulated over the prolonged period of time integration [37].

1.2.2 Electrodynamic Tether System

1.2.2.1 Challenges of Electrodynamic Tether System

In past decades, studies are devoted to study the dynamics and control strategy of EDT systems. There are many technical challenges and can be summarized as follows:

(i) **Accurate evaluation of electrodynamic force.** A critical issue for the application of EDT is to accurately evaluate electrodynamic force, which in turn depends on the accurate evaluation of electric current in EDT. Currently, the evaluation of current generation and tether dynamics are decoupled: the profiles of current and potential bias along EDT are evaluated by the orbital motion limited theory first without consideration of tether libration, then they are projected onto deformed tether in a librated position. It is noted such approach will lead to overestimate the current in EDT. Thus, a fully coupled multiphysics finite element method is needed to solve the tether dynamics precisely.

(ii) **Coupled elastic, thermal, and electrical effects.** The EDT experiences elastic and rigid-body motion in orbiting Earth. For instance, the diurnal variation of temperature affects internal stress, conductivity/resistance, and

longitudinal oscillation of tether. Moreover, the temperature induced variation of tether conductivity affects the electron collection efficiency that leads to the variation of electrodynamic force. Currently, these effects are considered separately in a sequential order. A high-fidelity multiphysics model of EDT that simultaneously consider all these coupling effects are needed.

1.2.2.2 Limitation of Existing Treatments

A critical issue for EDT systems is to evaluate the induced electrodynamic force or Lorentz force accurately. The force depends on the induced electric current in EDT according to the Lorentz law. There are two types of EDT systems: the insulated and bare EDT system. The insulated EDT system consists of an insulated conductive tether connected by two plasma contactors at ends. It consumes fuel to generate plasma at cathodic contactor to interact and expel electrons, which are attracted by the anode plasma contactor at other end, into the environment plasma in space. The bare EDT system consists of a bare conductive tether as anode to attract electrons from environment and expel electrons at cathode by a field effect emitter that does not need fuel. Due to its propellentless, compact design and low mass, it is proposed for space debris deorbit. One of objectives of the thesis is space debris and only bare EDT systems are considered in the thesis.

It is well known that the current in bare EDT systems obeys the orbital motion limited (OML) theory [5, 38]. Existing approaches decouple the EDT dynamics from the OML theory based on two assumptions [39-41]. First, the EDT is assumed straight, rigid,

and always aligned with the local vertical. Second, the motional electric field is constant along the entire tether length. The OML theory is transformed in dimensionless form in these approaches and solved with different approaches independently [38, 42-44]. Once the profile of electric current along the straight and vertical EDT is solved, it is projected onto a real tether that may be inclined and/or bent [9, 43, 44]. Obviously, the influence of tether dynamics and variation of motional electric field along tether is decoupled from the EDT dynamics. It is reported in the literature that such approach tends to overestimate the current in EDT. Thus, the coupled effect must be investigated by a true multiphysics modeling approach.

Next, the diurnal variation of EDT temperature affects internal stress, conductivity/resistance, and thermal properties, which leads to the variation of electrodynamic force and tether longitudinal oscillation. The effect of thermal expansion coefficients on the tether dynamics and deorbit has been conducted [44] and [6]. However, the effect of thermal fluctuation on the electrodynamic force and elastic dynamics of tethers, i.e., the coupled elastic, electric, and thermal effect on tether dynamics, has not been thoroughly investigated.

1.2.3 Electric Solar Wind Sail System

In past decades, studies are devoted to analyzing the dynamics and control strategy for E-sail and can be summarized as follows:

1.2.3.1 Challenge of Electric Solar Wind Sail System

The attitude of E-sail should be controlled to achieve thrust vectoring in orbital transfer for

space exploration. However, it is noted that the spin rate changes in the E-sail attitude maneuvering process because a force inside the spin plane is generated when the E-sail is inclined with respect to the incoming solar wind. A practical and easy implementation control strategy is needed for controlling the attitude of E-sails while suppressing the variation of spin rate for the stability of E-sail.

1.2.3.2 Limitation of Existing Treatments

In the existing studies of dynamics of E-sail, the attitude dynamics of main spacecraft is ignored due to the extremely large ratio of tether length over dimension of main spacecraft. Thus, the orientation of E-sail can be approximately represented by the spin axis of spin plane, which varies in the attitude maneuvering and must be determined dynamically. In the existing approaches, the spin axis of spin plane is determined by solving a differential equation about the angular momentum of E-sail [45]. However, it is time-consuming and complex. For attitude control, a simple and computational efficient approach to determine the attitude of E-sail is currently mission and needed to be developed.

Moreover, the thrust of E-sail depends on the Coulomb forces acting on the mail tethers. Intrinsically, by modulating the electric voltage of main tether individually will generate an angular moment to change the orientation of spin plane or attitude of E-sail, in addition to the thrust. This is called thrust vectoring in the literature. However, the influence of physical parameters, such as the number of main tethers, length of each main tether, initial spin rate, and the remote unit, influence on the attitude dynamics of E-sail is not well-known and not yet be thoroughly studied, especially when the applied voltage is

bounded due to the constraint of power supply of main spacecraft.

1.2.4 Tether Transportation System

1.2.4.1 Challenge of Tether Transportation System

The transport of payload by climbers moving along the TSS will generate a Coriolis force acting on the tether. The force will cause the libration motion of tether, which in turn will change the magnitude and orientation of the Coriolis force. Such interaction effect between climbers and tether needs to be carefully considered in evaluation of practicability of TTS. The incorporation of climbers into tether dynamics is technically challenging. A fully coupled model consideration of the coupling effect between the climber and tether is needed, where the dynamics of climber and tether are modeled and solved simultaneously.

1.2.4.2 Limitation of Existing Treatments

The incorporation of moving climbers along a librating tether into tether dynamics is technically challenging. To achieve this, two types of methods have been proposed in the literature: the uncoupled and coupled methods, respectively. The uncoupled method is simple and straightforward. It ignores the dynamic coupling effect between tether and climbers [46, 47]. The coupling method is that the dynamics of climber and tether are modeled separately and a constraint equation is introduced to couple the spatial position and velocity of climbers by Lagrangian multiplier method [48]. However, it needs to determine the position of climbers along tether in the process that is time consuming. Moreover, the position of climbers is projected to the undeformed state of tether for simplicity, which may be inaccurate if the tether is bent significantly [48].

1.3 Objectives of Research

To address the challenges and limitations of these three target systems, the objectives of research in this thesis are organized as follows.

1.3.1 Tethered Spacecraft System

The overarching objectives for the modeling of TSS are,

(i) Develop a high-fidelity model of TSS based on the nodal position finite element method with the consideration of elastic, electric and thermal properties of tether under two situations: fixed-length and variable-length tether.

(ii) Develop a variable-length element model that can easily deal with the movement of climbers along the tether and tether deployment and retrieval.

(iii) Develop a robust time integration scheme to overcome the numerical instability and eliminate error accumulation over long-term numerical integration for TSS.

1.3.2 Electrodynamic Tether System

The overarching objectives for EDT systems are,

(i) Apply the high-fidelity model of TSS developed above by considering space environmental perturbation forces using coupled multiphysics approach, including the evaluation of the temperature variation influence on the electron collection efficiency and tether dynamics.

(ii) Develop a fully coupled multiphysics finite element approach that couples the tether dynamics with the electric current generation, in which the orbital motion

limited theory is discretized simultaneously with the flexible tether dynamics by the same finite element mesh and shape function in different physical domains.

1.3.3 Electric Solar Wind Sail System

The overarching objectives for E-sail system are as follows:

(i) Apply the newly developed high-fidelity multiphysics model to investigate the coupling effects of orbital and self-spinning motions of the E-sail, and interaction between the axial/transverse elastic motions of tether and the Coulomb force.

(ii) Develop a control strategy to control the attitude motion of E-sails while suppress the variation of spin rate caused by attitude maneuvering.

(iii) Understand influence of physical parameters on attitude and orbital dynamics of E-sail.

1.3.4 Tether Transportation System

The overarching objectives for TTS are,

(i) Apply the newly developed high-fidelity tether model to investigate longitudinal and transverse oscillation of tether, and libration motion of TSS around the its CM.

(ii) Develop a unified approach that is capable to deal with multiple climbers and tether deployment and retrieval.

(iii) Understand influence of multiple climbers and tether deployment/retrieval on libration dynamics of TTS.

1.4 Methodology of Approach

The methodology of approach to achieve the research objectives begins with a literature review of mathematical modeling of TSS, followed by detailed reviews of the dynamics of EDT, E-sail, and TSS or TTS. Then, the detailed challenges and limitations of existing approaches of corresponding parts are identified. Based on the literature review, research approaches are defined and outlined in Fig. 1.1.

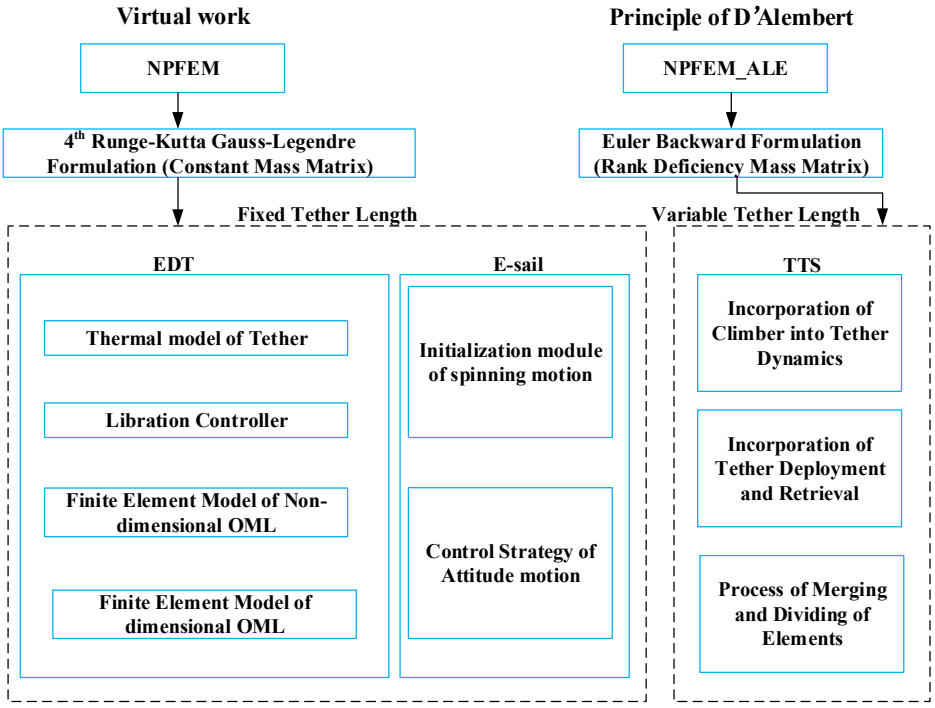

Figure 1.1 Methodology of approach.

As shown in Fig. 1.1, a generalized three-dimensional nonlinear finite element model of TSS is built, where position replacing displacement as state variables. For the fixed tether length case (EDT and E-sail), a high-fidelity three-dimensional Nodal Position Finite Element (NPFEM) model is developed based on the principle of virtual work, and a

high-order time integration scheme with Symplectic property is employed to eliminate the numerical accumulation error of long-term simulation. For the variable tether length case in TTS, the scheme of element birth and death is developed based on NPFEM in the framework of Arbitrary Lagrangian Eulerian and the principle of D'Alembert. A first-order Euler backward time integration scheme is employed together with the Newton-Raphson iteration algorithm to solve the system equation due to the rank deficiency of mass matrix in this approach.

For the EDT systems, the thermal effect of tether is incorporated into the tether dynamics to consider the coupled elastic, thermal, and electric effects. The is because the diurnal temperature variation affects the electron collection efficiency due to the temperature dependence of electrical conductivity. To keep a stable motion of EDT in the deorbit process, a practical and easy implementation control strategy is applied to suppress the libration motion of EDT systems. Furthermore, a fully coupled multiphysics model is developed, where the electric current generation and tether dynamics are modeled and solved simultaneously to accurately evaluate the electrodynamic force.

For the E-sail systems, a special simple and computational efficient routine is developed to start the numerical analysis of a self-spinning E-sail. Small numerical damping is used to damp out the initial transient oscillation of tether due to the unbalanced relationship among the position, velocity, and acceleration of an elastic tether. The numerical damping is eliminated once the system reaches the steady state of a spinning motion of E-sail. The latter is sent to the orbital motion of E-sail as initial conditions.

To describe the attitude of E-sail, the spin axis of the spin plane is determined by

an alternative approach instead of solving the angular momentum equation of E-sail systems. The alternative approach is derived from the viewpoint of geometrical configuration that has the advantages of fast speed, reliable, and easy implementation. Based on this attitude determination of E-sail, a modified control strategy is employed to control the attitude motion of a flexible E-sail system.

For the TTS, a material coordinate is introduced together with the position coordinate as the state variables in the Arbitrary Lagrangian Eulerian description. The coupling effect between tether and climbers is considered by enforcing kinematic constraints. In this approach, the nodes where the climbers reside are assumed as moving nodes, and elements connecting with the moving nodes are defined as the variable-length elements. The variation of the material coordinates of moving nodes follows the pre-defined trajectories of climbers. Thus, the movement of climbers can be implemented by changing the lengths of variable-length elements, where one element decreases while the other increases or vice versa. Furthermore, to avoid the length of variable-length element too long or too short, a process of merging (death) and dividing (birth) of element is developed. To accomplish the deployment and retrieval of the tether at end spacecraft, the nodes where the end spacecraft are located are assigned as the moving nodes, and the correspond connecting elements are the variable-length elements. The variation of the material coordinate is equal to the speed of deployment and retrieval.

For all approaches, numerical analyses are conducted and validated against the results by existing approaches whenever it is available.

1.5 Layout of Thesis

This thesis contains eleven chapters. After Chapter 1, a detailed literature review of the TSS, E-sail, and TTS is conducted in Chapter 2. Chapter 3 provides mathematical modeling of TSS under two situations, fixed tether length and variable tether length. Chapter 4 deals with the libration dynamics and control of bare EDT considering the multiphysics coupling effects. Chapter 5 studies the dynamic characteristics, and attitude dynamics and control of E-sail by a high-fidelity multiphysics model. Chapter 6 studies the dynamics of TTS with climbers and tether deployment or retrieval. Finally, Chapter 7 concludes the work, identifies original contributions of the thesis, and outlines the directions for future work.

1.6 Publications Related to This Thesis

The following is a full list of publications associated with this thesis.

1.6.1 Published Peer-Reviewed Journal Papers

(1) **G.Q. Li**, Z.H. Zhu, Long-term dynamic modeling of tethered spacecraft using nodal position finite element method and Symplectic integration, Celestial Mechanics and Dynamical Astronomy, 123 (2015) 363-386.

doi: 10.1007/s10569-015-9640-5

(2) **G. Li**, Z.H. Zhu, J. Cain, F. Newland, A. Czekanski, Libration Control of Bare Electrodynamic Tethers Considering Elastic–Thermal–Electrical Coupling, Journal of Guidance, Control, and Dynamics, 39 (2015) 642-654.

doi: 10.2514/1.G001338

(3) **G. Li,** Z.H. Zhu, S.A. Meguid, Libration and transverse dynamic stability control of flexible bare electrodynamic tether systems in spacecraft deorbit, Aerospace Science and Technology, 49 (2016) 112-129.

doi: 10.1016/j.ast.2015.11.036

(4) **G. Li,** Z.H. Zhu, Multiphysics Finite Element Modeling of Current Generation of Bare Flexible Electrodynamic Tether, Journal of Propulsion and Power, 33 (2016) 408-419.

doi: 10.2514/1.B36211

(5) C. Wang, **G. Li**, Z.H. Zhu, A. Li, Mass Ratio of Electrodynamic Tether to Spacecraft on Deorbit Stability and Efficiency, Journal of Guidance, Control, and Dynamics, 39 (2016) 2192-2198.

doi: 10.2514/1.G000429

(6) **G. Li**, Z.H. Zhu, S. Ruel, S.A. Meguid, Multiphysics elastodynamic finite element analysis of space debris deorbit stability and efficiency by electrodynamic tethers, Acta Astronautica, 137 (2017) 320-333.

doi:10.1016/j.actaastro.2017.04.025

(7) **G. Li**, Z.H. Zhu, Precise Analysis of Deorbiting by Electrodynamic Tethers Using Coupled Multiphysics Finite Elements, Journal of Guidance, Control, and Dynamics, 40 (2017) 3348-3357.

doi:10.2514/1.G002738

(8) **G. Li**, Z.H. Zhu, Parameter influence on electron collection efficiency of a bare electrodynamic tether, Science China Information Sciences, 61 (2017) 022201.

doi: 10.1007/s11432-017-9219-1

(9) H. Ding, Z.H. Zhu, X. Yin, L. Zhang, **G. Li**, W. Hu, Hamiltonian Nodal Position Finite Element Method for Cable Dynamics, International Journal of Applied Mechanics, 09 (2017) 1750109.

doi: 10.1142/s1758825117501095

(10) **G. Li**, G. Shi, Z.H. Zhu, Three-Dimensional High-Fidelity Dynamic Modelling of Tether Transportation System with Multiple Climbers, Journal of Guidance, Control, and Dynamics (**in press**)

(11) G. Shi, **G. Li**, Z. Zhu, Z.H. Zhu, A Novel Virtual Experiment for Tether Transportation System using Nodal Position Finite Element Method with Arbitrary Lagrangian-Eulerian Description, Nonlinear Dynamics, (2019) **in press**.

doi: 10.1007/s11071-018-4718-8

(12) G. Shi, **G. Li**, Z. Zhu, Z.H. Zhu, Dynamics and Operation Optimization of Tether Transportation System with Multiple Climbers, Advances in Space Research (2019), **in press**.

doi: 10.1016/j.asr.2019.01.022

(13) **G. Li**., Z.H. Zhu, C.G. DU. Characteristics of Coupled Orbital-Attitude Dynamics of Flexible Electric Solar Wind Sail. Acta Astronautica, (2019), **in press**.

doi.org/10.1016/j.actaastro.2019.02.009

(14) **G. Li**, Z.H. Zhu, On Libration Suppression of Partial Space Elevator with a Moving Climber, Nonlinear Dynamics, (2019), **in press**.

1.6.2 Submitted Peer-Reviewed Journal Paper

(1) **G. Li**, Z.H. Zhu, Flight Dynamics and Control Strategy of Electric Solar Wind Sail, Journal of Guidance, Control, and Dynamics (first review process).

Chapter 2 LITERATURE REVIEW

Summary: In this chapter, we review the literature of electrodynamic tether, electric solar wind sail, and tether transportation system. Based on literature review, research objectives and approach methodologies are suggested.

2.1 Mathematical Modeling of Tethered Spacecraft System

In this section, the literature review of TSS is conducted for the following categories: the TSS without tether length variation, the TSS with tether length variation, and associated time integration scheme.

2.1.1 Tethered Spacecraft System with Fixed Length

The high-fidelity modeling of TSS inevitably leads to a complex mathematical problem and consequently requires reliable numerical modeling techniques. Existing models includes one-piece dumbbell model [9, 30-32], two-piece dumbbell model [33], lumped mass model [6, 29], finite difference model [34], and finite element model [31, 35-37]. Kristiansen et al. explored the detailed relationship between different tether models including the massive/massless, slack-spring and dumbbell tether models [36]. Lanoix et al. studied spacecraft deorbiting efficiency by EDT using one-piece dumbbell model to demonstrate that the electrodynamic force could remove a spacecraft from orbit more effectively than atmosphere drag [9]. Using the same tether model, Jin et al. studied the in-plane dynamic motion of a short tether system in a station-keeping phase [32]. Jung et al.

modeled the dynamics of TSS with a moving mass along the tether with two-piece dumbbell model [49]. Woo and Misra investigated dynamic libration of a space elevator with multiple climbers by lumped mass model [29]. Many existing tether models ignored attitude dynamics of tethered spacecraft and its effect on orbital and attitude dynamics of TSS. This is due to the facts of extremely large ratio of tether length over spacecraft dimension. Works have been done in the coupled dynamics that considers the attitudes of both the TSS and the spacecraft to investigate the impact of tether tension on the spacecraft's attitude dynamics. Details can be found in a review chapter by Kumar [50]. Lee et al. developed a high-fidelity numerical model for TSS by considering coupled dynamics of spacecraft and space tether with the focus on the impact of spacecraft's attitude dynamics and tether handling system on the overall dynamic characteristic of TSS [37]. The study showed that the attitude dynamics of spacecraft could affect the relative position of tethered spacecraft and configuration of TSS could be significantly different if the tether was initially stretched by 25%. Fortunately, the tether elongation of TSS is extremely small if subject to gravitational field only. Thus, it is safe in the currently approach to ignore the attitude dynamics of spacecraft and model them as lumped masses only.

Among all modeling methods for TSS, the simplest one is the dumbbell model where the tether is simplified with a pair of force vectors or a massless rigid line with tethered spacecraft attached to the ends of tether as point masses. The tether mass is either ignored or lumped evenly to end masses. Here, the tether dynamics is completed ignored and the tether length is non-stretchable. The tether tension becomes a state variable and the system equation becomes singular if tether tension approaches to zero. It is widely used in

the dynamic modeling and control of tethered spacecraft due to its mathematical simplicity.

The next simple approach is the lumped mass method. In this approach, the tether is discretized into a series of nodes that are joined by finite length of massless tether segments that are either rigid or elastic. The tether mass and external forces are lumped to nodes. It simplifies the nonlinear partial differential equations of a tether into a set of ordinary differential equations [6, 51]. They could model the translational deformation of tether such as bent and twist, elastic elongation if tether segment is modeled by springs and dampers. In general, it is a special case of finite element method to be discussed later.

The finite difference method based on Kane's equation approximates the dynamic equations of TSS by a set of differential equations along tether length [52]. It is widely used in the tether dynamics due to its mathematical simplicity [34, 53]. Although effective, the finite different method is application specific and hard to be implemented in general-purpose codes for complex tether systems with different physical properties along the tether or multiple tether branches.

The direct integration method recast the boundary value problem of tether dynamics as a set of initial value problems [54]. This approach is applicable for limited cases with special initial conditions.

Finally, the FEM is the most appealing among all numerical methods. The main advantage of the FEM is its flexibility and capability in handling complex tether properties and configurations and boundary conditions of a TSS compared to other methods. However, it is yet widely adopted in the dynamic modeling of tethered spacecraft system, where the tether experiences large displacements/rotations coupled with small elastic axial

deformation. The challenge arises from the conventional FEM where the current position of a tether is obtained by adding the tether displacement within a time step to its previous position. Typical nonlinear FEM schemes such as the floating frame reference, the incremental and the large rotation vector formulations are used to solve for the displacement in each time step. For instance, consider a straight tether moving rigidly in a plane as shown in Fig. 2.1. The Green-Lagrangian strain and the strain energy of the tether should be zero, such that,

$$\varepsilon = \varepsilon_L + \varepsilon_N = 0 \tag{2.1}$$

$$U = \int_0^L EA\varepsilon^2 ds = \int_0^L EA\left(\varepsilon_L^2 + 2\varepsilon_L\varepsilon_N + \varepsilon_N^2\right) ds = 0 \tag{2.2}$$

where $\varepsilon_L = cos\,\theta - 1$ and $\varepsilon_N = \frac{1}{2}[(cos\,\theta - 1)^2 + sin^2\,\theta]$ are the linear and nonlinear strain components.

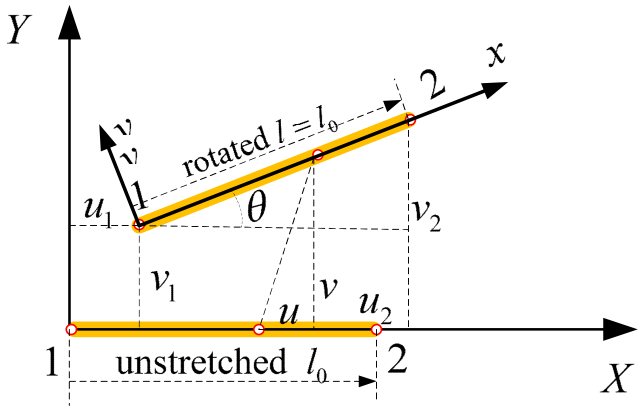

Figure 2.1 Schematic of tether element subject to large rotation.

The nonlinear higher order term ε_N^2 in the strain energy is ignored in the existing FEM if one assumes small strain and moderate rotation within each time step, such that,

$$U = \frac{1}{2}\int_0^L EA\varepsilon^2 ds = \int_0^L EA\left(\varepsilon_L^2 + 2\varepsilon_L\varepsilon_N\right)ds = -\frac{1}{2}EAL\left(cos\,\theta - 1\right)^2 \tag{2.3}$$

Equation (2.3) indicates that the existing FEM will result in spurious strain energy that approaches zero only if there is no rigid body rotation, such that, $\cos\theta \approx 1$. Although the error is small or infinitesimal in each time step, the accumulated errors may eventually lead to erroneous and unstable solutions over a very long period of numerical integration [55, 56]. For instance, a typical process of the end-of-mission deorbit of spacecraft by the EDT technology may last up to 25 years [57]. The challenge has been addressed in two related areas in the literature respectively, i.e., the formulation of FEM and the numerical integration scheme.

In the area of FEM, there are two challenges associated with the tether dynamics: the coupling of large rigid body rotation and/or displacement with small elastic deformation and the singularity, or ill-posedness, in low-tension tethers [36, 58-61]. The first challenge was addressed by describing the tether motion directly with the nodal position instead of displacement to avoid the decoupling of elastic deformation from rigid body motion in the existing FEM. There are two approaches in this regard in the literature: absolute nodal coordinate finite element method (ANCFEM) [48], and nodal position finite element method (NPFEM) [62, 63]. Both methods use the nodal position as state variables. The difference between them is that NPFEM enforces the continuity of tether position at nodes while ANCFEM enforces the continuity of tether position and slope at nodes. As the result, ANCFEM doubles degrees of freedom that that of NPFEM and requires excessive numbers of elements in the region where tether bends significantly. Given the fact of low

tension in TSS, the local bending of tether does not affect the overall dynamics of TSS. Thus, the excessive numbers of elements in local high bending area of tether do not affect the dynamic characteristic of TSS. In addition, the integration period in TSS is extremely long and computational efficiency is paramount in the study. Based upon above consideration, the approach of NPFEM by Zhu et al. [62, 63] is adopted in the current study.

The second challenge of singularity in the low-tension scenario is caused by the small and dynamically fluctuating tension vanishing anywhere along the tether, which can be best illustrated by the elastic transverse wave propagation along the tether. The wave velocity is proportional to $\sqrt{T/\lambda}$ if the tether is modeled as a string, where T is the tension and λ is the linear density of tether. The zero tension in a tether leads to the singularity in the model. To address the challenge, Zhu and Meguid incorporated the bending stiffness of tether into the tether model so that the wave propagation velocity is revised to $\sqrt{(EI/L^2)(1+T/F_c)}$ [58-60, 64, 65], where EI and F_c are the tether's bending rigidity and Euler's critical buckling force of a simply supported slender beam. Obviously, the singularity is attenuated by allowing the tether to be subjected to a finite compressive load until it buckles and becomes singular. [61]. It should be noted that the introduction of bending stiffness may result in ill-conditioned stiffness matrix due to the large ratio of longitudinal to bending stiffness of a tether. For instance, the stiffness ratio of a tether with circular cross-section is proportional to square of length over diameter, such that, $\left(EA/L\right)/\left(EI/L^3\right) = AL^2/I = 16\left(L/D\right)^2$. For a typical short space tether mission, such

as OEDIPUS-A [66], the stiffness ratio is $AL^2 / I = 16\left(958 / 0.0009\right)^2 = 1.8 \times 10^{13}$. To avoid the ill-condition in the stiffness matrix, one approach is to discretize the tether into many short elements to reduce the ratio of *L/D* within each element [65], which inevitably leads to practically unacceptable small time step for the long-term dynamic modeling of space tether system. To attenuate this issue, a two–node straight truss element is used to model the space tethers with sufficient accuracy and acceptable computational loads [43, 67] by NPFEM approach.

2.1.2 Tethered Spacecraft System with Variable Length

TSS with variable length is referred to tethered transportation system (TTS) with climbers and tether deployment and retrieval. First, the length segment of tether between climbers or climber and end spacecraft varies when climbers moving along the tether. The mathematical modeling of TTS can be decomposed into two parts, (i) the modeling of tether dynamics and (ii) the incorporation of climbers into tether dynamics. In the past decades, many modeling methods have been proposed to study the dynamic behavior of TSS, such as, the lumped mass method [46-48, 68, 69], finite difference method [6], Kane's method [52], modal method [70], rigid element method [71-74], ANCFEM [48], and NPFEM [43, 63, 67, 75-77]. As mentioned in Section 2.1.1, the NPFEM is the most appealing due to its flexibility and capability in handling complex tether properties and boundary conditions of TSS, and ease of implementation. However, the incorporation of a moving climber along the tether into the tether dynamics is technically challenging. To

achieve this, two types of methods have been proposed: the uncoupled and coupled methods, respectively. The uncoupled method is simple and straightforward. It ignores the dynamic coupling effect between the tether and climber [46, 47]. Instead, the climber is replaced by a force vector moving along the tether at a given climbing velocity. The coupled method consists of two categories in terms of the coupling techniques. The first is the sequential coupling, where the dynamics of the climber and tether are modeled separately and a constraint equation is introduced to couple the spatial position and climbing velocity by the Lagrangian multiplier method [48]. However, it needs to determine the position of climber along the tether in the process. Moreover, the position of climber is projected to the undeformed state of tether for simplicity, which may be inaccurate if the tether is bent significantly [48]. The second is the true coupled approach, where the dynamics of climber and tether are modeled and solved simultaneously. To achieve this, a variable-length element model is introduced [68]. The movement of climber is represented by changing the lengths of two elements connecting to the climber with one being increasing and the other being decreasing. This approach is superior to the sequential coupled approach because it can describe not only the climber movement along the tether but also the variable length problems, such as, the tether deployment and retrieval of TTS. Therefore, the true coupled approach is adopted for this thesis.

2.1.3 Time Integration Scheme

The common time integration schemes for the analysis of TSS in the literature are classical explicit Runge-Kutta, Newmark and Generalized-α methods. Although effective, the

conservation of energy of numerical models is not guaranteed due to the geometrical nonlinearity of the tethered spacecraft and the stability of numerical solution may deteriorate due to the accumulated approximation errors over prolonged period of time integration [37]. Many efforts have been devoted to the development of energy-conservative time integration scheme for various (linear and nonlinear) systems [37, 55, 78]. For instance, Kristiansen et al. solved the dynamics of elastic tethers by an implicit three-stage Gauss-Legendre Symplectic scheme with the consideration of tether bending stiffness [36, 61]. Lee et al. (2014) studied the dynamics of TSS using the implicit Lie group variational Symplectic integrator of second order accuracy by considering the tether longitudinal stiffness, spacecraft attitude dynamics, and a reeling mechanism [37]. Aristoff et al. developed a new implicit Gauss–Legendre Runge–Kutta based approach with controlled variable-step strategy for the orbit and uncertainty propagation [79]. Numerical results showed the performance of the scheme is robust. Therefore, the time integrator with a characterization of symmetric and Symplectic characteristics is remarkable for the long-term integration problem, such as the orbiting tethered spacecraft, orbital propagation, asteroid surveillance and tracking and maneuver detection. This thesis will investigate the suitability of such kind of time integration scheme in solving TSS problem.

2.2 Electrodynamic Tether System

2.2.1 Dynamics and Control

EDT technology is very appealing in the space debris removal due to its advantages of low

mass, compact size, fuel-less and ease of operation [80]. Particularly, it can function independently and does not rely on having a working spacecraft it resides to re-enter. However, the application of EDT technology is impeded by the unstable libration motion, resulting from the periodic excitation by electrodynamic force if no control is applied [40, 81].

Studies have been devoted to the investigation of libration stability and control of EDT systems. The dynamic instability of EDT systems is affected by the induced electric current in tether [82]; orbital inclination; altitude and eccentricity [9]; mass ratio of EDT to main spacecraft [81], and transverse dynamic motion of tether [83]. The temperature variation of tether results in additional adverse effects [83, 84] on the libration stability due to the thermal stress in tether and the thermally induced variation in electrical and physical properties of tether. In the early studies of libration stability of EDT systems, the dumbbell model was widely adopted due to its simplicity. However, it was revealed that the dumbbell model could not predict the elastic instability of tether, which may lead to the global instability of a tether system faster than the tether libration [85, 86]. A tether model consisting of two rigid-bars was proposed to assess the influence of transverse dynamics on the libration stability of EDT in circular [81] or elliptic inclined orbits with high eccentricity [87, 88]. Furthermore, a lumped mass model was proposed to capture the high order modes of transverse motion of tether [83]. The analysis results indicated that the flexible mode transverse dynamics of tether is not negligible in the stability analysis of EDT systems.

Compared to other effects, the effect of thermal perturbation on the libration

dynamics and stability of EDT is less studied. For the TSS, Williams et al. showed that the temperature variation along the tether strongly influenced the dynamics of capture maneuvers [84]. Yu and Jin found that the thermal effect had a quite different dynamic effect during the retrieval of tethered spacecraft [89]. For the EDT system, Kawamoto et al. recommended a parametric analysis of EDT stability considering different thermal expansion coefficients of the tether [44]. Furthermore, Zanutto et. al. analyzed the orbital descending process by EDT with consideration of the thermal flux in flexible tethers [83].

In addition to the libration dynamic analysis, many works have been devoted to developing the libration control strategy for EDT system. Because the libration instability is caused fundamentally by the electrodynamic force pumping energy into the libration motion, it is natural to derive control strategy based on system libration energy. The first approach is to reduce system libration energy by dissipation, for instance, the inclusion of mechanical dissipating [38, 90] or wave absorbing mechanisms [91]. The former consists of a conductive tether and a long segment of inert tether combined with an internal damper, while the latter involves a moving tether attachment to weaken the propagation of elastic transverse wave along the tether. The second approach is to control energy input to EDT system, such as, zero net energy input [92] and controlled energy input [93, 94]. For instance, William [92] developed a controller based on energy rate feedback with zero net energy input to stabilize the libration of an EDT system. Many other control strategies that track the reference periodic solutions are also based on the same concept. Different from the zero net energy input, Corsi and Iess [93] and Takeichi [94] defined a specific Lyapunov candidate function as a stability function to control the libration motion by

bounding energy input until the EDT system reaches the target deorbit altitude. The last approach is based on the relationship between the electric current and the secular change of orbital elements. For instance, Tragesser and San [95, 96] developed a control law with feedback of electric current to affect a desired change of orbital elements by current regulation during orbital maneuvering.

These existing control strategies in the published literature provide a good understanding of the peculiar characteristic of EDT systems. Nevertheless, the rigid tether simplification [94, 97], the complex design of energy dissipation mechanisms [38, 90], and the gross oversimplification in control strategy and continuous electric current control [98, 99] impede their practical applications. For the engineering application of EDT technology, a simple and efficient control strategy is highly desired.

2.2.2 Coupling Effects

The orbital perturbation forces that EDTs may experience in LEO includes 1) the electrodynamic force acting on current-carrying tethers, 2) the non-homogeneous gravity field and oblateness of Earth, 3) the Earth's atmospheric drag, 4) the lunisolar gravitational forces, 5) the solar radiation pressure, and 6) the thermal fluctuation of tethers. We will focus on the study of coupling effects, such as the coupling effect between tether dynamics and electron collection efficiency, the coupling among thermal, elastic, and electric effects.

First, the critical issue in the EDT dynamics is the proper evaluation of the Lorentz or electrodynamic force due to the interaction between the current carrying tether and the Earth magnetic field. A motional electric field will be generated along tether that makes

the tether partially positive and negative biased with respect to ambient plasma. Consequently, the bare tether will attract free electrons from ambient plasma and complete a current loop if electrons are emitted back to plasma at the cathodic end of EDT [5]. Unlike the insulated EDTs, the electric current in a bare EDT depends on electron collection by EDT [5, 100-102] and potential drop by emitting devices at the cathodic end [101]. The induced current obeys the OML theory [38]. However, it is found that the existing works estimate the electron collection by assuming (i) the tether is rigid and straight in the local vertical direction, and (ii) the motional electric field E_m is constant along the tether and its value is evaluated at the center of mass of EDT system [6, 40, 103-106]. The differential equation of OML theory is transformed in dimensionless form in these approaches and solved with different approaches [38, 43, 44, 107]. Obviously, the influence of (i) tether geometrical shape and attitude with respect to local vertical direction and (ii) variations of ambient plasmas density and motional electric field along tether is decoupled from the OML theory. To address the deficiency, the motional electric field of a bent and inclined tether was modified by a factor $\alpha \cdot E_m$, where the factor was defined as $\kappa = L^* / L$ (L^* is the shortest distance between two ends of the bent tether and L is the total tether length) [106]. Although simple to implement, this ad hoc technique lacks physical meaning and is not theoretically rigorous. Moreover, although the approach is effective in some cases, this treatment cannot differentiate tethers with different bent profiles with the same end positions.

Second, the thermal perturbation has a remarkable influence on the dynamics and

stability of EDTs. Williams et al. showed that the variation of temperature along the tether strongly influence the dynamics of capture maneuvers [84]. Yu and Jin found that the thermal effect had a quite different dynamic effect during the retrieval of tethered spacecraft [35]. For EDT systems, the diurnal temperature variation of tethers affects the internal stress, conductivity/resistance, and thermal properties. It leads to the variation of electrodynamic force and tether longitudinal oscillation. Sanmartin et al. discussed the simplified tether heating calculation for tape and circular cross-section tethers [8]. Moreover, Kawamoto et al. recommended to investigate the effect of different thermal expansion coefficients on the dynamics of tethers [44]. Considering the thermal effect, Zanutto analyzed the orbital deorbit by EDTs [6]. However, there lacks a unified model that can consider all these coupling effects together.

2.3 Electric Solar Wind Sail System

2.3.1 Dynamic Modeling

The E-sail consists of inter-connected tethers with a main spacecraft at the center of E-sail and remote units at the tips of main tethers. Many efforts have been devoted to the modelling of E-sail [13]. Initially, the E-sail was simplified by modeling the main tethers and remote units at its tip as a spherical rigid pendulum model to investigate attitude dynamic behavior subjected to tether voltage [21, 108]. The complicated dynamic behavior of E-sail caused by tether dynamics is completely omitted. The early study was later expanded by modeling each main tether as a rigid bar to study the coupled orbital-attitude

dynamics of E-sail in a heliocentric transfer mission [21, 109, 110]. However, the rigid bar model ignores the influence of spring effect of tether on the configuration and attitude of E-sail, which is critical for its application in space exploration. To address the challenge, main tethers were modeled by elastic catenary theory, and the shape of main tether was parameterized by the ratios of E-sail force over centrifugal force and spin plane orientation over solar wind direction [111]. In this respect, an interesting mathematical model is developed, and an analytical expression of thrust and torques is obtained for the axisymmetric grid of E-sail [112]. Although effective, both the rigid bar and elastic catenary models cannot describe the slack phenomenon of tethers that may happen dynamically. Furthermore, the analytical solution of elastic catenary exists only in limited cases. To solve the problem, the discretized model of tether has been proposed. A typical approach is to discretize tethers into a series of lumped mass connected by massless springs and dampers [14, 45]. It transforms the nonlinear partial differential equations of a tether system into a set of ordinary differential equations. This is actually a special case of FEM [60]. The current thesis expands the existing work by modeling the E-sail using NPFEM.

2.3.2 Attitude Control

The attitude control of E-sail is realized by modulating the voltage of each main tether individually [14, 45, 108, 113, 114] due to the direction relationship between the applied voltage and the exerted Coulomb force [108, 113]. Different voltage on each main tether results in different Coulomb force, which leads to a turning moment or torque in addition to the thrust. Initially, a scale-factor method through the modulation of voltage is proposed

for the spherical pendulum model of E-sail to change the attitude of E-sail. However, it was found that the attitude of E-sail has a remarkable effect on the spin rate [108]. For example, study shows that a net deceleration or acceleration of spin rate is generated for the inward or outward spiraling orbit, respectively. This is because a Coriolis force is generated when the E-sail inclines to the direction of solar wind with an angle [108, 113, 115]. This effect is equivalent to a small adjustment of tether voltage [45, 108]. Though this scale-factor method helps to understand characteristics of attitude dynamics of E-sail, it is not sufficiently good due to the simplification of the model. For the discretized FEM tether model, the control strategy needs to be modified accordingly. Later, a throttling factor method of the modulation of voltage of each main tether is proposed together with the elastic E-sail's model [45, 113]. It can be observed again that the spin rate increases when the attitude of E-sail completes its attitude maneuvering [45]. For example, the spin rate increases up to 25% from its initial value when the attitude of E-sail reaches 45 deg angle with respect to solar wind direction. The reason is that a thrust component in the spin plane is generated through the modulation of each main tether's voltage [114, 116]. Therefore, three improved design configurations of E-sail system have been proposed to overcome the variation of spin rate caused by the attitude maneuvering of spin plane. The first type is to connect the remote units at the tip of each main tether with non-conductive auxiliary tethers, the thruster at the remote unit is employed to adjust the spin rate [13, 113]. The second type is to assemble photonic blades between main tethers and remote units with or without non-conductive auxiliary tethers [111]. In the third type (called TI model), all main tethers are connected with charged auxiliary tethers at the remote units

where main tethers are electrically connected to auxiliary tethers at every two main tethers [45, 113]. The TI model show promising performance in suppressing the variation of spin rate due to its simple technical hardware and high technical readiness level [45]. Therefore, the TI model of E-sail is adopted in the thesis to suppress variation of spin rate.

2.4 Tether Transportation System

2.4.1 Dynamic Modeling and Libration Suppression

TTS is an attractive alternative to the classical space elevator due to its ability in long-range payload transfer between two spacecraft at low cost [28]. It generally consists of a main spacecraft, a sub spacecraft, and one or multiple climber(s) moving along the tether [29].

Past decades have witnessed many efforts devoted to the dynamics of TTS. Cohen and Misra [117] studied the dynamics of TTS with one climber based on assumption of two-piece dumbbell model. Since then, the influence of TTS parameters, such as, initial libration angles, mass, velocity of moving climber, and tether length, on the dynamic characteristics of TTS has been studied extensively by this two-piece dumbbell model [49, 118]. Cohen and Misra further expended the two-piece dumbbell model by considering the elasticity of tether to investigate the influence of longitudinal and transverse oscillations of tether on the libration of TTS [70]. However, the coupling mechanism of climber moving along the tether was glossily simplified by varying the lengths of two tether segments. Williams [68] replaced the two-piece dumbbell model by a lumped mass model with a viscoelastic-spring element. Two approaches were developed to treat the dynamics of

climber: dynamic and kinematic approaches. The dynamic approach couples the tether and climber dynamics via local force (normal and friction) balance at contact point. The kinematic approach applies position and velocity constraints on tether and climbers. For instance, Sun et al. [48] studied the dynamics of a TTS with one climber by the absolute nodal coordinate formulation. The dynamics of the climber is independently established and the coupling between tether and climber is achieved by projecting the climber's velocity onto the tether with Lagrange multiplier method.

In addition to the one-climber scenario, the case of multiple climbers was also investigated. The concept of multiple climbers with proper phase shift was first proposed to alleviate the libration of TTS in payload transfer [117]. Then, a multibody dynamic model was developed to investigate the effect of transient motion of multiple climbers on the libration of tether [29]. Furthermore, the simultaneous/dual operation of descending and ascending climbers is proposed to suppress the tether libration via canceling the Coriolis forces acting on the tether induced by climbers' motion [47]. Although effective, there are still aspects of TTS with multiple climbers not fully investigated. For example, the orbital radius of Center of Mass (CM) of TTS may vary during the transfer of payloads [118]; the coupling of longitudinal and transverse oscillations of tether are not fully considered [49, 117]; the constraint equations that couples motion of tether and climber are oversimplified [48, 68]; the out-of-plane motion is not considered [52], and the tether model is built at a rotational frame by implying the orbital plane fixed spatially [47, 48, 68], just to name a few. To gain full insight of these areas, a model with high fidelity and ease of implementation is highly desired, which inevitably involves the modeling of tethers

and tethered spacecraft with full dynamics.

In addition to suppressing the libration of TTS with fixed length tether by moving multiple climbers, the alternative approach is by varying tether length. This is because the Coriolis force generated by a moving climber could be canceled by the Coriolis force acting on the sub-spacecraft by deploying or retrieving tether. For example, the deployment of tethered sub-spacecraft produces a positive effect on the libration stability of a TTS, and the retrieval of tether produces a negative effect [118, 119]. This type of three-body tethered space systems was first investigated by a two-piece dumbbell model [120] and then by more comprehensive models [33]. A new suppression strategy by deploying or retrieving of tether at the sub spacecraft was proposed [118]. Furthermore, the optimization of the speed of deployment and retrieval was conducted to control the libration motion of TTS in a fast manner [119]. All these works were done with the two=piece dumbbell model. This thesis will expand the dynamic modeling and libration suppression of TTS by the high-fidelity FEM tether model in arbitrary Lagrangian-Eulerian description, which is developed in this thesis.

Chapter 3 MATHEMATICAL MODELING OF TETHERED SPACECRAFT SYSTEM

Summary: This chapter deals with dynamic modeling of TSS using nodal position finite element method in two situations. One is the TSS with fixed tether length, the other is the TSS with variable tether length.

3.1 Tethered Spacecraft System with Fixed Length

3.1.1 Nodal Position Finite Element Method Formulation

3.1.1.1 Coordinate Systems and Kinematics in Element

Consider the TSS shown in Fig. 3.1, where the tether is discretized into n two-node straight tether elements with (n+1) nodes. Because the tether length is greater than the dimensions of spacecraft by several orders in magnitude, the attitude dynamics of main and sub-spacecraft is ignored. The spacecraft are modeled as lumped masses attached to the first and last nodes, respectively. The motion of each element is described by three generalized coordinate systems: the global geocentric inertial frame of the Earth (*OXYZ*), the Earth-fixed frame (*OX'Y'Z'*) and the local frame of element (*oxyz*). The origin *O* of the global frame is at the Earth's center, where the positive *X*-axis points in the vernal equinox direction, the positive *Z*-axis points to the North and aligns with the rotational axis of the Earth, and the *Y*-axis completes a right-hand coordinate system. The local frame is fixed to the element and defined at the element level and is given in Chapter 4. The Earth-fixed

frame co-rotates with the Earth about the Z-axis of the global geocentric inertial frame, with its Z'-axis coincides with the Z-axis points to the same positive direction.

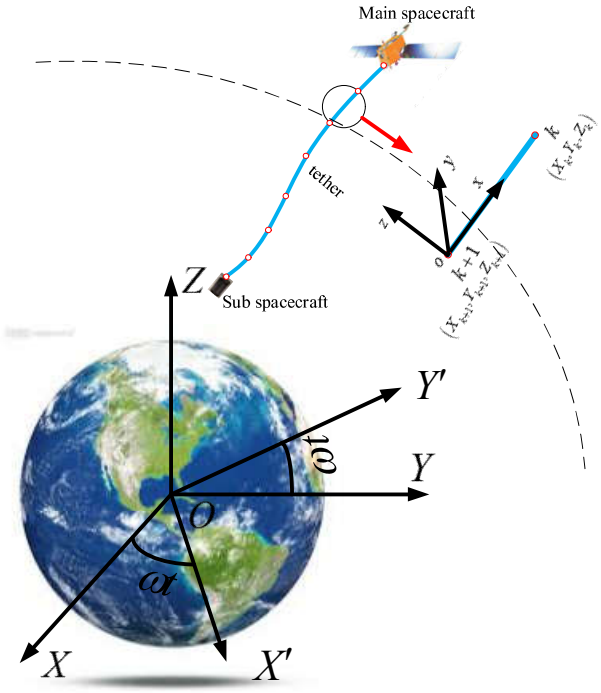

Figure 3.1 Schematic of TSS and the three coordinate systems.

Consider a two-node straight tether element in the global frame. The local frame is defined as follows. The x-axis is aligned with the k-th element and points from the (k+1) node to the k node, the z-axis is perpendicular to the x-axis and the mean velocity vector of the element, and the y-axis completes a right-hand coordinate system. Here, the mean velocity vector of the element is defined as the mean velocity of two nodal velocities. Thus, the geometry and motion of element can be described by nodal positions, velocities, and accelerations in the global frame, such that,

$$\boldsymbol{X} = \boldsymbol{N}_{a,k}\boldsymbol{X}_{a,k} \qquad \boldsymbol{V} = \dot{\boldsymbol{X}} = \boldsymbol{N}_{a,k}\dot{\boldsymbol{X}}_{a,k} \qquad \boldsymbol{A} = \ddot{\boldsymbol{X}} = \boldsymbol{N}_{a,k}\ddot{\boldsymbol{X}}_{a,k} \tag{3.1}$$

where $\boldsymbol{X}=\left(X,Y,Z\right)^T$, $\boldsymbol{V}=\left(V_X,V_Y,V_Z\right)^T$ and $\boldsymbol{A}=\left(A_X,A_Y,A_Z\right)^T$ are the position, velocity and acceleration vectors of an arbitrary point within the element, the subscript *k* denotes the *k-th* element in this chapter, $\boldsymbol{X}_{a,k}=\left(X_k,Y_k,Z_k,X_{k+1},Y_{k+1},Z_{k+1}\right)^T$ is the nodal coordinate vector, $\boldsymbol{N}_{a,k}$ is the shape function matrix, and the symbol of overhead dot denotes the derivatives with respect to time.

The shape function matrix of the *k-th* element is defined as,

$$\boldsymbol{N}_{a,k}=\begin{bmatrix}1-\xi & 0 & 0 & \xi & 0 & 0\\ 0 & 1-\xi & 0 & 0 & \xi & 0\\ 0 & 0 & 1-\xi & 0 & 0 & \xi\end{bmatrix} \tag{3.2}$$

where $\xi = x/L_{a,k}$, $L_{a,k}=\sqrt{\left(X_k-X_{k+1}\right)^2+\left(Y_k-Y_{k+1}\right)^2+\left(Z_k-Z_{k+1}\right)^2}$ is the instantaneous length of the *k-th* element and *x* is the distance of an arbitrary point inside the *k-th* element measured from the *k-th* node.

Thus, the axial Green-Lagrangian strain of the *k-th* element is defined accordingly,

$$\xi_{x,k}=\frac{L_{a,k}-L_{ao,k}}{L_{ao,k}}=\boldsymbol{B}_{a,k}\boldsymbol{X}_{a,k}-1 \tag{3.3}$$

where $L_{ao,k}$ is the original length of the *k-th* element and $\boldsymbol{B}_{a,k}$ is the strain matrix. The strain matrix can be further decomposed into the product of the strain matrix $\boldsymbol{B}_{ao,k}$ in the local frame and the coordinate transformation matrix $\boldsymbol{Q}_k$,

$$\boldsymbol{B}_{a,k} = \boldsymbol{B}_{ao,k}\boldsymbol{Q}_k \tag{3.4}$$

where

$$\boldsymbol{B}_{ao,k} = \begin{bmatrix} -\dfrac{1}{L_{ao,k}} & 0 & 0 & \dfrac{1}{L_{ao,k}} & 0 & 0 \end{bmatrix}$$

$$\boldsymbol{Q}_k = \begin{bmatrix} \cos\theta_x & \cos\theta_y & \cos\theta_z & 0 & 0 & 0 \\ 0 & 0 & 0 & 0 & 0 & 0 \\ 0 & 0 & 0 & 0 & 0 & 0 \\ 0 & 0 & 0 & \cos\theta_x & \cos\theta_y & \cos\theta_z \\ 0 & 0 & 0 & 0 & 0 & 0 \\ 0 & 0 & 0 & 0 & 0 & 0 \end{bmatrix}$$

$$\cos\theta_x = \frac{X_k - X_{k+1}}{L_{a,k}} \qquad \cos\theta_y = \frac{Y_k - Y_{k+1}}{L_{a,k}} \qquad \cos\theta_z = \frac{Z_k - Z_{k+1}}{L_{a,k}}$$

Based on the Hooke's law, the elastic stress in the *k-th* element can be written as,

$$\tau_{x,k} = E_k \varepsilon_{x,k} = \boldsymbol{D}_k \boldsymbol{X}_{a,k} - E_k \,\mathrm{ZXC} \tag{3.5}$$

where E is the Young's modulus of material of the *k-th* element, and $\boldsymbol{D}_k = E_k \boldsymbol{B}_{ao,k}$ is the elastic matrix.

3.1.1.2 Mass Matrix

The mass matrix of *k-th* element is derived from the kinetic energy,

$$T = \frac{1}{2}\int_0^{L_{a,k}} \rho_k A_k \dot{\boldsymbol{X}}_{a,k}^T \dot{\boldsymbol{X}}_{a,k} dx = \frac{1}{2} \dot{\boldsymbol{X}}_{a,k}^T \boldsymbol{M}_{a,k} \dot{\boldsymbol{X}}_{a,k} \tag{3.6}$$

where ρ_k and A_k are the density and cross-section or stress area and $\boldsymbol{M}_{a,k}$ is the mass matrix expressed in the global frame, such that,

$$\boldsymbol{M}_{a,k} = \frac{\rho_k A_k L_{a,k}}{6} \begin{bmatrix} 2 & 0 & 0 & 1 & 0 & 0 \\ 0 & 2 & 0 & 0 & 1 & 0 \\ 0 & 0 & 2 & 0 & 0 & 1 \\ 1 & 0 & 0 & 2 & 0 & 0 \\ 0 & 1 & 0 & 0 & 2 & 0 \\ 0 & 0 & 1 & 0 & 0 & 2 \end{bmatrix} \tag{3.7}$$

It is worth pointing out that the elemental mass matrix is constant in the global frame. This is a remarkably advantage because the matrix needs to be inversed only at the beginning of simulation to reduce computational effort.

3.1.1.3 Stiffness Matrix and Elastic Force Vector

The stiffness matrix of the *k-th* element is derived from the elastic strain energy, such that,

$$U = \frac{1}{2}\int_0^{L_{a,k}} E_k A_k \varepsilon_{x,k}^2 dx = \frac{1}{2}\boldsymbol{X}_{a,k}^T \boldsymbol{K}_{a,k} \boldsymbol{X}_{a,k} - \boldsymbol{X}_{a,k}^T \boldsymbol{F}_{e,k} + \frac{1}{2} E_k A_k L_{ao,k} \tag{3.8}$$

where the subscript k denoting the *k-th* element, E_k is the Young's modulus of element, $\boldsymbol{K}_{a,k}$ is the stiffness matrix and $\boldsymbol{F}_{e,k}$ is the generalized nodal elastic force vector resulting from the elasticity of *k-th* element in the global frame. The third constant term at the right-hand side of above equation is constant and has no effect in deriving stiffness matrix.

From Eq. (3.8), the stiffness matrix and generalized nodal force vector due to elastic strain can be expressed as,

$$\boldsymbol{K}_{a,k} = E_k A_k \boldsymbol{B}_{a,k}^T \boldsymbol{B}_{a,k} = E_k A_k \boldsymbol{Q}_k^T \boldsymbol{B}_{ao,k}^T \boldsymbol{B}_{ao,k} \boldsymbol{Q}_k = \boldsymbol{Q}_k^T \boldsymbol{K}_{ao,k} \boldsymbol{Q}_k \tag{3.9}$$

$$\boldsymbol{K}_{ao,k} = E_k A_k \boldsymbol{B}_{ao,k}^T \boldsymbol{B}_{ao,k} = \frac{E_k A_k}{L_{ao,k}} \begin{bmatrix} 1 & 0 & 0 & -1 & 0 & 0 \\ 0 & 0 & 0 & 0 & 0 & 0 \\ 0 & 0 & 0 & 0 & 0 & 0 \\ -1 & 0 & 0 & 1 & 0 & 0 \\ 0 & 0 & 0 & 0 & 0 & 0 \\ 0 & 0 & 0 & 0 & 0 & 0 \end{bmatrix}$$

and

$$\boldsymbol{F}_{e,k} = E_k A_k L_{ao,k} \boldsymbol{B}_{a,k}^T = E_k A_k L_{ao,k} \boldsymbol{Q}_k^T \boldsymbol{B}_{ao,k}^T \tag{3.10}$$

where $\boldsymbol{B}_{ao,k}$, $\boldsymbol{Q}_k$ and $\boldsymbol{K}_{ao,k}$ are defined in Eqs. (3.4) and (3.9), respectively. It is worth noting that the $\boldsymbol{B}_{ao,k}$ and $\boldsymbol{K}_{ao,k}$ are the same as the strain and stiffness matrices of conventional two-node truss element. This makes the NPFEM easy to be integrated into existing general-purpose FEM codes.

3.1.1.4 Gravitational Force

The gravitational force exerted on TSS can be derived from the Earth's non-homogeneous gravitational potential [121], such that,

$$U = \frac{\mu_g}{r}\left(1 + \sum_{l=2}^{N_g}\sum_{m=0}^{l}\left(\frac{R_\oplus}{r}\right)^l P_{l,m}\left[\sin(\phi)\right]\left[C_{l,m}\cos(m\lambda) + S_{l,m}\sin(m\lambda)\right]\right) \tag{3.11}$$

where μ_g is the gravitational constant of the Earth (μ_g=3.9873483576×10^{14} m^3/s^2), N_g = 35 is the order of gravitational field, $R_\oplus$ and r are the Earth's mean equatorial radius($R_\oplus$ = 6.378137×10^6 m) and the distance from an arbitrary point of the element to the Earth's center, $P_{l,m}$ is the classical associated Legendre polynomials, $C_{l,m}$ and $S_{l,m}$ are the harmonic

coefficients resulted from the long-term spacecraft observation, ϕ and λ are the latitude and longitude of an arbitrary point in the element in the Earth-fixed frame, respectively.

By taking the partial derivatives of Eq. (3.11) with respect to spherical coordinate variables r, ϕ, λ, the gravitational acceleration vector $\boldsymbol{g}_s = \left\{ g_r, g_\phi, g_\lambda \right\}^T$ can be expressed in the Earth-fixed frame in term of spherical coordinates,

$$\begin{aligned} g_r &= -\frac{\mu_g}{r^2}\left(1+\sum_{l=2}^{N_g}\sum_{m=0}^{l}\left(\frac{R_\oplus}{r}\right)^l (l+1)P_{l,m}\left[\sin(\phi)\right]\left[C_{l,m}\cos(m\lambda)+S_{l,m}\sin(m\lambda)\right]\right) \\ g_\phi &= = -\frac{\mu_g}{r^2}\left(\sum_{l=2}^{N_g}\sum_{m=0}^{l}\left(\frac{R_\oplus}{r}\right)^l \left\{P_{l,m+1}\left[\sin(\phi)\right]-m\tan(\phi)P_{l,m}\left[\sin(\phi)\right]\right\}\times \right. \\ &\qquad \left. \left[C_{l,m}\cos(m\lambda)+S_{l,m}\sin(m\lambda)\right]\right) \\ g_\lambda &= -\frac{\mu_g}{r^2\cos\phi}\left(\sum_{l=2}^{N_g}\sum_{m=0}^{l}\left(\frac{R_\oplus}{r}\right)^l mP_{l,m}\left[\sin(\phi)\right]\left[-C_{l,m}\sin(m\lambda)+S_{l,m}\cos(m\lambda)\right]\right) \end{aligned} \tag{3.12}$$

where.

Accordingly, the nodal gravitational force vector can be derived from the virtual work done by the gravitational force for the *k-th* element, such that,

$$\delta W_g = \int_0^{L_{a,k}} \delta \boldsymbol{X}_{a,k}^T \rho_k \boldsymbol{g}_{g,k} A dx = \delta \boldsymbol{X}_{a,k}^T \boldsymbol{F}_{g,k} \tag{3.13}$$

$$\boldsymbol{F}_{g,k} = \int_0^{L_{a,k}} \boldsymbol{N}^T \rho_k \boldsymbol{g}_{g,k} A_k dx = \frac{\rho_k A_k L_{a,k}}{2}\sum_{i=1}^{N_{GA}} w_i \boldsymbol{N}^T\left[\frac{L_{a,k}}{2}\left(1+\xi_i\right)\right]\boldsymbol{g}_{g,k}\left[\frac{L_{a,k}}{2}\left(1+\xi_i\right)\right] \tag{3.14}$$

where $\boldsymbol{g}_{g,k}$ and $\boldsymbol{F}_{g,k}$ are the gravitational acceleration and nodal gravitational force vectors in the global frame, and (w_i, ξ_i) are the Gaussian integration weights and abscissae, respectively. N_{GA} is the order of Gaussian integration points that will be presented in the simulation part.

The transformation of gravitational acceleration vector from the spherical form of the Earth-fixed frame to the global inertial frame is defined by,

$$\boldsymbol{g}_{g,k} = \boldsymbol{T}_{f2g}\boldsymbol{g}_{f,k} = \boldsymbol{T}_{f2g}\boldsymbol{T}_{s2f}\boldsymbol{g}_{s,k} \tag{3.15}$$

$$\boldsymbol{T}_{s2f} = \begin{bmatrix} \cos\phi\cos\lambda & -\sin\phi\cos\lambda & -\sin\lambda \\ \cos\phi\sin\lambda & -\sin\phi\sin\lambda & \cos\lambda \\ \sin\phi & \cos\phi & 0 \end{bmatrix} \tag{3.16}$$

$$\boldsymbol{T}_{f2g} = \begin{bmatrix} \cos\omega_z t & -\sin\omega_z t & 0 \\ \sin\omega_z t & \cos\omega_z t & 0 \\ 0 & 0 & 1 \end{bmatrix} \tag{3.17}$$

where $\boldsymbol{T}_{s2f}$ is the transformation matrix from spherical to Cartesian coordinates in the Earth-fixed frame, $\boldsymbol{T}_{f2g}$ is the transformation matrix from the Earth-fixed frame to the global frame, $r = \sqrt{X^2 + Y^2 + Z^2}$, and ω_z is the z-axis component of angular rotational velocity vector of the Earth, respectively.

3.1.2 Equation of Motion

The finite element equation of motion of TSS is derived from the principle of virtual work, such that

$$\delta U - \delta T - \delta W_g = 0 \tag{3.18}$$

Substituting Eqs. (3.6), (3.8), and (3.13) into Eq. (3.18) leads to the finite element equation of motion for the *k-th* element as,

$$\boldsymbol{M}_{a,k}\ddot{\boldsymbol{X}}_{a,k} + \boldsymbol{K}_{a,k}\boldsymbol{X}_{a,k} = \boldsymbol{F}_{e,k} + \boldsymbol{F}_{g,k} \tag{3.19}$$

Once the equation of motion of *k-th* element of TSS is obtained, then the equation

of motion for the TSS can be obtained by assembling Eq. (3.19) by standard FEM assembly procedures as listed in Eq. (3.20). The spacecraft attached to each end of the tether is assumed as a lumped mass without attitude, then the masses of lumped body are added into the mass matrix of tether,

$$\boldsymbol{M}_a\ddot{\boldsymbol{X}}_a + \boldsymbol{K}_a\boldsymbol{X}_a = \boldsymbol{F}_e + \boldsymbol{F}_g \tag{3.20}$$

where $\boldsymbol{M}_a$ and $\boldsymbol{K}_a$ are the global mass and stiffness matrices of EDT, $\boldsymbol{X}_a$ and $\ddot{\boldsymbol{X}}_a$ are the vectors of position coordinates and the corresponding acceleration of EDT, $\boldsymbol{F}_e$ and $\boldsymbol{F}_g$ are the vectors of global elastic and gravitational forces, respectively.

Since there is damping in any structural system, we introduce a damping matrix into the equation of motion in Eq. (3.20),

$$\boldsymbol{M}_a\ddot{\boldsymbol{X}}_a + \boldsymbol{C}_a\dot{\boldsymbol{X}}_a + \boldsymbol{K}_a\boldsymbol{X}_a = \boldsymbol{F}_e + \boldsymbol{F}_g \tag{3.21}$$

The damping matrix $\boldsymbol{C}_a$ is calculated using Rayleigh damping model, such that,

$$\boldsymbol{C}_a = \beta\boldsymbol{M}_a + \gamma\boldsymbol{K}_a \tag{3.22}$$

where β and γ are the Rayleigh damping coefficients, respectively.

It is worth pointing out that the fundamental variables in NPFEM are changed to nodal position coordinates instead of nodal displacements in conventional FEMs. Furthermore, the global mass matrix $\boldsymbol{M}_a$ in Eq. (3.22) is constant, which is advantageous in term of numerical integration. Equation (3.22) is highly nonlinear because the matrix of stiffness and the force vectors depend on the current position $\boldsymbol{X}_a$ and velocity $\dot{\boldsymbol{X}}_a$, and has to be solved numerically. The damping matrix coefficients β and

γ are set as zero due to the unknown damping coefficient of tether material in space.

3.1.3 Symplectic Runge-Kutta Time Integrator

The equation of motion of the TSS will be solved numerically by a Symplectic 4th order Runge-Kutta Gaussian-Legendre scheme. Assume $\boldsymbol{P}_a = \boldsymbol{M}_a \dot{\boldsymbol{X}}_a$ and substitute it into Eq. (3.20) lead to two first-order differential equations as follows,

$$\begin{cases} \dot{\boldsymbol{X}}_a = \boldsymbol{M}_a^{-1} \boldsymbol{P}_a \\ \dot{\boldsymbol{P}} = \boldsymbol{F}_e + \boldsymbol{F}_g - \boldsymbol{K}_a \boldsymbol{X}_a \end{cases} \tag{3.23}$$

Define a vector with new states $\boldsymbol{Z}_a = \left(\boldsymbol{X}_a, \boldsymbol{P}_a\right)^T$ and substitute it into Eq. (3.23). Then, the equation of motion of the TSS and its initial condition become:

$$\begin{cases} \dot{\boldsymbol{Z}}_a = \boldsymbol{F}\left(t, \boldsymbol{Z}_a\right) \\ \boldsymbol{Z}_a\left(t_0\right) = \left[\boldsymbol{X}_a\left(t_0\right), \boldsymbol{P}_a\left(t_0\right)\right]^T \end{cases} \tag{3.24}$$

where

$$\boldsymbol{F}\left(t, \boldsymbol{Z}_a\right) = \begin{bmatrix} \boldsymbol{0} & \boldsymbol{M}_a^{-1} \\ -\boldsymbol{K}_a & \boldsymbol{0} \end{bmatrix} \boldsymbol{Z}_a + \begin{pmatrix} \boldsymbol{0} \\ \boldsymbol{F}_e + \boldsymbol{F}_g \end{pmatrix}$$

A two-stage Runge-Kutta Gaussian-Legendre integration scheme is adopted here. It is defined by its weight coefficients $b_j = \left(b_1, b_2\right)$ at abscissae $c_j = \left(c_1, c_2\right)$ and an integration matrix $a_{2\times 2}$ [122]. It has been proved that the Runge-Kutta method is Symplectic if these coefficients satisfy the following relationship [123], such that,

$$b_i a_{ij} + b_j a_{ji} - b_{ij} = 0 \quad i, j = 1, 2 \tag{3.25}$$

As Ref. [122] presented that the conditions in Eq. (3.25) can only be satisfied by

the implicit scheme [122, 123]. Thus, the implicit Runge-Kutta with Gaussian-Legendre collation has a characterization of symmetric and Symplectic. Although it requires more computational efforts due to the iteration at each interval than the explicit method, the implicit scheme could use a large time-step size stably to compensate for the extra computation cost.

3.1.4 Numerical Results and Discussion

To examine the robust of proposed approach, two benchmark tests were conducted. The benchmark study was based on a TSS and their physical properties are shown in Table 3.1. The CM of TSS is assumed flying in a circular polar orbit with an altitude of 500km. The initial latitude and longitude of the orbital plane are 90 degrees. Furthermore, the tether is assumed to align with the local vertical with the main spacecraft on the top and the sub spacecraft at the bottom. The initial velocity and acceleration at each node of the tether, main and sub spacecraft are calculated based on the steady state of the TSS in that orbit. In this chapter, the hybrid mass model is used, which denotes a consistent mass matrix for the tether and a lumped mass model for the main and sub spacecraft. Furthermore, the tolerance and the maximum iteration number of Newton iteration within each time step were set up to 10^{-13} and 100, respectively.

Table 3.1 Physical properties of TSS

Parameters	Values
Mass of main spacecraft (kg)	5.0
Mass of sub spacecraft (kg)	1.75
Mass of the tether (kg)	0.25
Tether length (m)	500

Diameter of the tether (m)	0.0005
Dimensions of the main spacecraft (m)	0.2×0.2×0.2
Dimensions of the sub spacecraft (m)	0.1×0.17×0.1
Elastic modulus of the tether (N/m^2)	7.2×10^{10}
Initial orbit latitude (deg) / altitude (km)	90/500

Two cases are considered with and without the effect of Earth's oblateness. Non-conservative forces such as the atmosphere drag and electrodynamic forces were not included in this chapter, which implies the total energy of the TSS will be conservative and the main spacecraft and sub spacecraft connected by a constant length tether will maintain in the initial orbit. The TSS is modeled by NPFEM and solved by the implicit 4^{th} order Symplectic Gaussian-Legendre Runge-Kutta algorithm using parallel in-house developed codes (IGLRK_S). The analysis results are compared with the results from an explicit 4^{th} order Runge-Kutta integrator (ERK4_NS).

It is noted in the simulation that an artificial axial vibration in the tether was introduced by the discretization of the tether, namely, the approximation of the continuous gravitational force into the equivalent nodal force vector. The initial vibration has an important effect to the accuracy of the analysis, because there is no damping in the TSS to damp it out. Two major parameters are found to contribute the vibration, namely, (i) the order of Gaussian integration in evaluating the nodal gravitational force vector within each element and (ii) the number of tether elements. Although the increase of the order of Gaussian integration and tether element numbers will improve the accuracy of nodal force evaluation, the associated computational loads will have a detrimental effect on the long-term simulation of the tethered spacecraft. To find a good balance between accuracy and

computational loads, these two effects are examined and shown in Fig. 3.2, where the vertical axis is the variation of the altitude of main spacecraft versus its initial position using different order of Gaussian integration and tether element numbers. As shown in Fig. 3.2(a), the vibration of tether with only one tether element is reduced as the order of Gaussian integration increases and the difference between fourth and fifth order of Gaussian integration is negligible. Hence, fifth order Gaussian integration are used in the following calculations. Figure 3.2(b) shows that the vibration is almost eliminated as the element number increases to 32. Thus, the tether is divided into 32 elements in the following cases.

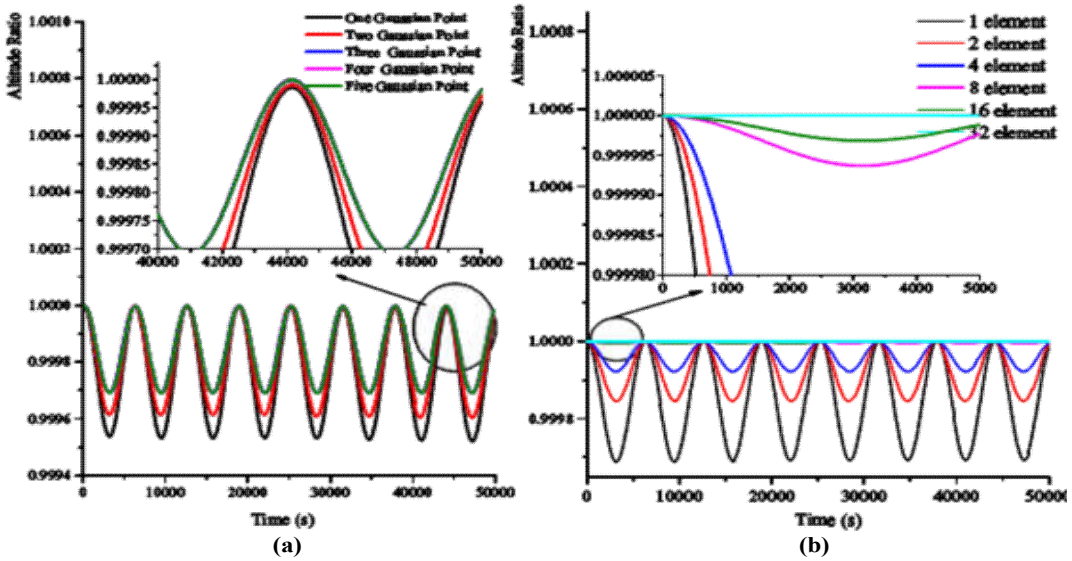

Figure 3.2 Altitude of main spacecraft (normalized by the initial altitude). (a) Sensitivity of order of Gaussian integration with one tether element. (b) Sensitivity of element numbers with fifth order Gaussian integration per element.

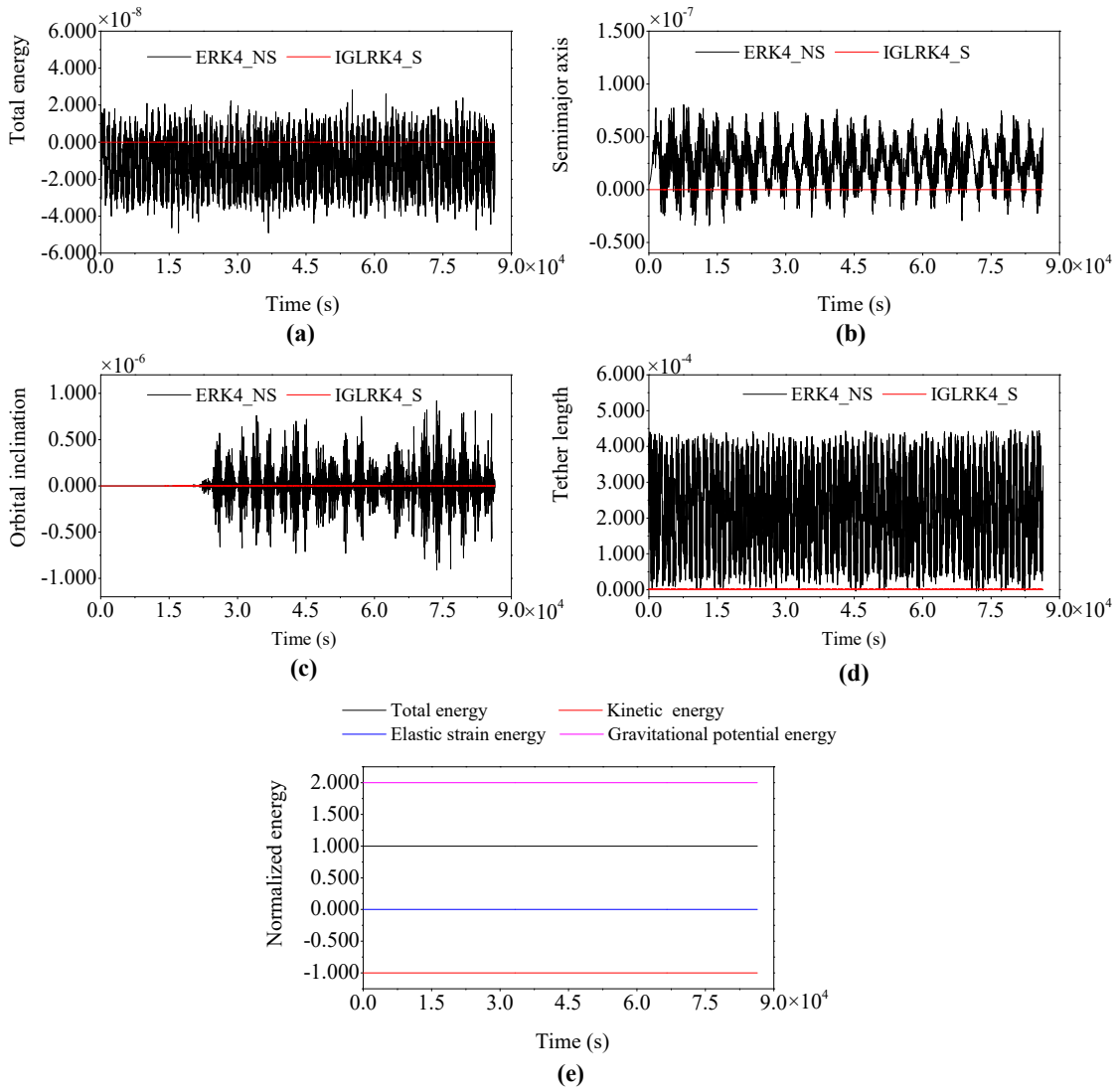

Figure 3.3 The relative error against time. (a) Total system energy. (b) Orbital semi-major axis, (c) Orbital inclination (d) Tether length. (e) The normalized energy components of tethered system by the Symplectic integrator.

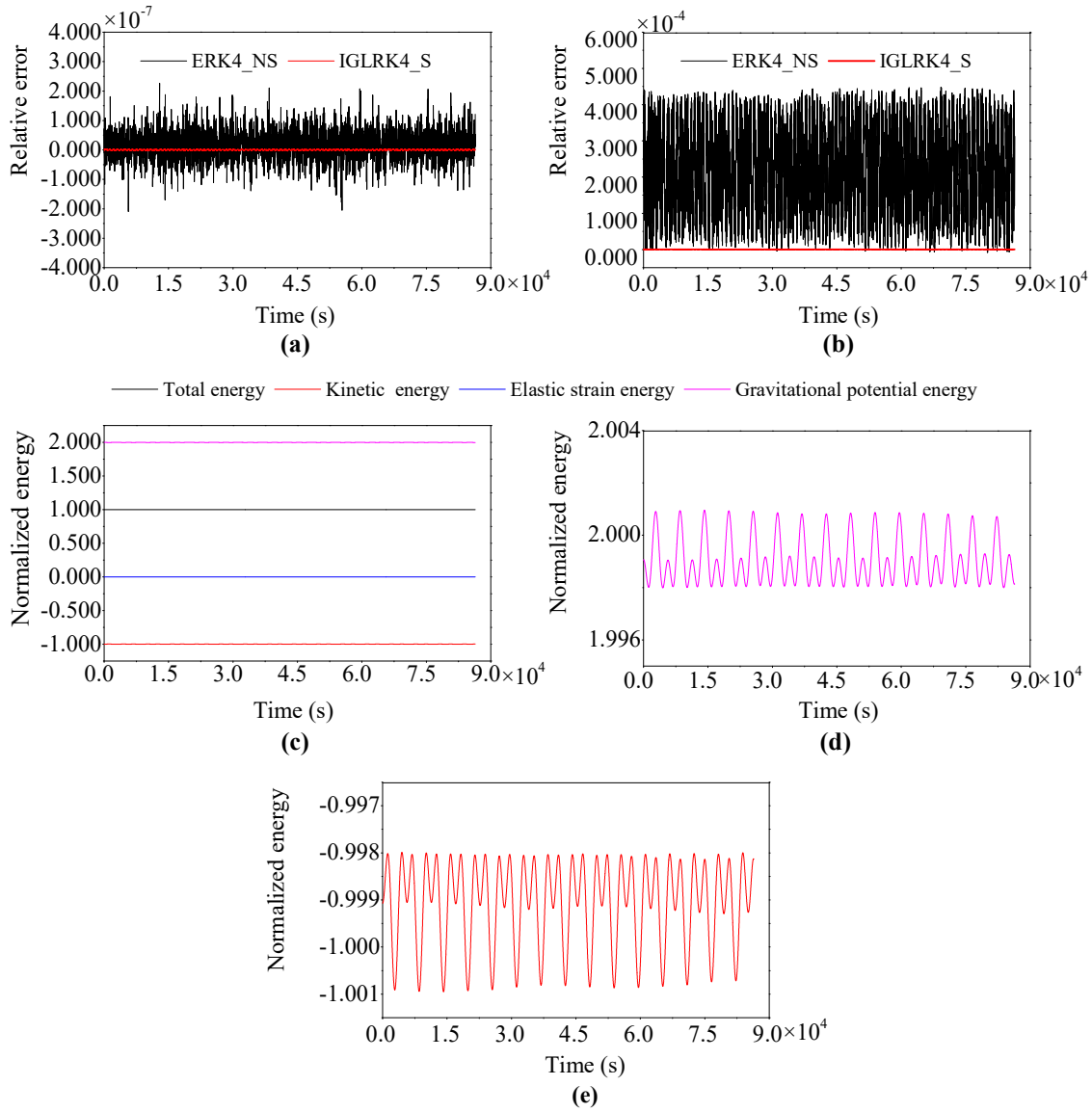

Figure 3.4 The relative error of total system energy and tether length. (c)-(e) The energy transfer of IGLRK4_S method (normalized by the initial total energy value) of tethered system with EGM2008 model

In the first case, the central gravity field is employed, the time step size for the two integration methods were both set to 0.001s and the simulation period was 86,400s. The total number of integration step has reached 8.64 million, which is sufficiently large to

evaluate the performance character with different integrators. The robust of the proposed approach is further examined by the system energy, orbital parameters of system and the tether length. Without any external perturbative force, those parameters such as system's orbital parameters, total energy and tether length should be constant all the time. The initial total energy, the system orbital semi-major axis, inclination and the initial tether length are -2.245633468×10^{8} J, 6.878816122×10^{6}m, 90 degrees and 500m, respectively. As expected, the TSS is a conservative system. Figure 3.3(a-d) shows the comparisons of relative error of system parameters by two integration schemes. It shows that the 4^{th} order Symplectic implicit Gaussian Legendre Runge-Kutta method is superior to the 4^{th} order Explicit Runge-Kutta scheme method. The system parameters maintain constant in the IGLRK4_S while they vary in the ERK4_NS. The total energy of the system consists of the gravitational potential and kinetic energy of the spacecraft as well as the elastic potential energy of the tether. Figure 3.3 (e) plots the energy transfer for the whole period by the IGLRK4_S method. It shows that the total energy of system and its three components are constant over the time as expected. Therefore, the 2-stage Gaussian-Legendre Runge-Kutta integration possesses the global numerical stability and high accuracy.

In the second case, the perturbative effect of Earth oblateness is considered by using the high-fidelity gravity model (EGM2008 model with up to degree 35 and order 35). The TSS is found oscillating around its equilibrium position due to the periodic perturbative gravity force. Figure 3.4(a-b) shows the relative error of system total energy and the tether length. The results verify the fact that the entire system is still conservative even under the perturbative effect of the Earth oblateness. Moreover, it shows that the tether length is

constant all the time, which indicates that the properties of energy conservation and accuracy of the Symplectic IGLRK4_S method are superior to the ERK4_NS. Furthermore, Figure 3.4(c-e) shows the energy transfer within the system (normalized by the initial total energy -2.247723873E$\times 10^8$ J). Although the perturbative gravity force causes the periodic variations of gravitational potential energy and kinetic energy show in Fig. 3.4 (c-e), the total energy of the system is always conservative and constant over the time. Finally, the analyses demonstrate that the proposed numerical approach by NPFEM and the 2-stage Gaussian-Legendre Runge-Kutta integration is globally stable and is suitable for the long-term dynamic simulations of tethered spacecraft.

3.2 Tethered Spacecraft System with Variable Length

3.2.1 Arbitrary Lagrangian-Eulerian Finite Element Method

3.2.1.1 Arbitrary Lagrangian-Eulerian Description

Consider climbers moving along the tether as shown in Fig. 3.5. First, taking the *k-th* element as an example, the position inside an element can be expressed by linear interpolation function with nodal coordinates,

$$\boldsymbol{X} = \boldsymbol{N}_{a,k}\boldsymbol{X}_{a,k} \tag{3.26}$$

where $\boldsymbol{X}_{a,k} = \left(X_k, Y_k, Z_k, X_{k+1}, Y_{k+1}, Z_{k+1}\right)^T$ is the vector of nodal coordinates of *k-th* element, and $\boldsymbol{N}_{a,k}$ is the shape function matrix [43, 67],

$$\boldsymbol{N}_{a,k} = \left[\frac{1-\xi}{2}\boldsymbol{I}_{3\times 3}, \frac{1+\xi}{2}\boldsymbol{I}_{3\times 3}\right] \tag{3.27}$$

where $\boldsymbol{I}_{3\times3}$ is the 3×3 identity matrix and $\xi\in[-1,1]$ denotes the dimensionless position inside the element.

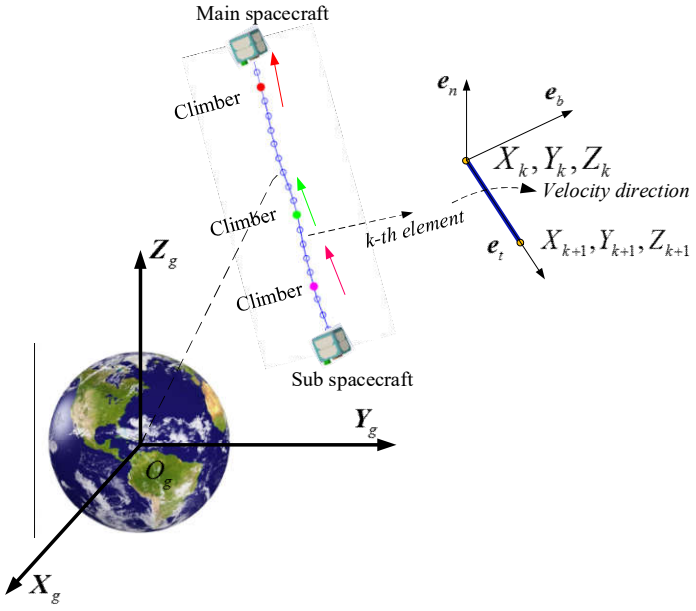

Figure 3.5 Tethered spacecraft system with climbers

Next, define a material coordinate p in the ALE description. The material coordinate p of an arbitrary point inside the k-th element can be defined as,

$$p=\frac{1-\xi}{2}p_k(t)+\frac{1+\xi}{2}p_{k+1}(t)\quad -1\le\xi\le1 \tag{3.28}$$

where $p_k(t)$ and $p_{k+1}(t)$ are the time varying material coordinates associated with the nodal points k and k+1.

Then, the dimensionless parameter ξ can be expressed by the material coordinates [124],

$$\xi = \frac{2p - p_k(t) - p_{k+1}(t)}{p_{k+1}(t) - p_k(t)} \tag{3.29}$$

Therefore, the position of an arbitrary point inside the *k-th* element can be rewritten in term of material coordinate,

$$\boldsymbol{X} = \boldsymbol{N}_{a,k}\left[p, p_k(t), p_{k+1}(t)\right]\boldsymbol{X}_{a,k} \tag{3.30}$$

The associated velocity and acceleration of this point can be derived as,

$$\dot{\boldsymbol{X}} = \boldsymbol{N}_{a,k}\dot{\boldsymbol{X}}_{a,k} + \frac{\partial \boldsymbol{N}_{a,k}}{\partial t}\boldsymbol{X}_{a,k} = \boldsymbol{N}_{e,k}\dot{\boldsymbol{X}}_{e,k} \tag{3.31}$$

$$\ddot{\boldsymbol{X}} = \frac{d}{dt}\left[\boldsymbol{N}_{a,k}\dot{\boldsymbol{X}}_{a,k} + \left(\frac{\partial \boldsymbol{N}_{a,k}}{\partial p_k}\dot{p}_k + \frac{\partial \boldsymbol{N}_{a,k}}{\partial p_{k+1}}\dot{p}_{k+1}\right)\boldsymbol{X}_{a,k}\right] = \boldsymbol{N}_{e,k}\ddot{\boldsymbol{X}}_{e,k} + \boldsymbol{a}_{p,\mathrm{k}} \tag{3.32}$$

$$\begin{aligned}\boldsymbol{a}_{p,\mathrm{k}} = {} & 2\left(\frac{\partial \boldsymbol{N}_{a,k}}{\partial p_k}\dot{p}_k + \frac{\partial \boldsymbol{N}_{a,k}}{\partial p_{k+1}}\dot{p}_{k+1}\right)\dot{\boldsymbol{X}}_{a,k} + \\ & \left(\frac{\partial^2 \boldsymbol{N}_{a,k}}{\partial p_k^2}\dot{p}_k^2 + 2\frac{\partial^2 \boldsymbol{N}_{a,k}}{\partial p_k \partial p_{k+1}}\dot{p}_k\dot{p}_{k+1} + \frac{\partial^2 \boldsymbol{N}_{a,k}}{\partial p_{k+1}^2}\dot{p}_{k+1}^2\right)\boldsymbol{X}_{a,k}\end{aligned} \tag{3.33}$$

where $\boldsymbol{N}_{e,k} = \left(\boldsymbol{N}_{a,k}, \frac{\partial \boldsymbol{N}_{a,k}}{\partial p_k}\boldsymbol{X}_{a,k}, \frac{\partial \boldsymbol{N}_{a,k}}{\partial p_{k+1}}\boldsymbol{X}_{a,k}\right)$ is the extended shape function matrix, $\boldsymbol{X}_{e,k} = \left(\boldsymbol{X}_{a,k}^T, p_k, p_{k+1}\right)^T$ is the extended vector of nodal coordinate, $\dot{\boldsymbol{X}}_{e,k}$ and $\ddot{\boldsymbol{X}}_{e,k}$ are the extended vectors of velocity and acceleration respectively, and $\boldsymbol{a}_{p,\mathrm{k}}$ is the additional term associated with rate of material coordinates at both ends of the *k-th* element [124], and it contains five terms.

3.2.1.2 Extended Mass Matrix and Inertia Force

The extended mass matrix is derived from the virtual work done by inertial force,

$$\delta W_i = \int_{p_k}^{p_{k+1}} \delta \boldsymbol{X}_{e,k}^T \rho_k A_k \ddot{\boldsymbol{X}} dp = \int_{p_k}^{p_{k+1}} \delta \boldsymbol{X}_{e,k}^T \rho_k A_k \ddot{\boldsymbol{X}} dp = \delta \boldsymbol{X}_{e,k}^T \left(\boldsymbol{M}_{e,k} \ddot{\boldsymbol{X}}_{e,k} + \boldsymbol{F}_{p,k} \right) \quad (3.34)$$

where the subscript *k* denotes the *k-th* element, ρ_k and A_k are the density and cross-section or stress area of *k-th* element, $\delta \boldsymbol{X}_{e,k}$ is the virtual displacement where the symbol δ represents the variational operator, $\boldsymbol{M}_{e,k}$ is the extended mass matrix of the *k-th* element in the global frame, $\boldsymbol{F}_{p,k}$ is the additional inertial force caused by the mass flow of the material points, which is associated with variation of the material coordinate of *k-th* element. The detailed expressions of mass matrix and inertial force are

$$\boldsymbol{M}_{e,k} = \begin{bmatrix} \boldsymbol{M}_{11} & \boldsymbol{M}_{12} & \boldsymbol{M}_{13} \\ \boldsymbol{M}_{12}^T & \boldsymbol{M}_{22} & \boldsymbol{M}_{23} \\ \boldsymbol{M}_{12}^T & \boldsymbol{M}_{23}^T & \boldsymbol{M}_{33} \end{bmatrix} \quad (3.35)$$

where the sub-matrix $\boldsymbol{M}_{11}$ is the same as Eq. (3.7) in the NPFEM, the other sub-matrices are defined in Appendix A.

$$\boldsymbol{F}_{p,k} = \frac{p_{k+1} - p_k}{2} \int_{-1}^{1} \rho_k A_k \boldsymbol{N}_{e,k}^T \boldsymbol{a}_{p,k} d\xi = \sum_{j=1}^{5} \boldsymbol{F}_{p,k}^j \quad (3.36)$$

where $\boldsymbol{F}_{p,k}^j \left(j = 1, \ldots 5 \right)$ can be found in Appendix B.

3.2.1.3 Elastic Force

The vector of elastic force can be derived from the virtual work done by the elastic force, such that,

$$\delta W_e = -\int_{p_k}^{p_{k+1}} \delta \boldsymbol{\varepsilon}^T \boldsymbol{\sigma} A_k dp = -\delta \boldsymbol{X}_{e,k}^T \boldsymbol{F}_{e,k} \quad (3.37)$$

where $\boldsymbol{F}_{e,k}$ is the vector of elastic force.

$$\boldsymbol{F}_{e,k} = \frac{p_{k+1} - p_k}{2} \int_{-1}^{1} E_k A_k \left(\varepsilon + c\dot{\varepsilon}\right) \left(\frac{\partial \varepsilon}{\partial \boldsymbol{X}_{e,k}} \right)^T d\xi \tag{3.38}$$

$$\varepsilon = \frac{1}{2}\left(\boldsymbol{X}_k'^T \boldsymbol{X}_k' - 1 \right) = \frac{1}{2}\left[\left(\frac{2}{p_{k+1} - p_k} \right)^2 \boldsymbol{X}_{a,k}^T \left(\frac{\partial \boldsymbol{N}_{a,k}}{\partial \xi} \right)^T \left(\frac{\partial \boldsymbol{N}_{a,k}}{\partial \xi} \right) \boldsymbol{X}_{a,k} - 1 \right] \tag{3.39}$$

where ε is the Green strain due to its axial deformation of tether, and $\dot{\varepsilon}$ is its rate. c is the damping coefficient of tether material.

Substituting Eq. (3.39) into Eq. (3.38) yields the elastic force vector $\boldsymbol{F}_{e,k} = \left(\boldsymbol{F}_{e,k}^1, \boldsymbol{F}_{e,k}^2, \boldsymbol{F}_{e,k}^3 \right)^T$, their detailed information can be found in Appendix C.

3.2.1.4 Gravitational Force

The vector of gravitational force is derived from the virtual work done by the gravitational force, such that,

$$\delta W_g = \int_{p_k}^{p_{k+1}} \delta \boldsymbol{X}_{e,k}^T \boldsymbol{f}_{g,k} A_k dp = \delta \boldsymbol{X}_{e,k}^T \boldsymbol{F}_{g,k} \tag{3.40}$$

$$\boldsymbol{F}_{g,k} = \frac{p_{k+1} - p_k}{2} \int_{-1}^{1} \boldsymbol{N}_{e,k}^T \boldsymbol{f}_{g,k} d\xi \tag{3.41}$$

where $\boldsymbol{F}_{g,k}$ is the vector of gravitational force as listed in Appendix D, and $\boldsymbol{f}_g = \rho_k A_k \boldsymbol{g}_{g,k}$ is the gravitational force per unit length, and $\boldsymbol{g}_{g,k}$ is the vector of gravitational acceleration as listed in Eq. (3.15).

3.2.2 Equation of Motion

Based on the principle of D'Alembert, the sum of the virtual work done by the inertial and applied forces on the virtual displacements of TSS should be zero at any arbitrary moment,

that is,

$$\delta W_e + \delta W_g - \delta W_i = 0 \tag{3.42}$$

where δW_e, δW_g, and δW_i are the virtual work done by the elastic, gravity, and inertial forces, respectively,

Substituting Eqs. (3.34)-(3.40) into Eq. (3.42) yields the equation of motion of *k-th* element in the global inertial coordinate system [75],

$$\boldsymbol{M}_{e,k}\ddot{\boldsymbol{X}}_{e,k} = \boldsymbol{F}_{e,k} + \boldsymbol{F}_{g,k} - \boldsymbol{F}_{p,k} \tag{3.43}$$

It should be noted that there are two major differences between the NPFEM-ALE and the existing NPFEM [75]. First, the extended mass matrix $\boldsymbol{M}_{e,k}$ of *k-th* element is no longer a constant matrix as it is in the NPFEM. The rank of $\boldsymbol{M}_{e,k}$ is six while its dimension is 8×8, which indicates that normal solvers, such as the Symplectic Runge-Kutta method, does not work because it requires the inversion of mass matrix [43, 67]. Second, there is an additional force term $\boldsymbol{F}_{p,k}$ generated by the variation of its material coordinate caused by the length variation. This term vanishes when the material coordinates of *k-th* and (*k+1*)*-th* nodes are constant.

Once the equation of motion of the *k-th* element are obtained, the equations of motion of the TSS can be obtained by assembling Eq. (3.43) with the standard assembly procedure in FEM [67, 75],

$$\boldsymbol{M}_e\ddot{\boldsymbol{X}}_e = \boldsymbol{F}_e + \boldsymbol{F}_g - \boldsymbol{F}_p \tag{3.44}$$

where $\boldsymbol{M}_e$ is the extended and rank deficient mass matrix of TSS, $\ddot{\boldsymbol{X}}_e$ is the vector of

acceleration of TSS, $\boldsymbol{F}_e$, $\boldsymbol{F}_g$, and $\boldsymbol{F}_p$ are the vectors of elastic, gravitational, and time-varying material coordinate induced forces. It should be noted the internal damping of the tether is not considered due to the lack of experimental data in space. Nonetheless, the damping effect suppresses the disturbance to TSS. Thus, the neglection of damping will not affect the validation of current method. In addition, the material coordinate of tether increases monotonically from the first node (main spacecraft) to the (n+1)-*th* node (sub spacecraft). The damping coefficient c of tether material is temporal set as zero due to unknown damping coefficient of tether material in space.

3.2.3 Constraint Equations for Material Points

The coupling of climber and tether dynamics is achieved by enforcing the kinematic relationship between climber and material coordinate of tether. There are two types of nodes are defined to deal with the climbers. One type is the moving nodes representing the climbers moving along tether or tether deployment and retrieval, where the material coordinate varies. The other type is the normal node of FEM, where the material coordinate is fixed.

3.2.3.1 Material Points Related to Climbers

The coupling of climber and tether dynamics is done by constraining the kinematic relationship between tether and climber [49, 118]. In this approach, the position of climber is determined by adjusting the lengths of tether on either side of the climber. The approach ignores the dynamic interaction between two (normal and friction forces), and it is

computationally efficient. Assume a moving node is assigned to represent the climber, in which the material coordinate of the moving node can varies. The two elements connecting with this moving node are defined as the variable-length elements, one increases while the other decreases. Therefore, the changing rate of material coordinate of moving node represents the velocity of climber. Accordingly, a constraint equation can be introduced to represent the motion of climber along the tether. For the TSS with q climbers, the constraint equations of these climbers are defined as,

$$C_{1,j}\left(p,t\right)=p_j-p_{j,\text{desired}}=0 \quad \text{or} \quad \boldsymbol{C}_1\left(p,t\right)=\boldsymbol{0} \tag{3.45}$$

where subscribe j denotes the node number of the moving node, $p_{j,\text{desired}}$ denotes the pre-defined trajectory of the climber. In current paper, the climber is assumed to move constantly, $p_{j,\text{desired}}=p_{j,ini}+\dot{p}_{j,\text{desired}}\Delta t$ with $p_{j,ini}$ and $\dot{p}_{j,\text{desired}}$ representing the initial value of material coordinate and velocity of climber, respectively. Δt is the duration of tether deployment or retrieval.

3.2.3.2 Material Points Related to Tether Deployment or Retrieval

Assume both main and sub spacecraft can deploy or retrieve tether. Define the first (main spacecraft) and last (sub spacecraft) nodes as the moving nodes. Correspondingly, the first and last elements are variable-length elements. For example, as shown in Fig. 3.6(a), to accomplish tether deployment or retrieval at the main spacecraft, the following constraint equation should be satisfied,

$$C_2\left(p,t\right)=p_1-p_{1,\text{main}}=0 \quad \text{or} \quad \boldsymbol{C}_2\left(p,t\right)=\boldsymbol{0} \tag{3.46}$$

where $p_{1,\text{main}} = p_{1,main}^{origin} + \dot{p}_{1,\text{main}}\Delta t$ with $p_{1,main}^{origin}$ and $\dot{p}_{1,\text{main}}$ representing the initial value of material coordinate and the deployment or retrieval velocity at the main satellite, respectively. $\dot{p}_{1,\text{main}} > 0$ represents tether retrieval, and $\dot{p}_{1,\text{main}} < 0$ represents tether deployment.

Moreover, the mass conservation at the main spacecraft should satisfy the following equation to account for the loss or gain of mass by deployment or retrieval of tether, such that,

$$m_1 = m_{1,origin} + \dot{p}_{1,\text{main}} A_1 \rho_1 \Delta t \tag{3.47}$$

where $m_{1,origin}$ is the mass of main spacecraft before deployment or retrieval of tether, ρ_1 and A_1 are the material density and cross-section area, respectively, subscript $(\ )_1$ represents the index of element.

The same process is applied for the sub spacecraft when it deploys or retrieves tether. As shown in Fig. 3.6(b), the following constraint equation should be satisfied,

$$C_3(p,t) = p_{n+1} - p_{\text{n+1,sub}} = 0 \quad \text{or} \quad \boldsymbol{C}_3(p,t) = \boldsymbol{0} \tag{3.48}$$

where $p_{\text{n+1,sub}} = p_{n+1,\text{sub}}^{ini} + \dot{p}_{n+1,\text{sub}}\Delta t$ with $p_{n+1,sub}^{ini}$ and $\dot{p}_{\text{n+1,sub}}$ representing the initial value of material coordinate and the deployment or retrieval velocity at the sub satellite, respectively.

Similarly, the following equation due to the conservation of mass of sub spacecraft should be satisfied,

$$m_{n+1} = m_{\text{n+1},ini} + \dot{p}_{\text{n+1,sub}} A_{n+1} \rho_{n+1} \Delta t \tag{3.49}$$

where $m_{\mathrm{n+1},origin}$ is the initial value of the mass of main spacecraft before starting the tether deployment or retrieval.

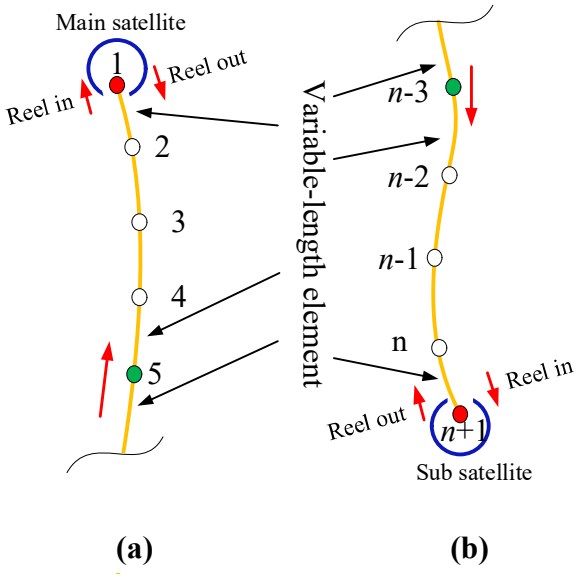

Figure 3.6 (a) Deployment/Retrieval of tether at the main spacecraft. (b) Deployment/Retrieval of tether at the sub spacecraft

3.2.3.3 Material Points Related to Normal Nodes

Except for the moving nodes, the rest of the nodes are the normal nodes, which mean their material coordinates are constant. Accordingly, the following constraint equations should be satisfied,

$$C_{4,k}(p,t) = p_k - p_{k,ini} = 0 \ (k = 2, j-1, j+1 \ldots n) \quad \text{or} \quad \boldsymbol{C}_4(p,t) = \boldsymbol{0} \tag{3.50}$$

where $p_{k,ini}$ represents the initial value of material coordinate of normal node, and it is kept constant.

3.2.4 Equation of Motion with Constraints

The equation of motion for the TSS can be obtained by combining Eqs. (3.44)-(3.50),

$$\begin{cases} \boldsymbol{M}_e \ddot{\boldsymbol{X}}_e + \left(\dfrac{\partial \boldsymbol{C}_1}{\partial \boldsymbol{X}_e}\right)^T \boldsymbol{\lambda}_1 + \left(\dfrac{\partial \boldsymbol{C}_2}{\partial \boldsymbol{X}_e}\right)^T \boldsymbol{\lambda}_2 + \left(\dfrac{\partial \boldsymbol{C}_3}{\partial \boldsymbol{X}_e}\right)^T \boldsymbol{\lambda}_3 + \left(\dfrac{\partial \boldsymbol{C}_4}{\partial \boldsymbol{X}_e}\right)^T \boldsymbol{\lambda}_4 = \boldsymbol{F}_e + \boldsymbol{F}_g - \boldsymbol{F}_p \\ \boldsymbol{C}_1(p,t) = \boldsymbol{0} \\ \boldsymbol{C}_2(p,t) = \boldsymbol{0} \\ \boldsymbol{C}_3(p,t) = \boldsymbol{0} \\ \boldsymbol{C}_4(p,t) = \boldsymbol{0} \end{cases} \tag{3.51}$$

where $\boldsymbol{\lambda}_1, \cdots, \boldsymbol{\lambda}_4$ denote the vectors of Lagrange multipliers corresponding to these constraint equations.

3.2.5 Time Integration Scheme

First, the first equation of Eq. (3.51) is transformed into two first-order differential equations with state variable $\boldsymbol{X}_e$ and $\dot{\boldsymbol{X}}_e = \boldsymbol{V}_e$ as,

$$\begin{cases} \dot{\boldsymbol{X}}_e = \boldsymbol{V}_e \\ \boldsymbol{M}_e \dot{\boldsymbol{V}}_e + \left(\dfrac{\partial \boldsymbol{C}_1}{\partial \boldsymbol{X}_e}\right)^T \boldsymbol{\lambda}_1 + \left(\dfrac{\partial \boldsymbol{C}_2}{\partial \boldsymbol{X}_e}\right)^T \boldsymbol{\lambda}_2 + \left(\dfrac{\partial \boldsymbol{C}_3}{\partial \boldsymbol{X}_e}\right)^T \boldsymbol{\lambda}_3 + \left(\dfrac{\partial \boldsymbol{C}_4}{\partial \boldsymbol{X}_e}\right)^T \boldsymbol{\lambda}_4 = \boldsymbol{F}_e + \boldsymbol{F}_g - \boldsymbol{F}_p \\ \boldsymbol{C}_1(p,t) = \boldsymbol{0} \\ \boldsymbol{C}_2(p,t) = \boldsymbol{0} \\ \boldsymbol{C}_3(p,t) = \boldsymbol{0} \\ \boldsymbol{C}_4(p,t) = \boldsymbol{0} \end{cases} \tag{3.52}$$

Then, the backward Euler formulation is employed, a series of algebraic nonlinear equations are generated as follows,

$$\boldsymbol{G}=\begin{pmatrix}\boldsymbol{G}_1\\ \boldsymbol{G}_2\\ \boldsymbol{G}_3\\ \boldsymbol{G}_4\\ \boldsymbol{G}_5\\ \boldsymbol{G}_6\end{pmatrix}=\begin{pmatrix}\boldsymbol{X}_e^{n+1}-\boldsymbol{X}_e^{n}-\Delta t\boldsymbol{V}_e^{n+1}\\ \boldsymbol{M}_e^{n+1}\left(\boldsymbol{V}_e^{n+1}-\boldsymbol{V}_e^{n}\right)+\Delta t\sum_{j=1}^{4}\left(\frac{\partial \boldsymbol{C}_j}{\partial \boldsymbol{X}_e^{n+1}}\right)^T\boldsymbol{\lambda}_j^{n+1}-\Delta t\left(\boldsymbol{F}_e^{n+1}+\boldsymbol{F}_g^{n+1}-\boldsymbol{F}_p^{n+1}\right)\\ \boldsymbol{C}_1(p,t)\\ \boldsymbol{C}_2(p,t)\\ \boldsymbol{C}_3(p,t)\\ \boldsymbol{C}_4(p,t)\end{pmatrix}=\boldsymbol{0} \tag{3.53}$$

where a new set of unknown variables $\boldsymbol{Z}_e^{n+1}=\left(\boldsymbol{X}_e^{n+1},\boldsymbol{V}_e^{n+1},\boldsymbol{\lambda}_1^{n+1},\boldsymbol{\lambda}_2^{n+1},\boldsymbol{\lambda}_3^{n+1},\boldsymbol{\lambda}_4^{n+1}\right)^T$ are defined.

Then, 6(n+1) algebraic nonlinear equations can be obtained as shown in Eq. (3.53) with 6(n+1) unknown variables $\boldsymbol{Z}_e^{n+1}$. In the current work, the iterative Newton-Raphson method is employed to solve these nonlinear algebraic equations [124-126], and the detailed process is as follows,

A: *Initial calculations*

1.Initialize $\boldsymbol{X}_e^0$, $\boldsymbol{V}_e^0$ *and* $\boldsymbol{A}_e^0$

B: *For each time step*

1.Newton iteration loop(*m representing the* m^{th} *iteration number*)

$$
\begin{cases}
1.\ \textit{Estimate initial iteration values}\ \boldsymbol{Z}_{e,m}^{n+1} \\
\quad \begin{cases} \textit{Tether values}\ \boldsymbol{X}_{e,m}^{t+\Delta t}\ \textit{and}\ \boldsymbol{V}_{e,m}^{t+\Delta t}\ \textit{by the forward Euler method} \\ \quad \boldsymbol{X}_{e,m}^{n+1} = \boldsymbol{X}_e^n + \boldsymbol{V}_e^n \Delta t \quad \textit{and}\ \boldsymbol{V}_{e,m}^{n+1} = \boldsymbol{V}_e^n + \boldsymbol{A}_e^n \Delta t \\ \textit{Lagrangian multipliers,}\ \boldsymbol{\lambda}_{1,m}^{n+1},\ \boldsymbol{\lambda}_{2,m}^{n+1},\ \boldsymbol{\lambda}_{3,m}^{n+1},\ \boldsymbol{\lambda}_{4,m}^{n+1} \end{cases} \\
2.\ \textit{Form Mass matrix}\ \boldsymbol{M}_{e,m}^{n+1},\ \textit{Force matrices}\ \boldsymbol{Q}_{e,m}^{n+1}, \boldsymbol{Q}_{g,m}^{n+1},\ \boldsymbol{Q}_{p,m}^{n+1} \\
4.\ \textit{Form Jacobian matrix of algebraic equation}\ \boldsymbol{G}_{\boldsymbol{Z}}^m = \dfrac{\partial \boldsymbol{G}^m}{\partial \boldsymbol{Z}_{e,m}^{n+1}}, \textit{as listed in Eq.}\ (3.52) \\
5.\textit{Calculation algebraic equations}\ \boldsymbol{G}^m \\
6.\textit{Calculation the difference}\ \boldsymbol{Z}_{e,m+1}^{n+1} - \boldsymbol{Z}_{e,m}^{n+1} = \left(\boldsymbol{G}_{\boldsymbol{Z}}^m\right)^{-1} \boldsymbol{G}^m \\
7.\textit{Evalute the convergency conditions} \\
\quad \varepsilon = \boldsymbol{G} \le \varepsilon_{tolerance} \quad \textit{and}\ m \ge m_{max}
\end{cases}
$$

2.Calculation accleration

1.Form Mass matrix $\boldsymbol{M}_{e,m+1}^{n+1}$, *Force matrices* $\boldsymbol{Q}_{e,m+1}^{n+1}, \boldsymbol{Q}_{g,m+1}^{n+1}, \boldsymbol{Q}_{p,m+1}^{n+1}$

$$
2.\ \ddot{\boldsymbol{X}}_e^{n+1} = \left(\boldsymbol{M}_{e,m+1}^{n+1}\right)^{-1} \left[\boldsymbol{Q}_{e,m+1}^{n+1} + \boldsymbol{Q}_{g,m+1}^{n+1} - \boldsymbol{Q}_{p,m+1}^{n+1} - \sum_{j=1}^{4} \left(\frac{\partial \boldsymbol{C}_j}{\partial \boldsymbol{X}_{e,m+1}^{n+1}} \right)^T \boldsymbol{\lambda}_{j,m}^{n+1} \right]
$$

$$\frac{\partial \boldsymbol{G}^m}{\partial \boldsymbol{Z}_{e,m}^{n+1}} = \begin{bmatrix} \boldsymbol{I} & -\Delta t\boldsymbol{I} & \boldsymbol{0} & \boldsymbol{0} & \boldsymbol{0} & \boldsymbol{0} \\ \boldsymbol{0} & \boldsymbol{M}_{e,m}^{n+1} & \Delta t\left(\frac{\partial \boldsymbol{C}_1}{\partial \boldsymbol{X}_{e,m}^{n+1}}\right)^T & \Delta t\left(\frac{\partial \boldsymbol{C}_2}{\partial \boldsymbol{X}_{e,m}^{n+1}}\right)^T & \Delta t\left(\frac{\partial \boldsymbol{C}_3}{\partial \boldsymbol{X}_{e,m}^{n+1}}\right)^T & \Delta t\left(\frac{\partial \boldsymbol{C}_4}{\partial \boldsymbol{X}_{e,m}^{n+1}}\right)^T \\ \frac{\partial \boldsymbol{C}_1}{\partial \boldsymbol{X}_{e,m}^{n+1}} & \boldsymbol{0} & \boldsymbol{0} & \boldsymbol{0} & \boldsymbol{0} & \boldsymbol{0} \\ \frac{\partial \boldsymbol{C}_2}{\partial \boldsymbol{X}_{e,m}^{n+1}} & \boldsymbol{0} & \boldsymbol{0} & \boldsymbol{0} & \boldsymbol{0} & \boldsymbol{0} \\ \frac{\partial \boldsymbol{C}_3}{\partial \boldsymbol{X}_{e,m}^{n+1}} & \boldsymbol{0} & \boldsymbol{0} & \boldsymbol{0} & \boldsymbol{0} & \boldsymbol{0} \\ \frac{\partial \boldsymbol{C}_4}{\partial \boldsymbol{X}_{e,m}^{n+1}} & \boldsymbol{0} & \boldsymbol{0} & \boldsymbol{0} & \boldsymbol{0} & \boldsymbol{0} \end{bmatrix} \tag{3.54}$$

where subscripts m and m+1 represent the m^{th} and $(m+1)^{th}$ iteration number. In current work, the allowable tolerance $\varepsilon_{tolerance}$ and maximum iteration number m_{max} are set as 10^{-11} and 100, respectively.

3.2.6 Merging and Dividing Elements

3.2.6.1 Movement of Climber

As shown in Fig. 3.7, the lengths of variable-length elements change when the moving node varies. The variable-length element will be divided if its length is too long or merged with the adjacent constant-length element to form a new variable-length element if its length is too short. Four parameters are defined to control the process of merging and/or dividing of element: the standard length L_s, the upper bound length L_{max}, the low bound length L_{min}, and the acceptance tolerance δ_e, respectively. There are two general rules to determine the values of L_{max} and L_{min}. First, the lengths of variable-length elements cannot

too short or long, which means the values should close to the standard-length L_s. Second, the condition $L_{\min} + L_{\max} > 2L_s$ should be satisfied. The purpose for this condition is to avoid the processes of merging and dividing elements happen simultaneously, which may lead to an abrupt oscillation in solution. The values of these parameters will be given in the simulation part.

Merging elements

If the length of the variable-length element is smaller than the lower bound length L_{min}, it will be merged with the adjacent constant-length element. For example, as shown in Fig. 3.7(a), the (k+2)-*th* node is a moving node that represents the climber moving in the arrow direction. If the following equation is satisfied,

$$L_{k+1} = p_{k+2} - p_{k+1} \le L_{\min} \tag{3.55}$$

Then, the (k+2)-*th* element is ready to be merged with (k+1)-*th* element. The actual merge occurs once the condition $\|\Delta \boldsymbol{r}\| \le \delta_e$ is satisfied, where $\Delta \boldsymbol{r}$ is the normal distance from (k+1)-*th* node to the line connecting the *k-th* and (k+2)-*th* nodes. $\delta_e = 0.01\ m$ is the tolerance to avoid the oscillation caused by the merge of node. Then the nodes and elements are renumbered after the (k+1)-*th* node is removed.

Dividing elements

The variable-length element will be divided if the element's length exceeds the upper bound length L_{max}. For example, as shown win Fig. 3.7(b), the (k+1)-*th* node is a moving node that represents the climber moving in the arrow direction. If the following condition

is satisfied,

$$L_{k+1} = p_{k+2} - p_{k+1} \geq L_{\max} \tag{3.56}$$

Then, the (k+1)-*th* element will be divided into two new elements by inserting a new node between the (k+1)-*th* and (k+2)-*th* nodes. The position, velocity, and acceleration of the newly inserted node can be obtained via interpolation. Then, the nodes and elements after the (k+1)-*th* node are renumbered. Due to its connection with the moving node, the new (k+1)-*th* element is a variable-length element with the length $L_{k+1} - L_s$. The length of new (k+2)-*th* element is equal to the standard length L_s. The property of this element, either constant-length or variable-length, is depending on whether the original (k+2)-*th* node is a normal node or a moving node in case of multiple climbers.

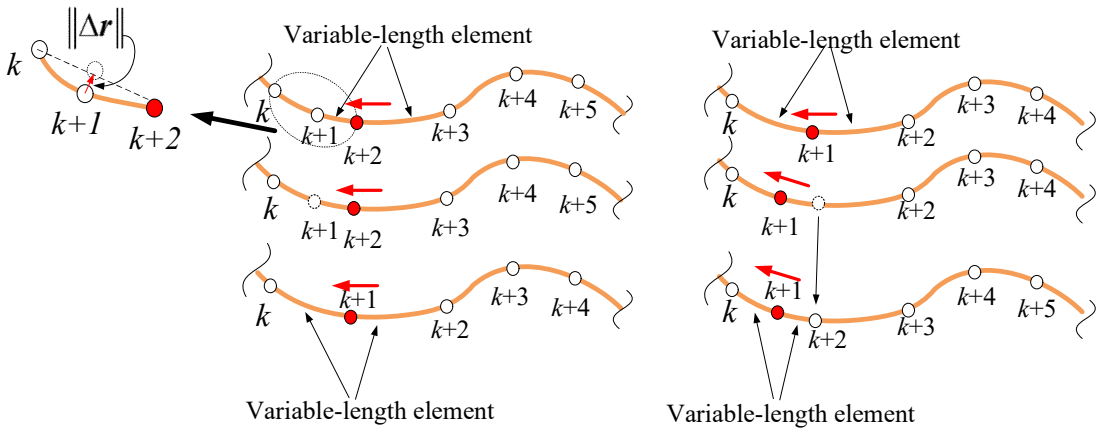

Figure 3.7 Dividing and merging of element.

3.2.6.2 Deployment and Retrieval of Tether

As shown in Fig. 3.8(a), the climber is supposed to move up while the main spacecraft is retrieving the tether. Then, the properties of nodes and elements of the segment closing to the main spacecraft are shown in Fig. 3.8, where two moving nodes are defined, one represents the climber, and the other represents the tether retrieval. In addition, the elements connecting with moving nodes are defined as the variable-length elements. The detailed information relates to the process of merging and dividing of elements can be found in the section 3.2.6.1.

Merging elements

The variable-length element will merge with adjacent constant-length element if its length is smaller than the lower bound length L_{min}. For example, as shown win Fig. 3.8(a), the 5th node is a moving node representing the climber, and the climber moves along the arrow direction. If the following equations are satisfied,

$$L_{k+1} = p_5 - p_4 \le L_{\min} \tag{3.57}$$

the 4th node is ready to be removed until it satisfies additional tolerance condition $\|\Delta \boldsymbol{r}\| \le \delta_e$, where $\|\Delta \boldsymbol{r}\|$ is the normal distance from 4th node to the line connecting the 3rd and 4th nodes. In the current work, $\delta_e = 0.01\ m$ is used to suppress the oscillation caused by the numerical procedure to remove a node. After the fourth node is removed, the nodes and elements are renumbered.

There is only one exception for the process of merging of element if two connective

nodes are both the moving nodes. This situation happens when the climber moves close to the main spacecraft.

Dividing elements

The variable-length element will be divided if its length exceeds the upper bound length L_{max}. For example, as shown win Fig. 3.8(b), the 4th node is a moving node that represents the climber, and the climber moves along the arrow direction. If the following condition is satisfied,

$$L_4 = p_5 - p_4 \geq L_{\max} \tag{3.58}$$

Then, the 4th element is divided into two new elements by adding a new node between the 4th and 5th nodes. The position, velocity, and acceleration of the newly added node can be obtained via the linear interpolation method. After that, the nodes, and elements after the 4th node need to be renumbered. Due to its connection with the moving node, the new 4th element is a variable-length element with the length $L_4 - L_s$. The length of the new 5th element is equal to the standard-length L_s.

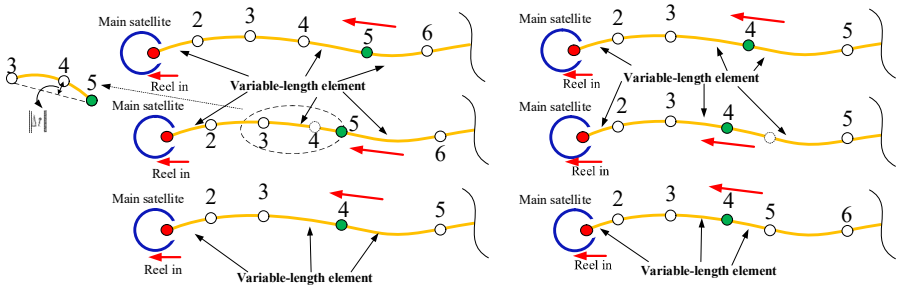

Figure 3.8 (a) Merging of element. (b) Dividing of element.

3.2.7 Libration of Discretized Tether System

The libration of TSS is originally defined based on two-piece dumbbell model. It is normally described in the orbital coordinate system [28, 29, 49, 117, 118]. For discretized tether system, there will be n sets of libration angles if the tether is discretized into n elements, which is impractical for dynamic analysis of TSS. Instead, a nominal libration definition is introduced as shown in Fig. 3.9. The origin O' of the coordinate system is located at the center of mass (CM) of the TSS with the Z_o-axis pointing to the origin of the global inertial coordinate system. The X_o-axis is lying in the orbital plane of TSS system and perpendicular to the Z_o-axis. The Y_o-axis completes a right-hand system. The transformation matrix from the orbital frame to the global inertial frame is the same as Ref. [43]. Different from the two-piece dumbbell model [49, 118], there are n sets of libration (pith and roll) angles if the tether is discretized into n elements. To keep consistent with the definition of libration angles of the two-piece dumbbell model, a series of virtual libration angels are defined by straight lines connecting the main spacecraft, the climbers, and the sub spacecraft, see the dotted lines in Fig. 3.9. Taking the case of three climber as an example, there are four dotted lines. The libration angles of those four lines are described in the orbital frame with the origin located at the CM of discretized model of TSS. The calculations of the in-plane angles $\alpha_i\left(i=1,\ldots,4\right)$ and out-of-plane angles $\beta_i\left(i=1,\ldots,4\right)$ are the same as those in Refs. [43, 127].

$$\begin{aligned}\alpha_i &= \tan^{-1}\left(\boldsymbol{R}_{X_o,i}/\boldsymbol{R}_{Z_o,i}\right),\\ \beta_i &= \tan^{-1}\left[-\boldsymbol{R}_{Y_o,i}/(\boldsymbol{R}_{Z_o,i}\cos\alpha_i + \boldsymbol{R}_{X_o,i}\sin\alpha_i)\right]\end{aligned} \tag{3.59}$$

where $\boldsymbol{R}_i = \left(\boldsymbol{R}_{X_o,i}, \boldsymbol{R}_{Y_o,i}, \boldsymbol{R}_{Z_o,i}\right)^T$ is the vector of a dotted line expressed in the orbital coordinate system with the subscript $i(1\sim4)$ representing the sequence of these four lines,

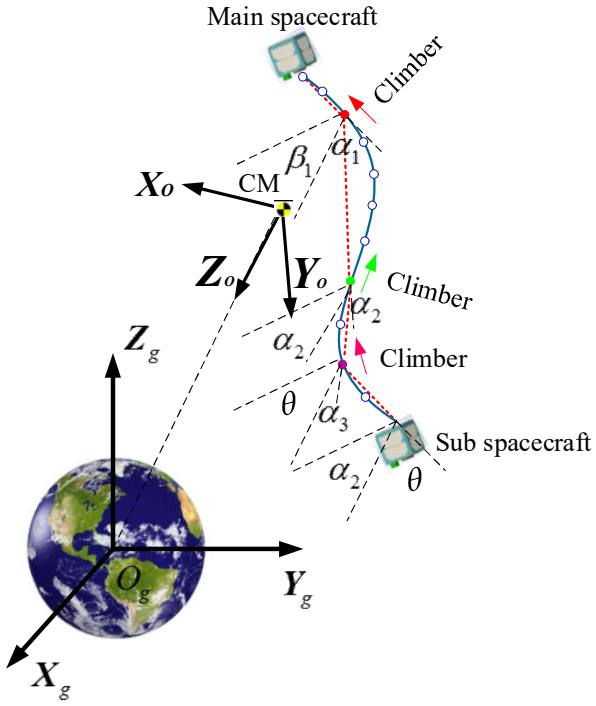

Figure 3.9 Definition of libration angles of TSS with three climbers.

3.2.8 Numerical Results and Discussion

The proposed approach is validated by comparing the dynamic responses against to those in the Refs. [49, 73, 118], in which the TSS contains only one climber. The physical properties of tether with climbers are listed in Table 3.2 and other parameters will be given

later. It should point out the ideal gravitational force is considered here.

Table 3.2 Physical properties of tether

Parameters	Values
Density (kg/m^3)	1440
Elastic modulus (10^9 N/m^2)	72
Cross section area (m^2)	2.0×10^{-6}

3.2.8.1 Tethered Transportation System with Climber Only

The existing analyses in the existing Refs. [49, 73, 118] are based on two-piece dumbbell model. For the sake of comparison, the tether is discretized into two variable-length elements so that the definition of libration angles of the current approach is the same as those in the Refs. [49, 73, 118]. Moreover, the degrees-of-freedom of the TSS model is constant as the climber moves along the tether, and the process of merging and dividing of element is not activated.

First, the total mass of the sub spacecraft m_s, the climber m_c, and the tether m_t is assumed negligible compared with the mass of the main spacecraft m_m. Thus, the CM of the TSS resides at the main spacecraft in the entire transportation of climber. The main spacecraft is orbiting in a circular orbit. The same initial conditions and physical parameters in [73] are used here, such that, $r(0)$ = 6,600km, $\psi(0)=1.177\times10^{-3}\ rad/s$, $\alpha_1(0)=\alpha_2(0)=\dot{\alpha}_1(0)=\dot{\alpha}_2(0)=0$, $L=100\ km$, $m_s=1000\ kg$, $m_c=1000\ kg$. The climber is assumed to move at a constant velocity $\dot{p}_{1,\text{desired}}$ = 14.99 m/s. Both upward and downward movements of the climber are analyzed, where $l_1(0) = 0.9L$ and $l_2(0) = 0.1L$ for the upward movement, $l_1(0) = 0.1L$ and $l_2(0) = 0.9L$ for the downward movement. The

simulation time is 5,336.14 *s*. The comparisons of libration and trajectory of climber are shown in Figs. 3.10-3.13. Since the definition of orbital coordinate system is different, the results from Ref. [73] are transformed into the current orbital coordinate system. Figures 3.10 and 3.11 show the comparisons of climber in the upward transfer, while Figures 3.12 and 3.13 show the comparisons of climber in the downward transfer. It is observed that both the libration angles and trajectory of the climber are in very good agreement with the results of two-piece dumbbell model in Ref. [73]. In addition, as shown in Figs. 3.10 and 3.12, the in-plane motion of TSS is the dominant mode. The out-of-plane motions are negligible and are not plotted in rest cases of TSS in this chapter.

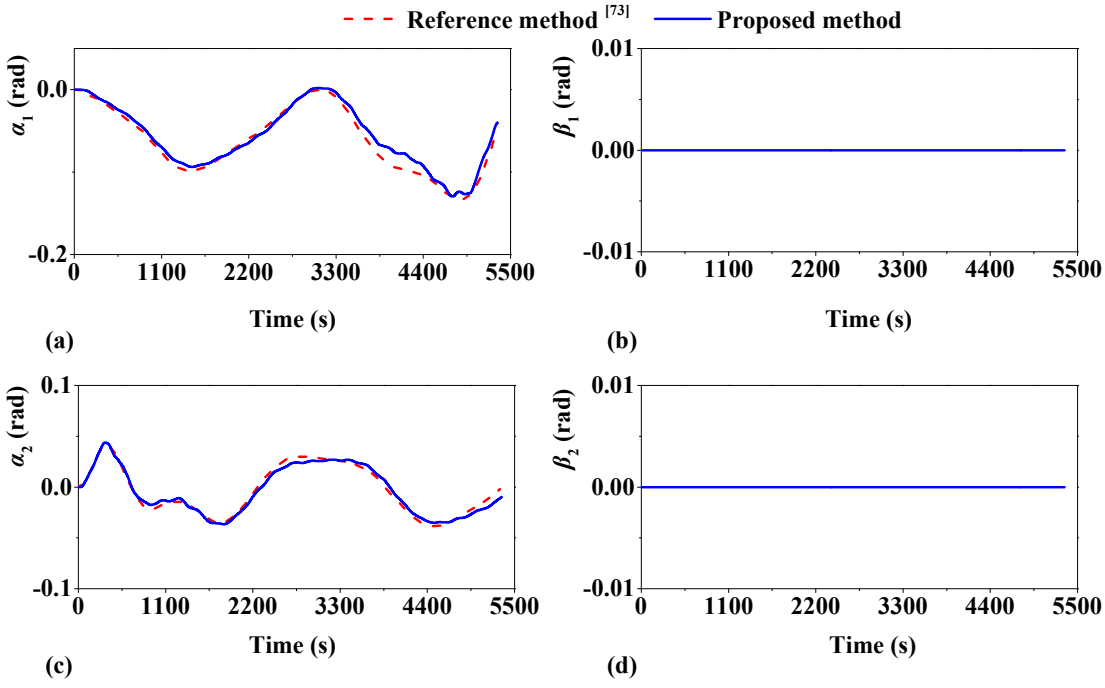

Figure 3.10 Comparison of libration angles of climber in upward transfer. (a) Libration angle α_1. (b) Libration angle β_2. (c) Libration angle α_2. (d) Libration angleβ_2.

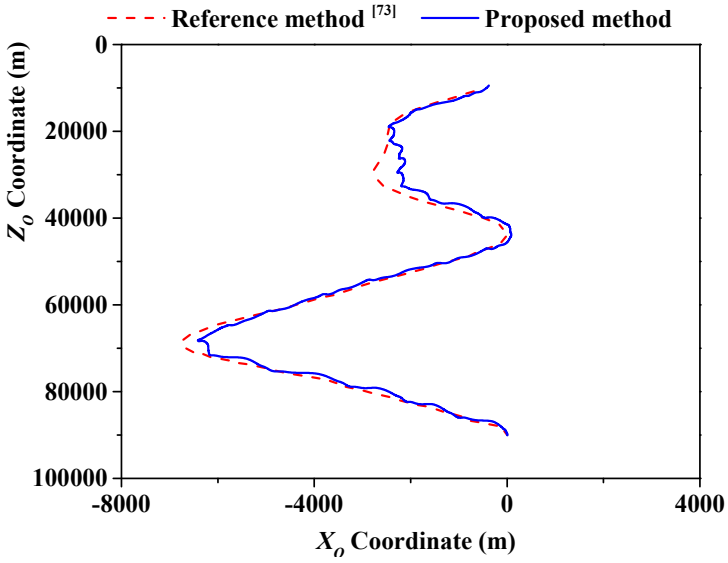

Figure 3.11 In-plane trajectory of climber with respect to CM in orbital frame in upward transfer.

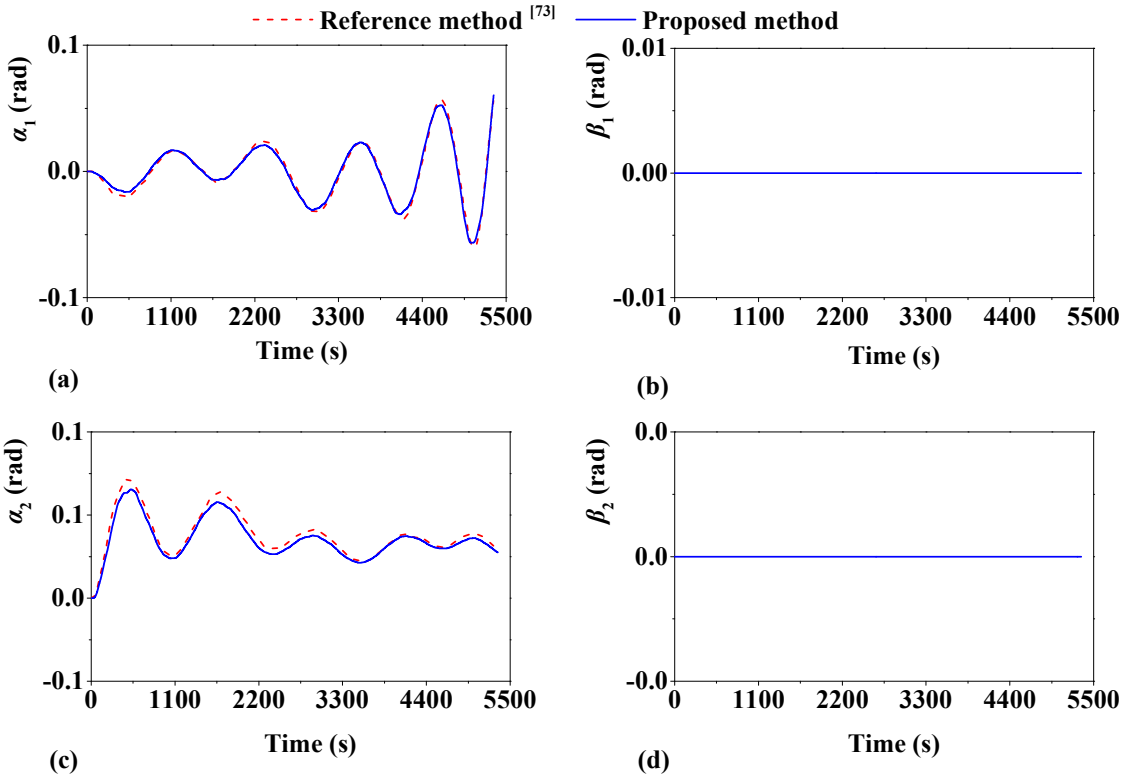

Figure 3.12 Comparison of libration angles of climber in downward transfer. (a) Libration angle α_1. (b) Libration angle β_2. (c) Libration angle α_2. (d) Libration angleβ_2.

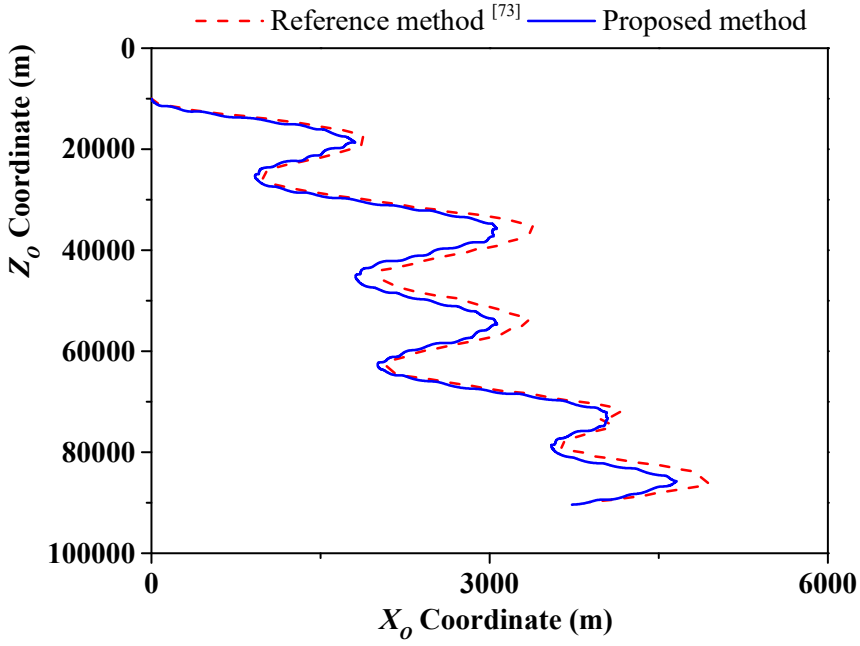

Figure 3.13 In-plane trajectory of climber with respect to CM in the orbital frame in downward transfer.

In the second verification case, the same initial conditions and physical parameters in [118] are used: $r(0) = 7{,}100km$, $\alpha_1(0)=\alpha_2(0)=\dot{\alpha}_1(0)=\dot{\alpha}_2(0)=0$, $L = 20km$, $m_s = 1000\ kg$, $m_c = 500\ kg$. The climber is assumed to move at a constant velocity $\dot{p}_{1,\text{desired}} = 4\ m/s$. Both upward and downward movements of the climber are analyzed, where $l_1(0)=0.975L$ and $l_2(0)=0.025L$ for the upward movement, $l_1(0)=0.025L$ and $l_2(0)=0.975L$ for the downward transfer. The comparison results of libration motion and trajectory of the climber are shown in Figs. 3.14-3.17. Since the definition of orbital coordinate system is different, the results from Ref. [118] are transformed and compared with the results the in current study. As shown in Figs 3.14 and 3.16, it is

observed that the libration angles computed in this study are in good agreement with those in Ref. [118]. Furthermore, the trajectories of the climber verify the results of both methods are the same, see Figs. 3.15 and 3.17.

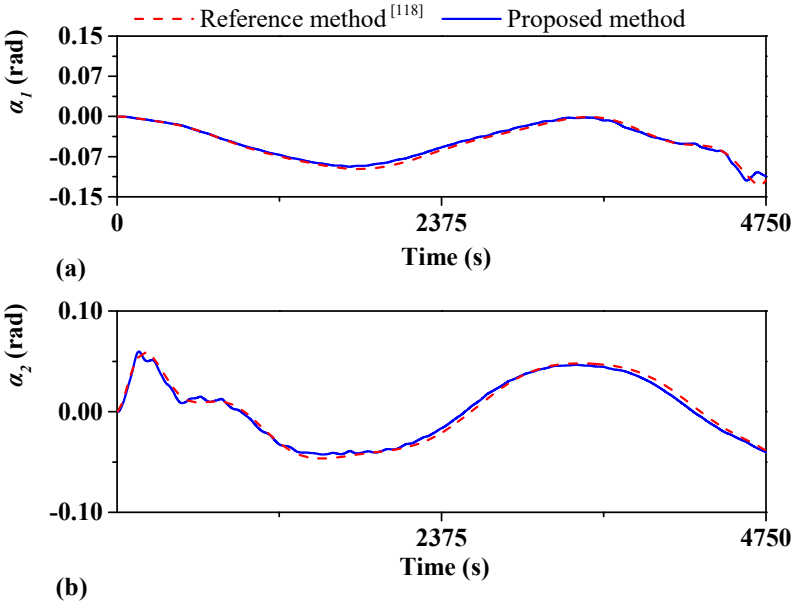

Figure 3.14 Comparison of libration angles of climber in upward transfer. (a) Libration angle α_1. (b) Libration angle α_2.

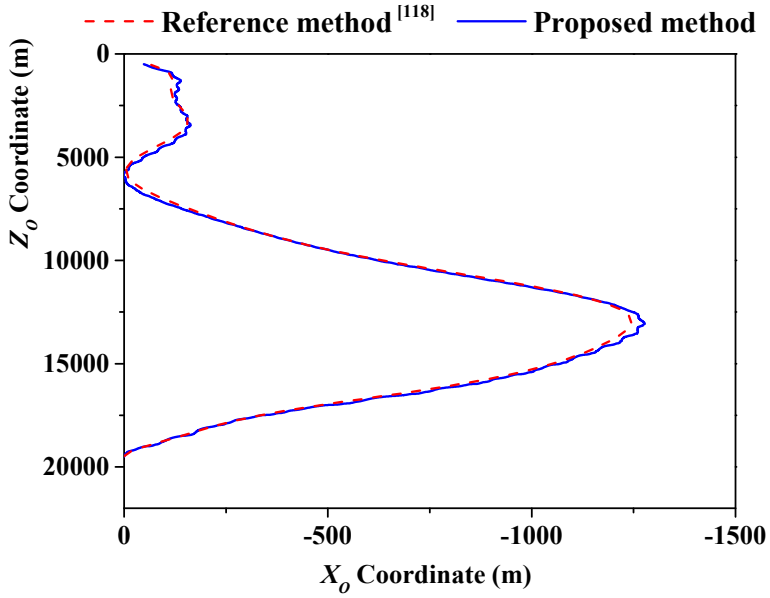

Figure 3.15 In-plane trajectory of climber with respect to CM in orbital frame in upward transfer.

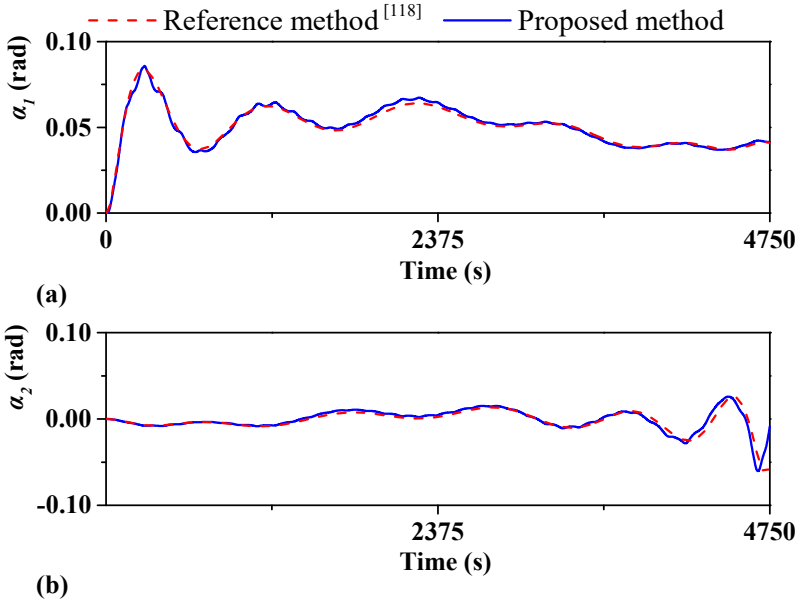

Figure 3.16 Comparison of libration angles of climber in downward transfer. (a) Libration angle α_1. (b) Libration angle α_2.

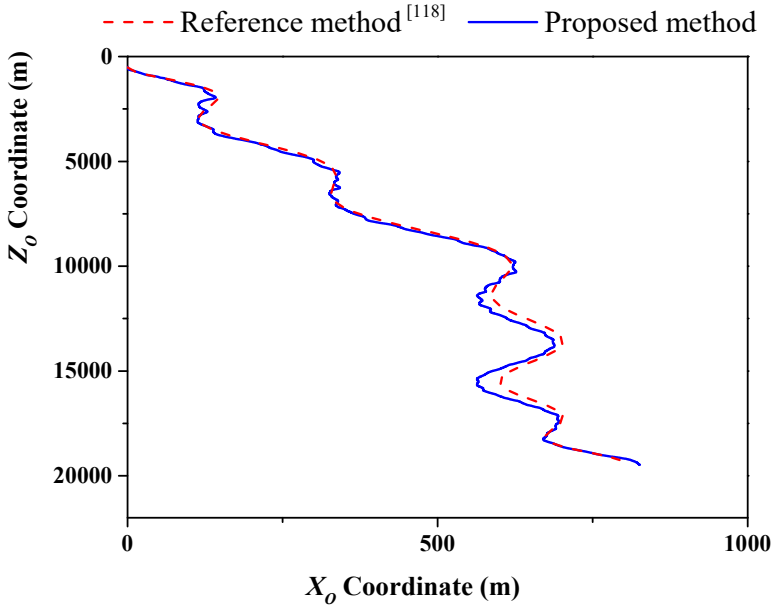

Figure 3.17 In-plane trajectory of t climber with respect to the CM in the orbital frame in downward transfer

In the third verification case, the masses of climber, sub spacecraft, and tether are no longer negligible compared with the mass of main spacecraft. The movement of the climber will change the CM position of TSS. The initial conditions and physical parameters in the Ref. [49] are used: $r(0) = 6{,}600km$, $\psi(0) = 1.178\times10^{-3}\ rad/s$, $\alpha_1(0) = \alpha_2(0) = \dot{\alpha}_1(0) = \dot{\alpha}_2(0) = 0$, $L = 10km$, $m_m = m_s = 1000\ kg$, $m_c = 100\ kg$, and $V = 1m/s$. Only the upward movement is considered here due to the similarity between upward and downward movement in this case. The climber starts at $100m$ from the sub spacecraft and travels upward 9,800 *m* along the tether. The comparisons of libration angles of TSS and the trajectory of climber are shown in Figs. 3.18 and 3.19. It can be seen that both libration angles and trajectory agree well in general with the results of two-piece dumbbell model of [49]. However, there is a significant difference in the variation of the orbital radius of CM, see Fig. 3.18(a). In the current model, the CM of the TSS system is increased only by 460m as the result of upward transfer, which is the same as the simple calculation based on energy balance. This result is also very similar to the result of Kojima et al. [73] in a similar case. The CM variation in Ref. [49] is about 30km, see Fig. 3.18(a). For a TSS with a 10km long tether, this implies the entire TSS is moving up and down by 30km. This is unlikely because the variation of orbital potential energy is much greater than the energy input to the TSS by moving the climber upwards. Because of this difference, noticeable differences in the variation trends of libration angles and the climber position are observed.

In conclusion, these cases verify that the proposed method.

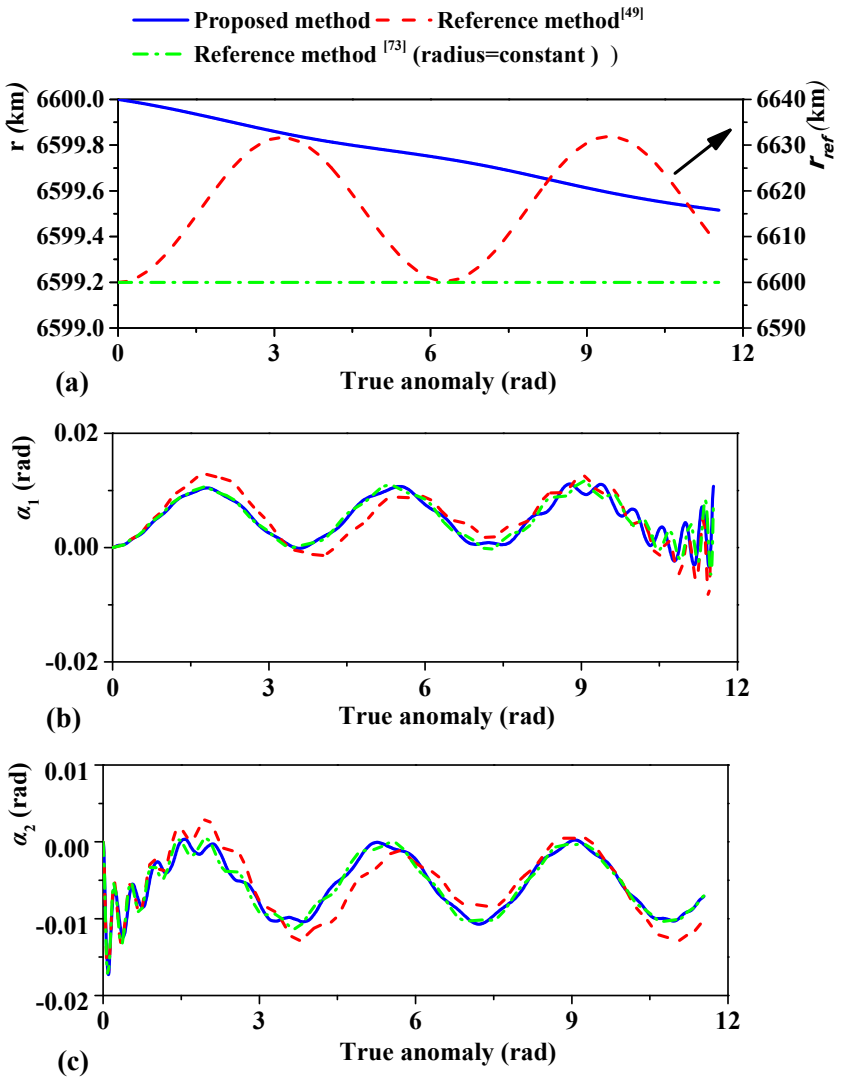

Figure 3.18 Comparison of libration angles of climber in upward transfer. (a) Orbital radius (b) Libration angle α_1. (c) Libration angle α_2.

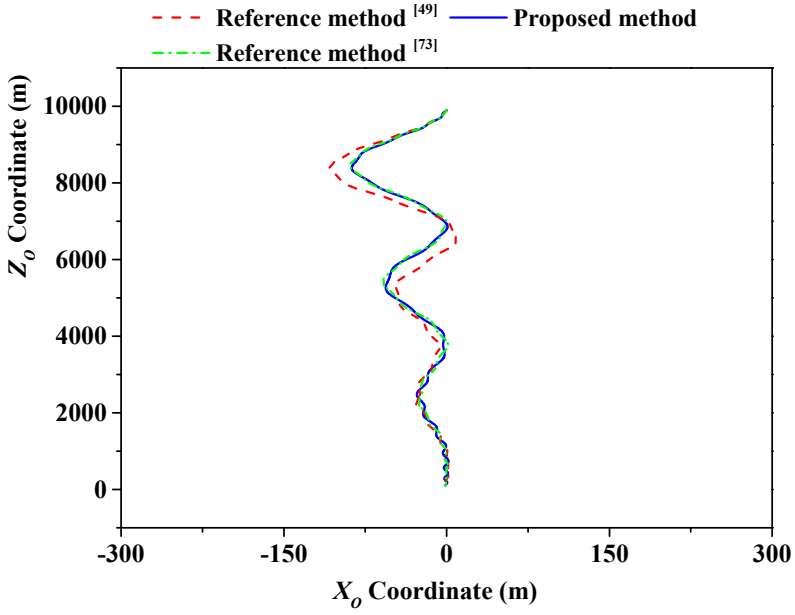

Figure 3.19 In-plane trajectory of climber with respect to CM in orbital frame in upward transfer.

3.2.8.2 Tethered Transportation System with Climber and Tether Deployment/Retrieval

In this section, the sample of two-piece dumbbell model in Ref. [118] is used for comparison. The same initial conditions and physical parameters in Ref. [118] are used, $r(0) = 7{,}100\ km$, $\alpha_1(0) = \alpha_2(0) = \dot{\alpha}_1(0) = \dot{\alpha}_2(0) = 0$, $L = 20\ km$, $m_s = 1{,}000\ kg$, and $m_c = 500\ kg$. Furthermore, it is noted that the CM of TSS is locates at the main spacecraft in Ref. [118]. To mimic this situation in our analysis, the mass of main spacecraft is assumed to be exceptionally large (m_m = 150,000 kg) as compared to the total mass of the sub spacecraft, climber, and tether. The tether is discretized with two variable-length elements as section 3.2.8.1 does. Thus, it is similar to the two-piece dumbbell model in Ref. [118]

except the tether can be elastically deformed in length in our model. Two cases are considered. The time step is set 0.01 s for the numerical integration.

In the first case, the climber moves upward at 4 m/s, while the sub spacecraft deploys the tether at 2 m/s simultaneously. The initial lengths of two elements are $l_1(0) = 19{,}500m$ (tether segment between main spacecraft and climber) and $l_2(0) = 500m$. Here, the material coordinate of climber changes from 19,500m to 500m. The comparison of libration angles of TSS and trajectories of climber and sub spacecraft in the orbital coordinate system are shown in Figs. 3.20-3.23. The dashed lines, refereed as "Reference method", represent the results of Ref. [118] while the solid lines, referred as "Proposed method", represent the results from the proposed method. It can be easily found in Fig. 3.20 that the libration angles computed by the current model are in good agreement with the results of Ref. [118]. Moreover, the same conclusion can be obtained from the variation of geometrical configuration of TSS, see Fig. 3.22. Therefore, it demonstrates the two-piece dumbbell model is a subset of the proposed model. However, a slight difference still be observed in the comparison results. The reason is caused by the high-frequency elastic oscillation of tether, which it was ignored in the reference method in Ref. [118]. For example, Figure 3.23 shows the tension variation in two elements connecting with the climber, where momentarily slack (zero tension) of tether is observed. When the first element experiences a slack, the climber loses the support from the first element and is pulled back by the second element that is not slack, and vice versa. In addition, as shown

in Fig. 3.20, it is noted that the amplitudes of libration-angle oscillation decrease as the sub spacecraft deploys the tether by comparing the results for the case of fixed-length tether, see in Fig. 3.14 [118]. This is because the tether deployment generates the Coriolis force on the sub spacecraft to reduce the libration of TSS [33, 118]. It can be concluded that, in the climber's upward transfer, the deployment of tether at the sub spacecraft produces a positive effect in reducing the libration of TSS.

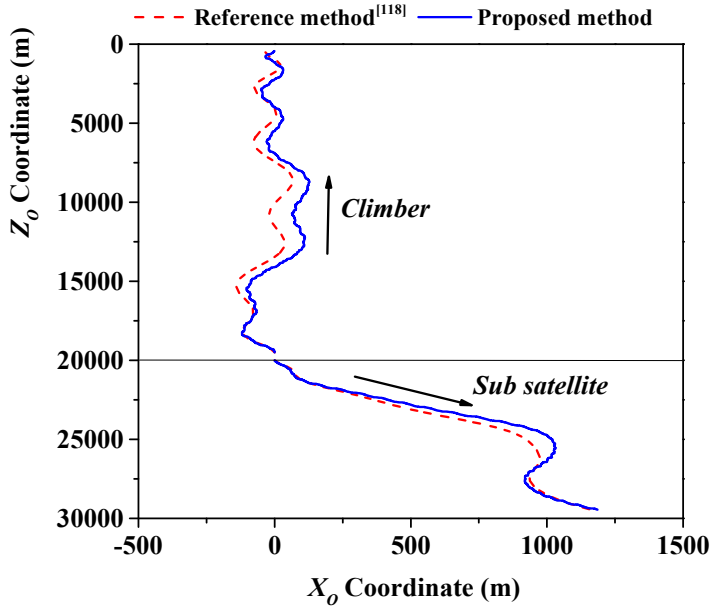

Figure 3.20 In-plane trajectories of climber and sub spacecraft in upward transfer.

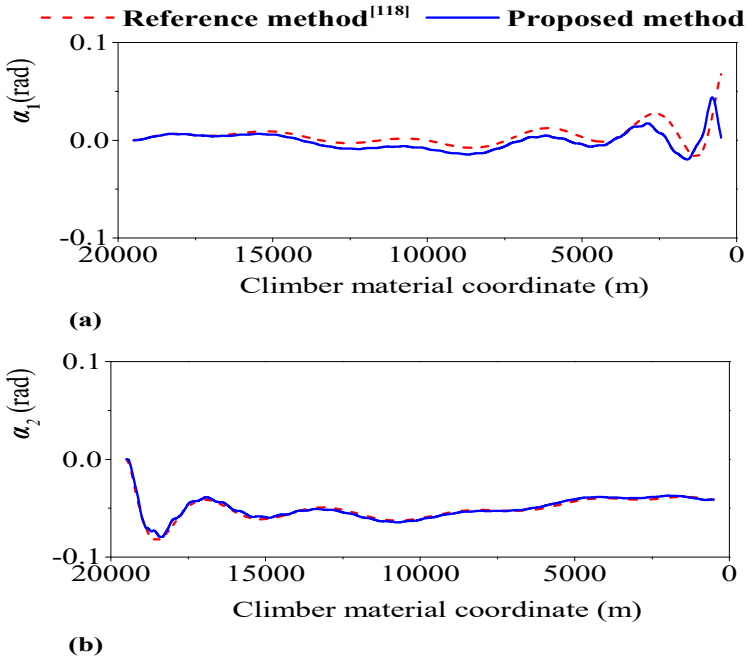

Figure 3.21 Comparison of libration angles in upward transfer: (a) Libration angle α_1. (b) Libration angle α_2.

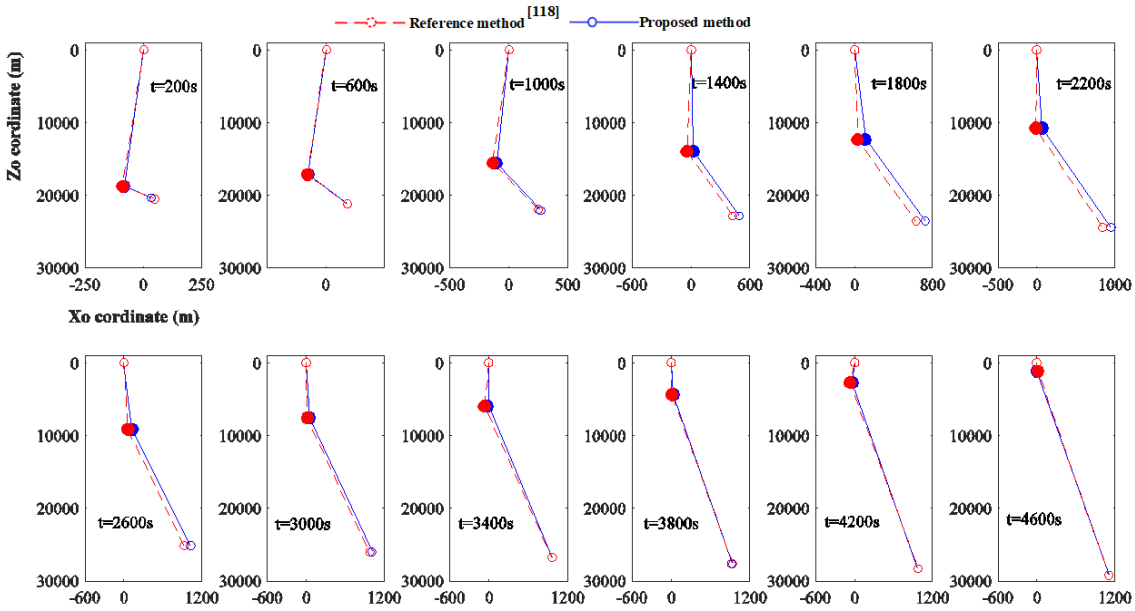

Figure 3.22 Comparison of geometrical configuration of TSS in upward transfer.

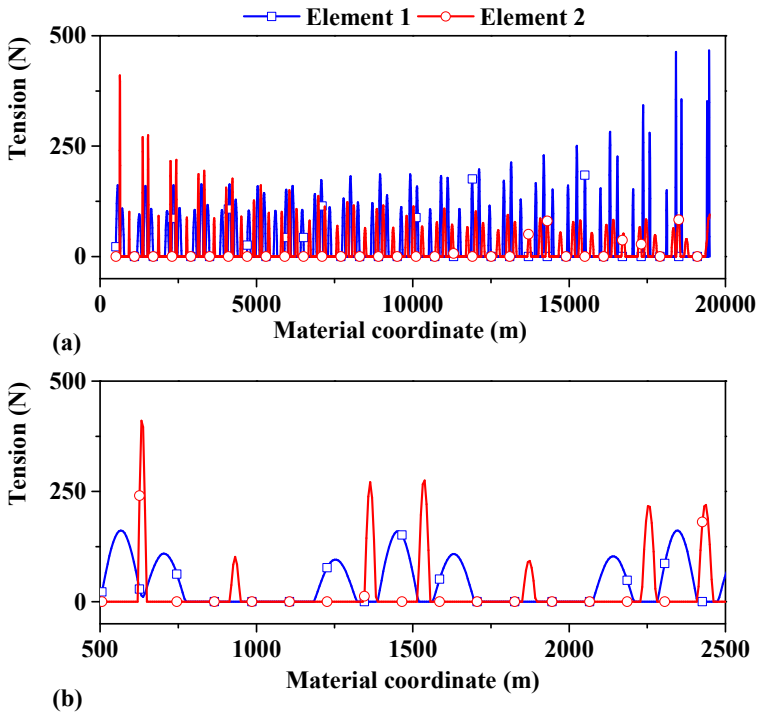

Figure 3.23 Variation of tether tension in upward transfer (a) global and (b) zoomed view.

In the second case, the climber moves downward at 4 m/s while the sub spacecraft retrieves the tether at 2 m/s simultaneously. The initial lengths of two elements are $l_1(0)=500m$ and $l_2(0)=19{,}500m$. Accordingly, the material coordinate of the climber changes from 500m to 19,500m, see the X-axis in Fig. 3.24 The comparison of trajectories of climber and sub spacecraft in the orbital coordinate system as well as libration angles of TSS are shown in Figs. 3.24 and 3.25. As shown in Figs. 3.24 and 3.25, the libration angles and geometrical configuration of TSS are also in good agreement with the results of two-piece dumbbell model in Ref. [33]. A slight difference is observed due the difference of these two models. The same reason attributes to this phenomenon, which is the elasticity

of tether that was ignored in the reference method. Figure 3.27 shows the variation of tension in two elements. The same slack tether situation tether as that in Fig. 3.23 is observed. In addition, it is found in Fig. 3.24 that the retrieval of tether of the sub spacecraft is helpful to suppress the tether libration.

From the comparison, it shows that the two-piece dumbbell model is a subset of the current elastic tether model. The proposed approach can model the slack tether situation that may occur as the climber moves upward or downward along the tether, which cannot be dealt properly by the two-piece dumbbell model with rigid tether assumption.

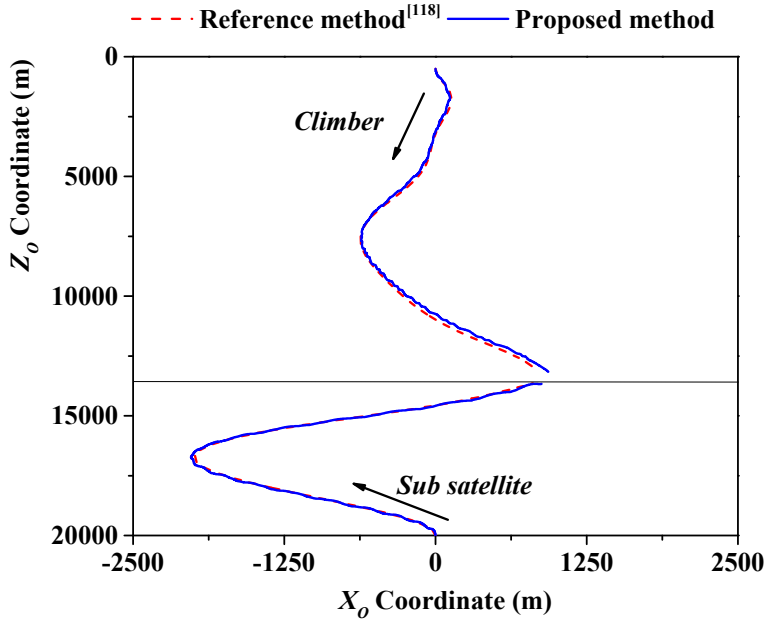

Figure 3.24 In-plane trajectories of climber and sub spacecraft in downward transfer.

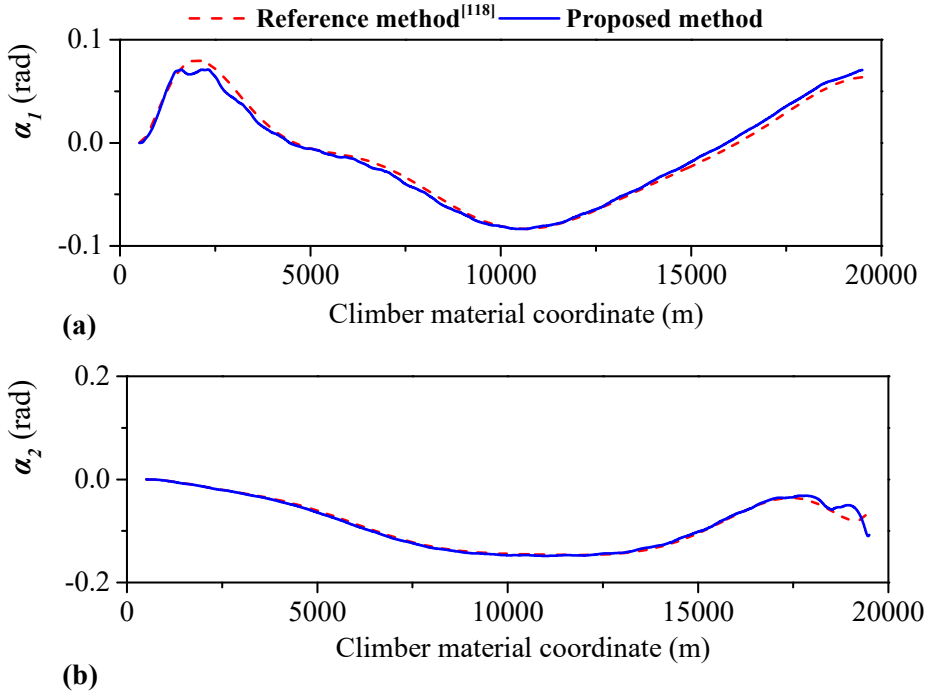

Figure 3.25 Comparison results of the libration angles in the climber's downward transfer motion. (a) Libration angle α_1. (b) Libration angle α_2.

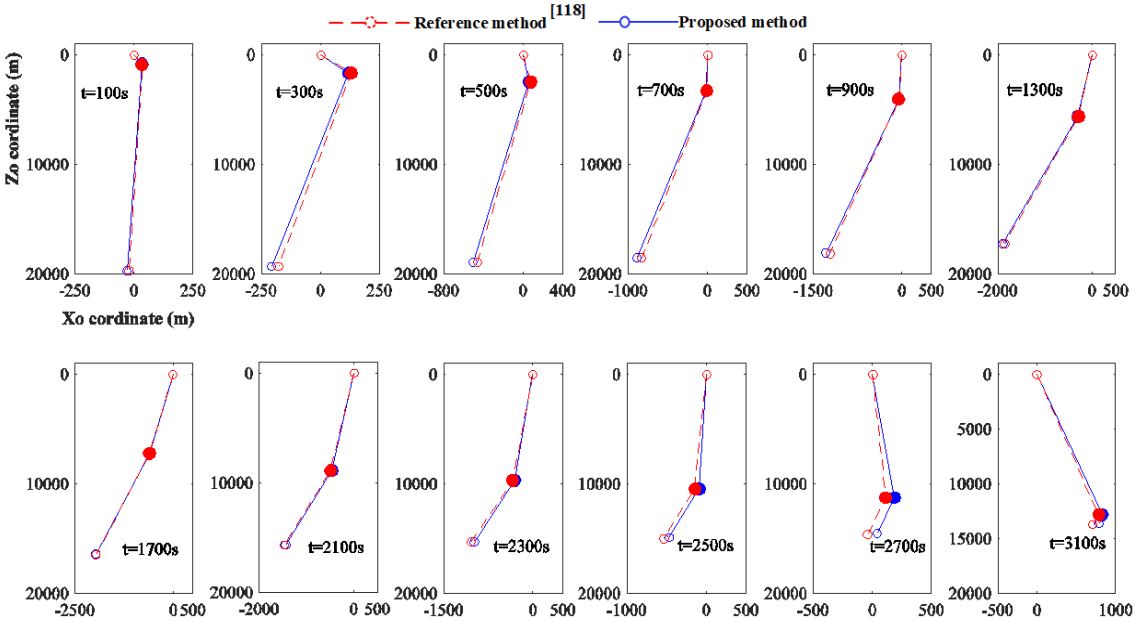

Figure 3.26 Comparison of geometrical configuration of TSS in downward transfer.

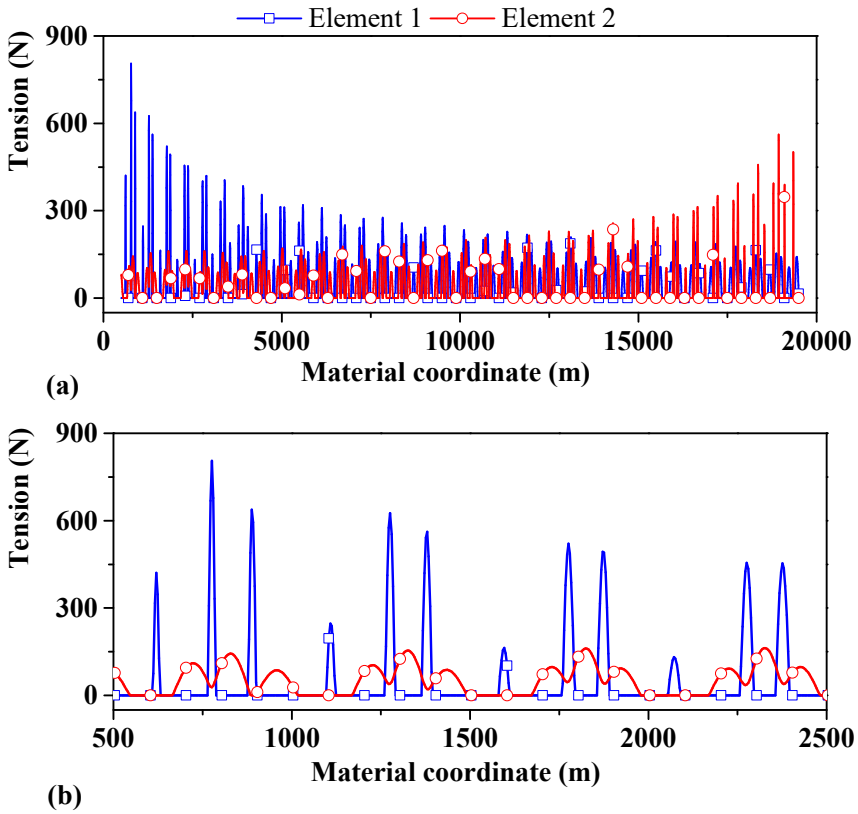

Figure 3.27 Variation of tether tension in upward transfer: (a) global and (b) zoomed views.

3.3 Conclusions

This chapter presents two dynamic models developed for TSS with fixed and variable tether length. For the first dynamic model, the implicit 4th order Symplectic implicit Runge-Kutta integrator is used for the long-term dynamic simulation of TSS. Two benchmark studies are analyzed with the Symplectic integration scheme compared with the classical 4th order explicit Runge-Kutta method. The results demonstrate that the Symplectic integrator possesses high accuracy and is robust. For the second dynamic model, the backward Euler formulation together with the Newton-Raphson iteration method are used

to solve the dynamics of TSS with variable tether length. The variable-length approach is explored to handle the length variation problem due to the movement of climber and the deployment or retrieval of tether at the end spacecrafts. The benchmark studies are analyzed to validate the proposed method under two scenarios, one is the climber moving along tether, the other is the climber is moving along the tether while the end spacecraft is deploying/retrieving tether. The results show the proposed method matches well with its counterpart, and the difference is observed due to the difference of the models.

Chapter 4 MULTIPHYSICS FINITE ELEMENT MODELING OF ELECTRODYNAMIC TETHERS

Summary: In this chapter, the model of tethered spacecraft system with fixed length is extended for an electrodynamic tether system. This leads to a high fidelity multiphysics finite element model for the electrodynamic tether system with consideration of all environmental perturbative forces. Then, this developed model is applied to study the long-term dynamic behavior of electrodynamic tether system in space debris deorbit process.

4.1 Dynamics and Control

4.1.1 Equation of Motion

The primary environmental perturbation forces acting on the EDT system are electrodynamic force, atmospheric drag, solar radiation pressure, heat flux in tethers and lunisolar gravitational perturbations [128]. In low Earth Orbit (LEO), the lunisolar gravitational perturbation is generally several orders of smaller in magnitude than other perturbations [40, 128] and can be safely ignored in the current thesis. It is worth pointing out here that the geodetic altitude, instead of geocentric altitude, should be used to calculate the atmospheric and plasma densities (in this chapter) in order to account for the Earth's oblateness and plasma variation [129].

As presented in Chapter 3.1, the equation of motion of *k-th* element is derived based on the principle of virtual work, as listed in Eq. (3.19). Then, the equation of motion of

TSS can be obtained through the assembly procedure in the finite element method, see in Eq. (3.20). However, it is noted that only the elastic and gravitational forces are considered for a TSS. For an EDT system, the other environmental perturbative forces are needed to be included,

$$\boldsymbol{M}_a\ddot{\boldsymbol{X}}_a+\boldsymbol{K}_a\boldsymbol{X}_a=\boldsymbol{F}_e+\boldsymbol{F}_g+\boldsymbol{F}_L+\boldsymbol{F}_d+\boldsymbol{F}_s \tag{4.1}$$

where $\boldsymbol{F}_L$, $\boldsymbol{F}_d$ and $\boldsymbol{F}_s$ are the vectors of nodal force resulting from the electrodynamic force, atmosphere drag, and solar radiation pressure, respectively. Moreover, the same coordinate systems in Chapter 3 are used, see Fig. 4.1.

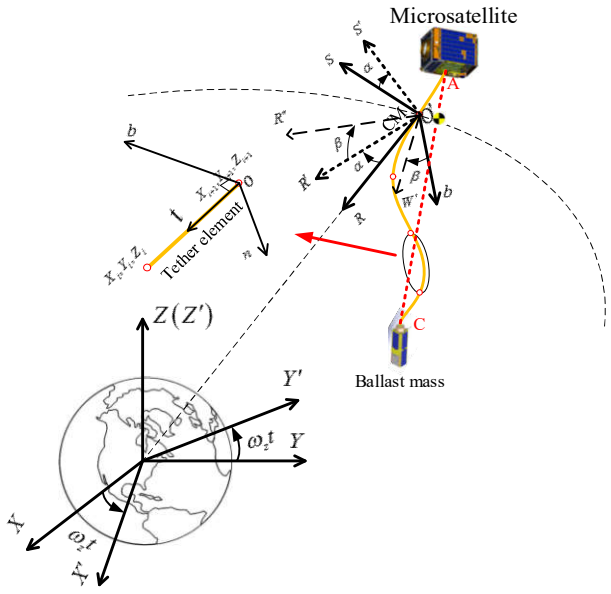

Figure 4.1 Schematic coordinate systems for EDT model.

4.1.1.1 Electrodynamic Force

The electrodynamic force exerted on a tether carrying electric current results from the interaction between Earth's magnetic field and current in tether. From the Lorentz law, the electrodynamic force is $\boldsymbol{F}_e = I\boldsymbol{e}_t \times \boldsymbol{B}$, where the I is the current in tether, $\boldsymbol{B}$ is the vector of magnetic field strength, and $\boldsymbol{e}_t$ is the unit vector of t-axis in the local frame.

Magnetic Field

The strength of magnetic field of Earth is derived from the Earth's scalar potential function [130], such that,

$$V(r,\phi',\lambda,t) = R\sum_{n=1}^{N}\sum_{m=0}^{n}\left(\frac{R}{r}\right)^{l+1} P_n^m\left[\cos(\phi')\right]\left[G_n^m(t)\cos(m\lambda) + H_n^m(t)\sin(m\lambda)\right] \qquad (4.2)$$

where R is the magnetic reference spherical radius (R = 6371.2 km) that is close to the mean Earth radius, r is the radial distance from the center of Earth to any point on the element, ϕ' is the geocentric co-latitude (*i.e.* 90°−latitude), λ is the east longitude, P_n^m is the Schmidt semi-normalized associated Legendre functions of degree n and order m, and (G_n^m, H_n^m) are the Schmidt semi-normalized spherical harmonic coefficients.

By taking the partial derivatives of Eq.(4.2) with respect to variables (r, ϕ', θ), the magnetic field strength $\boldsymbol{B}_{mst} = \left\{B_r, B_{\phi'}, B_\theta\right\}$ can be expressed in the Earth-fixed frame in term of spherical form of global coordinate system as,

$$
\begin{aligned}
B_r &= (n+1)\sum_{n=1}^{N}\sum_{m=0}^{n}\left(\frac{R}{r}\right)^{n+2} P_n^m\left[\cos(\phi')\right]\left[G_n^m\cos(m\lambda)+H_n^m\sin(m\lambda)\right] \\
B_{\phi'} &= -\sum_{n=1}^{N}\sum_{m=0}^{n}\left(\frac{R}{r}\right)^{n+2}\left[G_n^m\cos(m\lambda)+H_n^m\sin(m\lambda)\right]\frac{\partial P_n^m\left[\cos(\phi')\right]}{\partial\phi'} \\
B_{\lambda} &= -\frac{1}{\sin\phi'}\sum_{n=1}^{N}\sum_{m=0}^{n}\left(\frac{R}{r}\right)^{n+2} P_n^m\left[\cos(\phi')\right]m\left[-G_n^m\sin(m\lambda)+H_n^m\cos(m\lambda)\right]
\end{aligned}
\tag{4.3}
$$

If we consider a bare conductive tether across the Earth's magnetic field at the orbital velocity, a motional electric field will be induced, and its projection along the length of tether E_m can be expressed as,

$$
E_m = -\left(\boldsymbol{V}_r^l \times \boldsymbol{B}_{mst}^l\right)\cdot \boldsymbol{e}_t \tag{4.4}
$$

where the superscript $(\ )^l$ represents the variable expressed in the local frame. $\boldsymbol{B}_{mst}^l$ is the vector of magnetic strength in the local frame, $\boldsymbol{V}_r^{\,l}$ is the vector of relative velocity of the tether element.

Electron Emitter

The motional electric field makes the tether partially positive and partially negative biased with respect to the ambient plasma. Consequently, the bare tether will attract free electrons from the ambient plasma and complete a current loop if the electrons are emitted back to the plasma at the end of the tether as shown in Fig. 4.2. A current will be generated in the tether if the collected electrons are emitted back to the plasma by an electron emitter at the cathodic end *C* [38]. There are three types of electron emitters proposed in the literature, namely, the hollow cathode emitter, the thermionic cathode, and the Field Emitter Array (FEA) cathode including the Spindt field emitter array cathode and the carbon-nanotube

field emission cathode, respectively. The Spindt FEA cathode is selected in the thesis due to its low mass, low operational potential bias, compact size and high current density [131]. The current-voltage relationship of the Spindt FEA cathode can be derived from the Fowler-Nordheim equation [131],

$$I_t = S_e N_t a_e \Phi_t^2 \left(q_e\right)^{-b_e/\Phi_t} \tag{4.5}$$

where S_e is the area of emitter board, N_t is the number of emitter tips per unit area, q_e is the electron charge ($q_e = 1.60218 \times 10^{-19}$ C), the coefficients a_e and b_e are determined experimentally. These parameters will be given in the numerical simulation section. Once the potential bias Φ_t is defined, Eq. (4.5) determines the maximum current available in the bared tether, which is used as one boundary condition for the orbital motion limited theory [38, 132] in the following.

Orbital Motional Limited Theory

Assume that the tether diameter is smaller than the Debye length, then the current in tether obeys the orbital motion limited (OML) theory [5, 38, 132] as shown in Fig. 4.2. The relationship between current I and potential bias Φ is,

$$\begin{cases} \dfrac{dI}{ds} = q_e N_\infty D \sqrt{2 q_e \Phi / m_e} \\ \dfrac{d\Phi}{ds} = \dfrac{I}{\sigma A_t} - E_m \end{cases} \quad \Phi > 0 \text{ for segment } AB \tag{4.6}$$

$$\begin{cases} \dfrac{dI}{ds} = -\mu q_e N_\infty D\sqrt{2q_e|\Phi|/m_e} \\ \dfrac{d\Phi}{ds} = \dfrac{I}{\sigma A_t} - E_m \end{cases} \quad \Phi < 0 \text{ for segment } BC \tag{4.7}$$

with boundary conditions

$$\begin{aligned} &s = 0, && I = 0 \\ &s = s_B, && \Phi = 0 \\ &s = s_C = L, && V_{cc} + Z_T I_C = E_m(L - s_B) - \int_{s_B}^{L} \frac{I}{\sigma A_t} ds \end{aligned}$$

where $\Phi = V_t - V_p$ is the potential bias between tether and plasma with V_t and V_p being potential of tether and plasma, respectively. m_e is the electron mass, N_∞ is the electron density of ambient plasma determined by 2010 International Reference Ionosphere (IRI) model [133], σ is the conductivity of tether, D is the diameter of tether, A_t is the conductive area of tether, $\mu = \sqrt{m_e/m_i} = 1/172$ is the square root of mass ratio of electron to ion with m_i representing the mass of ion. I_c and V_{cc} are the current and potential bias of cathodic device at the end of C, and Z_T is the device's electrical resistance depending on the real structure at the cathodic end, respectively.

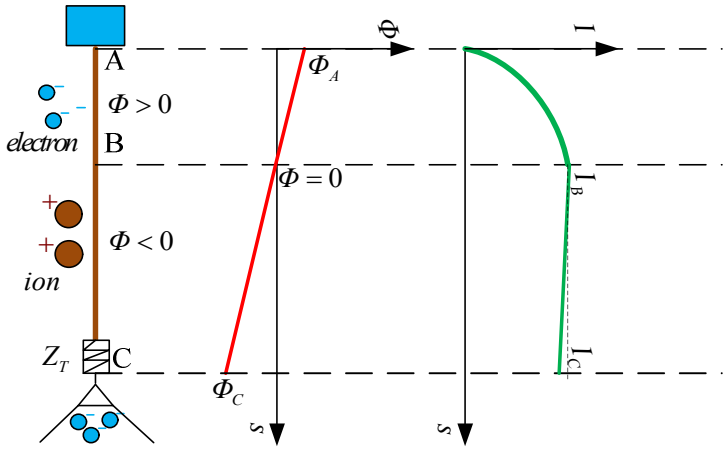

Figure 4.2 Scheme of a bare tether and voltage-current characteristic, *A* is the anode end of the tether, *C* denotes the cathode end and *B* is the point with zero potential bias.

For simplicity, the OML equation can be nondimensionalized [5, 8],

$$\begin{cases} \dfrac{di}{d\xi} = \dfrac{3}{4}\sqrt{\phi} \\ \dfrac{d\phi}{d\xi} = i - 1 \end{cases} \quad \phi > 0 \text{ for segment } AB \tag{4.8}$$

$$\begin{cases} \dfrac{di}{d\xi} = -\dfrac{3}{4}\mu\sqrt{-\phi} \\ \dfrac{d\phi}{d\xi} = i - 1 \end{cases} \quad \phi < 0 \text{ for segment } BC \tag{4.9}$$

$$\begin{aligned} &\xi = 0: && i = 0 \quad \phi = \phi_A \\ &\xi = \xi_B: && \phi = 0 \quad i = i_B \\ &\xi = \xi_C = l_t: && \phi = \phi_c = -(\Omega i_c + \tilde{\phi}_c) l_t \quad i = i_C \end{aligned} \tag{4.10}$$

where $i = I/I_{sc}$ is the dimensionless current in tether, I_{SC} is the short-circuit current of tether $I_{SC} = \sigma E_m A_t$, $\phi = \Phi_p / E_m L^*$ is the dimensionless potential bias of tether with respect to the ambient plasma, and $l_t = L/L^*$ is the dimensionless tether length [8], $\xi \in$ [0, l_t] is the dimensionless length measured from the anode end *A*, ϕ_C and ϕ_A are the potential bias at the cathodic and anode ends, i_C and i_B are the current at points *B* and *C*, $L^* = \left(9\pi m_e \sigma^2 E_m A_t / 128 q_e^3 N_e^2\right)^{1/3}$ is the characteristic length, $\tilde{\phi}_c = V_{cc}/E_m L$ is the dimensionless potential bias where V_{cc} is the potential bias at the cathodic end *C* with respect to the ambient plasma. The dimensionless resistance Ω of Spindt FEA cathode is given as follows [131],

$$\Omega = \frac{1}{R_e}\frac{d}{d\Phi_t}\left[S_e N_t a_e \Phi_t^2 \left(q_e\right)^{-b_e/\Phi_t} \right]\Big|_{\Phi_t = V_{cc}} \tag{4.11}$$

Once the current profile along tether is determined, the vector of nodal electrodynamic force of *k-th* element can be derived from the virtual work done by electrodynamic force, such that,

$$\delta W_L = \int_0^{L_{a,k}} \delta \boldsymbol{X}_{a,k}^T \boldsymbol{f}_L dx = \delta \boldsymbol{X}_{a,k}^T \boldsymbol{F}_{L,k} \tag{4.12}$$

$$\begin{aligned}
&\boldsymbol{F}_{L,k} = \int_0^{L_{a,k}} \boldsymbol{N}^T \boldsymbol{f}_L ds = \frac{L_{a,k}}{2}\sum_{i=1}^{N_{GA}} w_i \boldsymbol{N}^T \left[\frac{L_{a,k}}{2}(1+\xi_i)\right] \boldsymbol{f}_L \left[\frac{L_{a,k}}{2}(1+\xi_i)\right] \\
&\boldsymbol{f}_L \left[\frac{L_{a,k}}{2}(1+\xi_i)\right] = \boldsymbol{T}_{f2g} \boldsymbol{f}_L^{\boldsymbol{F}} \left[\frac{L_{a,k}}{2}(1+\xi_i)\right] \\
&\boldsymbol{f}_L^F \left[\frac{L_{a,k}}{2}(1+\xi_i)\right] = \begin{bmatrix} \boldsymbol{T}_{l2f} & 0 \\ 0 & \boldsymbol{T}_{l2f} \end{bmatrix}\Bigg|_{\frac{L_{a,k}}{2}(1+\xi_i)} \boldsymbol{f}_L^L \left[\frac{L_{a,k}}{2}(1+\xi_i)\right]
\end{aligned} \tag{4.13}$$

where $\boldsymbol{F}_{L,k}$ is the vector of nodal electrodynamic force of tether element in the global frame with subscript *k* denoting the *k-th* element, $\boldsymbol{f}_L^F$, and $\boldsymbol{f}_L^L$ are the electrodynamic force per unit length of tether in the Earth-fixed and local frames, respectively. The electrodynamic force in the local element frame is determined by the Lorentz law,

$$\boldsymbol{f}_L^L = -\boldsymbol{B}_L \times I \ \boldsymbol{e}_t \tag{4.14}$$

where $\boldsymbol{B}_L$ is the vector of magnetic field strength expressed in the local frame, and *I* is the induced current in the element.

In this chapter, three evaluation methods are used to determine the induced current and potential bias along the tether. They are listed as follows,

Method A

As shown in Fig. 4.2, the tether is divided into two parts, the anodic segment *AB* and cathodic segment *BC*,

$$l_t = l_{t,AB} + l_{t,BC} \tag{4.15}$$

where l_t is the non-dimensional length of tether with subscript AB and *BC* representing the anodic and cathodic segments, respectively.

As shown in Eq. (4.8), let the first equation divide the second equation, and integrate from point *A* to *B*, such that,

$$\begin{aligned} -\frac{3}{4}\sqrt{\phi}\,d\phi &= (1-i)\,di \\ i^2 - 2i &= \phi^{\frac{3}{2}} + C \end{aligned} \tag{4.16}$$

Then, applying the boundary conditions at A and B points as listed in Eq. (4.10) leads to,

$$\begin{aligned} i^2 - 2i &= \phi^{3/2} - \phi_A^{3/2} \\ (i-1) &= -\sqrt{\phi^{3/2} - \phi_A^{3/2} + 1} \end{aligned} \tag{4.17}$$

Substituting Eq. (4.17) into the second equation of Eq. (4.8), the dimensionless length of segment *AB* is obtained as,

$$l_{t,AB} = \int_0^{\left(2i_B - i_B^2\right)^{3/2}} \frac{d\varphi}{\left[\left(\varphi^{\frac{3}{2}} + \left(i_B - 1\right)^2\right)^{\frac{1}{2}}\right]} \tag{4.18}$$

The same process can be repeated for the cathodic segment *BC* with the corresponding boundary conditions, then, the dimensionless length of segment *BC* can be

obtained as,

$$l_{t,BC} = \int_{\varphi_C}^{0} \frac{d\varphi}{\left[\mu\left(-\varphi\right)^{\frac{3}{2}} + \left(i_B - 1\right)^2\right]^{1/2}} \tag{4.19}$$

Meanwhile, a relationship between current B and C can be obtained as,

$$\left(i_B - 1\right)^2 = \left(i_C - 1\right)^2 - \mu\left(\tilde{V}_{cc} l_t + i_C \Omega l_t\right)^{3/2} \tag{4.20}$$

Finally, substitute Eqs. (4.18)-(4.20) into Eq. (4.15) yields,

$$\begin{aligned} l_t = &\int_0^{\left[2i_C - i_C^2 + \mu\left(\tilde{\phi}_c l_t + i_C \Omega l_t\right)^{3/2}\right]^{2/3}} \left[\phi^{3/2} + \left(i_C - 1\right)^2 - \mu\left(\tilde{\phi}_c l_t + i_C \Omega l_t\right)^{3/2}\right]^{-1/2} d\phi + \\ &\int_{-\left(\tilde{\phi}_c l_t + i_C \Omega l_t\right)}^{0} \left[\mu\left(-\phi\right)^{3/2} + \left(i_C - 1\right)^2 - \mu\left(\tilde{\phi}_c l_t + i_C \Omega l_t\right)^{3/2}\right]^{-1/2} d\phi \end{aligned} \tag{4.21}$$

The Eq. (4.21) is highly nonlinear and must be solved numerically at each time step to obtain the unknown value of i_C [134]. Once the current i_C is determined by Eq. (4.21), the current i_B can be given as,

$$i_B = 1 - \sqrt{\left(i_C - 1\right)^2 - \mu\left(\tilde{\phi}_c l_t + i_C \Omega l_t\right)^{3/2}} \tag{4.22}$$

After currents of i_B and i_C are obtained, the profiles of current and potential along tether can be obtained by integrating Eqs. (4.8)-(4.9) Then, they are sent back to Eqs. (4.13)-(4.14) to evaluate the distributed electrodynamic force.

Method B

For this method, the dimensionless OML equations as listed in Eqs. (4.8)-(4.9) are directly discretized. The critical step in discretizing process is to determine the location of null

potential bias, point B of the tether, which is unknown in priori. Considering a flexible tether as shown in Fig. 4.3(a). Assume the point B is located inside the *k-th* element that will be determined later. Then, all *j-th* elements ($j < k$) obey Eq. (4.8) while all *l-th* elements ($l > k$) obey Eq.(4.9). The derivation of the discretized orbital motion limited theory starts from the first element.

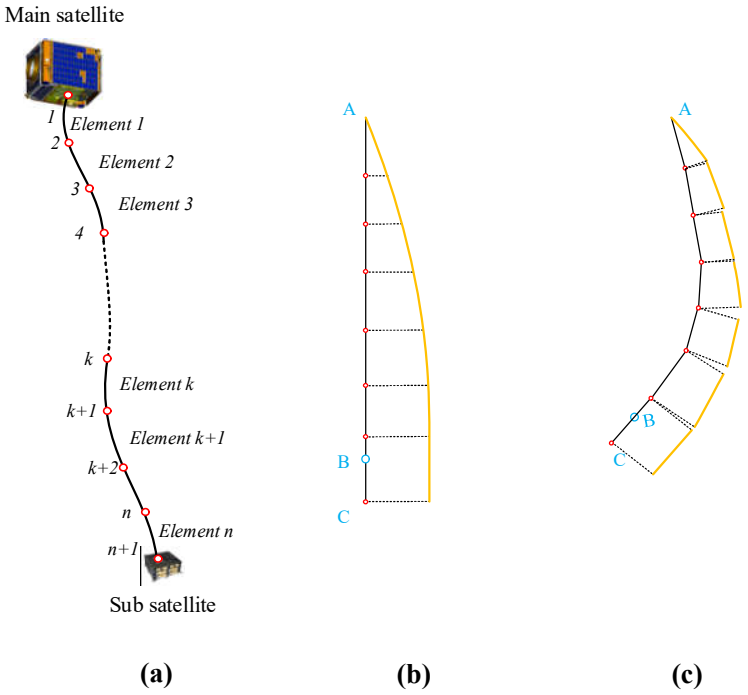

Figure 4.3 (a) Discretization of continuous tether. (b) Electric current profile of a straight and continuous tether. (c) Electric current profile of a bent and discretized tether.

Rearranging Eq. (4.8) yields,

$$\begin{cases} (i-1)\,di = \dfrac{3}{4}\sqrt{\phi}\,d\phi, & \phi \geq 0 \\ d\xi = (i-1)^{-1}\,d\phi \end{cases} \tag{4.23}$$

Integrating the first equation of Eq. (4.23) from node 1 (point A) to any point within the element yields,

$$\int_{i_1}(i-1)\,di=\int_{\phi_1}\frac{3}{4}\sqrt{\phi}\,d\phi \quad \Rightarrow \quad (i-1)^2-\phi^{3/2}=(i_1-1)^2-\phi_1^{3/2} \tag{4.24}$$

Substituting Eq. (4.24) into the second equation of Eq. (4.23) and integrating with the boundary conditions at nodes 1 and 2 lead to the dimensionless length of the first element ξ_1, which should be equal to the instant dimensionless length of that element $l_{t,1}$, such that,

$$\xi_1=-\int_{\phi_1}^{\phi_2}\frac{d\phi}{\left[(i_1-1)^2+\phi^{3/2}-\phi_1^{3/2}\right]^{1/2}}=l_{t,1} \tag{4.25}$$

where $\phi_1\left(=\phi_A\right)$ and ϕ_2 are the potential bias at the nodes 1 and 2 of the 1st element.

Applying the boundary condition at node 2 to Eq. (4.24) yields,

$$(i_1-1)^2-\phi_1^{3/2}=(i_2-1)^2-\phi_2^{3/2} \tag{4.26}$$

Equations (4.24)-(4.26) form the discretized governing equations of current and potential bias of the first element, where Eq. (4.25) will be integrated numerically by the Gaussian integration.

Applying the same process to the second element yields the discretized governing equations of current and potential bias of that element,

$$(i_{2,2}-1)^2-\phi_{2,2}^{3/2}=(i_3-1)^2-\phi_3^{3/2} \tag{4.27}$$

$$\xi_2=-\int_{\phi_{2,2}}^{\phi_3}\frac{d\phi}{\left[(i_{2,2}-1)^2+\phi^{3/2}-\phi_{2,2}^{3/2}\right]^{1/2}}=l_{t,2} \tag{4.28}$$

Note that the nodal current and potential bias of the second element at node 2, ($i_{2,2}$, $\phi_{2,2}$), may not necessarily equal to the nodal current and potential bias of the first

element at node 2, (i_2, ϕ_2). This is because the dimensionless element length of each element is normalized with the elemental characteristic length $L_*^k = \left(9\pi^2 m_e \sigma^2 E_m^k p_t^{\,2} / 128 e^3 N_e^{\,2}\right)^{1/3}$. The elemental characteristic length varies from element to element even for the tether made of same material because the motional electric field and the ambient electron density are evaluated at the location of the center of mass of element. This character of finite element method is advantageous compared with existing approaches as it can handle with the tether with variable electric conductivity and cross-section area.

To avoid the impact of the discontinuity at node, the nodal current and potential bias of the second element at node 2, ($i_{2,2}$, $\phi_{2,2}$) are adjusted by two scaling factors to enforce the continuity of electric current and potential bias at the node that links two elements, such that, ($i_{2,2} = \alpha_1 \cdot i_2$) and potential bias ($\phi_{2,2} = \beta_1 \cdot \phi_2$). The factors are defined by $\alpha_1 = I_{SC}^1 / I_{SC}^2$ and $\beta_1 = \Phi_{SC}^1 / \Phi_{SC}^2$, which are the ratios of short-circuit current and characteristic potential bias of two connecting elements, respectively. Thus, the discretized equations of current and potential bias of the second element become,

$$\left(\alpha_1 i_2 - 1\right)^2 - \left(\beta_1 \phi_2\right)^{3/2} = \left(i_3 - 1\right)^2 - \phi_3^{3/2} \tag{4.29}$$

$$\xi_2 = -\int_{\beta_1\phi_2}^{\phi_3} \frac{d\phi}{\left[\left(\alpha_1 i_2 - 1\right)^2 + \phi^{3/2} - \left(\beta_1 \phi_2\right)^{3/2}\right]^{1/2}} = l_{t,2} \tag{4.30}$$

Repeating the procedure for all *j-th* elements ($j<k$) yields the discrete current-potential bias relationships at nodes and the relationship between the calculated and the

instant dimensionless tether length of *j-th* element,

$$\left(\alpha_{j-1} i_j - 1\right)^2 - \left(\beta_{j-1}\phi_j\right)^{3/2} = \left(i_{j+1} - 1\right)^2 - \phi_{j+1}^{3/2} \tag{4.31}$$

$$\xi_j = -\int_{\beta_{j-1}\phi_j}^{\phi_{j+1}} \frac{d\phi}{\left[\left(\alpha_{j-1} i_j - 1\right)^2 + \phi^{3/2} - \left(\beta_{j-1}\phi_j\right)^{3/2}\right]^{1/2}} = l_{t,j} \tag{4.32}$$

where $\alpha_{j-1} = I_{SC}^{j-1} / I_{SC}^{j}$ and $\beta_{j-1} = \left(\Phi_{SC}^{j-1} / \Phi_{SC}^{j}\right)$ are the scaling factors that enforce the continuity of current and potential bias at nodes that link two elements.

For the *k-th* element where the null potential bias point *B* resides, it is divided into the anode and cathode segments. Applying the same procedure, the current and potential bias of the anode segment obey Eq. (4.8), such that,

$$\left(\alpha_{k-1} i_k - 1\right)^2 - \left(\beta_{k-1}\phi_k\right)^{3/2} = \left(i_B - 1\right)^2 - \phi_B^{3/2} \tag{4.33}$$

$$\xi_{k,1} = -\int_{\beta_{k-1}\phi_k}^{\phi_B} \frac{d\phi}{\left[\left(\alpha_{k-1} i_k - 1\right)^2 + \phi^{3/2} - \left(\beta_{k-1}\phi_k\right)^{3/2}\right]^{1/2}} \tag{4.34}$$

where $\alpha_{k-1} = I_{SC}^{k-1} / I_{SC}^{k}$ and $\beta_{k-1} = \left(\Phi_{SC}^{k-1} / \Phi_{SC}^{k}\right)$ are the scaling factors that enforce the continuity of current and potential bias at nodes that link two elements.

For the cathodic segment, the current and potential bias obey Eq. (4.9), such that,

$$\left(i_B - 1\right)^2 + \mu\left(-\phi_B\right)^{3/2} = \left(i_{k+1} - 1\right)^2 + \mu\left(-\phi_{k+1}\right)^{3/2} \tag{4.35}$$

$$\xi_{k,2} = -\int_{\phi_B}^{\phi_{k+1}} \frac{d\phi}{\left[\left(i_B - 1\right)^2 + \mu\left(-\phi_B\right)^{3/2} - \mu\left(-\phi\right)^{3/2}\right]^{1/2}} \tag{4.36}$$

Thus, the equation of current and potential bias and the constraint on the calculated dimensionless length of the *k-th* element can be written as,

$$\begin{aligned}&\left(\alpha_{k-1}i_k-1\right)^2-\left(\beta_{k-1}\phi_k\right)^{3/2}=\left(i_B-1\right)^2-\phi_B^{3/2}\\&=\left(i_{k+1}-1\right)^2+\mu\left(-\phi_{k+1}\right)^{3/2}\end{aligned}\tag{4.37}$$

$$\begin{aligned}&-\int_{\beta_{k-1}\phi_k}^{\phi_B}\frac{d\phi}{\left[\left(\alpha_{k-1}i_k-1\right)^2+\phi^{3/2}-\left(\beta_{k-1}\phi_k\right)^{3/2}\right]^{1/2}}\\&-\int_{\phi_B}^{\phi_{k+1}}\frac{d\phi}{\left[\left(i_B-1\right)^2+\mu\left(-\phi_B\right)^{3/2}-\mu\left(-\phi\right)^{3/2}\right]^{1/2}}=l_{t,k}\end{aligned}\tag{4.38}$$

Finally, all the *l-th* elements ($l>k$) are cathodic and obey the Eq. (4.9). Repeating the procedure for all *l-th* elements ($l>k$) yields the discrete current-potential bias relationships at nodes and the relationship between the calculated and the instant dimensionless tether length of *l-th* element,

$$\left(\alpha_{l-1}i_l-1\right)^2+\mu\left(-\beta_{l-1}\phi_l\right)^{3/2}=\left(i_{l+1}-1\right)^2+\mu\left(-\phi_{l+1}\right)^{3/2}\tag{4.39}$$

$$\xi_l=-\int_{\beta_{l-1}\phi_l}^{\phi_C}\frac{d\phi}{\left[\left(\alpha_{l-1}i_l-1\right)^2+\mu\left(-\beta_{l-1}\phi_l\right)^{3/2}-\mu\left(-\phi\right)^{3/2}\right]^{1/2}}=l_{t,l}\tag{4.40}$$

where $\alpha_{l-1}=I_{SC}^{l-1}/I_{SC}^{l}$ and $\beta_{l-1}=\Phi_{SC}^{l-1}/\Phi_{SC}^{l}$.

Thus, Eqs. (4.8)-(4.9) are discretized into the following finite element equations by equaling the calculated dimensionless element length to the instant dimensionless element length obtained from the dynamic analysis of tether, such that,

$$
\begin{aligned}
f_1 &= l_{t,1} - \xi_1 = l_{t,1} + \int_{\phi_1}^{\phi_2} \frac{d\phi}{\left[\left(i_1 - 1\right)^2 + \phi^{3/2} - \phi_1^{3/2}\right]^{1/2}} = 0 \\
f_2 &= l_{t,2} - \xi_2 = l_{t,2} + \int_{\beta_1\phi_2}^{\phi_3} \frac{d\phi}{\left[\left(\alpha_1 i_2 - 1\right)^2 + \phi^{3/2} - \left(\beta_1\phi_2\right)^{3/2}\right]^{1/2}} = 0 \\
&\vdots \\
f_{k-1} &= l_{t,k-1} - \xi_{k-1} = l_{t,k-1} + \int_{\beta_{k-2}\phi_{k-1}}^{\phi_k} \frac{d\phi}{\left[\left(\alpha_{k-2} i_{k-1} - 1\right)^2 + \phi^{3/2} - \left(\beta_{k-2}\phi_{k-1}\right)^{3/2}\right]^{1/2}} = 0 \\
f_k &= l_{t,k} - \xi_{k,1} - \xi_{k,2} = l_{t,k} + \int_{\beta_{k-1}\phi_k}^{\phi_B} \frac{d\phi}{\left[\left(\alpha_{k-1} i_k - 1\right)^2 + \phi^{3/2} - \left(\beta_{k-1}\phi_k\right)^{3/2}\right]^{1/2}} \\
&\qquad + \int_{\phi_B}^{\phi_{k+1}} \frac{d\phi}{\left[\left(i_B - 1\right)^2 + \mu\left(-\phi_B\right)^{3/2} - \mu\left(-\phi\right)^{3/2}\right]^{1/2}} = 0 \\
&\vdots \\
f_n &= l_{t,n} - \xi_n = l_{t,n} + \int_{\beta_{n-1}\phi_n}^{\phi_C} \frac{d\phi}{\left[\left(\alpha_{n-1} i_n - 1\right)^2 + \mu\left(-\beta_{n-1}\phi_n\right)^{3/2} - \mu\left(-\phi\right)^{3/2}\right]^{1/2}} = 0
\end{aligned}
\tag{4.41}
$$

with the discretized OML equations at tether nodes,

$$
\begin{aligned}
&f_{n+1} = \left[\left(i_1 - 1 \right)^2 - \phi_1^{3/2} \right] - \left[\left(i_2 - 1 \right)^2 - \phi_2^{3/2} \right] = 0 \\
&f_{n+2} = \left[\left(\alpha_1 i_2 - 1 \right)^2 - \left(\beta_1 \phi_2 \right)^{3/2} \right] - \left[\left(i_3 - 1 \right)^2 - \phi_3^{3/2} \right] = 0 \\
&\vdots \\
&f_{n+j} = \left[\left(\alpha_{j-1} i_j - 1 \right)^2 - \left(\beta_{j-1} \phi_j \right)^{3/2} \right] - \left[\left(i_{j+1} - 1 \right)^2 - \phi_{j+1}^{3/2} \right] = 0 \\
&f_{n+k} = \left[\left(\alpha_{k-1} i_k - 1 \right)^2 - \left(\beta_{k-1} \phi_k \right)^{3/2} \right] - \left[\left(i_{k+1} - 1 \right)^2 + \mu \left(-\phi_{k+1} \right)^{3/2} \right] = 0 \\
&\vdots \\
&f_{2n} = \left[\left(\alpha_{n-1} i_n - 1 \right)^2 + \mu \left(-\beta_{n-1} \phi_n \right)^{3/2} \right] - \left[\left(i_{n+1} - 1 \right)^2 + \mu \left(-\phi_{n+1} \right)^{3/2} \right] = 0
\end{aligned}
\tag{4.42}
$$

The discretized governing equations of *n* elements include all the nodal current and potential bias variables of EDT. There are $2 \times \left(n+1 \right)$ unknown variables including the current $i_j \left(j = 1 \cdots\cdots n+1 \right)$ and potential bias $\phi_j \left(j = 1 \cdots\cdots n+1 \right)$ with $2 \times n$ governing equations in Eqs. (4.41)-(4.42) and two boundary conditions shown in Eq. (4.10). The Newton-Raphson algorithm are adapted to solve this two-point boundary value problem to determine the location of null potential bias point *B*. The flowchart of the implementation is shown in Fig. 4.4. It should be noted that a good guess of initial input for the iteration yields a fast convergence. Therefore, the initial input is estimated by the semi-analytical method [38, 102] at each time step in the current work. Thus, the error in each step is not accumulated over the time.

Once the electric current profile along tether is determined, the distributed electrodynamic force acting on the tether element is calculated by Eqs. (4.13)-(4.14).

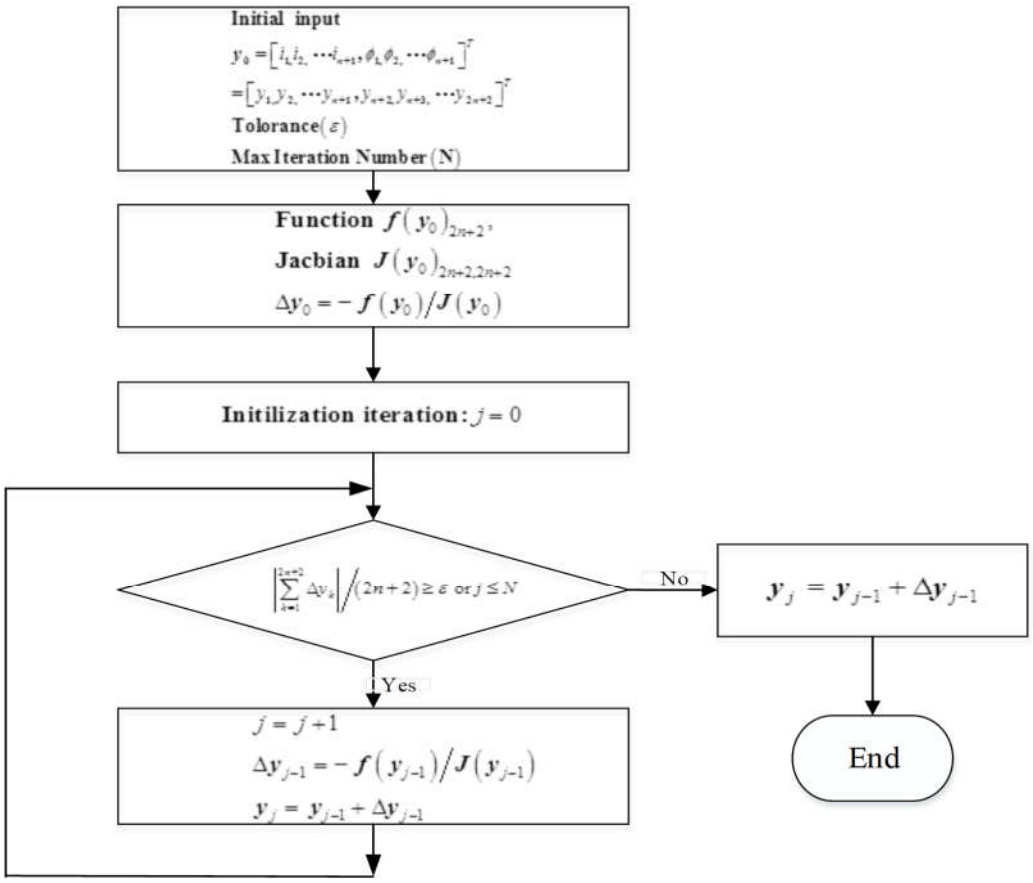

Figure 4.4 Flowchart of iteration for the current and potential bias profile.

Method C

For this method, the dimension OML equations as listed in Eqs. (4.6)-(4.7) are directly discretized. Rewrite Eqs. (4.6) -(4.7) as,

$$\begin{cases} \dfrac{dI}{ds} = a_1 a_2 \sqrt{\Phi} \\ \dfrac{d\Phi}{ds} = a_3 I - E_m \end{cases} \tag{4.43}$$

$$\begin{cases} \dfrac{dI}{ds} = -\mu a_1 a_2 \sqrt{-\Phi} \\ \dfrac{d\Phi}{ds} = a_3 I - E_m \end{cases} \tag{4.44}$$

where s is the arc-length measured from the anodic end, $a_1 = e\, p_t N_e / \pi$, $a_2 = \sqrt{2e/m_e}$ and $a_3 = 1/\sigma A_t$ are tether parameters. For the round type tether, $p_t = \pi d$. For the tape tether, $p_t = 2(w+t)$ is the perimeter of tether cross section with w and t representing the width and thickness. It should be noted that the parameters a_1 and E_m vary significantly along the tether length when the tether experiences a large bending deformation [42].

The OML in Eqs. (4.43)-(4.44) can be solved if the boundary conditions at the anodic and cathodic ends as well as the position of null potential bias inside the tether are known, such that,

$$\begin{array}{lll} s = 0, & I = 0 & \Phi = \Phi_A \\ s = L_B, & I = I_B & \Phi = \Phi_B = 0 \\ s = L_C, & I = I_C & \Phi = \Phi_C \end{array} \tag{4.45}$$

where L_B is the length of positively biased segment of tether, which ends at point B that is unknown in priori, L_C is the total length of deformed EDT tether, Φ and I are the electric potential bias and current along the tether, respectively. As shown in Fig. 4.6, the potential bias Φ_C at the cathodic end is a design parameter that can be modulated by connecting the tether either to a Spindt array emitter directly or via a standalone power source Φ_{PW}. There are two types of configuration at cathodic end,

$$\text{Type 1:} \qquad \Phi_C = -\left|\Phi_{CHE}\right| + I_C Z_T \tag{4.46}$$

Type 2: $$\Phi_C = |\Phi_{PW}| - |\Phi_{CHE}| + I_C Z_T \quad (4.47)$$

where Z_T is the equivalent impedance of the circuit, Φ_{CHE} is the gate potential bias applied to the emitter, and Φ_{PW} is the potential bias of the power source. All these parameters are known by design. In the second configuration, Φ_C could be set to zero, which represents the maximum efficiency of an EDT system.

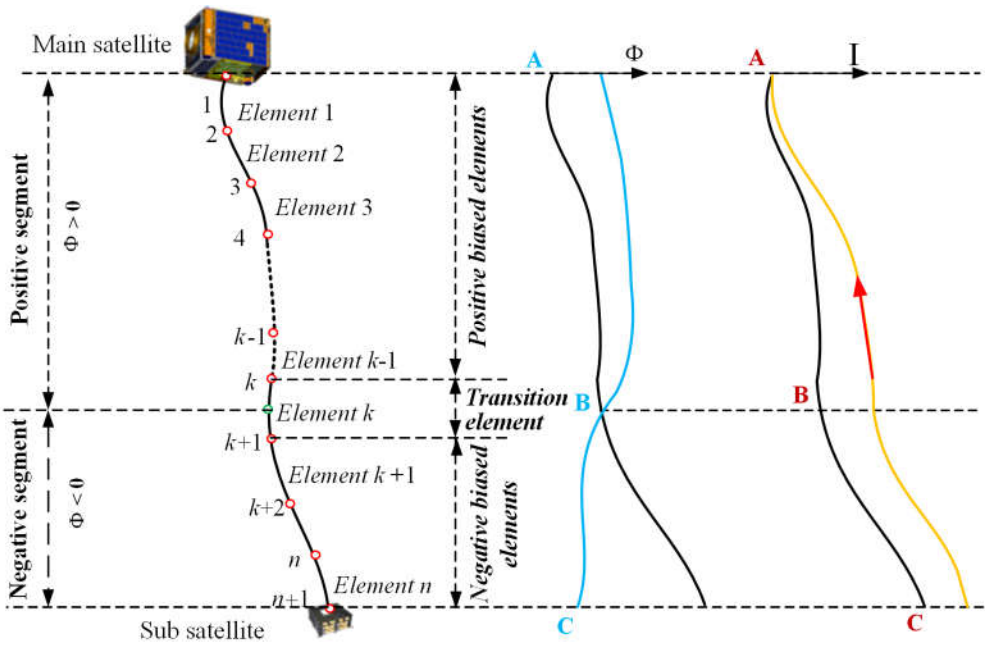

Figure 4.5 Schematic of current and potential bias along discretized bent tether.

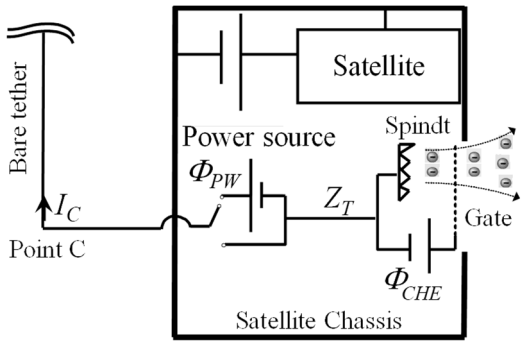

Figure 4.6 Design schematic of electric circuit at the cathodic end

The OML theory in Eqs (4.43)-(4.44) is directly discretized with the same mesh and element shape function of tether dynamics. The electric current and potential bias of an arbitrary point inside element are interpolated by their nodal values using a shape function, for example, the *j-th* element,

$$\boldsymbol{R} = \boldsymbol{N}\boldsymbol{R}_e \tag{4.48}$$

where $\boldsymbol{R}_e = \left(I_j, \Phi_j, I_{j+1}, \Phi_{j+1}\right)^T$ is the vector of nodal electric current and potential bias with subscripts referring to the nodal numbers for the *j-th* element, $\boldsymbol{R} = \left(I, \Phi\right)^T$ is the vector of electric current and potential bias inside the element, and $\boldsymbol{N}$ is the shape function of a two-noded straight element [63, 75],

$$\boldsymbol{N} = \begin{bmatrix} 1-\xi & 0 & \xi & 0 \\ 0 & 1-\xi & 0 & \xi \end{bmatrix} \tag{4.49}$$

where $\xi = s/L_{a,j}$, $L_{a,j} = \sqrt{\left(X_{j+1}-X_j\right)^2 + \left(Y_{j+1}-Y_j\right)^2 + \left(Z_{j+1}-Z_j\right)^2}$ is the instantaneous length of the *j-th* element, *s* is the distance measured from the *j-th* node of the *j-th* element, and $\boldsymbol{X}_a = \left(X_j, Y_j, Z_j, X_{j+1}, Y_{j+1}, Z_{j+1}\right)^T$ is the vector of nodal coordinates of the same element as listed in Chapter 3.1.

As shown in Fig. 4.5, the critical step in the discretization is to determine the location of null potential bias point *B*. It can be arbitrarily located in any elements, so it is assumed located inside the *k-th* element. Then all the elements can be categorized into three types, the positively biased element, the negatively biased element, and the transition element.

For any *j-th* element ($j < k$), it is positively biased against the ambient plasmas and obeys Eq. (4.43) to collect electrons. Substituting Eqs. (4.48)-(4.49) into the integrand of Eq. (4.43) yields the discretized OML equations of *j-th* element,

$$\boldsymbol{K}_c^j \boldsymbol{R}_e^j = \boldsymbol{F}_c^j \tag{4.50}$$

$$\boldsymbol{K}_c^j = \begin{bmatrix} -1/L_{a,j} & a_{1,j}a_{2,j}/\sqrt{\Phi_j} & 1/L_{a,j} & 0 \\ -a_{3,j} & -1/L_{a,j} & 0 & 1/L_{a,j} \end{bmatrix} \quad \text{and} \quad \boldsymbol{F}_c^j = \begin{pmatrix} 0 \\ -E_m^j \end{pmatrix} \tag{4.51}$$

where $\boldsymbol{K}_c^j$ is the coefficient matrix, $\boldsymbol{F}_c^j$ is the vector of EMF, $L_{a,j}$ is the instantaneous length of element, E_m^j is the EMF at the center of mass of element, and $a_{1,j}$, $a_{2,j}$ and $a_{3,j}$ are the tether parameters.

Similarly, for any *j-th* element ($j > k$), it is negatively biased against the ambient plasmas and obeys Eq. (4.44) to collect ions. Substituting Eqs. (4.48)-(4.49) into Eq. (4.44) and integrating along element length yield discretized OML equations in the same form of Eq. (4.50) but with different coefficient matrix and EMF vector,

$$\boldsymbol{K}_c^j = \begin{bmatrix} -1/L_{a,j} & -\mu a_{1,j}a_{2,j}/\sqrt{-\Phi_j} & 1/L_{a,j} & 0 \\ -a_{3,j} & -1/L_{a,j} & 0 & 1/L_{a,j} \end{bmatrix} \quad \text{and} \quad \boldsymbol{F}_c^j = \begin{pmatrix} 0 \\ -E_m^j \end{pmatrix} \tag{4.52}$$

For the transition *k-th* element, it is partially positively biased and partially negatively biased. Substituting the positively and negatively biased segments into Eqs. (4.43)-(4.44) respectively yields,

$$\begin{bmatrix} -1/L_{a,k}^P & a_{1,k}a_{2,k}/\sqrt{\Phi_k} & 1/L_{a,k}^P & 0 \\ -a_{3,k} & -1/L_{a,k}^P & 0 & 1/L_{a,k}^P \end{bmatrix} \begin{pmatrix} I_k \\ \Phi_k \\ I_B \\ \Phi_B \end{pmatrix} = \begin{pmatrix} 0 \\ -E_m^k \end{pmatrix} \tag{4.53}$$

$$\begin{bmatrix} -1/L_{a,k}^{N} & -\mu a_{1,k}a_{2,k}/\sqrt{-\Phi_B} & 1/L_{a,k}^{N} & 0 \\ -a_{3,k} & -1/L_{a,k}^{N} & 0 & 1/L_{a,k}^{N} \end{bmatrix} \begin{pmatrix} I_B \\ \Phi_B \\ I_{k+1} \\ \Phi_{k+1} \end{pmatrix} = \begin{pmatrix} 0 \\ -E_m^k \end{pmatrix} \tag{4.54}$$

where $L_{a,k}^{P}$ and $L_{a,k}^{N}$ are the lengths of positively and negatively biased segments to be determined. Intuitively, they can be first approximated by the solution of OML theory with assumptions of straight tether in the local vertical. Then, they will be updated iteratively, such as, $L_{a,k}^{P} = L_{a,k}\left|\Phi_k\right|/(\left|\Phi_k\right|+\left|\Phi_{k+1}\right|)$ and $L_{a,k}^{N} = L_{a,k} - L_{a,k}^{P}$, until the difference between successive estimations is less than a predefined tolerance. Eliminating the unknown variables I_B and Φ_B by combining Eqs. (4.53)-(4.54) yields the discretized OML equation of the transition *k-th* element in term of its nodal values,

$$\begin{bmatrix} b_{11} & b_{12} & b_{13} & b_{14} \\ b_{21} & b_{22} & b_{23} & b_{24} \end{bmatrix} \begin{pmatrix} I_k \\ \Phi_k \\ I_{k+1} \\ \Phi_{k+1} \end{pmatrix} = \begin{pmatrix} f_1 \\ f_2 \end{pmatrix} \tag{4.55}$$

where

$$b_{11} = -\left(1/L_{a,k}^{N} + \mu a_{1,k}a_{2,k}a_{3,k}L_{a,k}^{P}/\sqrt{E_m^k L_{a,k}^{P} - \Phi_k - a_{3,k}I_k L_{a,k}^{P}}\right)$$

$$b_{12} = -a_{1,k}a_{2,k}\left[L_{a,k}^{P}/L_{a,k}^{N}\sqrt{\Phi_k} + \mu/\sqrt{E_m^k L_{a,k}^{P} - \Phi_k - a_{3,k}I_k L_{a,k}^{P}}\right]$$

$$b_{13} = b_{24} = 1/L_{a,k}^{N},$$

$$b_{14} = b_{23} = 0,$$

$$b_{21} = -a_{3,k}\,L_{a,k}/L_{a,k}^{N},$$

$$b_{22} = -a_{1,k}a_{2,k}a_{3,k}L_{a,k}^{P} \Big/ \sqrt{\Phi_k} - 1 \Big/ L_{a,k}^{N}$$

$$f_1 = -\mu a_{1,k}a_{2,k}L_{a,k}^{P}E_m^k \Big/ \sqrt{E_m^k L_{a,k}^{P} - \Phi_k - a_{3,k}I_k L_{a,k}^{P}},$$

$$f_2 = -L_{a,k} \Big/ L_{a,k}^{N} E_m^k$$

Moreover, the boundary conditions at the anodic (1^{st} node) and cathodic (n+1 node) ends can be written as,

$$\begin{pmatrix} 1 & 0 & 0 & 0 \end{pmatrix} \begin{pmatrix} I_1 & \Phi_1 & I_2 & \Phi_2 \end{pmatrix}^T = 0 \tag{4.56}$$

$$\begin{pmatrix} 0 & 0 & -Z_T & 1 \end{pmatrix} \begin{pmatrix} I_n & \Phi_n & I_{n+1} & \Phi_{n+1} \end{pmatrix}^T = \begin{cases} -\left|\Phi_{CHE}\right| & \text{Type 1} \\ \left|\Phi_{PW}\right| - \left|\Phi_{CHE}\right| & \text{Type 2} \end{cases} \tag{4.57}$$

Finally, the discretized OML theory of an EDT system can be assembled by a standard finite element method,

$$\boldsymbol{G}_{2n+2} = \boldsymbol{K}_{(2n+2,2n+2)}\boldsymbol{R}_{2n+2} - \boldsymbol{F}_{2n+2} = 0 \tag{4.58}$$

where $\boldsymbol{K}_{(2n+2,\ 2n+2)}$, $\boldsymbol{R}_{2n+2}$ and $\boldsymbol{F}_{2n+2}$ are the global coefficient matrix, vector of nodal electric current and potential bias, and vector of nodal EMF, respectively.

Equation (4.58) is highly nonlinear with the unknown position of null potential bias point, or the location of *k-th* element. It is solved by the Newton-Raphson iterative algorithm subjected to the boundary conditions in Eqs. (4.56) and (4.57). Denote $\boldsymbol{R}_{2n+2}^{m}$ as an approximate solution after the m^{th} iteration, the true solution can be written as,

$$\boldsymbol{R}_{2n+2,true} = \boldsymbol{R}_{2n+2}^{m} + \Delta\boldsymbol{R}_{2n+2}^{m} \tag{4.59}$$

where the $\Delta\boldsymbol{R}_{2n+2}^{m}$ is the correction to the approximate solution.

Substituting Eq. (4.59) into (4.58) and expanding into a Taylor series by ignoring higher order terms yield,

$$0 = \boldsymbol{G}_{2n+2}\left(\boldsymbol{R}_{2n+2,true}\right) = \boldsymbol{G}_{2n+2}\left(\boldsymbol{R}^{m}_{2n+2} + \Delta\boldsymbol{R}^{m}_{2n+2}\right) \approx \boldsymbol{G}_{2n+2}\left(\boldsymbol{R}^{m}_{2n+2}\right) + \boldsymbol{J}^{m}_{(2n+2,2n+2)} \cdot \Delta\boldsymbol{R}^{m}_{2n+2} \tag{4.60}$$

where $\boldsymbol{J}^{m}_{(2n+2,2n+2)} = \partial\boldsymbol{G}/\partial\boldsymbol{R}\big|_{\boldsymbol{R}=\boldsymbol{R}^{m}_{2n+2}}$. Solving for the correction $\Delta\boldsymbol{R}^{m}_{2n+2}$ by the Newton-Raphson iteration until the residual of Eq. (4.58) satisfies $\varepsilon = \left|\boldsymbol{G}\left(\boldsymbol{R}^{m+1}_{2n+2}\right)\right| \Big/ \left(2n+2\right) \le 10^{-10}$ or iteration number $m = 50$.

Once the electric current profile along tether is determined, the distributed electrodynamic force acting on the tether element is calculated by Eqs. (4.13)-(4.14).

4.1.1.2 Atmospheric Drag

Assume the atmosphere is co-rotating with the Earth. Then, the atmospheric drags acting on the tether and spacecraft are defined as,

$$\boldsymbol{f}^{L}_{d\_t} = -\frac{1}{2}\rho_{a,k} C_d d \left|\boldsymbol{V}^{n}_{r}\right| \boldsymbol{V}^{n}_{r} \quad \text{and} \quad \boldsymbol{f}_{d\_s} = -\frac{1}{2}\rho_{a,k} C_d A^{n}_{s} \left|\boldsymbol{V}_{r}\right| \boldsymbol{V}_{r} \tag{4.61}$$

where $\boldsymbol{f}^{L}_{d\_t}$ is the drag per unit length of tether in the local frame of tether, $\boldsymbol{f}_{d\_s}$ is the drag acting on spacecraft in the global frame, $\boldsymbol{V}_r$ is the velocity of tethered system relative to the atmosphere, $\boldsymbol{V}^{n}_{r}$ is the component of relative velocity normal to the tether, $\rho_{a,k}$ is the density of atmosphere that is calculated from the Naval Research Laboratory Mass Spectrometer Incoherent Scatter Radar Expanded Model (NRLMSISR-00), d is the tether diameter, A_S is the projected area of spacecraft, and C_d is the drag coefficient [128] (C_d

= 2.2 for the tether, C_d =1.6 for the cubic spacecraft). The relative velocity $\boldsymbol{V}_r$ is determined by,

$$\boldsymbol{V}_r = \boldsymbol{T}_{f2g}^{-1}\boldsymbol{V}_g - \boldsymbol{\omega}_f \times \boldsymbol{r}_f \tag{4.62}$$

where $\boldsymbol{V}_g$ is the absolute velocity vector in the global frame, $\boldsymbol{\omega}_f$ is the angular velocity vector of the Earth (where $\omega_x = \omega_y = 0$, ω_z = 7.2921150×10^5 rad/s) and $\boldsymbol{r}_f$ is the position vector of EDT in the Earth-fixed frame.

The vector of nodal drag of the tether element can be derived from the virtual work done by the drag force. For the *k-th* element, it is

$$\delta W_d = \int_0^{L_{a,k}} \delta \boldsymbol{X}_{a,k}^T \boldsymbol{f}_{d\_t} ds = \delta \boldsymbol{X}_{a,k}^T \boldsymbol{F}_{d,k} \tag{4.63}$$

$$\begin{aligned}
\boldsymbol{F}_{d,k} &= \int_0^{L_{a,k}} \boldsymbol{N}^T \boldsymbol{f}_{d_t} ds = \frac{L_{a,k}}{2} \sum_{i=1}^{N_{GA}} w_i \boldsymbol{N}^T \left[\frac{L_{a,k}}{2}(1+\xi_i) \right] \boldsymbol{f}_{d_t} \left[\frac{L_{a,k}}{2}(1+\xi_i) \right] \\
\boldsymbol{f}_{d_t} \left[\frac{L_{a,k}}{2}(1+\xi_i) \right] &= \boldsymbol{T}_{f2g} \boldsymbol{f}_{d_\mathrm{t}}^F \left[\frac{L_{a,k}}{2}(1+\xi_i) \right] \\
\boldsymbol{f}_{d_\mathrm{t}}^F \left[\frac{L_{a,k}}{2}(1+\xi_i) \right] &= \begin{bmatrix} \boldsymbol{T}_{l2f} & 0 \\ 0 & \boldsymbol{T}_{l2f} \end{bmatrix}_{\frac{L_{a,k}}{2}(1+\xi_i)} \boldsymbol{f}_{d_\mathrm{t}}^L \left[\frac{L_{a,k}}{2}(1+\xi_i) \right]
\end{aligned} \tag{4.64}$$

where $\boldsymbol{F}_{a,k}$ is the nodal drag force vector of tether element in the global frame, $\boldsymbol{f}_{d\_t}$ is the drag per unit length of tether in the global frame, $\boldsymbol{T}_{l2f}$ is the transformation matrix from the local frame to the Earth-fixed frame, and (w_i, ξ_i) are the Gaussian integration weights and abscissae. The superscripts $(\ )^F$ and $(\ )^L$ represent the terms expressed in the Earth-fixed and local frame, respectively. The transformation matrix is defined as,

$$\boldsymbol{e}_x = \frac{X_k - X_{k+1}}{L_e}\boldsymbol{i}' + \frac{Y_k - Y_{k+1}}{L_e}\boldsymbol{j}' + \frac{Z_k - Z_{k+1}}{L_e}\boldsymbol{k}',\ \ \boldsymbol{e}_y = \frac{\boldsymbol{e}_x \times \boldsymbol{V}^f_{r\_m}}{\left\|\boldsymbol{e}_x \times \boldsymbol{V}^f_{r\_m}\right\|},\ \ \boldsymbol{e}_z = -\frac{\boldsymbol{e}_x \times \boldsymbol{e}_y}{\left\|\boldsymbol{e}_x \times \boldsymbol{e}_y\right\|} \quad (4.65)$$

$$\boldsymbol{T}_{l2f} = \begin{bmatrix} \dfrac{X_k - X_{k+1}}{L_e} & \dfrac{Y_k - Y_{k+1}}{L_e} & \dfrac{Z_k - Z_{k+1}}{L_e} \\ -\dfrac{e_{xY'}e_{yZ'} - e_{xZ'}e_{yY'}}{\left\|\boldsymbol{e}_x \times \boldsymbol{e}_y\right\|} & -\dfrac{e_{xZ'}e_{yX'} - e_{xX'}e_{yZ'}}{\left\|\boldsymbol{e}_x \times \boldsymbol{e}_y\right\|} & -\dfrac{e_{xX'}e_{yY'} - e_{xY'}e_{yX'}}{\left\|\boldsymbol{e}_x \times \boldsymbol{e}_y\right\|} \\ \dfrac{e_{xY'}V_{rZ'} - e_{xZ'}V_{rY'}}{\left\|\boldsymbol{e}_x \times \boldsymbol{V}^f_{r\_m}\right\|} & \dfrac{e_{xZ'}V_{rX'} - e_{xX'}V_{rZ'}}{\left\|\boldsymbol{e}_x \times \boldsymbol{V}^f_{r\_m}\right\|} & \dfrac{e_{xX'}V_{rY'} - e_{xY'}V_{rX'}}{\left\|\boldsymbol{e}_x \times \boldsymbol{V}^f_{r\_m}\right\|} \end{bmatrix} \quad (4.66)$$

where $\left(V_{rX'}, V_{rY'}, V_{rZ'}\right)$ are components of the element's relative mean velocity vector $\boldsymbol{V}^f_{r\_m}$ in the Earth-fixed frame, $\left(\boldsymbol{i}', \boldsymbol{j}', \boldsymbol{k}'\right)$ are the unit vectors of the Earth-fixed frame, and $\left(\boldsymbol{e}_x, \boldsymbol{e}_y, \boldsymbol{e}_z\right)$ are the unit vectors of the local frame, respectively.

4.1.1.3 Solar Radiation Pressure

The solar radiation pressure consists of three parts: absorption radiation, specular reflection radiation and diffuse reflection radiation. It can be expressed as [121],

$$\begin{aligned} \boldsymbol{f}^l_{sr\_t} &= -p_{sr} d \cos\gamma \left[2\left(C_{rd}/3 + C_{rs}\cos\gamma\right)\boldsymbol{p} + \left(1 - C_{rs}\right)\boldsymbol{q}\right] \\ \boldsymbol{F}^l_{sr\_s} &= -p_{sr} A_s \cos\gamma \left[2\left(C_{rd}/3 + C_{rs}\cos\gamma\right)\boldsymbol{p} + \left(1 - C_{rs}\right)\boldsymbol{q}\right] \end{aligned} \quad (4.67)$$

where the solar pressure per unite area is $p_{sr} = 4.57 \times 10^{-6} N \cdot m^{-2}$, A_s is the projected area of spacecraft for solar radiation pressure which is assumed the same as the projected drag area of spacecraft, $\boldsymbol{p}$ and $\boldsymbol{q}$ are the unit vectors of the normal and the incident solar radiation of tether projected area. γ is the incident angle of Sunlight, and C_{rd} = 0.8 and C_{rs} = 0.18 are the coefficients of diffuse and specular reflectivity, respectively.

The vector of the solar radiation pressure in the global frame can be expressed as,

$$\delta W_s = \int_0^{L_{a,k}} \delta \boldsymbol{X}_{a,k}^T \boldsymbol{f}_s^g ds = \delta \boldsymbol{X}_{a,k}^T \boldsymbol{F}_s$$
$$\boldsymbol{F}_{sr\_t,k}^g = \int_0^{L_{a,k}} \boldsymbol{N}^T \boldsymbol{f}_{sr\_t}^g ds = \frac{L_{a,k}}{2} \sum_{j=1}^{N_{GA}} w_j \boldsymbol{N}^T \left[\frac{L_{a,k}}{2}(1+\xi_j) \right] \boldsymbol{f}_{sr\_t}^g \left[\frac{L_{a,k}}{2}(1+\xi_j) \right] \quad (4.68)$$
$$\boldsymbol{F}_{sr\_t}^g = \sum_{j=1}^{N_{GA}} \boldsymbol{F}_{sr\_t,j}^g$$

where $\boldsymbol{f}_{sr\_t}^g = \boldsymbol{T}_{l'2g} \boldsymbol{f}_{sr\_t}^l$ with $\boldsymbol{T}_{l'2g}$ representing the transformation matrix from the local solar radiation frame to the global frame and its detailed definition is given in Ref. [121].

4.1.1.4 Heat Flux

The physical properties of tethers are generally temperature dependent, such as, the thermal expansion coefficient, electrical conductivity and electron collection efficiency [44, 135]. Consequently, the internal stress and electrodynamic force will be affected by temperature variation. The thermal equilibrium of a tether element in space is defined as,

$$\Delta T = T - T_{ini} = \frac{Q_{SL} + Q_{IR} + Q_{PEA} + Q_{AR} + Q_{OHM} + Q_{EI} - Q_{RE} + Q_{CON}}{\rho_t c_m} \Delta t \quad (4.69)$$

where T_{ini} is the initial temperature, $Q_{SL}, Q_{IR}, Q_{PEA}, Q_{AR}, Q_{OHM}, Q_{EI}, Q_{RE}$ and Q_{CON} are the heat flux of solar radiation, infrared radiation from Earth, Earth Albedo, atmospheric drag impact loss, Ohmic loss of EDT, electron impact loss, radiation emission of tether, and tether conduction flow, respectively. Since the heat flux due to the tether conduction flow Q_{CON} is less significant, it can be safely ignored in Eq. (4.69) [84]. The detailed expressions of each heat flux and correspondence coefficients can be found [84, 89].

Solar Radiation Heating

The heat flux due to the exposure to solar radiation is the main source for the temperature

variation in space, such as,

$$Q_{SL} = \varsigma \alpha_{sab} J_S L_e d\left(\boldsymbol{n}_S \cdot \boldsymbol{q}\right) \tag{4.70}$$

where ς is the eclipse index where $\varsigma = 0$ if the tether enters into the Earth's eclipse and $\varsigma = 1$ otherwise, α_{sab} is the solar absorptivity coefficient of tether material, and $J_S = 1{,}372 \ W \times m^{-2}$ is the average solar incident radiation at the Earth.

Earth Infrared Radiation Heating

The heat flux due to the infrared radiation from the Earth is defined as,

$$Q_{IR} = \alpha_{IR} k_b T_{eq}^4 f\left(\pi L_e d\right) \tag{4.71}$$

where $k_b = 5.670373 \times 10^{-8} \ Wm^{-2}K^{-4}$ is the Stefan-Boltzmann constant, $T_{eq} = 288 \ K$ is the equivalent temperature of the Earth, and f is the view factor for the tether, such that,

$$f = \frac{1}{\pi}\left\{\sin^{-1}\left(\frac{\left|\boldsymbol{R}_{SO}\right|}{\left|\boldsymbol{R}_{TO}\right|}\right) + 0.5\sin\left[2\sin^{-1}\left(\frac{\left|\boldsymbol{R}_{SO}\right|}{\left|\boldsymbol{R}_{TO}\right|}\right)\right]\right\} \tag{4.72}$$

where R_{SO} and R_{TO} are the position vectors illustrated in Fig. 4.7.

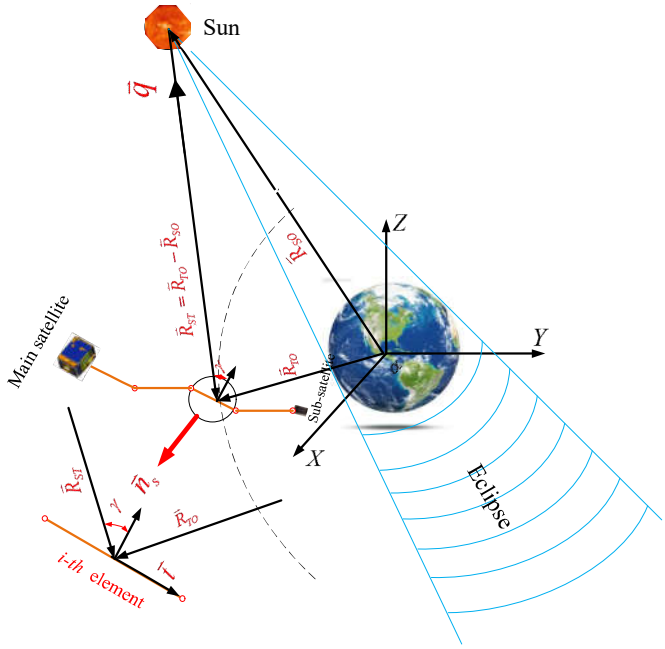

Figure 4.7 Schematic of incident solar radiation.

Earth's Albedo Heating

The heat flux due to the solar radiation reflected by the Earth is defined as,

$$Q_{PAR} = \varsigma \alpha_{al} J_S L_e d \left(\frac{\boldsymbol{n}_S \cdot \boldsymbol{R}_{TO}}{\left| \boldsymbol{R}_{TO} \right|} \right) \tag{4.73}$$

where α_{al} is the Albedo coefficient of the Earth.

Atmospheric Impact Heating

The atmospheric impact heating is caused by the heat transfer between free molecules and arresting surface of tether. The corresponding heat flux is defined as,

$$Q_{AD} = 0.5 \rho_a \left(\boldsymbol{V}_r^n \right)^3 L_e d \left(\boldsymbol{n}_S \cdot \boldsymbol{q} \right) \tag{4.74}$$

Ohmic and Electron Impact Heating

The operation of EDT will generate heat due to (i) the Ohmic loss by the induced electric current in the tether Q_{OHM}, and (ii) the electron impact at the orbital velocity Q_{EI}, such that,

$$Q_{OHM} = \int_0^{L_e} I^2(s) R_e ds \tag{4.75}$$

$$Q_{EI} = \int_0^{L_e} \dot{I}(s) \Delta\Phi(s) ds \tag{4.76}$$

where $I(s)$ is the induced electric current in the tether, the overhead dot denotes the time derivative, and $\Delta\Phi$ is the potential bias with respect to the ambient plasma. The electrical resistance and conductivity of the tether is temperature dependent, such that,

$$R_t = L_{e0}(1+\alpha_T \Delta T)/(\sigma A_t) \tag{4.77}$$

$$\sigma = 10^8 \times \left(C_a + C_b T + C_c T^2 + C_d T^3\right)^{-1} \tag{4.78}$$

where ΔT is the temperature variation, (C_a, C_b, C_c, C_d) are material dependent coefficients. For aluminum, they are: -2.37×10^{-1}, 8.15×10^{-3}, 5.48×10^{-6}, -1.97×10^{-9}.

Tether Radiation Emission

The thermal radiation emission from the tether can be expressed as,

$$Q_{RE} = \pi\sigma\varepsilon_e T^4 L_e d \tag{4.79}$$

where ε_e is the emissivity coefficient of the tether.

Then, the equivalent elasticity nodal force vector of NPFEM in Eq. (4.1) is revised to include the thermal strain as,

$$\boldsymbol{F}_e = \left(1+\alpha_{the}\Delta T\right)\boldsymbol{F}_{e0} \tag{4.80}$$

where α_{the} is the linear thermal expansion of tether material, $\boldsymbol{F}_{k0}$ is the equivalent elasticity nodal force vector of NPFEM without thermal strain, defined in Ref. [75].

4.1.2 Libration Motion of Flexible Tether Model

The libration motion of EDT systems is described in the orbital coordinate system as shown in Fig. 4.1. Its origin *O'* of the orbital coordinate system is located at the CM of the EDT system with the *R*-axis pointing to the origin of the global inertial coordinate system, the *S*-axis lying in the orbital plane of the EDT and perpendicular to the *R*-axis, and the *W*-axis completing a right-hand system. The libration angles (pitch and roll) of EDT are defined based on dumbbell model. For finite element approach, there will be *n*-sets of libration angles if the tether is discretized into *n* tether elements. Thus, the libration control strategy defined in the dumbbell model cannot be applied for the flexible tether model directly. To address this challenge, virtual pitch and roll angles are introduced here for the stability control of libration of flexible EDT systems, which are defined as the libration of a virtual rigid tether that connects the first and last notes of flexible EDT systems as shown in Fig. 4.1. Let the straight dot line *CA* connect the first and the last nodes. Then, the libration motion of line *CA* can be described through the in-plane angle α (pitch angle, rotating around the *W*-axis), followed by the out-of-plane angle β (roll angle, rotating around the S'-axis that is the S'-axis after first rotation). The direction of the virtual tether is defined as pointing from the first node to the last node in the global frame first and then transformed to the orbital frame, such as,

$$\boldsymbol{R}_{CA\_g} = \left(X_{n+1} - X_1, Y_{n+1} - Y_1, Z_{n+1} - Z_1\right) \tag{4.81}$$

$$\boldsymbol{R}_{CA\_O'} = \boldsymbol{T}_{g2O'} \boldsymbol{R}_{CA\_g} \tag{4.82}$$

where $R^R_{CA\_O'}, R^S_{CA\_O'}, R^W_{CA\_O'}$ are the components of $\boldsymbol{R}_{CA\_O'}$ in the orbital frame, and $\boldsymbol{T}_{g2O'}$ is the coordinate transformation matrix from the global frame to the orbital frame [67]. Thus, the libration angles of the virtual tether are described in the orbital frame with the origin *O*' located at the CM of the virtual tether system along the line *CA*, such as,

$$\begin{aligned} \alpha_{EDT} &= \tan^{-1}\left(R^S_{CA\_O'} \big/ R^R_{CA\_O'}\right), \\ \beta_{EDT} &= \tan^{-1}\left[-R^W_{CA\_O'} \big/ \left(R^R_{CA\_O'} \cos\alpha + R^S_{CA\_O'} \sin\alpha\right)\right] \end{aligned} \tag{4.83}$$

4.1.3 Libration Control

The EDT system is susceptible to the dynamic instability because the electrodynamic force continuously injects energy into the system and simultaneously excites the transverse dynamic motion. Thus, a simple and effective control strategy is to turn off the electric current when the power of electrodynamic force (electrodynamic force times libration velocity) is positive and vice versa. For a conservative system, the stability function can be examined by a Lyapunov candidate function derived from the system energy, such as the Hamiltonian function. The Hamiltonian of EDT systems can be defined as,

$$H = \frac{1}{2}\boldsymbol{\omega}_{rel} \cdot \boldsymbol{J}\boldsymbol{\omega}_{rel} + \frac{3}{2}\left(\bar{\boldsymbol{\omega}}_{orb} \cdot \bar{\boldsymbol{\omega}}_{orb}\right)\boldsymbol{R} \cdot \boldsymbol{J}\boldsymbol{R} - \frac{1}{2}\left(\boldsymbol{\omega}_{orb} \cdot \boldsymbol{\omega}_{orb}\right)\boldsymbol{W} \cdot \boldsymbol{J}\boldsymbol{W} \tag{4.84}$$

where $\boldsymbol{R}$ and $\boldsymbol{W}$ are the unit vectors of *R* and *W* axes in the orbital frame, $\boldsymbol{J}$ is the inertial tensor of an EDT system in the local frame [133]. When the system is at equilibrium, there exist $\alpha_{EDT} = \dot{\alpha}_{EDT} = 0, \beta_{EDT} = \dot{\beta}_{EDT} = 0$ and $H_0 = -\frac{1}{2} J \omega_{or}^2$. Then, the

Lyapunov function can be taken as,

$$H' = H - H_0 = \frac{1}{2}\boldsymbol{\omega}_{rel} \cdot \boldsymbol{J}\boldsymbol{\omega}_{rel} + \frac{3}{2}\left(\boldsymbol{\omega}_{orb} \cdot \boldsymbol{\omega}_{orb}\right)\boldsymbol{R} \cdot \boldsymbol{J}\boldsymbol{R} - \frac{1}{2}\left(\boldsymbol{\omega}_{orb} \cdot \boldsymbol{\omega}_{orb}\right)\boldsymbol{W} \cdot \boldsymbol{J}\boldsymbol{W} + \frac{1}{2}J\omega_{or}^2 \tag{4.85}$$

For convenience, Eq. (4.85) is normalized into the dimensionless form in the terms of libration angles and their derivatives,

$$\begin{aligned}
\bar{H}' &= \frac{H - H_0}{|H_0|} = \frac{1}{\omega_{orb}^2}\left[\begin{array}{l}\left(\dot{\beta}_{EDT}^2 + \dot{\alpha}_{EDT}^2 \cos^2\beta_{EDT}\right) + \\ \omega_{orb}^2\left(3\sin^2\alpha_{EDT} + 3\cos^2\alpha_{EDT}\sin^2\beta_{EDT}\right) + \omega_{orb}^2\sin^2\beta_{EDT}\end{array}\right] \\
&= \frac{1}{\omega_{orb}^2}\left\{\left[\dot{\beta}_{EDT}^2 + \dot{\alpha}_{EDT}^2\cos^2\beta_{EDT}\right] + \omega_{or}^2\left[3\sin^2\alpha_{EDT} + 3\cos^2\alpha_{EDT}\sin^2\beta_{EDT} + \sin^2\beta_{EDT}\right]\right\} \\
&= \frac{1}{\omega_{orb}^2}\left\{\left[\dot{\beta}^2 + \dot{\alpha}_{EDT}^2\cos^2\beta_{EDT}\right]\right\} + \left[3\left(1-\cos^2\alpha\right) + 3\cos^2\alpha_{EDT}\sin^2\beta_{EDT} + \left(1-\cos^2\beta_{EDT}\right)\right] \\
&= \frac{1}{\omega_{orb}^2}\left\{\left[\dot{\beta}_{EDT}^2 + \dot{\alpha}_{EDT}^2\cos^2\beta_{EDT}\right]\right\} + \left[4 - 3\cos^2\alpha_{EDT}\left(1-\sin^2\beta_{EDT}\right) - \cos^2\beta_{EDT}\right] \\
&= 4 - 3\cos^2\alpha_{EDT}\cos^2\beta_{EDT} + \frac{1}{\omega_{orb}^2}\left\{\left[\dot{\beta}_{EDT}^2 + \dot{\alpha}_{EDT}^2\cos^2\beta_{EDT}\right]\right\} - \cos^2\beta_{EDT} \\
&= 4 - 3\cos^2\alpha_{EDT}\cos^2\beta_{EDT} + \frac{1}{\omega_{orb}^2}\left\{\left[\dot{\beta}_{EDT}^2 + \left(\dot{\alpha}_{EDT}^2 - \omega_{orb}^2\right)\cos^2\beta_{EDT}\right]\right\} \\
&= 4 - 3\cos^2\alpha_{EDT}\cos^2\beta_{EDT} + \frac{1}{\omega_{orb}^2}\left\{\left[\dot{\beta}_{EDT}^2 + \left(\dot{\alpha}_{EDT}^2 - \dot{v}^2\right)\cos^2\beta_{EDT}\right]\right\} \\
&= 4 - 3\cos^2\alpha_{EDT}\cos^2\beta_{EDT} + \left[\dot{\beta}_{EDT}^2 + \left(\dot{\alpha}_{EDT}^2 - \dot{v}^2\right)\cos^2\beta_{EDT}\right] \Big/ \frac{\mu_g}{r_{orb}^3}
\end{aligned} \tag{4.86}$$

The total system energy will be minimum when the motion has a period solution, so a modification of Lyapunov function is derived [94],

$$\bar{H}' = 4 - 3\cos^2\left(\alpha_{EDT} - \alpha_p\right)\cos^2\beta_{EDT} + \frac{r_{or}^3}{\mu_g}\left[\dot{\beta}_{EDT}^2 + \left(\left(\dot{\alpha}_{EDT} - \dot{\alpha}_p\right)^2 - \dot{v}^2\right)\cos^2\beta_{EDT}\right] \tag{4.87}$$

where α_p and $\dot{\alpha}_p$ are the approximate periodical solutions [94],

$$\begin{cases} \alpha_P = e_E \sin\upsilon - 0.5e_E^2 \sin(2\upsilon) \\ \dot{\alpha}_P = n_{orb}\left[e_E \cos\upsilon - e_E^2 \cos(2\upsilon) \right] \end{cases} \tag{4.88}$$

Once the normalized libration energy exceeds a pre-set threshold $\bar{H}'_{th}$, the libration control is activated so that the electric current will be turned on/off by the sign of power of electrodynamic force. The equivalent electrodynamic torques of the virtual tether in the orbital frame is calculated as per Eq. (4.89). Equation (4.90) provides four cases of the power of electrodynamic force with different signs,

$$\boldsymbol{M}_{EDT} = M_{yaw}\boldsymbol{R} + M_{out}\boldsymbol{S} + M_{in}\boldsymbol{W} = \sum_{j=1}^{3}\left(\boldsymbol{r}_{jO'} \times \boldsymbol{F}_{L\_j} \right) \tag{4.89}$$

$$\begin{cases} M_{in}\dot{\alpha}_{EDT} \geq 0 & (a) \\ M_{in}\dot{\alpha}_{EDT} < 0 & (b) \\ M_{out}\dot{\beta}_{EDT} \geq 0 & (c) \\ M_{out}\dot{\beta}_{EDT} < 0 & (d) \end{cases} \tag{4.90}$$

The current should be turned off if Eqs. (4.90)(a) and (4.90)(c) are satisfied and turned on if Eqs. (4.90)(b) and (4.90)(d) are satisfied. However, the control strategy based on Eqs. (4.87)-(4.90) requires the feedback of EDT libration angles and their velocities, which is very demanding for the purpose of an end-of-mission deorbit operation. Previous studies showed that the roll motion destabilizes faster than the pitch motion in inclined orbits. Thus, the EDT system can be effectively controlled using the roll angle only by considering cases in Eqs. (4.90)(c) and (4.90)(d).

The threshold $\bar{H}'_{th}$ should be carefully selected to maximize the orbital descending efficiency while maintaining the libration stability. The $\bar{H}'^{Upper}_{th}$ is an upper bound

threshold of the dimensionless libration energy that corresponds to the maximum amplitude of libration motion, while the $\bar{H}_{th}^{\prime Lower}$ is a lower bound threshold of the dimensionless libration energy, which is especially designed for the flexible tether system in order to constrain the libration motion at the low energy level. Since the transverse instability of flexible tethers develops faster than the libration instability, the introduction of the lower bound threshold can effectively suppress the transverse dynamic motion of flexible tethers simultaneously. The flow chart of the proposed current on/off switch control is shown in Fig. 4.8; one additional variable flag is introduced to implement the proposed control strategy compared with existing ones. If the instant libration energy exceeds the upper bound threshold $\bar{H}_{th}^{\prime Upper}$, the control action is activated, and the flag variable is equal to 2. The current is turned off if the sign of electrodynamic force power is positive and vice versa. The control process continues until the libration energy is reduced to the lower bound threshold $\bar{H}_{th}^{\prime Lower}$, and the flag changes its value. Then, the current control is deactivated until the libration energy exceeds the upper threshold $\bar{H}_{th}^{\prime Upper}$ again.

The selection of $\left(\bar{H}_{th}^{\prime Lower}, \bar{H}_{th}^{\prime Upper}\right)$ is outlined as follows. First, the lower and upper bound thresholds should be defined initially as $\left(\bar{H}_{th}^{\prime Lower}, \bar{H}_{th}^{\prime Upper}\right) \in \left(0,\ 3.0\right)$ per Ref. [94]. Second, the upper bound threshold $\bar{H}_{th}^{\prime Upper}$ should be slightly greater than the energy of a libration motion without control to improve the orbital descent efficiency.

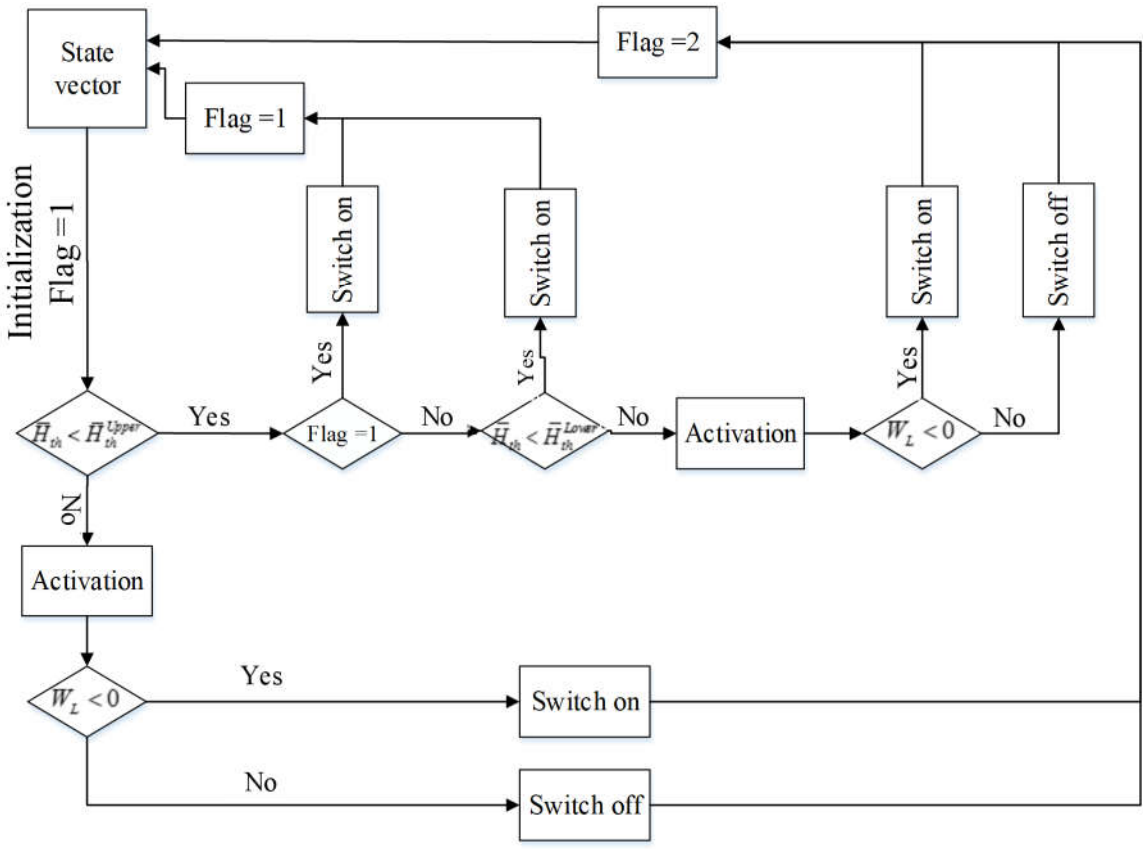

Figure 4.8 Current vs. applied voltage between emitter tip and positively biased gate.

4.2 Numerical Results and Discussion

This section investigates the thermal, elastic, and electrical coupling effect. First, method A is used to determine the current along tether, and the simple switch on/off control strategy is applied to suppress the libration motion in the deorbit process. Second, method B is used to determine the current along tether. Finally, method C is used to determine the current along tether. For the purpose of comparison, the existing approach for EDT dynamics in Ref. [129], called “the reference method”, is used as a benchmark case. Three assumptions are used for electric current generation in the reference method: (i) the tether is rigid and

straight, (ii) the motional electric field E_m is constant along the whole tether and (iii) the value of E_m is evaluated at the center of mass of the EDT system. The current profile is obtained by solving the orbital motion limited theory independently from the tether dynamics. Once the profile of current is obtained, it is projected onto the tether that may be bent and stretched.

4.2.1 Method A

In this section, the method A is used to determine the current in tether to investigate the coupled thermal, elastic, and electric effect on the dynamic behavior of EDT. The present analysis is conducted based on Advanced Integrated Micro-spacecraft platform [136]. The Micro-spacecraft is assumed initially in a circular orbit with an altitude of 900 km. The target altitude for the deorbit operation is 250 km. Based on the findings from previous studies [129], three representative orbits for EDT systems are considered, namely, equatorial, 57° inclined and polar orbits, respectively. An electron emitter is assumed at each end to improve the efficiency of electron attraction for higher deorbit efficiency of EDT systems in highly inclined orbits. The physical properties of the micro-spacecraft and the EDT system are listed in Table 4.1. As pointed out in Ref. [39], heavy sub spacecraft at the cathodic end have a positive effect to the dynamic stability of deorbit operation by EDT systems. In this section, the mass of sub spacecraft is assumed to be two times of the mass of tether for the sake of stability. The tether is modeled with four tether elements and the equivalent nodal force vectors of environmental perturbations are evaluated by Gaussian integration with 20 sample points (N_{GA}) in each element. The nonlinear governing

equation of EDT systems is numerically solved by the Symplectic 2-stage and fourth-order Gaussian-Legendre Runge-Kutta method as developed in Chapter 3.1 to avoid numerical errors accumulated over a prolonged period with a constant time step of 0.1s [60, 75]. In all cases, the tether is assumed initially straight and aligned with the local vertical of orbit and a special routine is used to start the dynamic simulation smoothly.

Table 4.1 Physical parameters of EDT system [136]

Parameters	Values
Tether material	Aluminum
Mass of main spacecraft (kg)	85.0
Mass of sub spacecraft (kg)	5.0
Mass of tether (kg)	2.5
Diameter of tether (m)	0.0005
Length of tether (m)	5,000
Dimensions of main spacecraft (m)	0.85×0.61×0.61
Dimensions of sub spacecraft (m)	0.1×0.1×0.1
Elastic modulus of tether (Nm^{-2})	7.2×10^{10}
Conductivity of tether at room temperature ($\Omega^{-1}m^{-1}$)	4.76×10^{7}

The emitting area of Spindt cathode array assumed S_e = 100 cm^2. The other parameters for Spindt array are obtained from Ref. [131], such as, the number of emitter tips per unit area N_t is 1.6×10^7 cm^{-2}, the designed maximum current is 1A, and the coefficients a_e and b_e are 3.14×10^{-8} $A\cdot V^{-2}$ and 771 V, respectively. The relationship between the gate voltage and emission current is shown in Fig. 4.9 as per Fowler-Nordheim equation in Eq. (4.5). It shows clearly that the Spindt array could reach an emission current of 1 A at a gate voltage less than 60 V. Since the emission current is slightly overestimated by the Fowler-Nordheim formula compared to the experimental data, the gate voltage Φ_{CHE}

is assumed 60V in this section to calculate the impedance of device, such that, Z_T = 3.347 Ohms. Furthermore, the potential bias between the emitter tips and ambient plasmas is assumed zero, i.e., $\Phi c = 0$. Both Z_T and Φ_{CHE} are used as the input parameters for the OML theory. Finally, the Golden-section search optimization algorithm is used to solve the Eq. (4.21) to obtain the current i_c the current and potential equation due to its numerical efficiency and simple implementation, instead of the semi-analytical and asymptotic methods used in the literature.

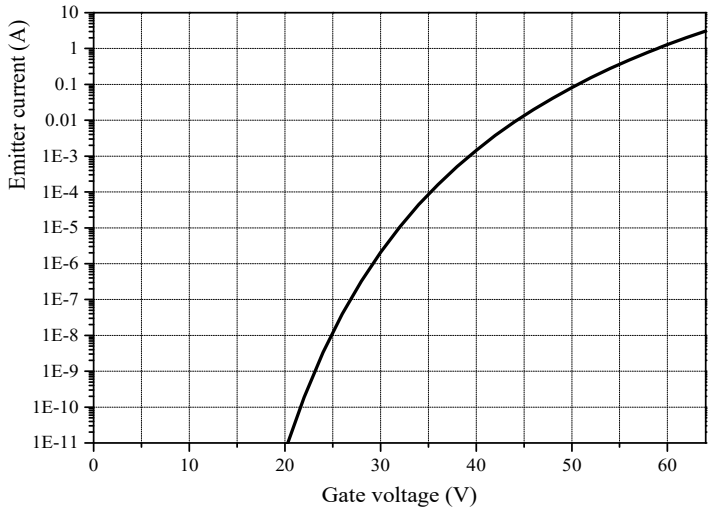

Figure 4.9 Emitted current vs. applied voltage between emitter tip and positively biased gate.

4.2.1.1 Thermal Effect

The thermal effect on the EDT system is studied by considering the thermal-induced variation of length and electrical conductivity, respectively. The temperature variations at the low end of an EDT system in the equatorial orbit in a 24-hour period are shown in Fig.

4.10(a-d). The ratio of thermal absorptivity to emissivity of tether is a design parameter and is assumed to 5 ($\alpha_{sab}/\varepsilon = 5$) in the present case. Figure 4.10(a-c) shows the increase rate of temperature is governed by the solar radiation (solid line). The effects of other heating effects, such as Ohmic heating, impact of electrons, atmospheric heating, and Earth's infrared and albedo heating are found very weak and negligible. The tether temperature drop is caused by the thermal emissivity of the tether, particularly when it enters Earth's eclipse (short dashed line). Figure 4.10(d) shows the maximum temperature of the tether is controlled by the ratio of thermal absorptivity to emissivity. The temperature difference between the maximum and the minimum is 234K when $\alpha_{sab}/\varepsilon = 5$. Therefore, one can conclude that the most important parameter in the thermal design for an EDT system is the ratio of absorptivity to emissivity of the tether. For a tether made of pure Aluminum, the associated ratio varies from 2.5 to 5.0. Accordingly, two sets of α_{sab}/ε ratios are used: 2.5 and 5.0, respectively, to investigate the impact of this ratio on the dynamics of EDT systems.

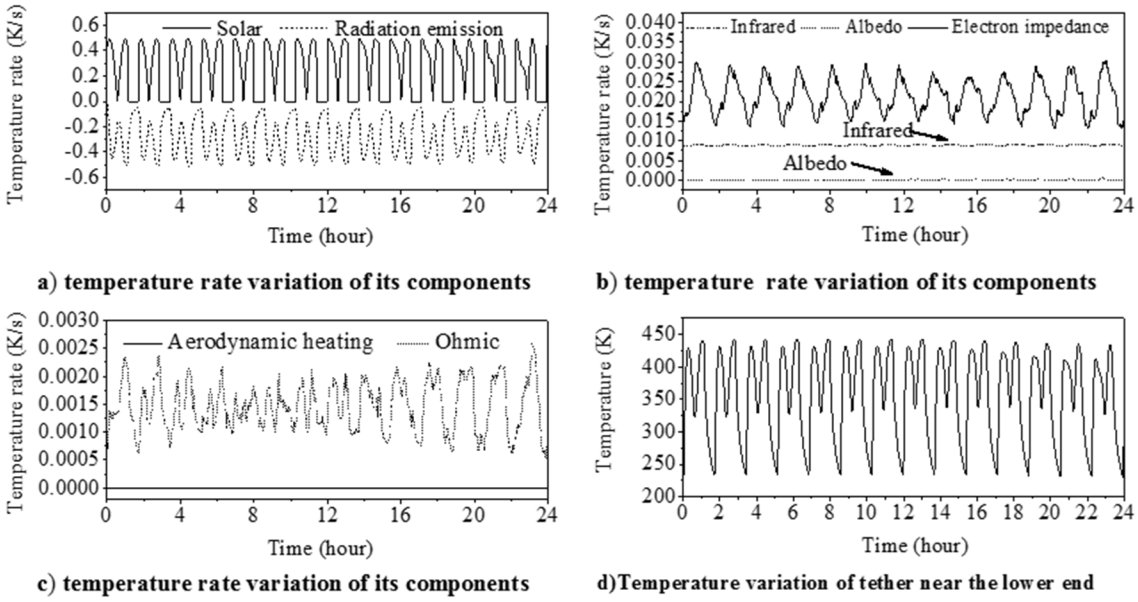

Figure 4.10 Temperature variation at lower end of tether in 24 hours in equatorial orbit.

Another setting that will affect the temperature variation is the Sun's position relative to the Earth. In the present study, the Sun is assumed aligned in the orbit periapsis. The initial condition of the temperature is assumed as the lowest temperature of the EDT system in 24 hours. The corresponding spatial position of the EDT system is unknown in advance and is assumed initially at the position just before the EDT system exits the Earth's eclipse and then adjusted by trial-and-error.

Furthermore, the temperature variation of the tether will lead to the variation of length and electrical resistivity of tether. The change of tether length will affect the longitudinal oscillation and the electron collection length, while the change of tether resistivity will alter voltage bias with respect to ambient plasma and the electron collection ability leading to a variation of electrodynamic force. In the following sections, the effect

of tether length variation is first analyzed by keeping the tether electrical conductivity constant. Then, the effect of tether conductivity variation is analyzed by keeping the tether length unchanged. Finally, the joint effects are studied by considering these two variations simultaneously.

4.2.1.2 Effect of Tether Length Variation

The tether length variation will cause the periodical variation of CM position of EDT system as it enters and exits Earth's eclipse. This effect is investigated by considering the ideal Earth gravity field without all other perturbation effects. A constant conductivity of aluminum ($4.76\times10^{7}\ \Omega^{-1}m^{-1}$) is used in this analysis.

First, the thermal-induced displacement of CM in the orbital plane and the corresponding libration motion are shown in Fig. 4.11. It can be easily noted that the displacement of CM is periodical as the EDT system enters and exits the Earth's eclipse. The magnitudes of displacement are proportional to the ratio of tether's thermal absorptivity to emissivity. The larger the ratio is, the greater the displacement of CM will be, see Fig. 4.11(d). The thermal-induced CM displacement causes a small periodical in-plane libration motion. The larger the variation of CM, the larger the amplitude of libration motion, see Fig. 4.11(a-d). However, it should be noted that this type of variation does not significantly affect the dynamics of EDT system, as shown in Fig. 4.11(c). Thus, for the orbital and libration motion of EDT system, the small thermal-induced variation of CM and in-plane libration have no distinguishable effect.

Second, the variation in tether length affects the electron collecting efficiency and

tether tension. The variation of tether length changes the total electric resistance of tether R_e and the dimensionless tether length l_t. This in turn affects the current collecting efficiency of tether by two dimensionless parameters $\Omega = Z_t / R_e$ and $l_t = L / L_*$. Figure 12(a-c) shows the variations of current at the cathodic end with and without consideration of thermal-induced tether length variation. For all the orbits considered, the current in tether is affected significantly by the orbital inclination but not the thermal-induced tether length variation. Furthermore, the difference of thermal-induced current variation due to different ratio of α_{sab}/ε is small. However, it is noted that the thermal-induced tether length variation affects tension and stability of EDT system. Figure 4.12(e-g) shows the variation of tension at the cathodic end with and without consideration of thermal-induced tether length variation. Obviously, the tension is affected dramatically by the thermal-induced tether length variation, although there is no significant difference between the variation and trends of tension by choosing the same ratio of α_{sab}/ε. The coupling effect of the current and tension is not obvious in the equatorial orbit but becomes significant in the 57° inclined and polar orbits compared to the results without thermal effect. This shows that the thermal, electrical, and elastic coupling effect is a key factor in the dynamic stability of the EDT system.

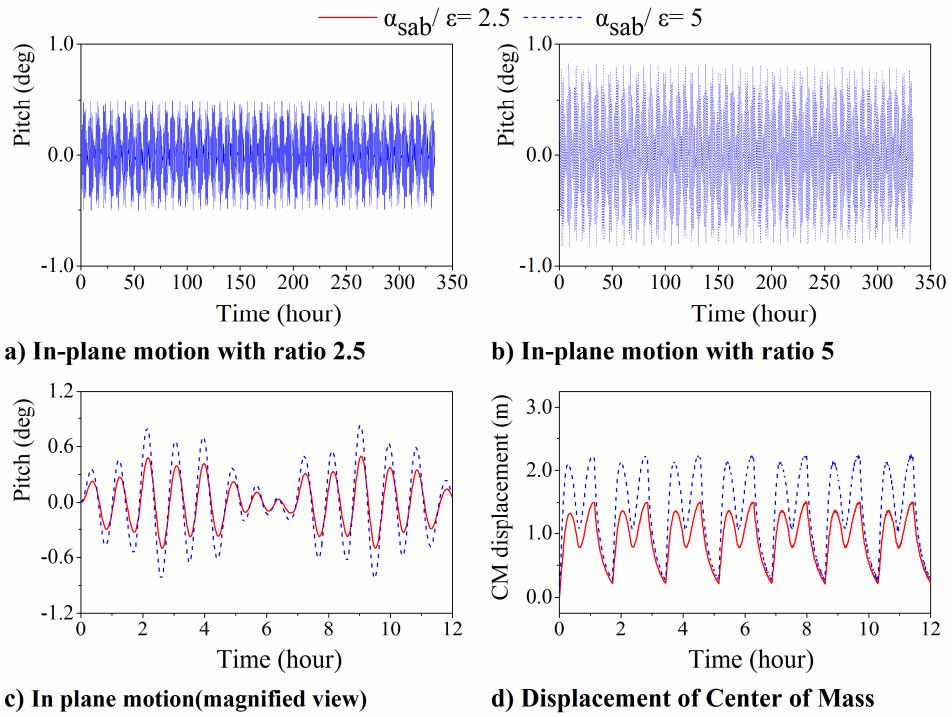

Figure 4.11 Time history of libration motion of CM in the equatorial orbit.

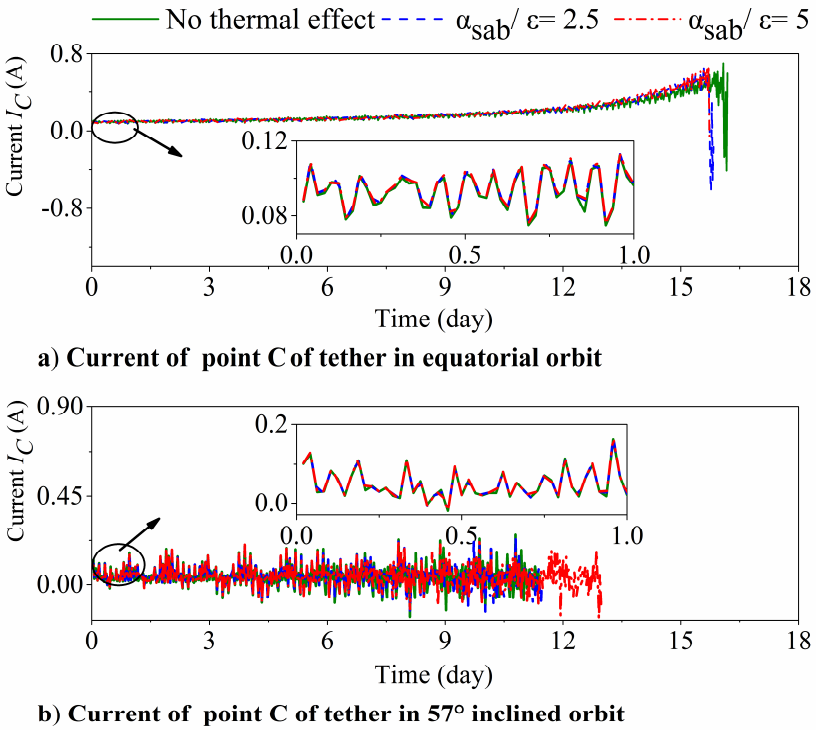

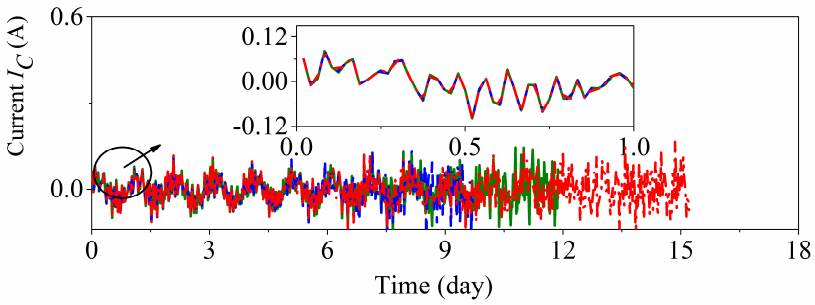

c) Current of point C of tether in ploar orbit

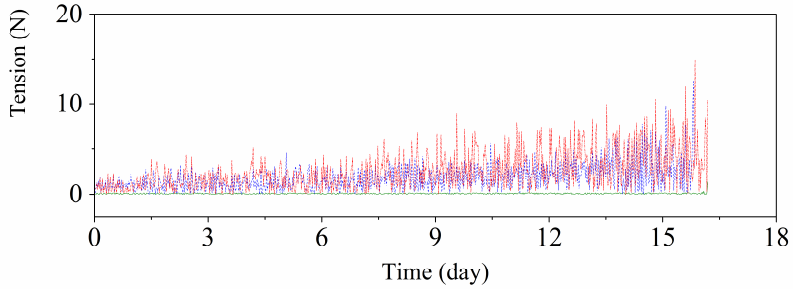

d)Tension of the last element near the ballast end in equatorial orbit

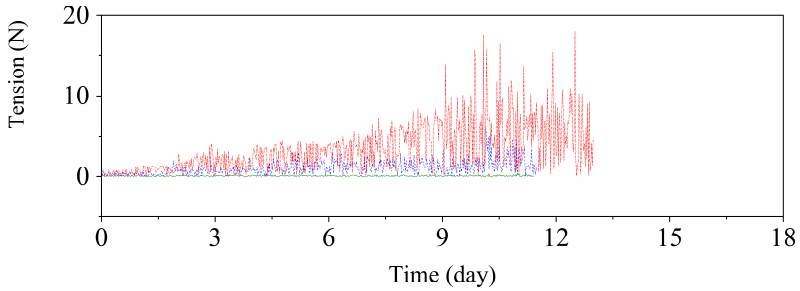

e)Tension of the last element near the ballast end in 57° inclined orbit

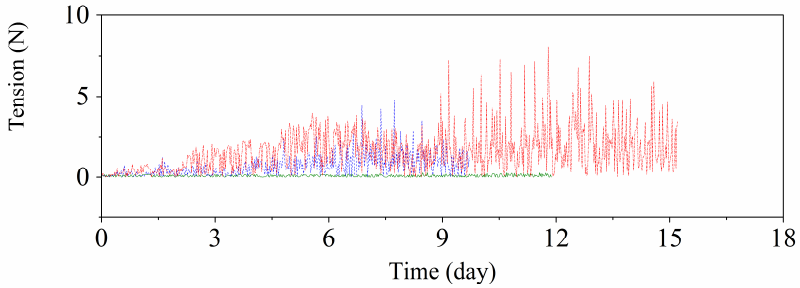

f)Tension of the last element near the ballast end in polar orbit

Figure 4.12 Variation of current and tension in different orbits due to thermal-induce tether length change.

4.2.1.3 Effect of Tether Conductivity

In this case, the length of tether is kept constant, while the electrical conductivity is assumed to vary as the temperature changes. The conductivity of tether has direct and indirect relationships with the dimensionless parameters Ω and l_t, respectively, which in turn affects the current collection by EDT. Small variation in Ω will result in a momentous change in the length of anodic segment AB, which is responsible for electron collection. For three different orbital inclinations, the temperature variation has the same trend due to the same initial temperature condition and the same incident solar pressure relative to EDT system.

Figure 4.13 shows the variations of electrical conductivity of tether and the corresponding total resistance of tether in one orbit in the equatorial orbit. It shows that the effect of α_{sab}/ε ratio is significant as it affects the thermal energy absorption and release. Within one orbital period, the conductivity of tether changes from the maximum value of $6.00\times10^{7}\Omega^{-1}m^{-1}$ to the minimum value of $3.08\times10^{7}\Omega^{-1}m^{-1}$ with the ratio $\alpha_{sab}/\varepsilon = 5.0$, see Fig. 4.13(a) (red dashed dot line). Consequently, the resistance of 5 km tether changes from 424 Ω to 827Ω. Next, the thermal-induced variation of resistance is quite significant (>50%) as shown in Fig. 4.13(a-b).

Figure 4.14(d-f) shows the variation of tension at the cathodic end with and without thermal effect in different orbits. This effect is not significant because the tether length is assumed constant in this case and the variation of tension is caused by the orbital parameters, such as, the orbital inclination. However, the thermal-induced variation of

tether electrical conductivity affects the stability of EDT system significantly as shown in Fig. 4.14(a-c), which is like the effect of tether length variation. It shows that the variation of electrical conductivity plays a crucial role in the electric current collection efficiency. It shows again that the thermal, electrical, and elastic coupling effect is a key factor in the dynamic stability of EDT systems.

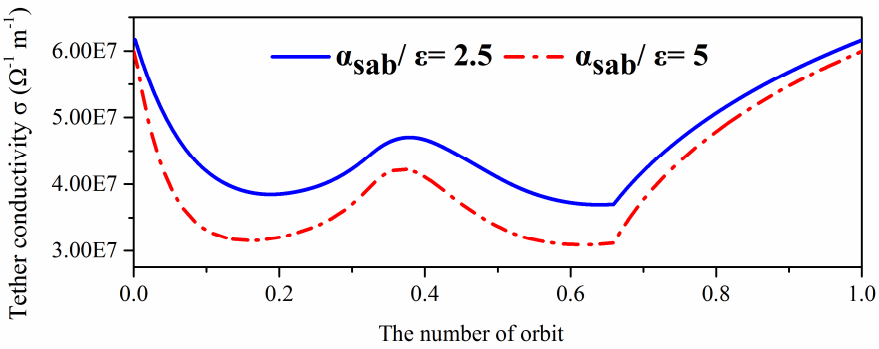

a) Tether conductivity σ

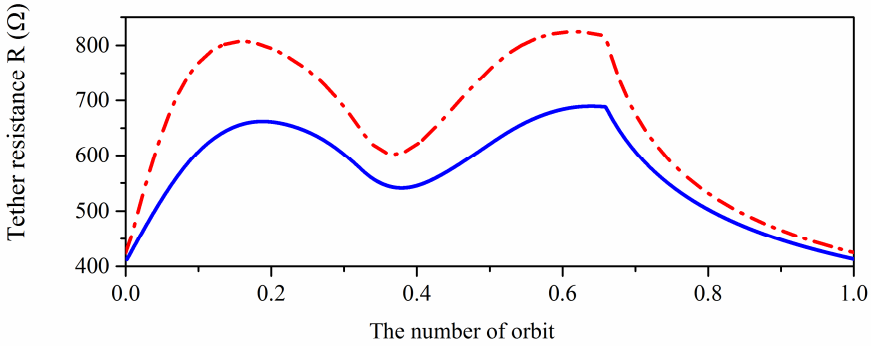

b) Tether resistance R_t

Figure 4.13 Variation of tether conductivity and resistance in one orbit in the equatorial orbit

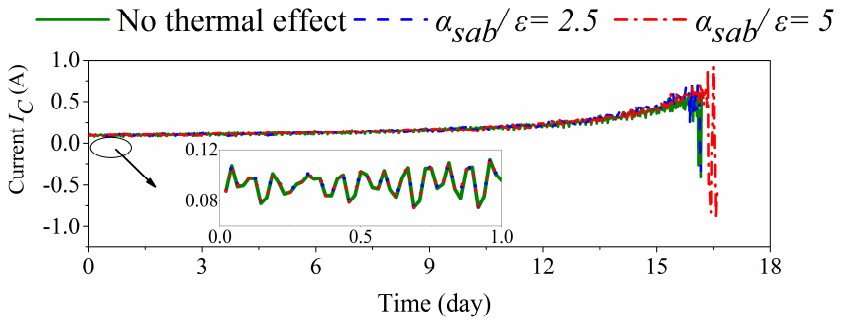

a) Current of Point C of tether in Equatorial orbit

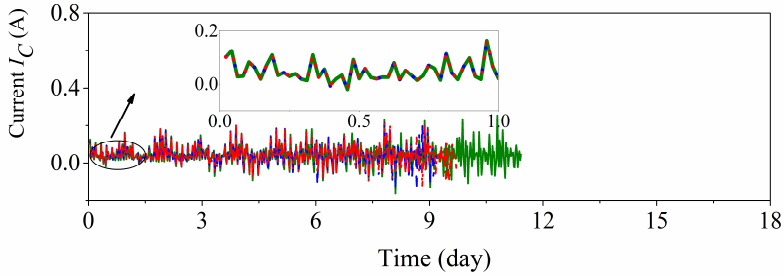

b) Current of Point C of tether in 57° inclined orbit

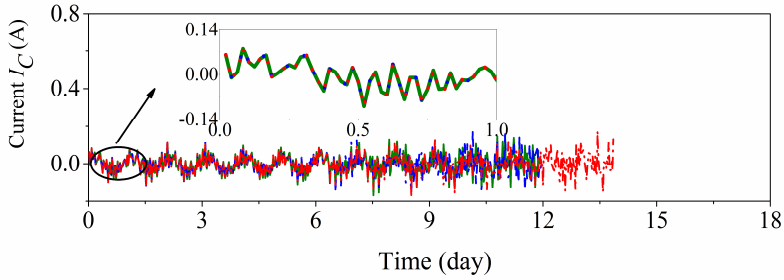

c) Current of Point C of tether in ploar orbit

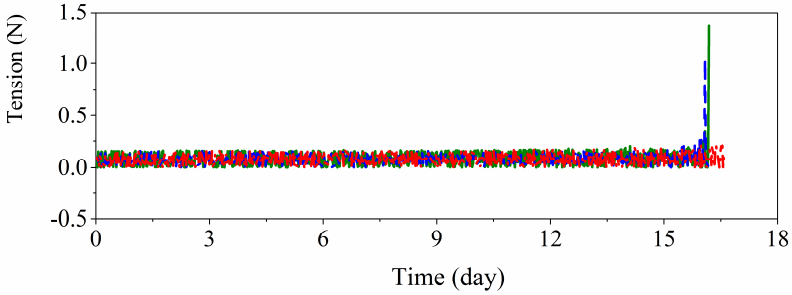

d)Tension of the last element near the ballast end in Equatorial orbit

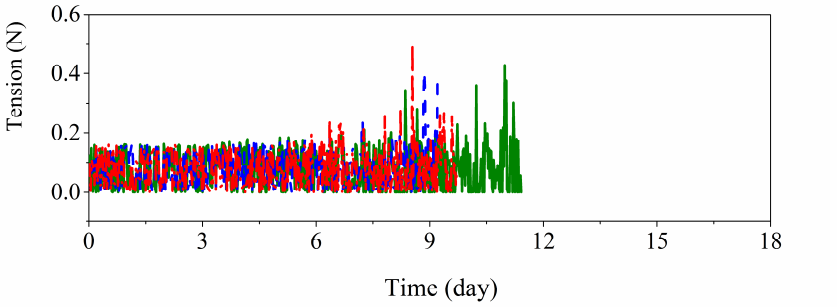

e)Tension of the last element near the ballast end in 57° inclined orbit

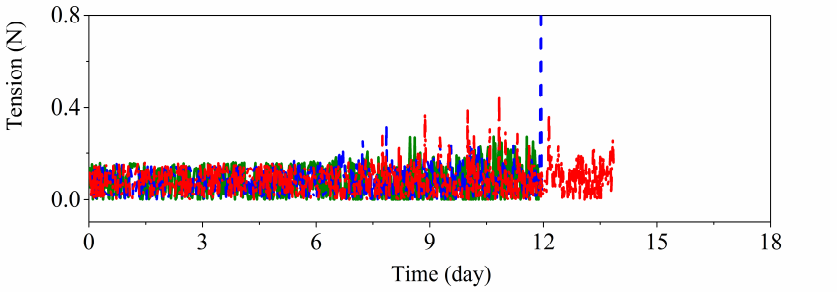

f)Tension of the last element near the ballast end in ploar orbit

Figure 4.14 Variation of current and tension due to tether resistivity change in different orbits.

4.2.1.4 Combined Effect of Tether Conductivity and Length

The combined effect of thermal-induced variations of tether length and conductivity is shown in Fig. 4.15. As shown before, the current collection efficiency is affected by two parameters electrical resistance Ω and non-dimensional tether length l_t. The electrical resistance depends on the tether conductivity while the non-dimensional tether length depends on the tether length and tether conductivity. The tension only depends on the elastic deformation of tether length. Hence, the combined thermal effect is slightly different from the case of considering the thermal-induced tether conductivity variation only, as shown in Fig. 4.15 (a-c). Compared Fig. 4.15 to Fig. 4.14, Figure 4.15(d-f) shows that the tension plays an indispensable role in dynamic stability of an EDT system considering

tether elasticity.

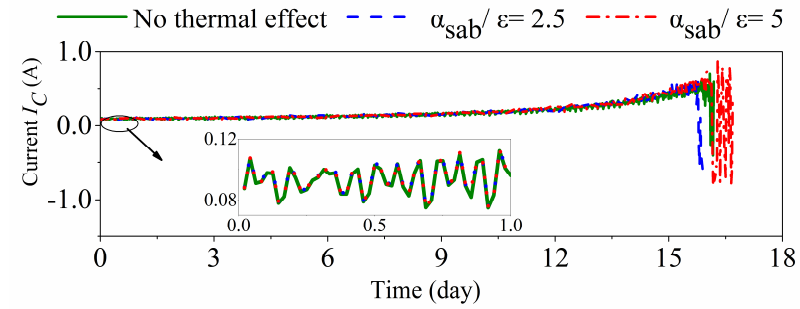

a) Current of Point C of tether in Equatorial orbit

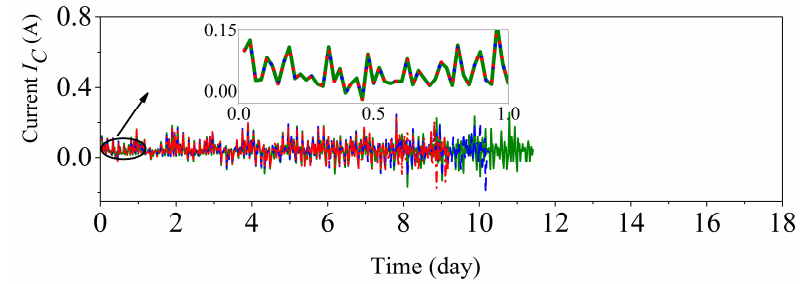

b) Current of Point C of tether in 57° inclined orbit

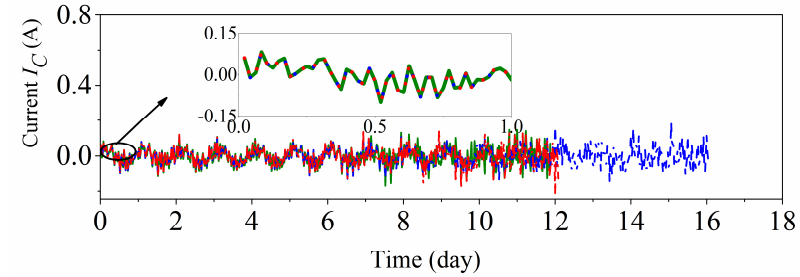

c) Current of Point C of tether in ploar orbit

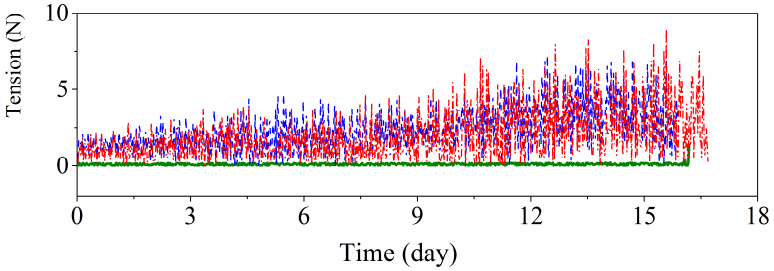

d) Tension of the last element near the ballast end in equatorial orbit

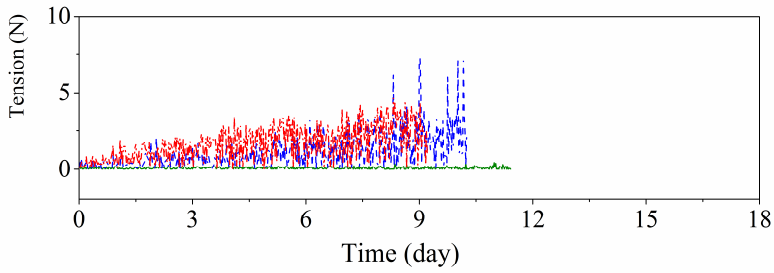

e) Tension of the last element near the ballast end in 57° inclined orbit

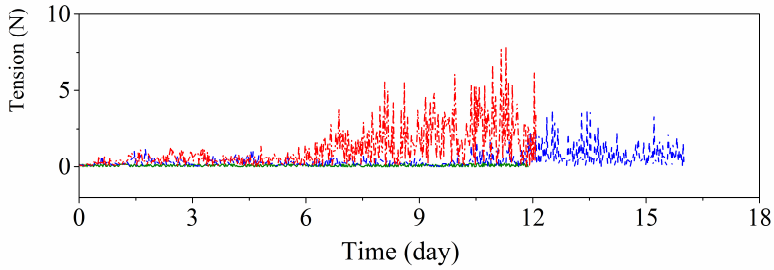

f) Tension of the last element near the ballast end in ploar orbit

Figure 4.15 Variation of current and tension in different orbits by combined thermal effect.

4.2.1.5 Deorbit with Current Regulation Control

The previous cases show that the thermal and electrical coupling effect continuously injects energy into the EDT system, excites the transverse dynamic motion, and finally causes the EDT system into unstable tumbling motion if no control is applied. To control the dynamic stability of EDT system, two simple and practical control strategies with current on/off are developed and applied. The first uses the libration energy as the stability criterion to control the current switching while the second uses a pair of in-plane and out-of-plane angles as the stability criterion. The switch on/off control is activated if the stability criteria are exceeded. The current is turned off to avoid further injection of energy into the EDT system if the sign of power of electrodynamic force is positive, and vice versa.

In the first control strategy, two energy thresholds $\bar{H}_{th}^{\prime Upper}$ and $\bar{H}_{th}^{\prime Lower}$ are used. When the instant libration energy exceeds the upper bound threshold $\bar{H}_{th}^{\prime Upper}$, the control law is activated to regulate the electric current. The current is turned on/off based on the sign of power of electrodynamic force to dissipate energy from the libration motion until the libration energy is reduced below the lower bound threshold $\bar{H}_{th}^{\prime Lower}$. This approach is different from the libration energy control strategy in Ref. [94]. Then, the current control is deactivated until the libration energy exceeds the upper bound threshold $\bar{H}_{th}^{\prime Upper}$ again. In the second strategy, the current control is based on the in-plane and out-of-plane angles. A pair of maximum pitch and roll angles is pre-defined. Once the libration angle exceeds either threshold, the control law is activated, and the current is turned on/off based on the sign of power of electrodynamic force as defined in the first strategy. The electrodynamic force dissipates energy from the libration motion until the libration energy reaches the lower bound libration energy $\bar{H}_{th}^{\prime Lower}$, then the control law is deactivated.

All thermal effects are considered and the ratio of absorptivity to emissivity is set to $\alpha_{sab}/\varepsilon = 2.5$. In case of the equatorial orbit, the values of $\bar{H}_{th}^{\prime Upper}$ and $\bar{H}_{th}^{\prime Lower}$ are set to 1.0 and 0.5 respectively, and the thresholds of pitch and roll angles are set to 30 degrees. Figure 4.16(a-d) shows the time history of EDT libration motion, libration energy, and semi-major axis of a deorbit process by these two control strategies. The results show that the libration energy control is more effective and robust than the libration angle control. It reaches the target orbital altitude very quickly and the libration angles are well bounded in the whole deorbit process. For the maximum libration angle control, it also successfully

reaches the target orbital altitude. However, the system's libration energy in this case is not bounded compared with the energy control law, see the solid line in Fig. 4.16(c) and the deorbit process takes a longer time, as shown in Fig. 4.16(d). The time to deorbit a micro-spacecraft by the energy control law is 22.4 days compared to the 36.1 days by the angle control law in the equatorial orbit. It is noted that the pitch angle is bounded to ±30° in most of the time while the roll angle hardly exceeds ±15°. It means the control of pitch angle can effectively stabilize both the in-plane and out-of-plane libration motion via nonlinear modal coupling between two libration modes. While the amplitude of pitch is bounded within ±30°, the in-plane angle is close to the critical angle of 90° shortly when the libration energy peaks at the points A and B as shown in Fig. 4.16(a) under the libration angle control. The reason for this is that there is a sudden switch-on the current due to the high density of ionosphere plasmas between 300 km and 400 km altitude, leading to an electrodynamic force pulse. Some constraints should be employed to avoid the libration angle accidentally going behind the range when the orbit altitude is lower than 400 km.

For the case of inclined orbits, the thresholds of $\bar{H}_{th}^{\prime Upper}$ and $\bar{H}_{th}^{\prime Lower}$ are set to 1.8 and 0.5, respectively, while the angular thresholds are kept the same as in the equatorial orbit. Figures 4.17(a-e) and 4.18(a-e) show the time history of EDT orbital motion and libration motion in the 57° inclined and polar orbits, respectively. It has been found that the libration motion of EDT system is dominated by the out-of-plane motion for the inclined orbits and it is the roll angle that triggers the current control, as shown in Figs. 4.17(a-b) and 4.18(a-b). The roll angle hardly exceeds the threshold value. It indicates that

the libration motion can be stabilized by controlling the roll angle only in the inclined orbit. This verifies our previous finding based on the rigid tether assumption without thermal effect. For the Advanced Integrated Micro-Spacecraft with a 5 km EDT, the deorbit time from the initial altitude of 900 km to the target altitude 250 km is just 82 and 176 days, respectively, with the current regulation control strategy even in the 57° inclined and polar orbits.

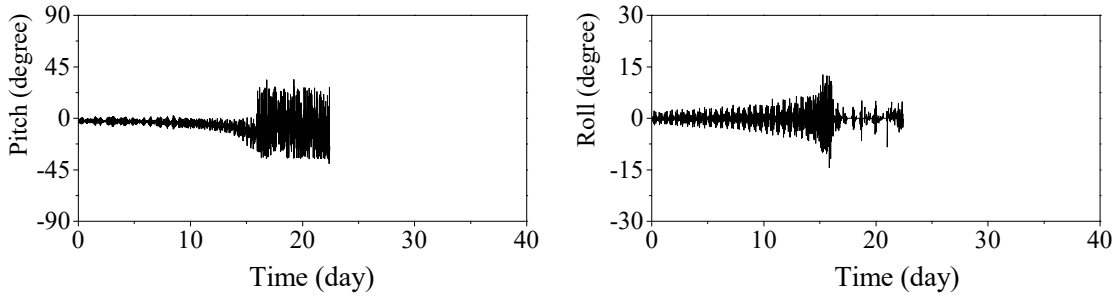

a) Libration motion under the energy control law

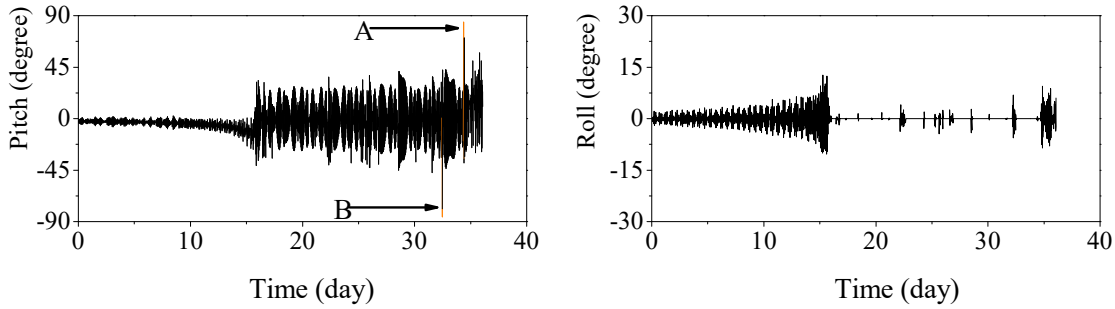

b) Libration motion under the angle control law

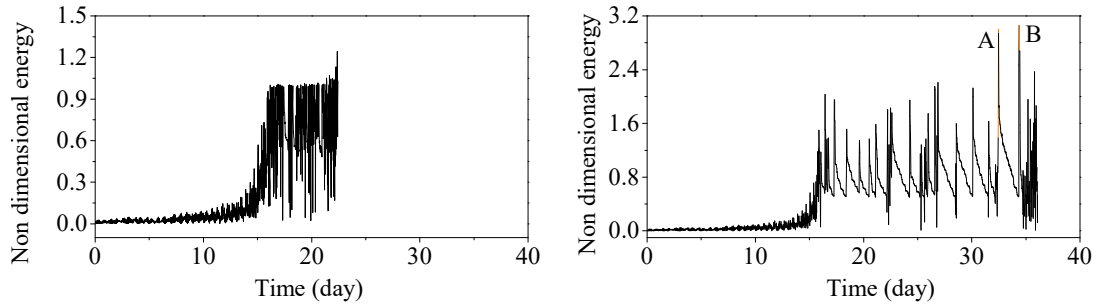

c) Libration energy under energy control law **d) Libration energy under angle control law**

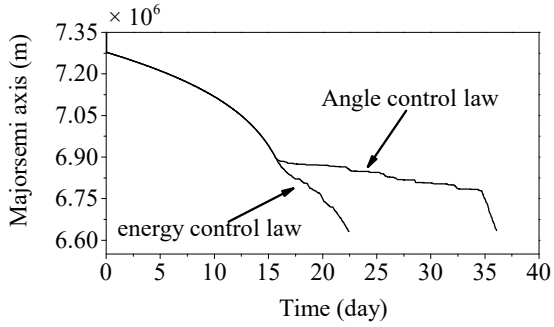

e)Semimajor axis of EDT system orbital plane

Figure 4.16 Time history of libration motion in equatorial orbit with libration control and thermal effect.

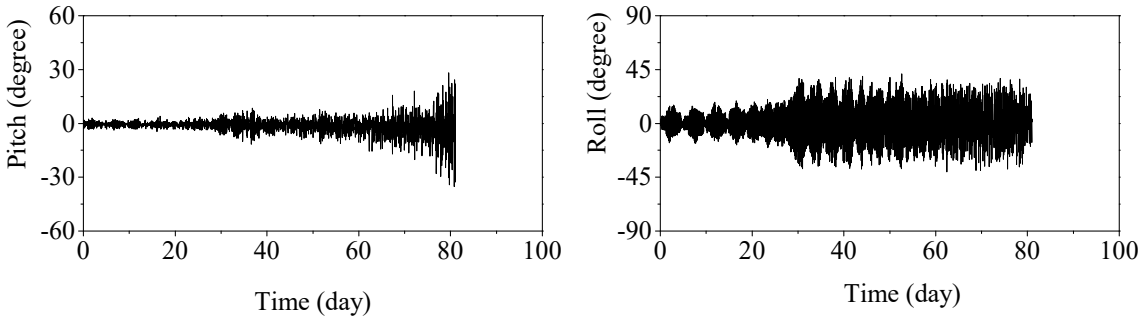

a) Libration motion under the energy control law

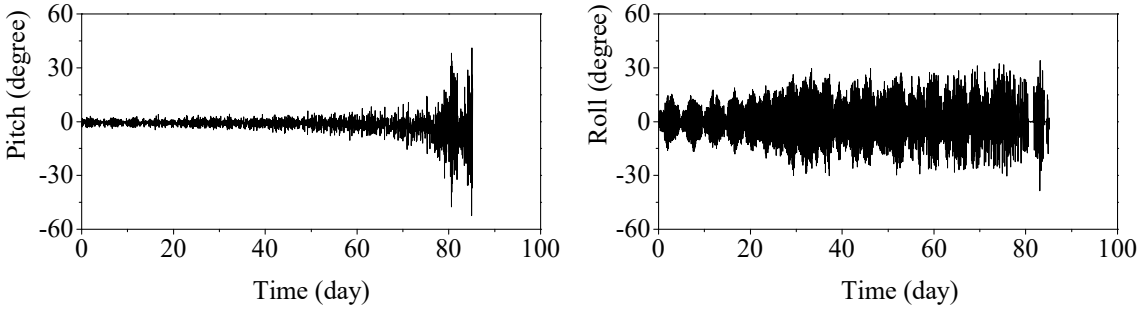

b) Libration motion under the angle control law

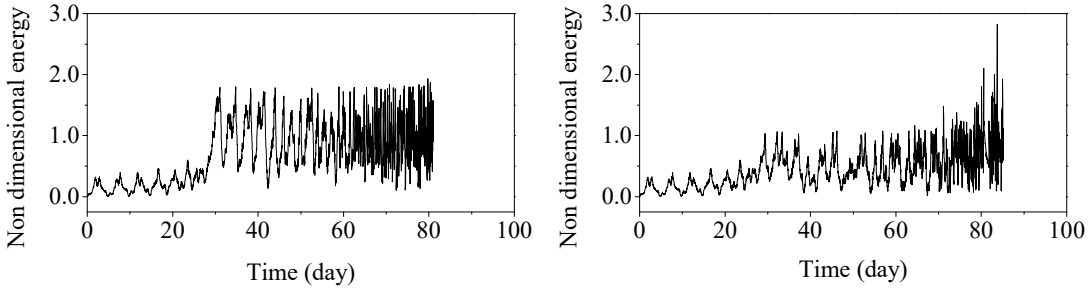

c) Libration energy under energy control law **d) Libration energy under angle control law**

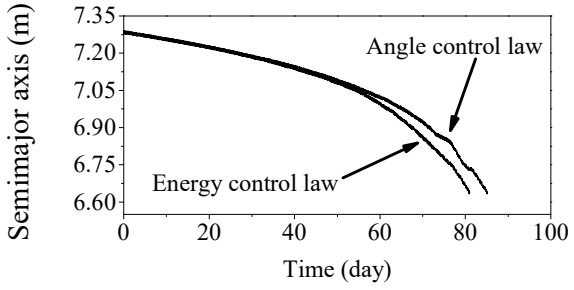

e)Semimajor axis of EDT system orbital plane

Figure 4.17 Time history of libration motion and orbital motion in 57° inclined orbit with libration control and thermal effect.

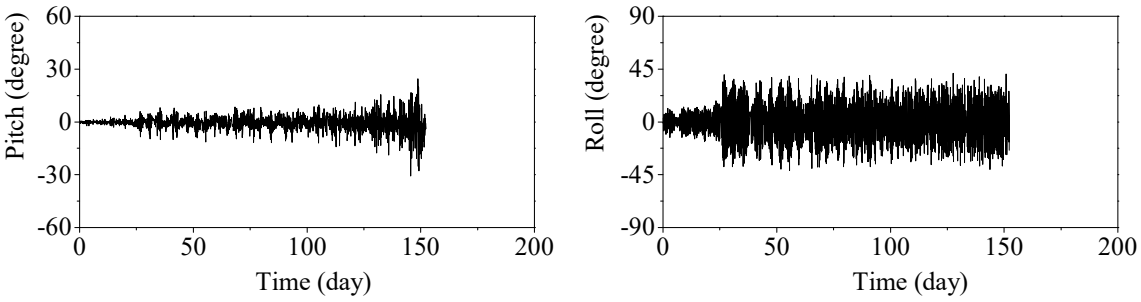

a) Libration motion under the energy control law

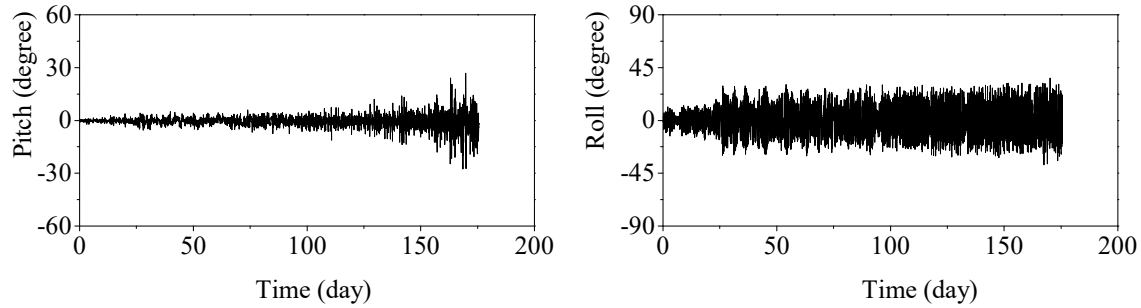

b) Libration motion under the angle control law

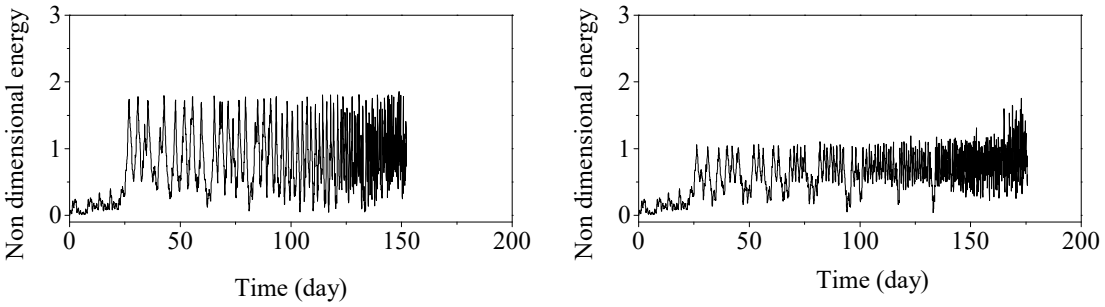

c) Libration energy under energy control law **d) Libration energy under angle control law**

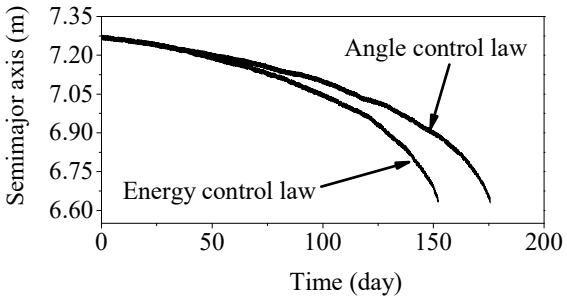

e)Semimajor axis of EDT system orbital plane

Figure 4.18 Time history of libration motion and orbital motion in polar orbit with libration control and thermal effect.

4.2.2 Method B

In this section, method B is used for the evaluation of current in tether. The impact of the new method is evaluated by comparing the results with the solutions based on the continuous electric current profile by the previous method in Refs. [6, 43, 106]. The only differences in the results by method B and the previous method will be caused by the tether deformation. Furthermore, To consider the tether deflection, the induced emotional field of method A is modified by a factor $\kappa \cdot E_m$, where the factor was defined as $\kappa = L^* / L$ (L^* is the shortest distance between two ends of the bent tether and L is the total tether length) [106]. Thus, the previous method called the modified method A in following.

The physical parameters of EDT system used in the study are given in Table 4.1. The initial altitude is assumed at 900 km and the EDT system is in a circular equatorial orbit. The effect of EDT deformation on the deorbit performance has been investigated and compared with the results obtained by the reference method with the rigid and straight tether assumption. The tolerance and the maximum iteration number for solving the discretized OML Eqs. (4.41) -(4.42) are set to 10^{-7} and 50, respectively. The initial input for the iteration is estimated by the semi-analytical method [38] to accelerate the iteration convergence. In addition, the Gaussian integration with 20 sample points (N_{GA}) is used to evaluate the nodal electrodynamic force vector in each element. The Symplectic 2-stage and fourth-order Gaussian-Legendre Runge-Kutta integrator [67] is adopted to solve the highly nonlinear governing equation of EDT system.

4.2.2.1 Sensitivity Analysis

In this section, the sensitivity of the number of tether elements and the bending deformation are investigated before method B is fully incorporated into the EDT debris analysis. The sensitivity of the number of tether elements has been studied in two scenarios: the straight and bent tethers, as shown in Fig. 4.19. Eight simulation cases have been conducted under two tether configurations: two by the modified method A and the rest by method B with different numbers of elements. The simulation results are shown in Table 4.2 and Fig. 4.20. As shown in Fig. 4.20 (a-b), the current profile along the tether by these two methods are remarkably close with slight difference. This is caused by the slight discrepancy in the calculated characteristic tether length L_*, which is the function of location dependent electron density and motional electric field. The previous studies have revealed that the dimensionless tether length $l_t = L/L_*$ is a sensitivity parameter for the induced current profile [38]. The value of L_* varies slightly from element to element in method B while it is constant along the tether in modified method A. As the tether length increases, it is expected that the difference will increase.

The results of the calculated dimensionless tether length, maximum current and motional electric field by the comparison methods are listed in Table 4.2. Obviously, the trend of numerical results shows that more elements lead to the better approximation of geometry of tether and consequently the higher accuracy of results. For example, the maximum difference between these two methods by 10 elements is about 2.5% in the case of straight tether. Meanwhile, the difference rises to 4.5% in the case of bent tether. The

reason for this phenomenon is that the actual motional electric field E_m varies along tether and the method B accounts for this effect. It indicates that the method B is more realistic with the consideration of tether flexural deformation. Furthermore, the difference between different element discretization schemes is small for both cases. Thus, the tether is divided into 5 elements in the following cases of section 4.2.2.

Table 4.2 Sensitivity analysis of number of elements

Name	Parameters	Reference Method	Method B		
			5 elements	8 elements	10 elements
Straight tether	l_t	0.5744	0.5793	0.5797	0.5799
	I_B (A)	1.2322	1.2600	1.2626	1.2635
	E_m(V/m)	0.1750	0.1751	0.1751	0.1751
Bent tether	l_t	0.5782	0.5714	0.5709	0.5722
	I_B (A)	1.2191	1.1725	1.1647	1.1667
	E_m(V/m)	0.1716	0.1717	0.1717	0.1717

Note: The value of motional electric field of the proposed method is an average value.

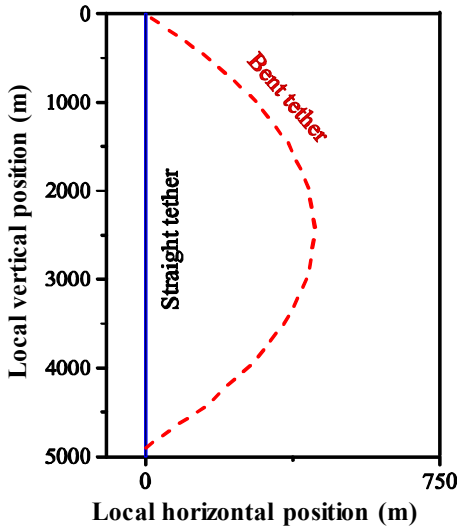

Figure 4.19 The sensitivity analysis by considering tether geometry.

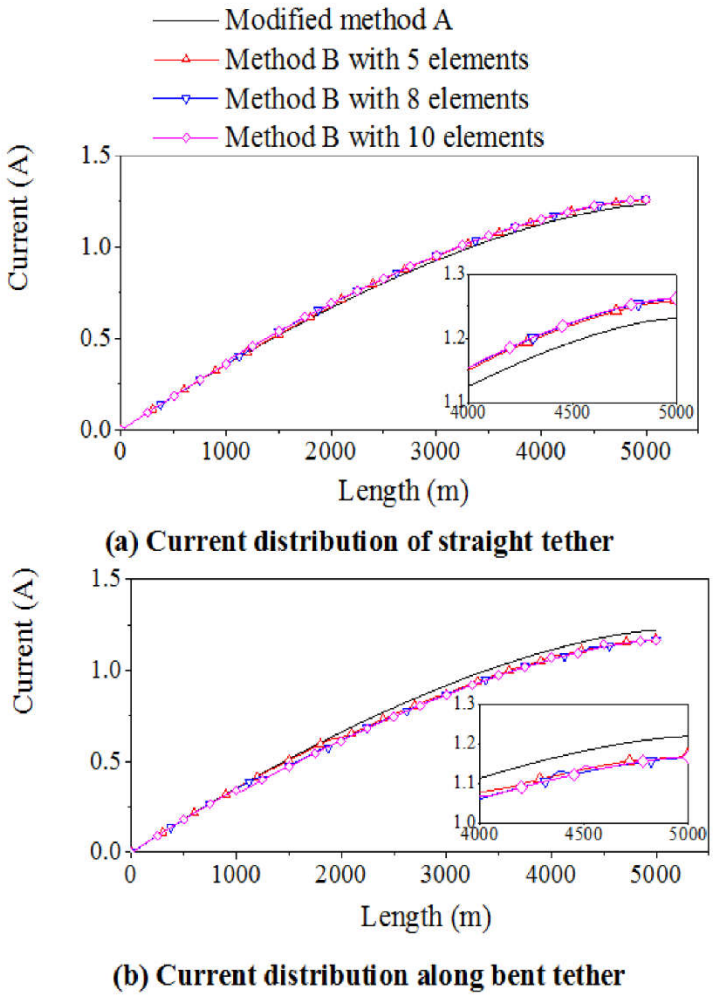

Figure 4.20 Comparison of current profile along tether in different cases.

Next, define a new parameter $\gamma = \delta / L$ with δ is the maximum distance deviates from the local vertical position for the bent tethers and L is the total tether length, as shown in Fig. 4.21. The sensitivity of different profiles of bent tether are investigated by varying γ from 0 to 0.17 with the increment being 0.02. Nine cases are considered by method B and the modified method A. The simulation results are shown in Fig. 4.22 and Table 4.3. As shown in Fig. 4.22(a-i), there is a slight difference between two methods, and it

increases as expected as the bending of tether increases. This is caused by the distinct variation of motional electric field E_m along the tether when it experiences a bending deformation. However, it should be noted that the maximum difference between these two methods is less than 5% because the tether length is moderate. Thus, the ad hoc solution in the modified method A [106] is acceptable in the preliminary analysis if the tether length is not very long.

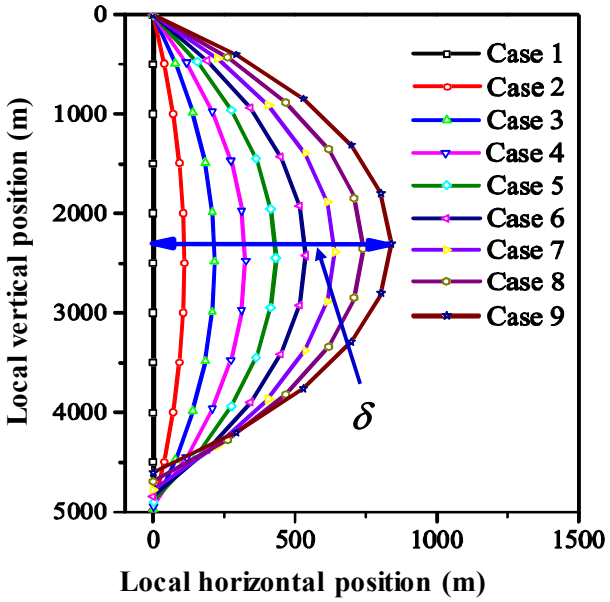

Figure 4.21 The tether profile in sensitivity analysis of bent effect.

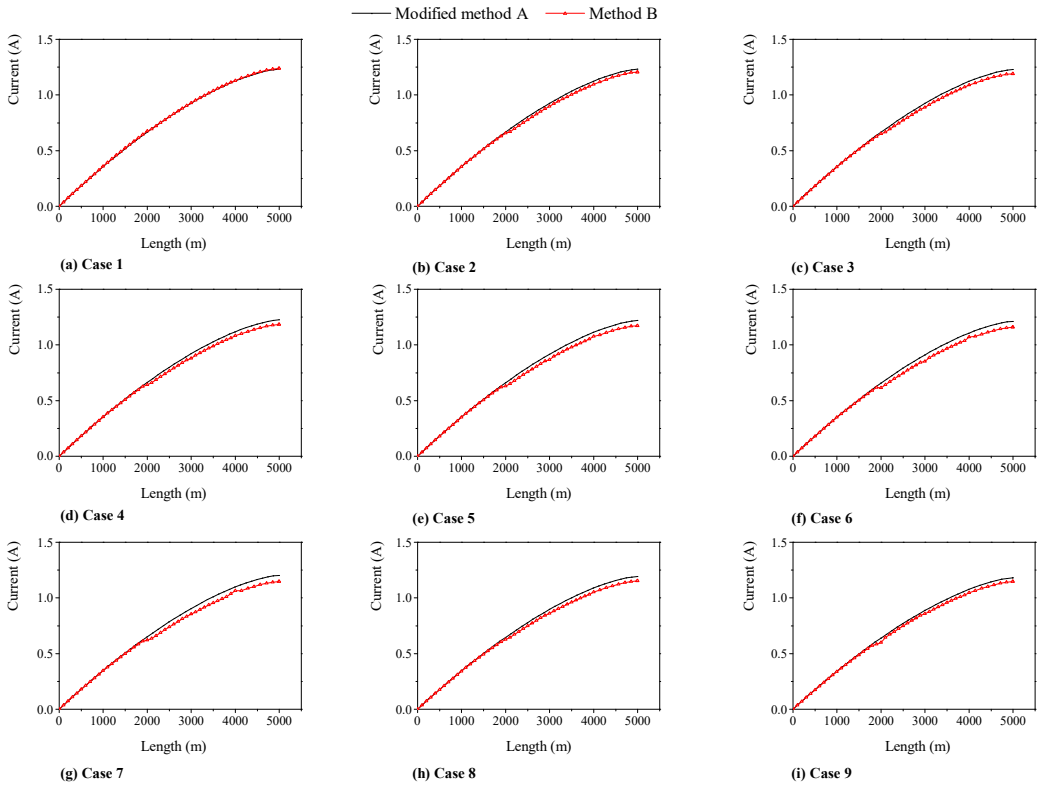

Figure 4.22 Comparison of current distributions with different bent tethers.

Table 4.3 Comparison of the maximum current I_B

Case Name	Case 1	Case 2	Case 3	Case 4	Case 5
Reference Method	1.2322	1.2314	1.2289	1.2248	1.2191
Finite Element Method	1.2598	1.2062	1.1909	1.1833	1.1725
Case Name	Case 6	Case 7	Case 8	Case 9	
Reference Method	1.2118	1.2029	1.1923	1.1801	
Finite Element Method	1.1587	1.1468	1.1520	1.1458	

4.2.2.2 Impact on Libration Motion and Deorbit Performance

The impact of different methods in solving OML equation on the libration motion of an EDT system and deorbit performance is investigated here. The EDT system is started at the 900 km altitude in a circular orbit with 0 inclination. Once the libration angle (in-plane

angle) exceeds the limit (90 degrees), the EDT system is deemed unstable and the simulation is stopped. The environmental force models and the initial condition are the same in the simulation for both methods. As stated in the section 4.2.2.1, the tether is divided into five elements. The simulation results are shown in Figs. 4.23-4.24.

The variations of the motional electric field and the characteristic length by two methods over the time are shown in Fig. 4.23(a-d). It can be easily observed that the induced motional electric field E_m of each element in the method B is varied significantly when the libration motion becomes large. Figure 4.23(a) shows the variations of E_m estimated at the center of each element over the time. They deviate each other quickly as the tether starts to liberate and bend. Correspondingly, the characteristic length of each element has the same trend as the motional electric field, see Fig. 4.23(c). This is because the characteristic length depends on the motional electric field. The motional electric field and the characteristic length of the whole tether system calculated by the modified method A are shown in Fig. 4.23(b-d). They are close to the averaged motional electric field and characteristic length calculated from each element. This is expected because the modified method A assumes the motional electric field is constant over the tether length is equivalent to average the results of each element in certain degrees. Furthermore, Figure 4.23(d) shows there are two sudden changes of the characteristic length calculated by the reference method before 500s. Interestingly, the same phenomenon is observed in the characteristic length of the first element in Fig. 4.23(c). Further investigation indicates the phenomenon is caused by the coarse interpolation of plasma density N_e. This phenomenon is not observed in Fig. 4.23(a-b) due to the average effect by integration over the length in solving

the current profile. A fine interpolation of plasma density N_e could make the changes smoother, but the variation does exist. The method B helps to understand this phenomenon and its root. Therefore, the variation of electron collection efficiency from element to element should be considered when the large flexural deflection of tether is developed, especially for extreme long tethers. The analyses indicate that the modified method A is acceptable for the preliminary analysis in the mission-planning phase. The finite element approach is more accurate and should be used in the detailed engineering design phase.

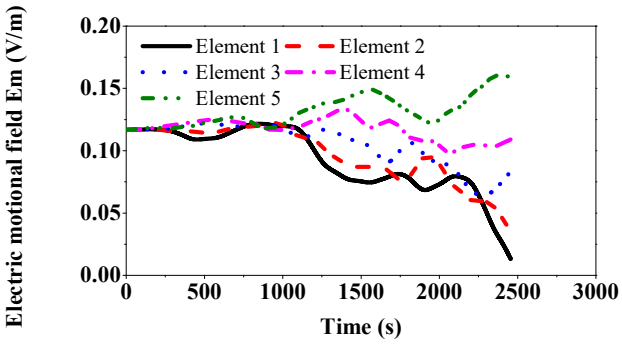

(a) Motional electric field of each element

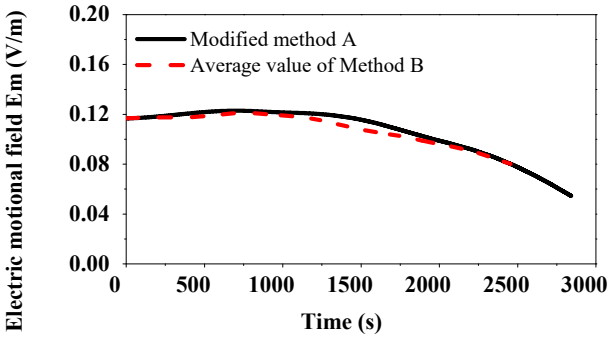

(b) Motional electric field of tether system

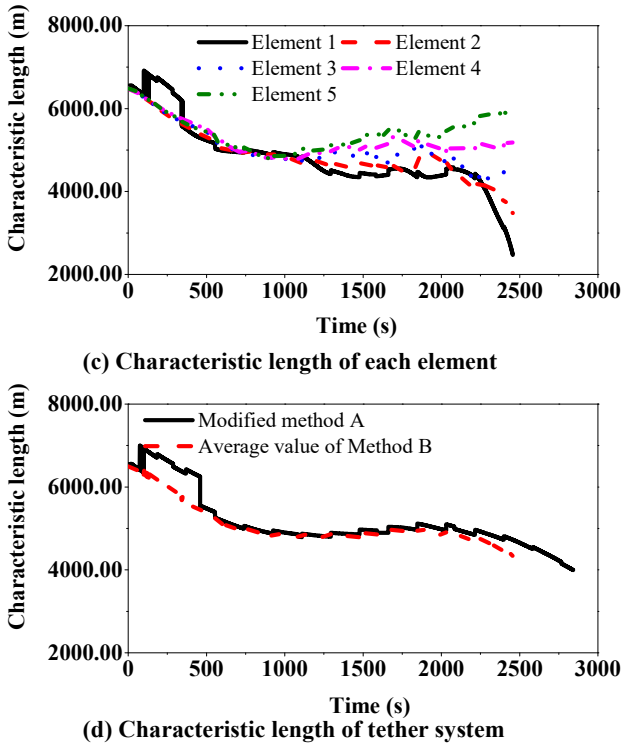

Figure 4.23 Comparison of motional electric field and characteristic length by different methods.

Next, comparisons of time history of current at null bias point *B* by two methods are shown in Fig. 4.24(a). It shows the current at point *B* calculated by the modified method A does not change smoothly at the initial stage - an artificial sudden drop and then a sudden rise in the magnitude of current occurs in the first 500s. This corresponds to the characteristic length calculated by the modified method A in Fig. 4.24(d). On the contrast, the current calculated by the method B does not show such sudden changes in the initial stage. This is because the method B accounts the variation of motional electric field along the tether, which is more realistic and accurate. Figure 4.24(b–d) shows the current profiles along the tether at three different time instants by two methods. As the libration motion

develops, the difference in the current profile increases, see Fig. 4.24(b-d). The results indicate that the tether deflection affects the efficiency of electron collection by EDT significantly.

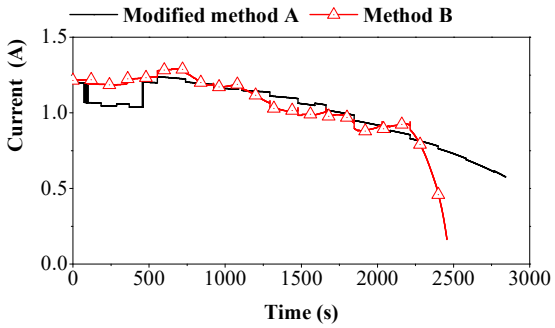

(a) Current at position B

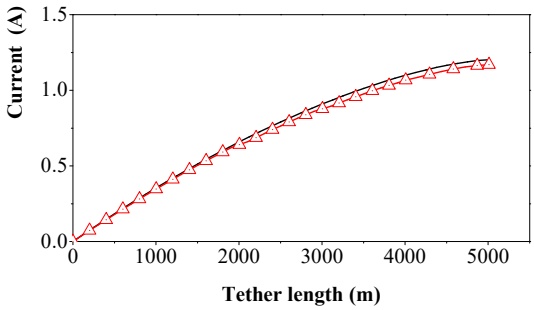

(b) Current distribution at 500s

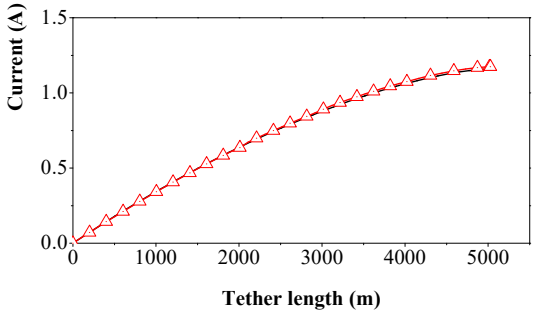

(c) Current distribution at 1000s

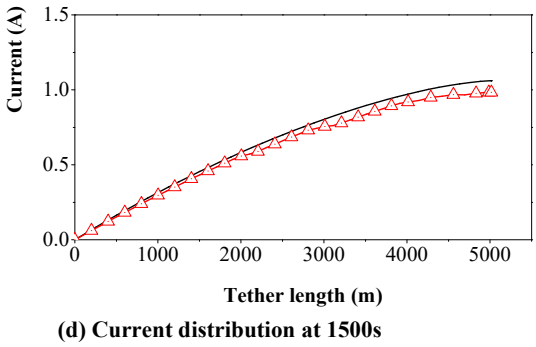

Figure 4.24 (a) Time history of current at B point, (b-d) Current distribution along the tether.

The different current profiles lead to different electrodynamic force acting on the dynamic model of EDT system, resulting in different tether profiles, as shown in Fig. 4.25(a-d). It shows clearly that the difference increases as the time passes and the method B predicts the unstable state occurring faster than the reference method that does not fully couple the tether dynamics with the OML theory. The time histories of in-plane libration angle of selected tether elements (No. 1, 3, 5) at different time instants are shown in Fig. 4.25(a-c). The same trend is reflected in the in-plane angle. The analysis indicates that the modified method A underestimates the dynamic disturbance caused by the electrodynamic force. For real engineering design, the more accurate method B should be used.

Finally, the impact of two methods on the prediction of deorbit performance, stability and efficiency of the EDT system is shown in Fig. 4.26 where the orbit descent rate and the corresponding work done by the electrodynamic force are depicted. It should be mentioned that the prediction of deorbit performance in this study is without applying any stability control strategies. The simulation stops once the system becomes unstable, i.e., the libration angle is greater than 90 degrees. It shows that the orbit descent rates

predicted by two methods are close. However, the method B predicts the EDT system becomes unstable faster than the reference method, see Fig. 4.26(a). In addition, Figure 4.26(b) shows the work done predicted by the method B is greater than the modified method A because the former includes the work done associated with the tether deflection in addition to its libration motion.

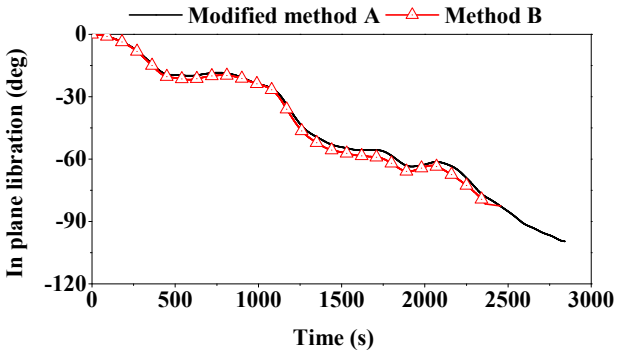

(a) Element 1

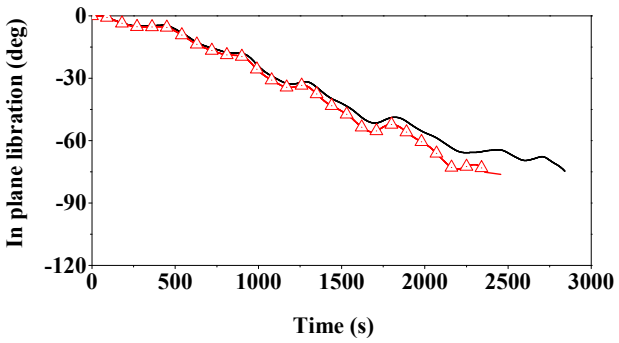

(b) Element 3

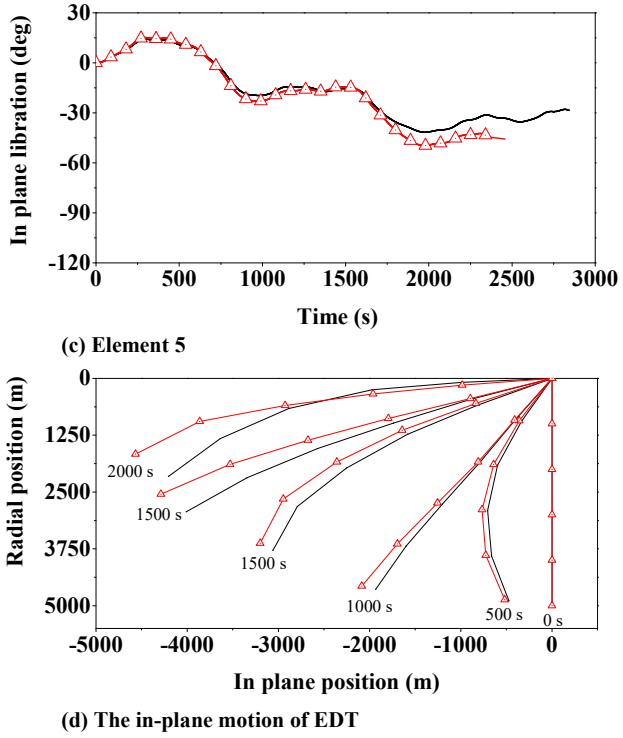

Figure 4.25 Comparison of element libration angles and libration motion of flexible tether (snapshots of tether taken at 500 s interval) by different methods.

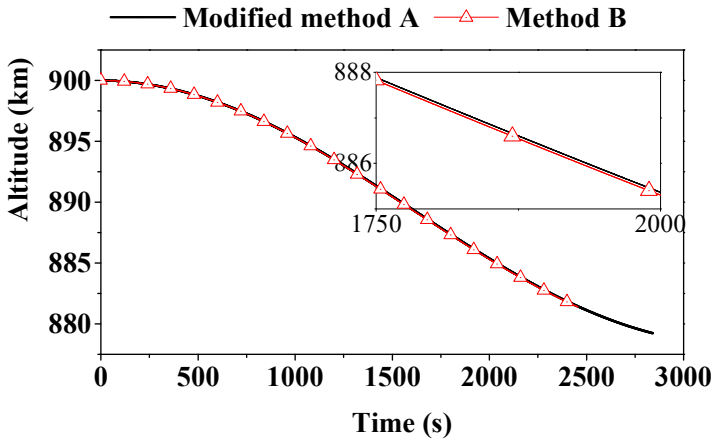

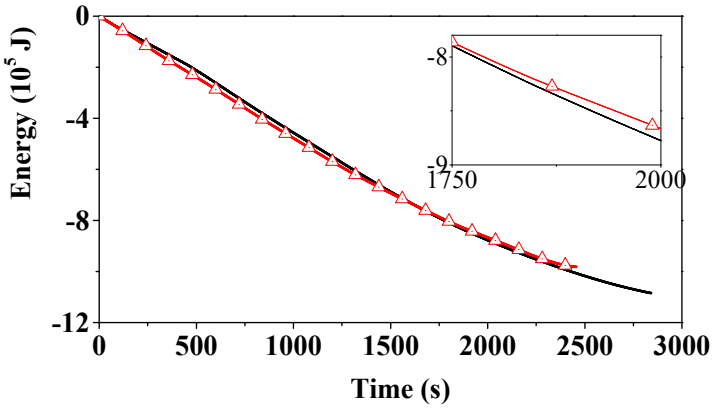

(b) Working done by the electrodynamic force

Figure 4.26 Comparison of predicted deorbit performance by two methods.

4.2.3 Method C

The method C is first compared with reference method (called modified method A) in Ref. [106] and method B in Ref. [42] to demonstrate its effectiveness and necessity. The physical parameters of EDT system in Table 4.1 are used here, except the tether length is 4,000 km. The tape tether is used in this section. The Symplectic 2-stage and fourth-order Gaussian-Legendre Runge-Kutta integrator [67] is adopted to solve the highly nonlinear equations of EDT system.

4.2.3.1 Comparison Results

The profiles of electric current and potential bias along bent/straight EDTs are evaluated by the method C and modified method A and shown in Fig. 4.27. The tether is assumed deployed downwards and aligned with the local vertical initially at the altitude of 900 km in a circle equatorial orbit (Case A). Then, the tether is bent into two different geometrical

configurations, semicircle (Case B) and two-semicircle (Case C), but with the same end position. Moreover, the type 2 design configuration at the cathodic end is selected as listed in Eq. (4.47), and the corresponding values of Φ_{PW}, Φ_{CHE} and Z_T are given as $50V$, $0V$ and 0Ω, respectively.

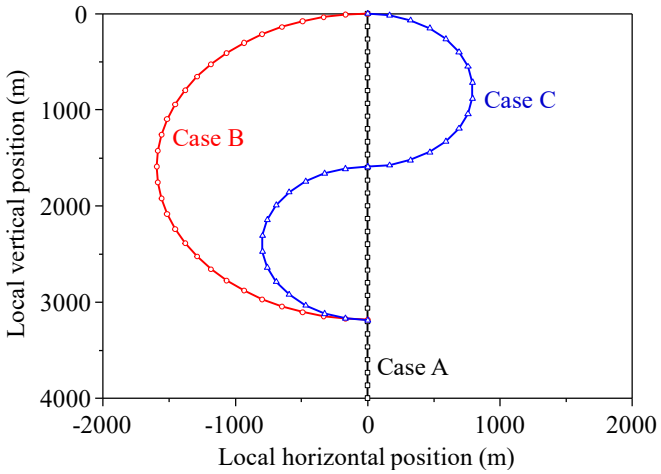

Figure 4.27 Three different tether geometries

First, the convergence of finite element solution of EMF along the tether has been studied. The results are shown in Fig. 4.28 with four different meshes: 6, 10, 20 and 30 elements. For the straight tether, the difference between different meshes is small and negligible. For the bent tethers, large element number improves EMF accuracy but with higher computational effort. Noting that the EMF solution converges after 20 elements, the 20-element mesh is used in the following cases inside this section.

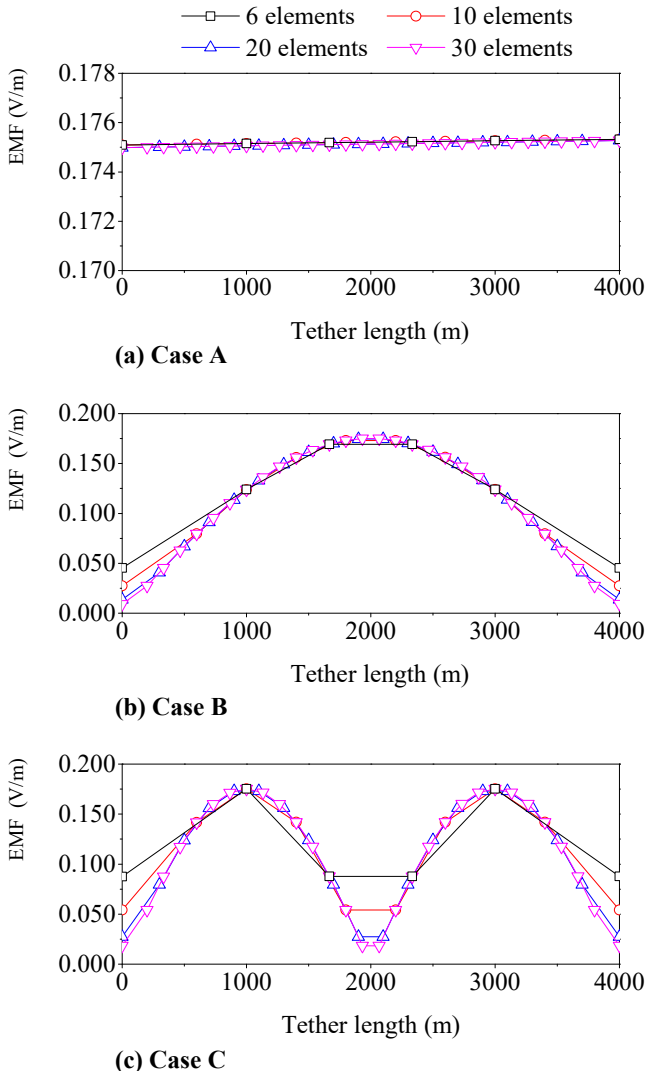

Figure 4.28 Comparison of EMF solution along tether by different numbers of tether elements.

Second, the resulting profiles of electric current and potential bias are compared between the method C and modified method A and results are shown in Figs. 4.29 and 4.30 and Table 4.4. As expected, Figure 4.29(a) shows that the difference of EMF predicted by two methods is negligible in case of straight tether. The difference becomes significant when the tether is bent (cases B and C), see Fig. 4.29(b-c). The comparison reveals that (i)

the EMF profile is not constant along the bent tether, and (ii) the profiles of cases B and C are completely different, but the modified method A is unable to differentiate them and gives the same results. In addition, the difference in the calculated length L_B between these two methods increases as the tether is bent, as listed in Table 4.4. For example, the difference ratio is 0.74% in the case A, and increases to 13.46% in the case B. Thus, the method C is much accurate than the modified method A due to the consideration of coupling effect between the tether deformation and the electric current generation.

Table 4.4 Comparison of segment L_B predicted by two comparison methods.

Name	Modified method A	Method C	Difference (%)
Case A	3662.69 m	3690.06 m	0.74
Case B	3457.61 m	3047.30 m	13.46
Case C	3459.36 m	3332.90 m	3.79

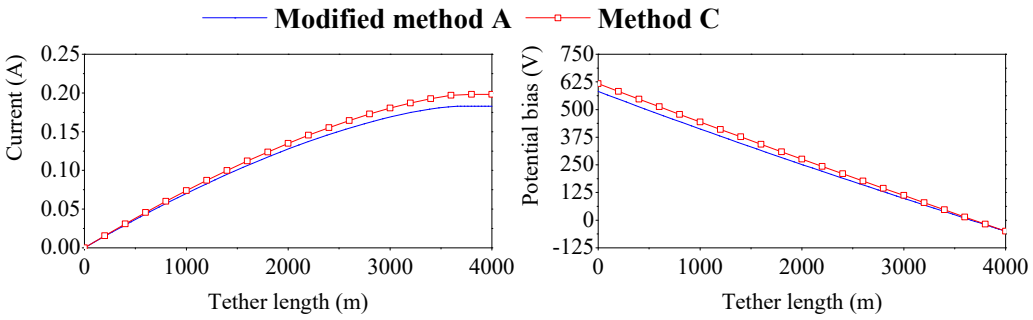

(a) Case A

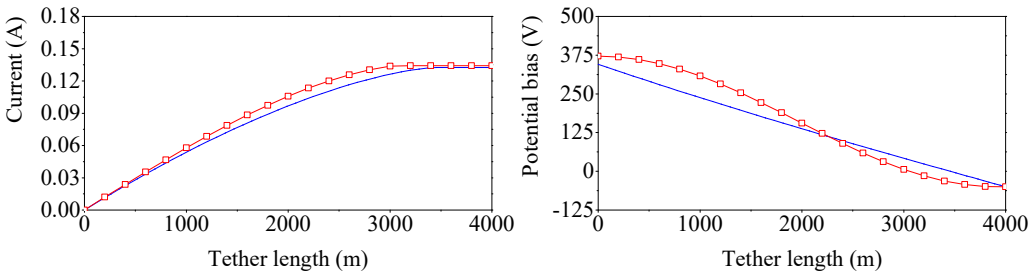

(b) Case B

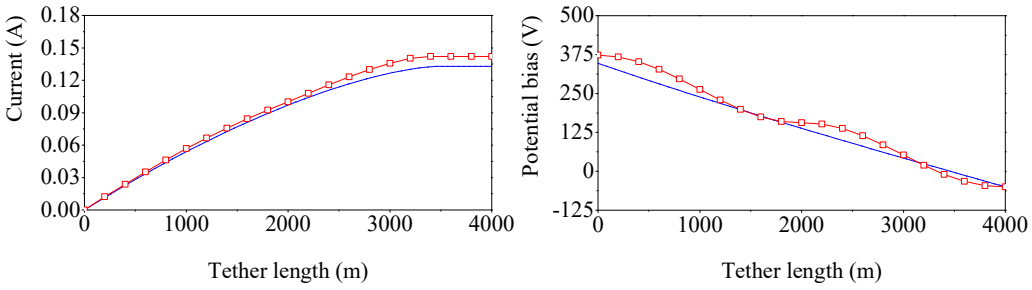

(c) Case C

Figure 4.29 Comparison of EMF profiles along tether by two methods in different cases

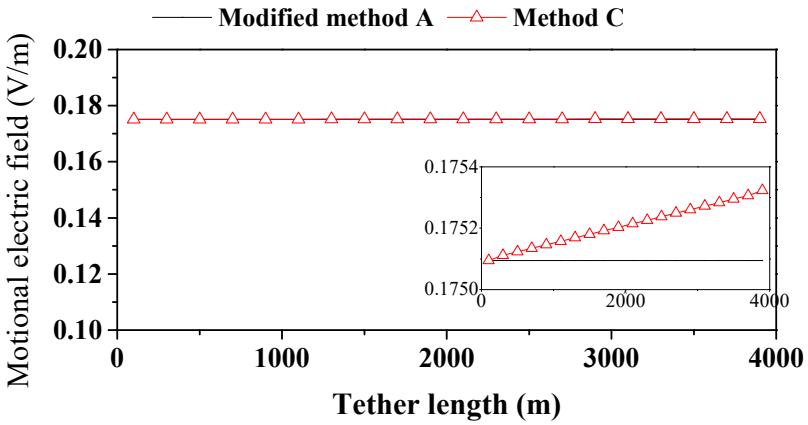

(a) Case A

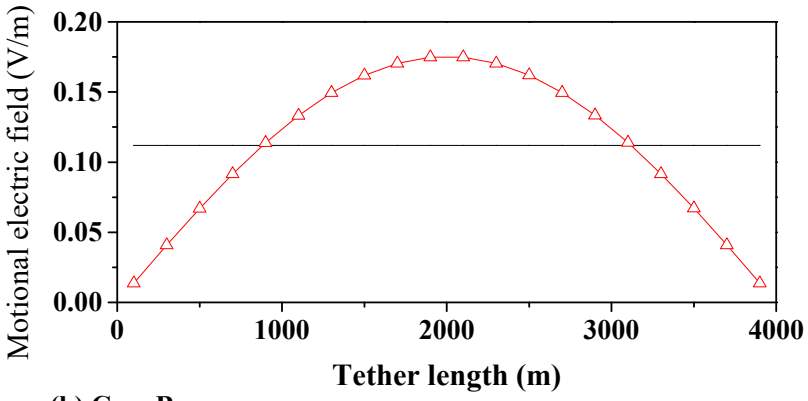

(b) Case B

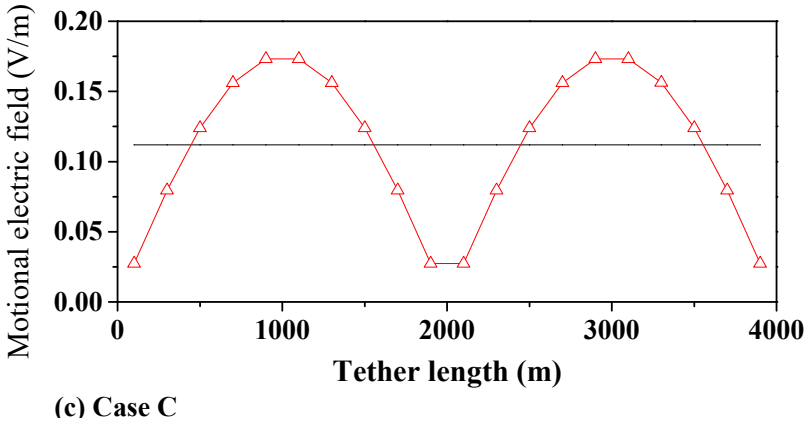

Figure 4.30 Comparison of profiles of electric current and potential bias along tether by two methods in different cases

Third, the method C can handle EDTs with large curvature. Consider the Case B in Fig. 4.27. Currently, no theoretical solution is available for this problem. Our method can find the true solution by loose initial guess. For example, the numerical solution converges within the error margin (ε_{conv} = 1.0^{-10}) for the loosely selected initial guess in Table 4.5. The corresponding results are shown in Fig. 4.31 and Tables 4.5 and 4.6. This shows the method C is numerical robust.

Table 4.5 Comparison of initial guess and final solution of OML equation.

Node No	Currant(A)		Potential Bias (V)	
	Initial Guess	Final Solution	Initial Guess	Final Solution
1	0.0000	0.0000	421.3597	371.3554
2	0.0124	0.0124	418.6024	368.5944
3	0.0247	0.0247	410.5722	360.5607
4	0.0369	0.0369	397.4713	347.4565
5	0.0488	0.0488	379.6298	329.6119
6	0.0605	0.0605	357.4971	307.4765
7	0.0717	0.0717	331.6317	281.6089

8	0.0825	0.0825	302.6867	252.6621
9	0.0927	0.0927	271.3935	221.3678
10	0.1023	0.1023	204.9704	154.9441
12	0.1023	0.1191	238.5440	121.4990
13	0.0927	0.1261	271.3935	89.0329
14	0.0825	0.1322	302.6867	58.3732
15	0.0717	0.1371	331.6317	30.3040
16	0.0605	0.1406	357.4971	5.5454
17	0.0488	0.1410	379.6298	-15.2612
18	0.0369	0.1410	397.4713	-31.6077
19	0.0247	0.1410	410.5722	-43.0449
20	0.0124	0.1410	418.6024	-49.2426

Table 4.6 Iteration number and error.

Iteration Num	ε	Iteration Num	ε
1	9.4984×10^{1}	5	9.9380×10^{-7}
2	5.3554×10^{-2}	6	2.0569×10^{-9}
3	5.3443×10^{-1}	7	4.2675×10^{-12}
4	5.3653×10^{-4}		

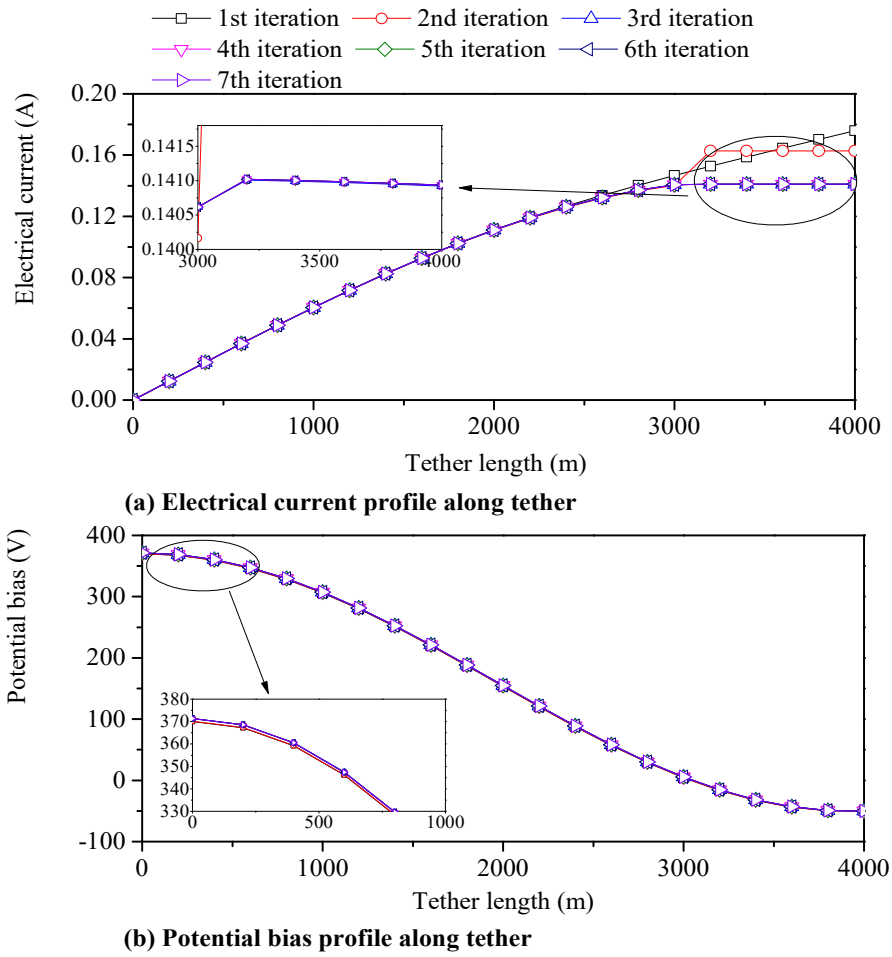

Figure 4.31 Profiles of true electric current and potential bias along bent tether.

Finally, the method C is compared with the method B a bent tether situation [42], see Fig. 4.32. The reason for choosing this configuration is that the difference of electric current profile along EDT can be distinguished between these two comparison methods. The results of the profiles of electric current and potential bias along tether are shown in Fig. 4.33. As shown in Fig. 4.33(a), it can be easily noted that the profile of electric current is not smooth for the method B, and the difference between these two methods is noticeable. The non-smooth phenomenon of electric current along EDT is caused by the

manual adjustment of electric current value at common node between two elements to ensure the continuity condition.

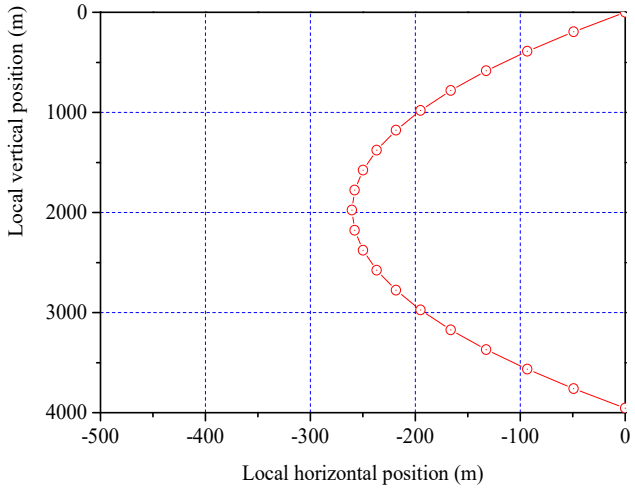

Figure 4.32 Bent tether configuration.

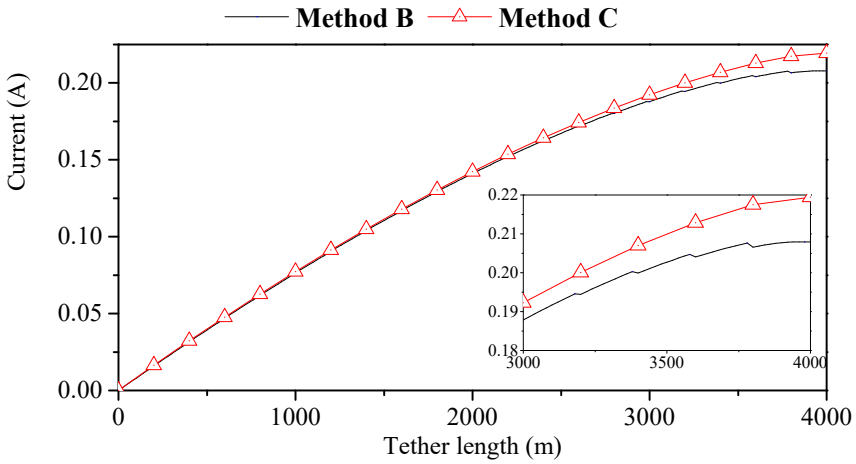

(a) Electrical current profile along tether

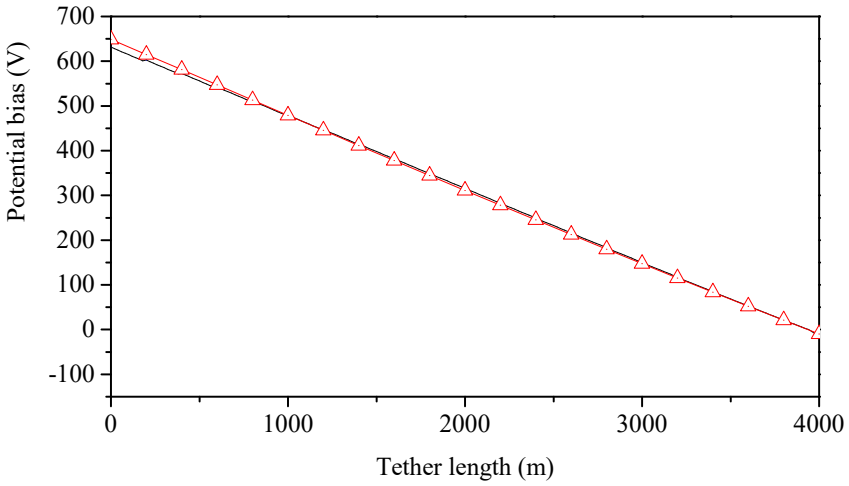

(b) Potential bias profile along tether

Figure 4.33 Profiles of electric current and potential bias along a bent tether.

4.2.3.2 Influence of Tether Deformation and Boundary Condition on Electric Current Estimation

First, the impact of tether deformation on electric current estimation is investigated by changing the ratio (δ) of the sagitta of bent tether over its length [42] from 0.00 (straight tether) to 0.32 as shown in Fig. 4.34(a). The orbit is assumed a circular equatorial orbit with an altitude of 900 km. The type 2 configuration of emitter circuit is taken as the cathode boundary condition, where the conductive tether is connected to the Spindt array emitter via a power source. Let Φ_{CHE}, Φ_{PW} and Z_T be defined as 50 V, 0 V, and 0 Ω, respectively. The other physical parameters are the same as those in Table 4.1, except for the tether length as stated at beginning of this section. Distinct variations of EMF along bent tethers are shown in Fig. 4.34(b). Accordingly, the electric current and potential bias profiles vary significantly along the tether due to its direct relationship with the EMF as

presented in Eqs. (4.6)-(4.7), see Fig. 4.34(c-d). For example, the maximum current I_B at the null potential bias point B decreases from 0.198A to 0.141A as the ratio δ increases. In addition, the same trends are observed for the length of the positively biased segment L_B. Table 4.7 shows that it decreases from 3690.06 m to 3053.47 m as the ratio δ increases. Therefore, the full coupling effect between the efficiency of EDT systems and the tether's curvature should be considered in the EDT deorbit analysis as the electrodynamic force can be reduced by a bent EDT.

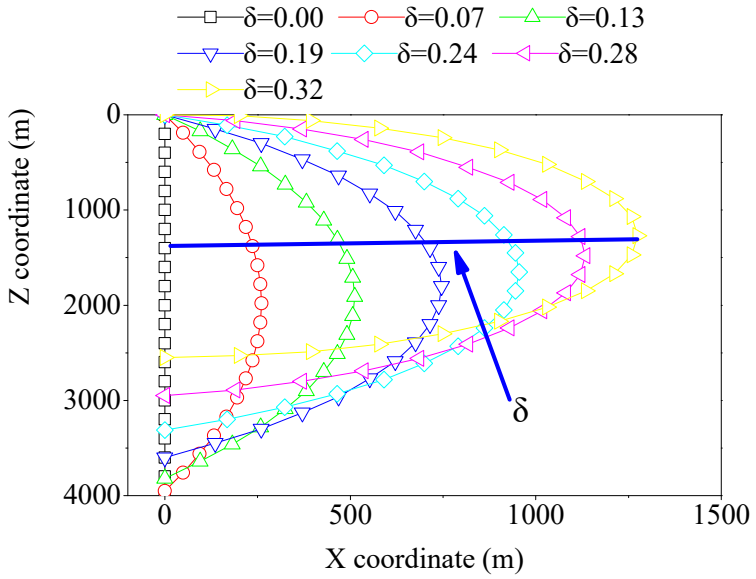

(a) Tether profile

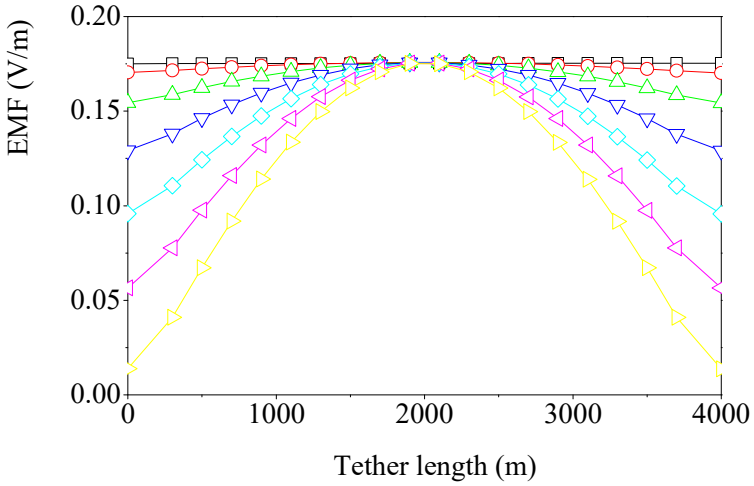

(b) EMF profile along tether

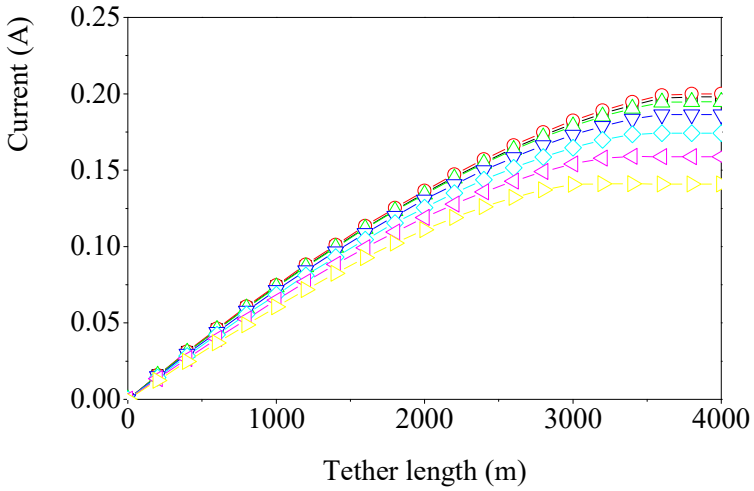

(c) Current profile along tether

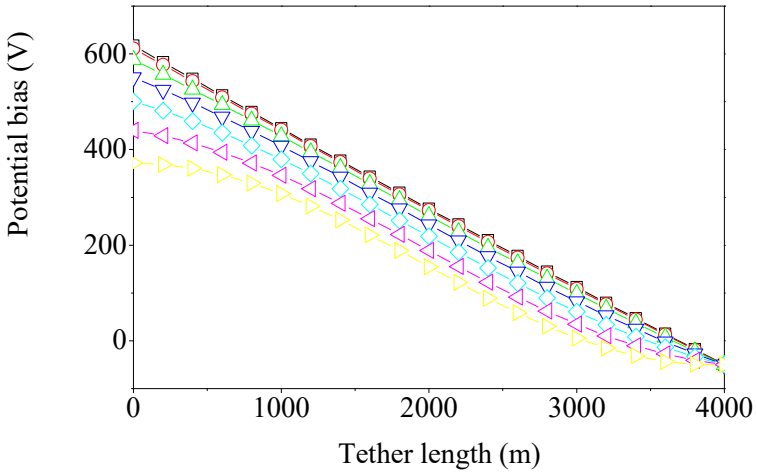

(d) Potential bias profile along tether

Figure 4.34 The sensitivity study of bent tether profile.

Table 4.7 Positively biased segment length L_B vs sagitta of bent tether.

Parameter δ	Length L_B	Parameter δ	Length L_B
δ = 0.00	3690.06 m	δ = 0.24	3447.53 m
δ = 0.07	3680.50 m	δ = 0.28	3300.40 m
δ = 0.13	3648.78 m	δ = 0.32	3053.47 m
δ = 0.19	3585.70 m		

Next, the impact of potential bias Φ_C on the electric current generation is investigated by varying Φ_{PW} from $50V$ to $0V$, with an increment of -$25V$ while the Φ_{CHE} and Z_T are fixed at $50V$ and 0Ω, respectively. The bent tether of Case B in Fig. 4.27 is considered with the same orbit. The results of electric current and potential bias profiles along tether are shown in Fig. 4.35. It is interesting to note that the potential bias profile has a constant offset for each power source Φ_{PW}, which is proportional to the potential drop of power source Φ_{PW}. At the same time, the magnitude of induced electric current is reduced; see Fig. 4.35(a-b). This indicates that the potential bias Φ_C can be controlled by

changing the power source Φ_{PW}, which in turn controls the electric current in EDT. Thus, the efficiency of an EDT system can be controlled by regulating the standalone power source.

Finally, the impact of impedance Z_T at the cathodic end on the electric current is investigated. The tether is assumed to be straight and aligned with the local vertical, and the initial altitude is 450km in a circular equatorial orbit. Further, Z_T varies from 5Ω to 200Ω with increment of 50Ω while the value of Φ_{PW} is fixed at $50V$. As shown in Fig. 4.36, it is observed that the potential bias at the cathodic end Φ_C is significantly affected by the change of electric impedance Z_T. Thus, as shown in Fig. 4.36(a), the variation trend of the profiles of electric current along EDT is evident. For example, the potential bias Φ_C changes from -0.5353 to -16.8703 whereas the maximum current I_C decreases from $0.1071A$ to $0.0844A$. This indicates that the variation of impedance Z_T can significantly affect the electron collection efficiency of EDT system. Moreover, the phenomenon of momentous change of impedance may occur when the additional battery is draining out. Therefore, the effect of changing the impedance Z_T should be considered in refined mission analysis.

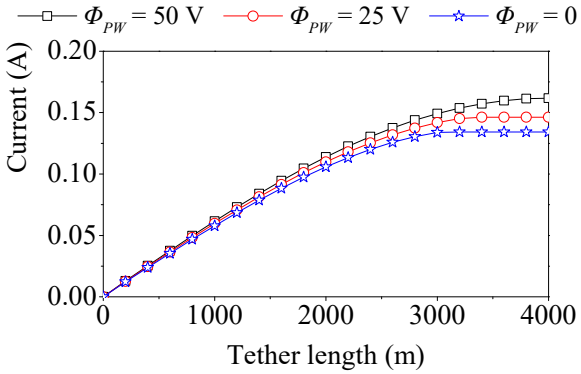

(a) Current profile along tether

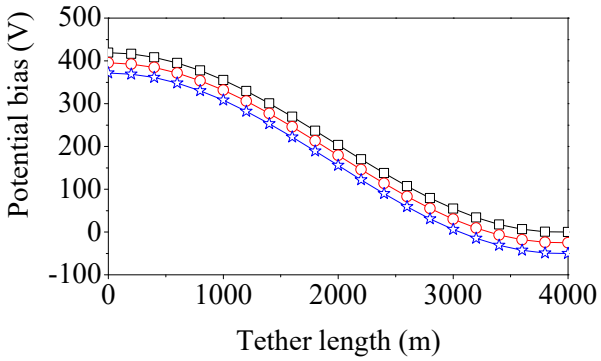

(b) Potential bias profile along tether

Figure 4.35 Influence of power source Φ_{PW} on electric current and potential bias profiles along tether.

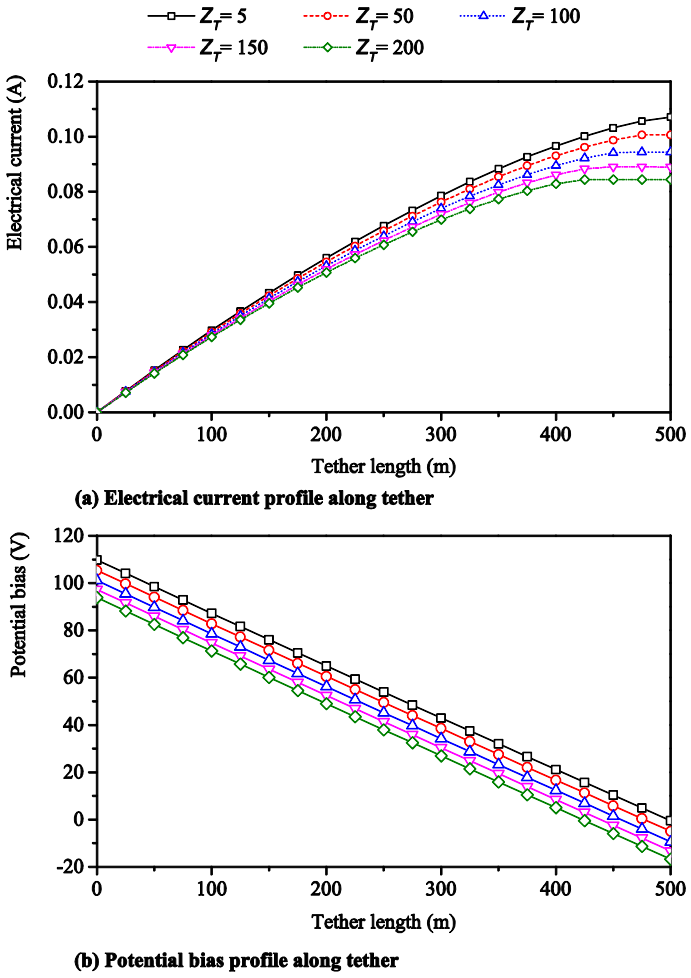

Figure 4.36 Influence of impedance Z_T on electric current and potential bias profiles along tether.

4.2.3.3 Impact of Tether Flexibility on EDT Libration in Deorbit Process

The impact of the method C on prediction of libration dynamics of EDT system is investigated. As a comparison, the electric current and potential bias profiles are also evaluated by the modified method A in Ref. [106] and then are input to the same flexible tether dynamics model. The type 2 configuration of emitter circuit at the cathodic end is chosen, in which the Φ_{CHE}, Φ_{PW} and Z_T are defined as $50V$, $50V$, and 0Ω, respectively. This

represents a full power condition of an EDT system, as the EDT is completely positively biased for current generation [40]. Three typical orbits, the equatorial, 57° inclined, and polar orbits, are considered where the EDT is initially steady and aligned with the local vertical at an altitude of 900 km. The time step is $0.002s$. Once the libration angle of the first element equals or exceeds 90 degrees, the EDT system is deemed unstable, and the simulation is stopped.

Equatorial Orbit

First, the results for the equatorial orbit are shown in Figs. 4.36-4.37. Because the EMF is different in each element in the method C, the averaged EMF of all elements is plotted in Fig. 4.36(a). As shown in Fig. 4.36, the difference in EMF between the method C and modified method A is small initially. In addition, the variation of EMF along the tether is not large, see in Fig. 4.36(b). However, the difference becomes noticeable as the time increases and the tether deforms. Correspondingly, the difference in libration of EDT predicted by two methods becomes noticeable as shown in Fig. 4.37 (a)-(b). This is due to the coupling effect between the flexural deformation of tether and EMF. It is noted from Fig. 4.37(a) that the modified method A is less effective in predicting the unstable condition. The method C predicts the EDT will become unstable faster than the reference method. Thus, the coupling between the tether deformation and the electric current generation cannot be ignored in the EDT deorbit analysis.

57 Degree Inclined Orbit

Next, the results of 57-degree inclined orbit are shown in Figs. 4.39-4.40. Figure 4.39(a) shows the difference of EMF predicted by two methods increases very quickly over the time, while Figure 4.39(b) shows that the variation of EMF from element to element is much significant than in the equatorial orbit. The stable period predicted by the method C is less than half of that predicted by the modified method A. Correspondingly, the difference in the libration of EDT predicted by two methods is more significant, see Fig. 4.40(a)-(c). The analysis demonstrates again that the coupling effect between the tether deformation and the electric current generation must be considered in the EDT deorbit analysis.

Polar Orbit

Finally, the results of polar orbit are shown in Figs. 4.41-4.42. Figure 4.41(a-b) shows that the same phenomenon is observed for the EMF and the stable deorbit period. However, the difference in dynamic responses predicted by the method C and modified method A are maximized, see Fig. 4.41. For instance, the stable deorbit period is reduced by three times by the method C. In summary, the comparison in three orbits shows that the coupling effect between the tether dynamics and the OML theory must be considered in the EDT deorbit analysis, especially in the inclined orbits.

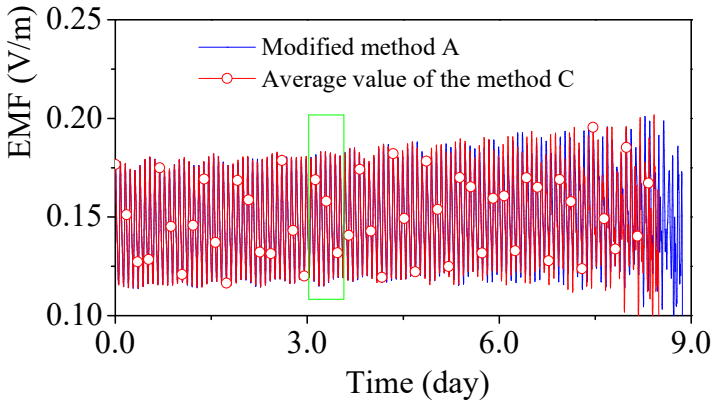

(a) Comparison of EMF between two methods

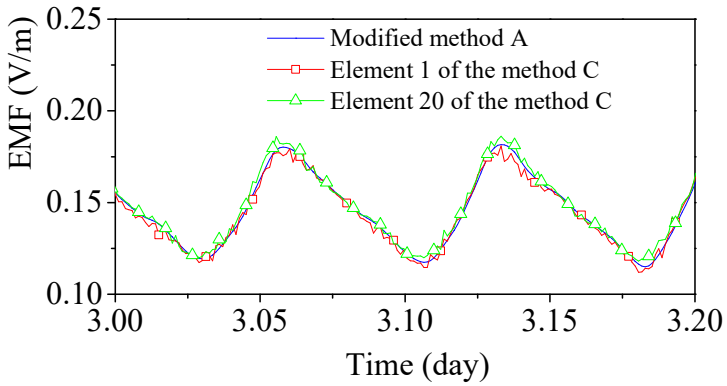

(b) Amplification image

Figure 4.37 Variation of EMF in the equatorial orbit

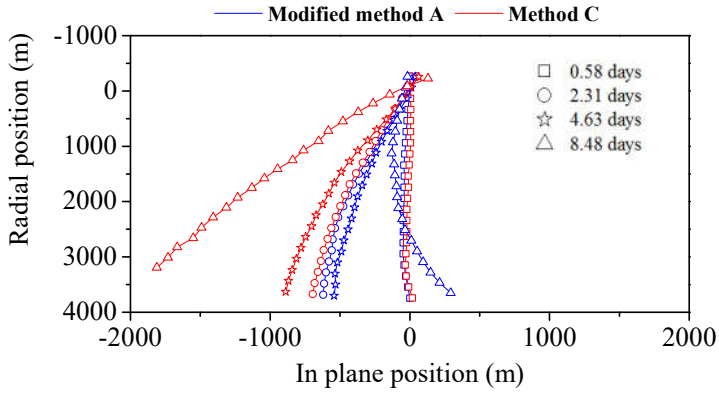

(a) In-plane motion

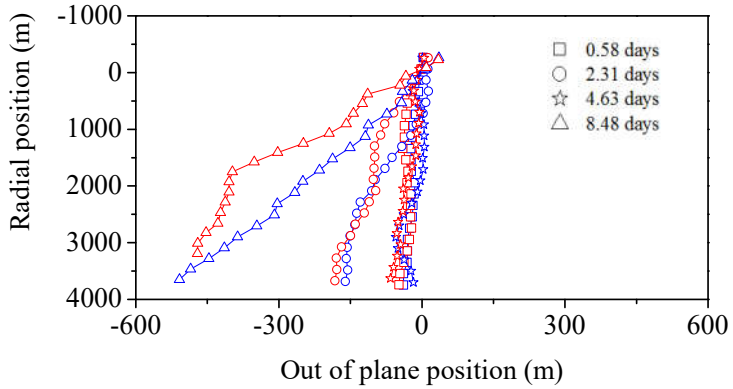

(b) Out-of-plane motion

Figure 4.38 Libration of flexible EDT in the equatorial orbit.

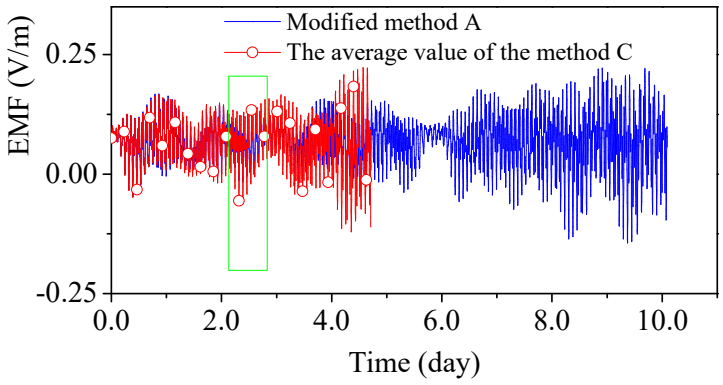

(a) Comparison of EMF between two methods

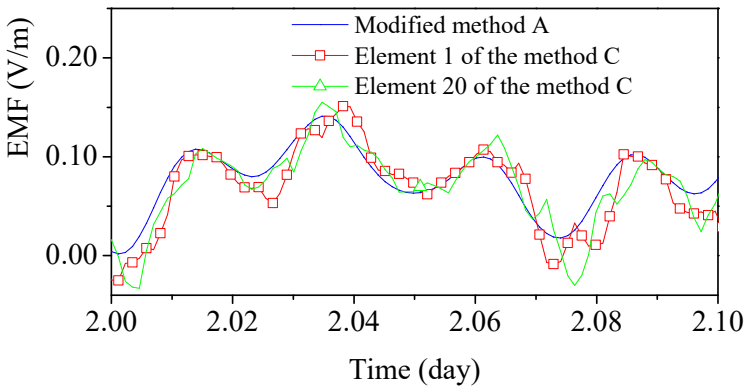

(b) Amplification image

Figure 4.39 Variation of EMF in the 57° inclined orbit.

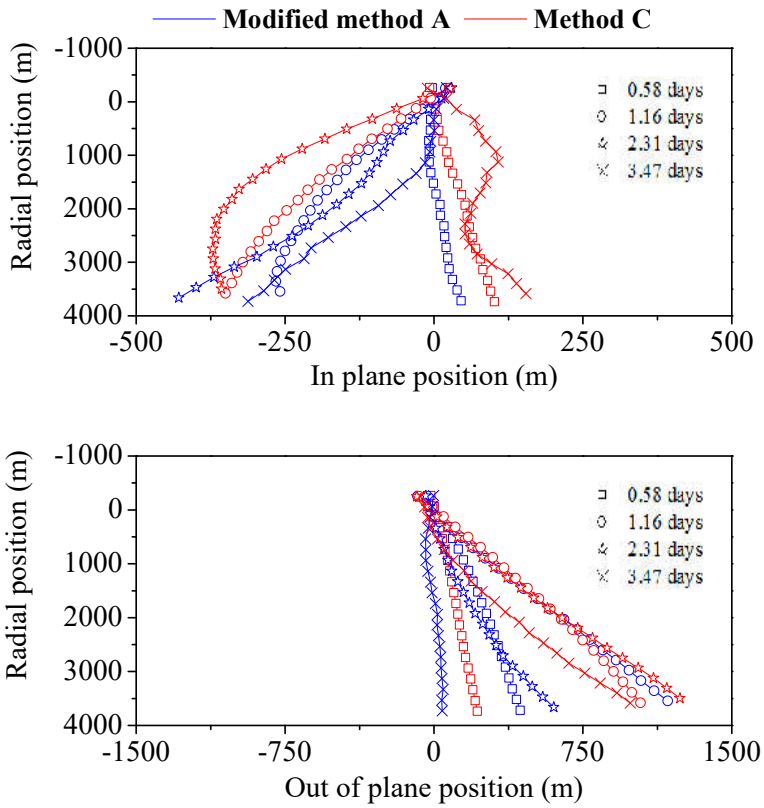

(b) Out-of-plane motion

Figure 4.40 Libration of flexible EDT in the 57° inclined orbit.

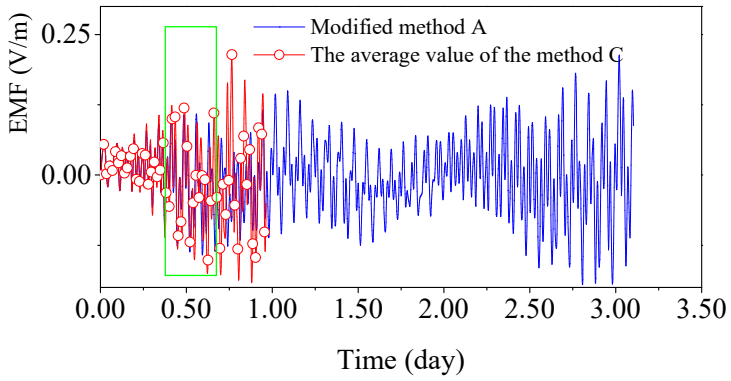

(a) Comparison of EMF between two methods

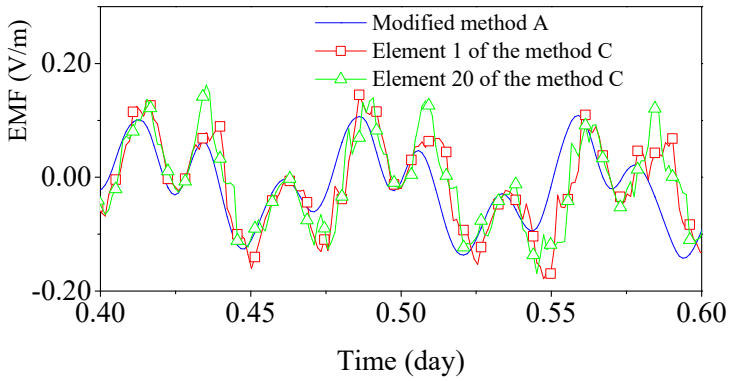

(b) Amplification image

Figure 4.41 Variation of EMF in the polar orbit.

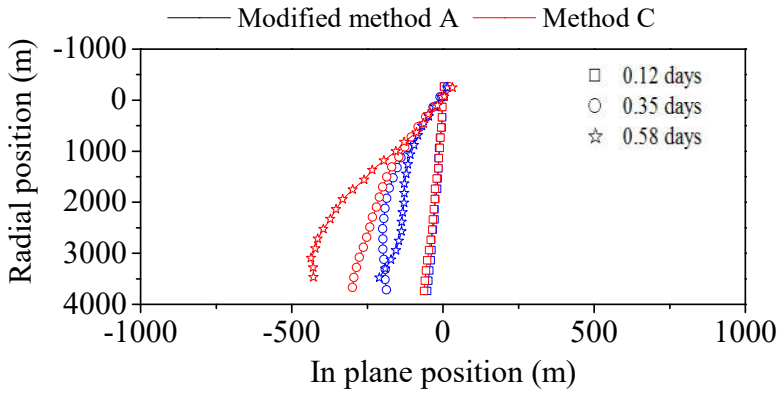

(a) In-plane motion

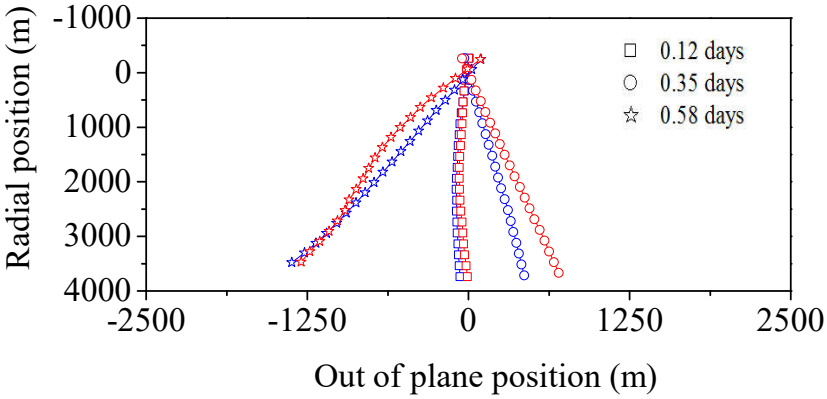

(b) Out-of-plane motion

Figure 4.42 Libration of flexible EDT in the polar orbit.

4.3 Conclusion

This Chapter presents a high-fidelity multiphysics finite element method for the dynamic analysis of bare EDT and their application in spacecraft deorbit process. First, the effect of temperature variation of EDT systems and its coupling with the dynamics of elastic tether systems are parametrically investigated. The analysis shows that the thermal effect has a significant impact on the dynamic stability of EDT systems. Second, the electron collection efficiency by a bare tether is fully coupled with elastic tether dynamics. The numerical results show the methods B and C are accurate and should be used for detailed engineering design. Finally, it presents a precise coupled multiphysics finite element method for dynamic analysis of bare EDT and their application in spacecraft deorbit. The simulation results demonstrate the coupling between the tether deformation and the electric current generation must be considered in the EDT deorbit analysis.

Chapter 5 DYNAMICS AND CONTROL OF ELECTRIC SOLAR WIND SAIL

Summary: In this chapter, the model of TSS with fixed tether length is extended, and the high-fidelity multiphysics model developed in previous chapter is applied to investigate the dynamics of coupled orbital and self-spinning motion of E-sail with the consideration of interaction between axial/transverse elastic motion of tether and Coulomb force. Then, a control strategy is applied to control attitude motion of an E-sail system.

5.1 Nodal Position Finite Element Formulation

5.1.1 Coordinate Systems

The E-sail system will be modelled by the nodal position finite element method in this chapter. Consider an E-sail as shown in Fig. 5.1, where main and auxiliary tethers are divided into finite numbers of elements. Each element is assumed as a tensile member only with zero compressive stiffness. Both main spacecraft and remote units are modeled as lumped masses without considering attitude dynamics. The motion of E-sail can be described by three generalized coordinate systems: the global heliocentric-ecliptic inertial coordinate system ($O_g X_g Y_g Z_g$), the orbital coordinate system ($O_o X_o Y_o Z_o$) and the body-fixed local coordinate system of tether element ($otnb$), as shown in Figs. 5.1 and 5.2. The origin O_g of the heliocentric-ecliptic inertial coordinate system is at the center of the Sun, where the positive X_g-axis points in the vernal equinox direction, the positive Z_g-axis is

along the normal direction of the ecliptic plane, and the positive Y_g-axis completes a right-hand coordinate system. The origin O_o of the orbital coordinate system is at the CM of the E-sail, where the positive Z_o-axis points from the Sun to the CM, the positive X_o-axis is perpendicular to the Z_g-axis and Z_o-axis, and the positive Y_o-axis completes a right-hand coordinate system. When the Z_o-axis is in parallel with the Z_g-axis, the positive X_o-axis is perpendicular to the X_g-axis and Z_o-axis instead to avoid the singularity. The local coordinate system is fixed to the element with the origin at the center of element as shown in Fig. 5.2(a). Given the *k-th* element as an example, the positive *t*-axis points from the (*k*+1)-*th* node to the *k-th* node, the positive *b*-axis perpendicular to the t-axis and the relative mean velocity of element, and the positive *n*-axis completes a right-hand coordinate system. Thus, the transformation matrix from the local coordinate to the global heliocentric-ecliptic inertial coordinate system is given as,

$$\boldsymbol{T}_{l2g}=\begin{bmatrix} \dfrac{X_k-X_{k+1}}{L_{e,k}} & \dfrac{Y_k-Y_{k+1}}{L_{e,k}} & \dfrac{Z_k-Z_{k+1}}{L_{e,k}} \\ -\dfrac{e_{t,2}e_{b,3}-e_{t,3}e_{b,2}}{\left\|\boldsymbol{e}_t\times\boldsymbol{e}_b\right\|} & -\dfrac{e_{t,3}e_{b,1}-e_{t,1}e_{b,3}}{\left\|\boldsymbol{e}_t\times\boldsymbol{e}_b\right\|} & -\dfrac{e_{t,1}e_{b,2}-e_{t,2}e_{b,1}}{\left\|\boldsymbol{e}_t\times\boldsymbol{e}_b\right\|} \\ \dfrac{e_{t,2}V_{rm,3}-e_{t,3}V_{rm,2}}{\left\|\boldsymbol{e}_t\times\boldsymbol{V}_{rm}\right\|} & \dfrac{e_{t,3}V_{rm,1}-e_{t,1}V_{rm,3}}{\left\|\boldsymbol{e}_t\times\boldsymbol{V}_{rm}\right\|} & \dfrac{e_{t,1}V_{rm,2}-e_{t,2}V_{rm,1}}{\left\|\boldsymbol{e}_t\times\boldsymbol{V}_{rm}\right\|} \end{bmatrix} \tag{5.1}$$

with

$$\boldsymbol{e}_t=\frac{X_k-X_{k+1}}{L_e}\boldsymbol{i}+\frac{Y_k-Y_{k+1}}{L_e}\boldsymbol{j}+\frac{Z_k-Z_{k+1}}{L_e}\boldsymbol{k},\ \ \boldsymbol{e}_b=\frac{\boldsymbol{e}_t\times\boldsymbol{V}_{rm}}{\left\|\boldsymbol{e}_t\times\boldsymbol{V}_{rm}\right\|},\ \ \boldsymbol{e}_n=-\frac{\boldsymbol{e}_t\times\boldsymbol{e}_b}{\left\|\boldsymbol{e}_t\times\boldsymbol{e}_b\right\|} \tag{5.2}$$

where $\left(X_k,Y_k,Z_k\right)^T$ and $\left(X_{k+1},Y_{k+1},Z_{k+1}\right)^T$ are the nodal position vectors of *k-th* element. (***i***, ***j***, and ***k***) are the unit vectors of the heliocentric-ecliptic inertial coordinate

system, $\boldsymbol{e}_t = \left(e_{t,1}, e_{t,2}, e_{t,3}\right)^T$, $\boldsymbol{e}_n = \left(e_{n,1}, e_{n,2}, e_{n,3}\right)^T$, and $\boldsymbol{e}_n = \left(e_{b,1}, e_{b,2}, e_{b,3}\right)^T$ are the unit vectors of the local element coordinate system expressed in the heliocentric-ecliptic inertial coordinate system, $\boldsymbol{V}_{rm} = \left(V_{rm,1}, V_{rm,2}, V_{rm,3}\right)^T$ is the relative mean velocity vector of *k-th* element expressed in the heliocentric-ecliptic inertial coordinate system.

The relative mean velocity is calculated

$$\boldsymbol{V}_{rm} = \frac{\boldsymbol{V}_k^{rm} + \boldsymbol{V}_{k+1}^{rm}}{2} = \frac{\left(\boldsymbol{V}_k - \boldsymbol{V}_{plasma}\right) + \left(\boldsymbol{V}_{k+1} - \boldsymbol{V}_{plasma}\right)}{2}$$

where $\boldsymbol{V}_k$ and $\boldsymbol{V}_{k+1}$ are the nodal velocity vectors of *k-th* element, $\boldsymbol{V}_{plasma}$ is the vector of solar wind plasma expressed in the heliocentric-ecliptic inertial coordinate system.

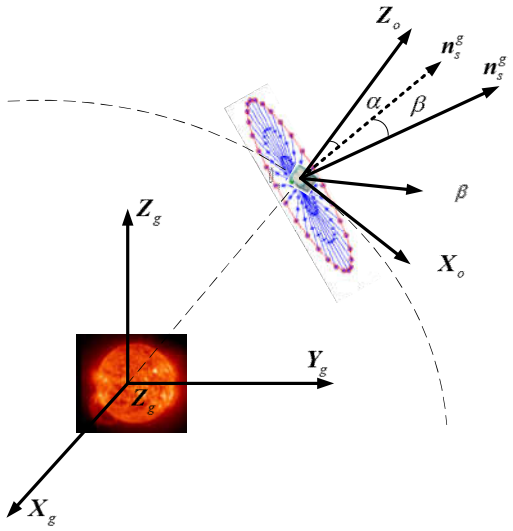

Figure 5.1 Coordinate systems for E-sail.

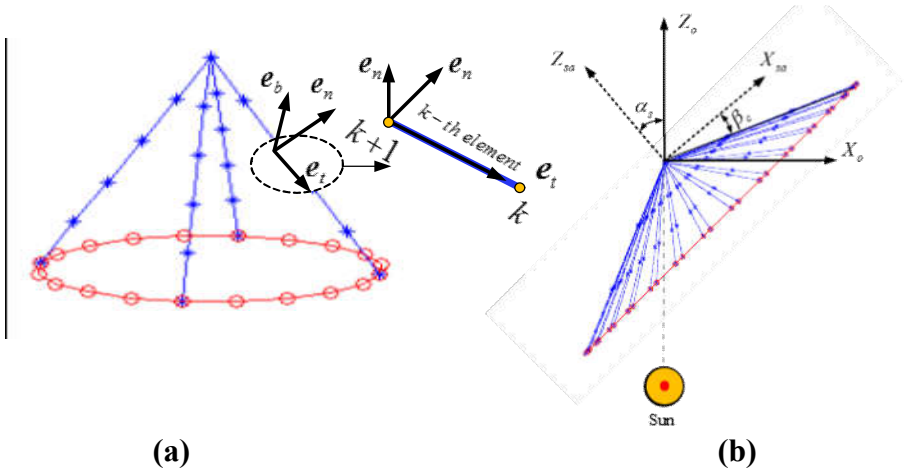

(a) **(b)**

Figure 5.2 Geometrical configuration and local element coordinate system.

5.1.2 Geometrical Configuration of E-sail

The flight orientation or attitude of E-sail can be described by two angles, such that, the sail α_s and coning β_c angles as shown in Fig. 5.2(b). Accordingly, a geometrical coordinate system $O_o X_{sa} Y_{sa} Z_{sa}$ is defined to describe the geometrical configuration of E-sail. For instance, assume the sail and coning angles are 30 deg., the number of main tethers is 10, and each main tether is 10km long. Let the main and auxiliary tethers be divided into three and two elements, respectively. The corresponding geometrical representation of E-sail in finite element mothed in the orbital coordinate system is shown in Fig. 5.3(a), the numbering of nodes and elements as well as the results of the connectivity relationship are shown in Fig. 5.3(b).

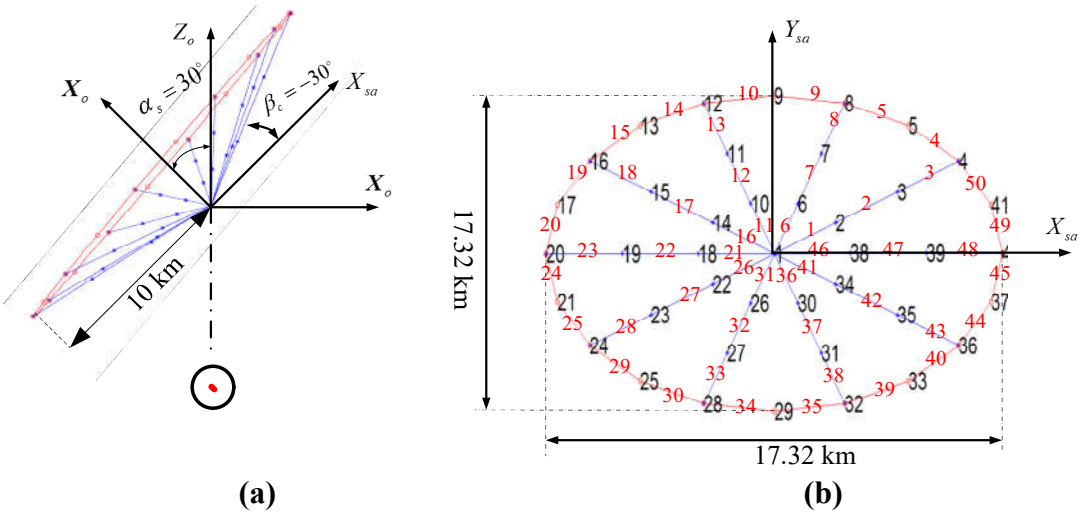

Figure 5.3 Geometrical configuration of E-sail in (a) $X_{sa}Z_{sa}$-plane, and (b) $X_{sa}Y_{sa}$-plane with node and element numbers

5.1.3 Nodal Position Coordinate Formulation

As presented in Chapter 3.1, the equation of motion of a tether element in Eq. (3.19) contains only the elastic and gravitational forces. For the E-sail system, the external forces include Coulomb force, such that,

$$\boldsymbol{M}_{a,k}\ddot{\boldsymbol{X}}_{a,k} + \boldsymbol{K}_{a,k}\boldsymbol{X}_{a,k} = \boldsymbol{F}_{e,k} + \boldsymbol{F}_{g,k} + \boldsymbol{F}_{c,k} \tag{5.3}$$

where $\boldsymbol{F}_{c,k}$ the vector of Coulomb force.

$$\boldsymbol{F}_{c,k} = \int_0^{L_{a,k}} \boldsymbol{N}^T \boldsymbol{f}_c^g dx = \frac{L_{a,k}}{2} \sum_{i=1}^{N_{GA}} w_i \boldsymbol{N}_k^T \left[\frac{L_{a,k}}{2}(1+\xi_i) \right] \boldsymbol{T}_{l2g} \boldsymbol{f}_c^l \left[\frac{L_{a,k}}{2}(1+\xi_i) \right] \tag{5.4}$$

where n_G is the order of Gauss integration ($n_G = 4$), (w_i, ζ_i) are the Gaussian integration weights and abscissae, $\boldsymbol{T}_{l2g}$ is the transformation matrix from the local coordinate system to the global inertial coordinate system, $\boldsymbol{f}_c^l$ is the Coulomb force per unit length expressed in the element local coordinate system to be listed in Eq.(5.5). The superscript

$(\ )^T$ represents the transpose matrix.

The Coulomb force per unit length in the element local frame $\boldsymbol{f}_c^l$ can be written as [13, 157],

$$\boldsymbol{f}_c^l = \frac{K_c m_p V_{sw\_nb}^2 \sqrt{n_e \varepsilon_0 T_e}}{q_e \sqrt{\exp\left[\frac{m_p V_{sw}^2}{q_e V} \ln\left(\frac{\lambda_e}{r_w}\right)\right] - 1}} \tag{5.5}$$

$$n_e = 7.2\left(\frac{r_\oplus}{r}\right)^2 + 1.95\times10^{-3}\left(\frac{r_\oplus}{r}\right)^4 + 8.1\times10^{-7}\left(\frac{r_\oplus}{r}\right)^6 \tag{5.6}$$

$$T_e = \begin{cases} 3.0\times10^5\left[1.0 + 0.55\left(\frac{r_\oplus}{r}\right)^{4/3}\right] & \text{Fast model} \\ 4.4\times10^4\left[1.0 + 1.50\left(\frac{r_\oplus}{r}\right)^{4/3}\right] & \text{Slow model} \end{cases} \tag{5.7}$$

where K_c is the constant determined by numerical simulation or experiment [13, 157]. $V_{sw,nb}$ is the component of solar wind normal to the element, m_p is the mass of proton $m_p = 1.67262\times10^{-27}$, n_e is the electron density in solar wind as listed in Eq. (5.6), ε_0 is the permittivity of vacuum $\varepsilon_0 = 8.84542\times10^{-12}$, λ_e is two times of Debye length $\lambda_e = 2\sqrt{\frac{\varepsilon_0 T_e}{n_e q_e^2}}$, and T_e is the temperature of electron in the solar wind as given in Eq. (5.7) [158], which refers to the fast and slow solar wind models, respectively.

The equation of motion of E-sail can be obtained by assembling Eq. (5.3) with the standard assembly procedure in the finite element method [53, 54].

$$\boldsymbol{M}_a\ddot{\boldsymbol{X}}_a+\boldsymbol{K}_a\boldsymbol{X}_a=\boldsymbol{F}_k+\boldsymbol{F}_g+\boldsymbol{F}_c \tag{5.8}$$

where $\boldsymbol{M}_a$ and $\boldsymbol{K}_a$ are the mass and stiffness matrices [44, 56], $\ddot{\boldsymbol{X}}_a$ and $\boldsymbol{X}_a$ are the vectors of nodal position and acceleration of E-sail, $\boldsymbol{F}_k$ is the vector of elastic force [54], $\boldsymbol{F}_g$ and $\boldsymbol{F}_c$ are the vectors of gravitational force and Coulomb drag expressed in the heliocentric-ecliptic inertial coordinate system. The masses of main spacecraft and remote unit are the lumped mass, which leads the mass matrix of E-sail is a hybrid mass matrix.

5.1.4 Attitude Motion of E-sail

As shown in Fig. 5.4, the attitude of an E-sail is described in the orbital coordinate system in terms of in-plane and out-of-plane angles of spin axis (α_{sa} and β_{sa}) or the normal vector of spin plane, such that,

$$\begin{aligned}\alpha_{sa}&=ar\tan\left(\frac{\boldsymbol{n}_{s,x}^{o}}{\boldsymbol{n}_{s,z}^{o}}\right)\\ \beta_{sa}&=ar\tan\left(\frac{\boldsymbol{n}_{s,y}^{o}}{\sqrt{\left(\boldsymbol{n}_{s,x}^{o}\right)^2+\left(\boldsymbol{n}_{s,z}^{o}\right)^2}}\right)\end{aligned} \tag{5.9}$$

where superscripts $(\ )^o$ and $(\ )^g$ represent the orbital and global heliocentric-ecliptic inertial coordinate systems respectively, $\boldsymbol{n}_s^o=\left(\boldsymbol{n}_{s,x}^o,\boldsymbol{n}_{s,y}^o,\boldsymbol{n}_{s,z}^o\right)^T=\boldsymbol{T}_{g2o}\boldsymbol{n}_s^g$ is the unit vector of spin axis or the normal vector of the spin plane, $\boldsymbol{T}_{g2o}=\boldsymbol{T}_{o2g}^T$ is the transformation matrix from the global heliocentric-ecliptic inertial coordinate system to the orbital coordinate system.

It should be mentioned that the unit vector $\boldsymbol{n}_s^g$ or $\boldsymbol{n}_s^o$ is a variable that is usually

calculated by solving the momentum equation of E-sail [45]. To simplify the calculation, we propose an alternative approach based on the geometry aspect. Assume there exists a stable spin plane after a proper spin rate is chosen. Then, the normal vector $\boldsymbol{n}_s^g$ of the spin plane can be defined,

$$\boldsymbol{n}_s^g = \frac{\boldsymbol{X}_{21}^g \times \boldsymbol{X}_{23}^g}{\left\| \boldsymbol{X}_{21}^g \times \boldsymbol{X}_{23}^g \right\|} \tag{5.10}$$

where $\boldsymbol{X}_{21}^g = \boldsymbol{X}_2^g - \boldsymbol{X}_1^g$ and $\boldsymbol{X}_{23}^g = \boldsymbol{X}_2^g - \boldsymbol{X}_3^g$. Here, $\boldsymbol{X}_j^g \left(j = 1,2,3 \right)$ are the position vectors of three remote units as shown in Fig. 5.4.

Assume the desired direction of spin axis $\boldsymbol{n}_t^b = \begin{pmatrix} 0 & 0 & 1 \end{pmatrix}^T$ is defined in the body-fixed coordinate system. Once the target in-plane and out-of-plane angles (α_{sa}^t and β_{sa}^t) are given, then the target direction of spin axis $\boldsymbol{n}_t^o$ expressed in the global coordinate system can be obtained, as

$$\boldsymbol{n}_t^g = \boldsymbol{T}_{o2g} \boldsymbol{n}_t^o = \boldsymbol{T}_{o2g} \left(\alpha_{sa}^t, \beta_{sa}^t \right) \boldsymbol{T}_{b2o} \boldsymbol{n}_t^b \tag{5.11}$$

where $\boldsymbol{T}_{o2b} \left(\alpha_{sa}^t, \beta_{sa}^t \right)$ is the transformation matrix from the orbital coordinate system to the body-fixed coordinate system with the target libration angles (α_{sa}^t and β_{sa}^t),

$$\boldsymbol{T}_{o2b} \left(\alpha_{sa}, \beta_{sa} \right) = \begin{bmatrix} \cos\alpha_{sa} & 0 & -\sin\alpha_{sa} \\ \sin\alpha_{sa}\sin\beta_{sa} & \cos\beta_{sa} & \cos\alpha_{sa}\sin\beta_{sa} \\ \sin\alpha_{sa}\cos\beta_{sa} & -\sin\beta_{sa} & \cos\alpha_{sa}\cos\beta_{sa} \end{bmatrix} \tag{5.12}$$

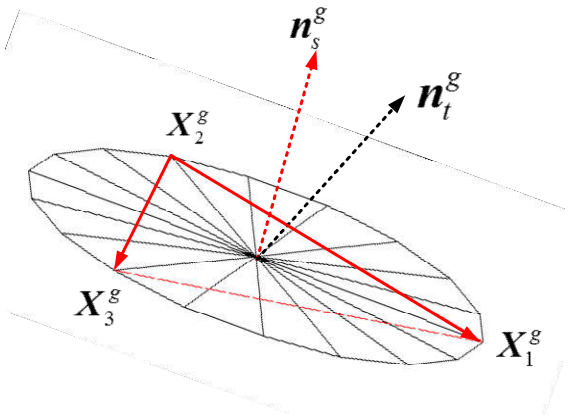

Figure 5.4 Definition of the normal direction of the spin plane.

5.1.5 Attitude Control

As mentioned in Refs. [45, 108, 114], a simple and intuitive attitude control strategy for E-sail can be achieved by modulating voltages of each main tether because the thrust is directly proportional to the applied voltage. Taking the *k-th* main tether as an example, the command for voltage modulation V_k can be determined as [45],

$$V_k = \left(f_{1,k} f_{2,k} f_{3,k} f_{4,k}\right) V_b \tag{5.13}$$

where V_b is the baseline tether voltage and ($f_{1,k}$, $f_{2,k}$, $f_{3,k}$, $f_{4,k}$) are the control factors related to the orientation of spin axis or the attitude of spin plane, change of relative ratio of spin rate ($\left|\boldsymbol{n}_s^g\right| / \left|\boldsymbol{n}_{s,or}^g\right|$), station keeping of spin axis orientation, and damping of collective oscillation of tethers. The control factors are defined as follows,

$$f_{1,k} = \max\left[0,\ \left(1 - u_1 \boldsymbol{e}_{r,k}^g \cdot \left(\boldsymbol{n}_t^g \times \boldsymbol{n}_s^g\right) / \left\|\boldsymbol{n}_t^g \times \boldsymbol{n}_s^g\right\|\right)\right] \tag{5.14}$$

$$f_{2,k} = \max\left\{c_{\min},\ \min\left[\pm u_2 \left(c_d - \left|\boldsymbol{n}_s^g\right| / \left|\boldsymbol{n}_{s,or}^g\right|\right) \boldsymbol{v}_k^g \cdot \boldsymbol{n}_{sw}^g,\ c_{\max}\right]\right\} \tag{5.15}$$

$$f_{3,k} = u_3 \frac{\sqrt{2}}{\left\| \left(\boldsymbol{n}_z^b - \boldsymbol{e}_{r,k}^b \right) / \left\| \boldsymbol{n}_z^b - \boldsymbol{e}_{r,k}^b \right\| \right\|} \tag{5.16}$$

$$f_{4,k} = 1 + \min\left(0,\ u_4 \sum_k^n \boldsymbol{v}_{k,z}^b \Big/ \sum_k^n \left| \boldsymbol{v}_k^b \right| \right) \tag{5.17}$$

where u_i $(i = 1,2,3,4)$ are the control gains, ($\boldsymbol{e}_{r,k}^g$, $\boldsymbol{e}_{r,k}^b$) and ($\boldsymbol{v}_k^g$, $\boldsymbol{v}_k^b$) are the unit vectors of position and velocity of *k-th* remote unit relative to the main spacecraft (1st node) in the global and body-fixed frames, $c_{\min}$ and $c_{\max}$ are the lower and upper bounds of relative ratio of spin rate, c_d is the desired relative ratio of spin rate, $\boldsymbol{n}_s^g$ and $\boldsymbol{n}_{s,or}^g$ are the instant and initial unit vectors of spin axes respectively, $\boldsymbol{n}_{sw}^g = \boldsymbol{T}_{o2g} \boldsymbol{n}_{sw}^o$ with $\boldsymbol{n}_{sw}^o$ being the unit vector of solar wind direction in the orbital plane frame, the minus/plus signs are for even/odd-numbered main tethers respectively.

In addition, the command for voltage modulation should be subject to upper and lower bounds due to limited capability of power supply of E-sail system,

$$V_{k,\min} \le V_k \le V_{k,\max} \tag{5.18}$$

5.2 Simulation Results and Discussion

Consider an E-sail is fully deployed and self-spinning at a given constant rate. The equations of E-sail are solved numerically by an implicit 4th order Runge-Kutta Gaussian-Legendre time integration scheme presented in Chapter 3.1 [67]. The maximum iteration number and error tolerance of each iteration step are set to 10 and 10^{-9}, respectively.

5.2.1 Steady State of E-sail

Consider an E-sail with physical parameters listed in Table 5.1. However, the equilibrium conditions, such as the equilibrium tether tension for the given spin rate, are unknown. To reduce the impact of transient response at the start of simulation due to the initial unbalance in tether tension, a special start-up procedure is developed with small numerical damping to damp out the initial transient oscillation until the steady state of spinning E-sail is obtained. The boundary condition for the special start-up procedure is shown in Fig. 5.5, where is the center of the E-sail (No. 1 node) is fixed. This boundary condition can be imposed into tether dynamics by the Lagrange multiplier method as described in Eq. (5.23). Only the centrifugal force is considered in this special procedure. The numerical damping is removed after 500s and then the simulation continued for another 5,900s. Once the steady state of spinning E-sail is obtained, the boundary condition of node 1 are released and the other external forces, such as, the gravitational and Coulomb forces are included.

The results of the steady state of spinning E-sail are shown in Fig. 5.6. As expected, the numerical damping successfully damps out the transient oscillation in the first 500s, see Fig. 5.6(a). Then, the state is kept steady in the rest of 5,900*s* as expected. The same phenomena can be observed in the tension of main and auxiliary tethers, and the angular velocity of remote units, seen in Fig. 5.6(b-c).

$$\begin{cases} \boldsymbol{M}_a\ddot{\boldsymbol{X}}_a + \boldsymbol{K}_a\boldsymbol{X}_a + \left(\dfrac{\partial \boldsymbol{C}}{\partial \boldsymbol{X}_a}\right)^T \boldsymbol{\lambda} = \boldsymbol{F}_k + \boldsymbol{F}_g + \boldsymbol{F}_c \\ \boldsymbol{C}(\boldsymbol{X}) = \boldsymbol{0} \ or\ \left(X_1 = 0, Y_1 = 0, Z_1 = 0\right) \end{cases} \tag{5.19}$$

Table 5.1 Physical properties of an E-sail.

Parameters	Values
Mass of main spacecraft (*kg*)	100.0
Mass of Remote Unit (*kg*)	1.5
Number of main tethers (auxiliary tethers)	10 (10)
Length of each main tether (*km*)	10.0
Material type of main/auxiliary tether	Aluminum/Kapton
Material density of main tether (kg/m^3)	2,700.0
Material density of auxiliary tether (kg/m^3)	1,420.0
Elastic modulus of main tether (10^9 N/m^2)	70.0
Diameter of main tether (*m*)	7.38×10^{-5}
Elastic modulus of the auxiliary tether (10^9 N/m^2)	2.5
Width of auxiliary tether (*m*)	0.03
Thickness of auxiliary tether (m)	12.7
Orbital radius of E-sail (*AU*)	1.0
Initial spin rate (*deg/s*)	0.24
Potential bias of main tether (*kV*)	15.0

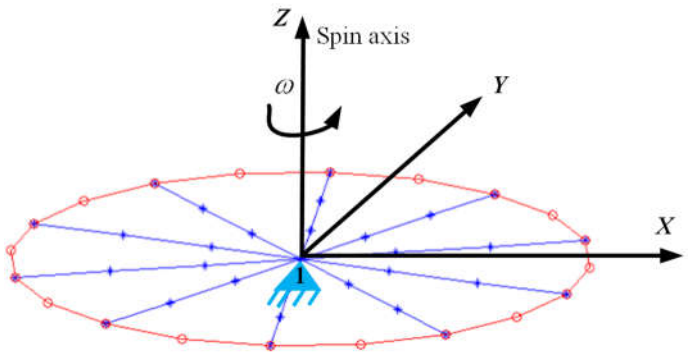

Figure 5.5 Boundary condition of a self-spinning E-sail for this start-up procedure.

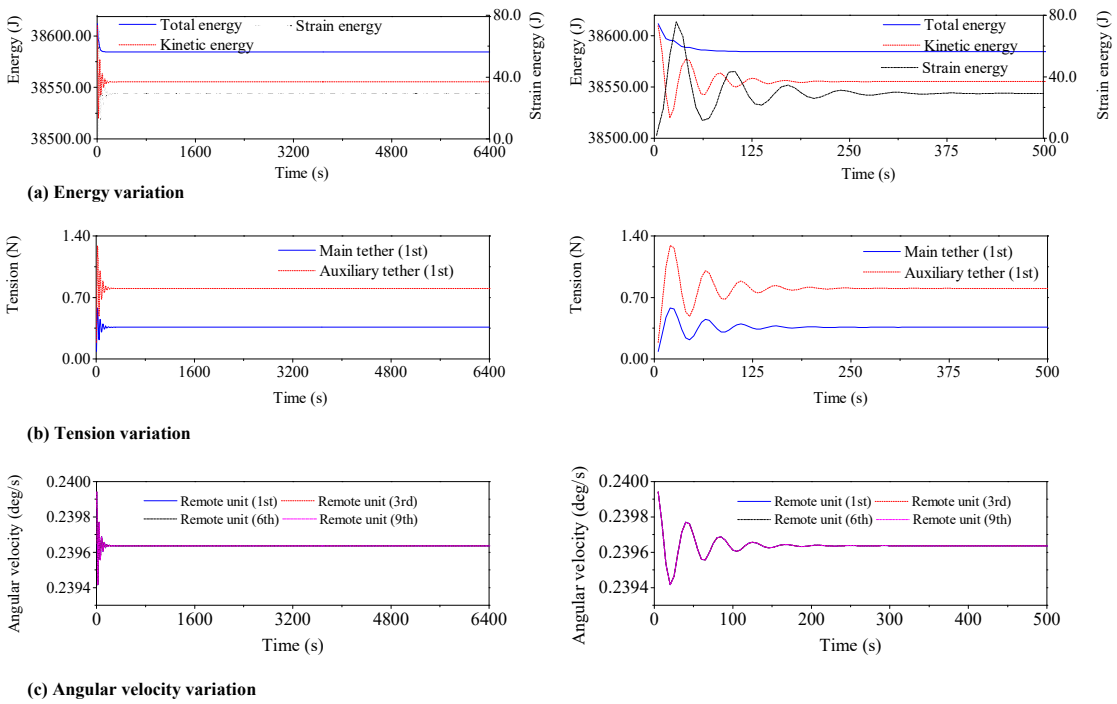

Figure 5.6 Steady state of self-spinning E-sail: (a) energy, (b) tension in main and auxiliary tethers, (c) angular velocity of remote unit.

5.2.2 Impact of Flight Orientation on Thrust

The flight orientation of E-sail is expressed by two angles, sail angle α_s and conning angle β_c. Thus, before analyzing the dynamics of E-sail under Coulomb force, it is necessary to know the variation of Coulomb force (per unit length of tether) with different sail and conning angles. Moreover, the evaluation results of previous methods are based on the spherical pendulum model, which may be not accurate enough. In this section, the impact of the flight orientation of E-sail on the thrust (Coulomb force) is investigated. The orbital radius R of a circular orbit and initial spin rate ω of E-sail are assumed as 1AU and 0.24deg/s, respectively. The initial spin axis of E-sail is aligned with the negative Y_g-axis

in the global inertial coordinate system. As shown in Eq. (5.7), there are two empirical models to evaluate the solar electron temperature T_e: the fast and slow solar wind models [138]. The slow solar wind model is used in the simulation to evaluate the Coulomb force since the slow solar wind dominates in the heliocentric-ecliptic orbital plane, where the E-sail is located. Moreover, the solar wind is assumed propagating radially from the Sun at 400 km/s [138].

The impacts of sail and coning angles on the thrust are shown in Figs. 5.7 and 5.8 with the sail and coning angles (α_s and β_c) varying from -40*deg* to 40*deg* and 0*deg* to 60*deg*, respectively. It should be mentioned that there is no thrust along the Z-axis since the E-sail is symmetric along the XZ plane in the global heliocentric-ecliptic coordinate system. Furthermore, the results of the negative sail angles have the same trend as the result of positive sail angles due to the symmetric geometry. Therefore, only the results of positive sail angle cases are plotted in Fig. 5.8.

Two conclusions can be obtained. First, the main thrust is in the *Y* component and it strongly depends on the coning angle. It decreases as the coning angle increases, even for the small sail angle cases. Second, the descend gradient of main thrust decreases as the sail angle α_s increases. Obviously, these two conclusions are different from the results in Ref. [114] derived from a simplified model.

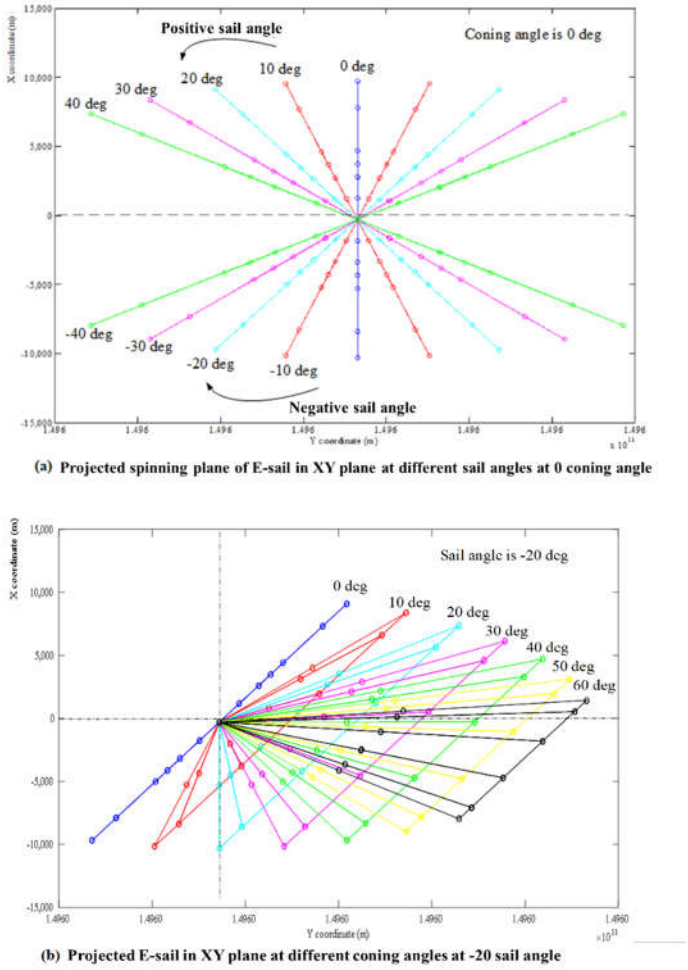

(a) Projected spinning plane of E-sail in XY plane at different sail angles at 0 coning angle

(b) Projected E-sail in XY plane at different coning angles at -20 sail angle

Figure 5.7 Projected E-sail configuration on XY plane in the inertial coordinate system with different sail and coning angles.

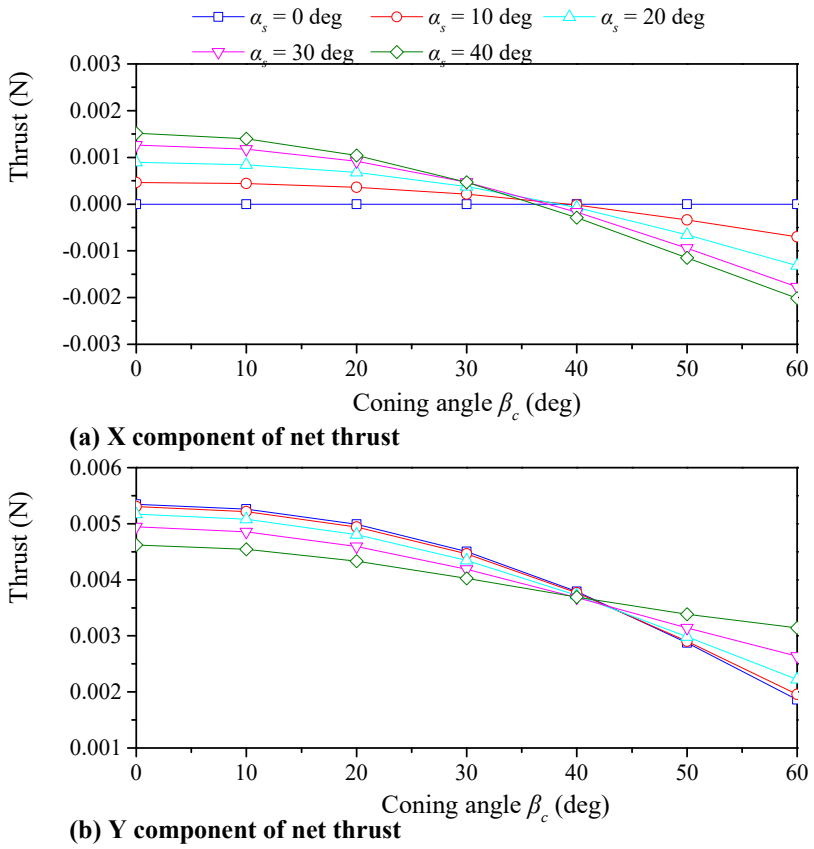

Figure 5.8 Variation of thrust of E-sail vs sail and coning angles.

5.2.3 Dynamics of E-sail without Control

In this section, the effects of the initial spin rate and sail angle α_s on the flight dynamic behavior of E-sail are investigated by flexible tether model. The gravitational and Coulomb forces are considered, and no control is applied. To include the effect of the transverse dynamics of tethers, the main and auxiliary tethers are discretized into four and one elements, respectively. The velocity of solar wind is set 400 km/s, and the CM of E-sail start at 1AU locating at the positive *Y* axis. The time step and simulation time are 0.005*s* and 259,200*s*, respectively.

First, the effect of initial spin rate on the dynamic behavior of E-sail is investigated. Three values of initial spin rate (0.12, 0.24 and 0.36) are used while the initial sail angle being 0 deg. The results are shown in Figs. 5.9-5.12. Figure 5.9(a) shows the orbital radius of CM of E-sail increases due to the radial thrust resulting from solar wind, as expected. The increase trends are the same for all given initial spin rates. The other orbital parameters also change over the time as the orbital radius increases. Moreover, as shown in Fig. 5.10, it is noticed that a higher spin rate causes a higher average tension in the main and auxiliary tethers because of the effect of centrifugal force. Figure 5.11 shows the variation of geometrical configuration of E-sail in the orbital coordinate system. It reveals that a higher spin rate is helpful to maintain the geometrical configuration of E-sail because the centrifugal term stiffens main tethers. For example, as shown in Fig. 5.12, it shows the magnitude of the displacement in the radial direction of E-sail decreases as the spin rate increases. Therefore, it can be concluded that, a higher spin rate is helpful for the structural stability of E-sail system, and the geometrical configuration has a significant impact on the magnitude of thrust.

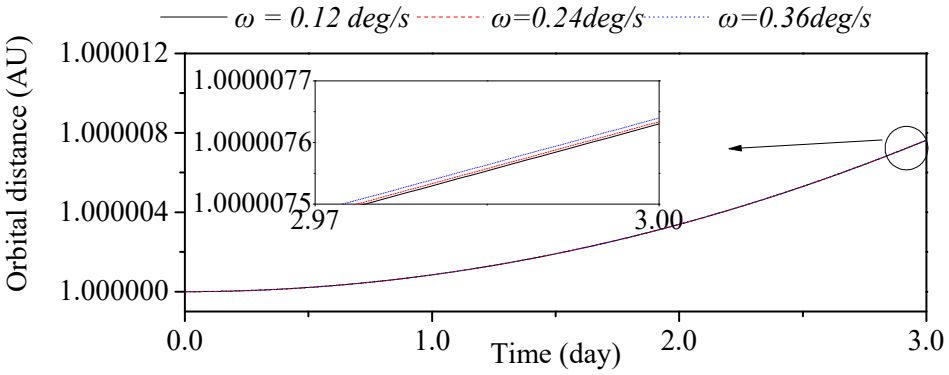

(a) Orbital radius of E-sail

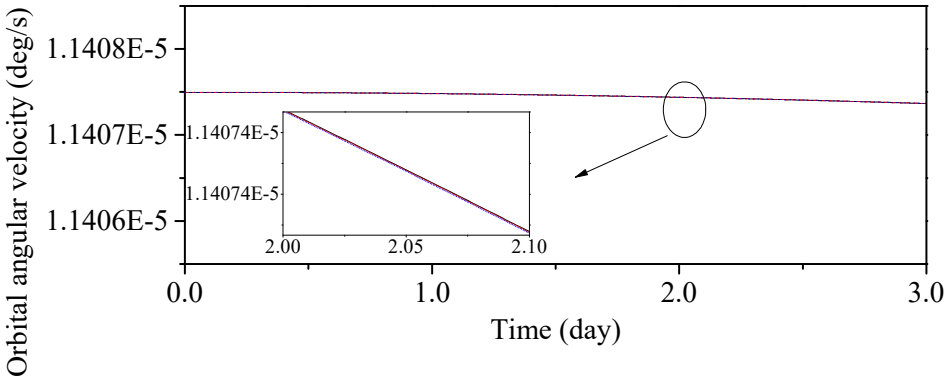

(b) Orbital angular velocity of E-sail

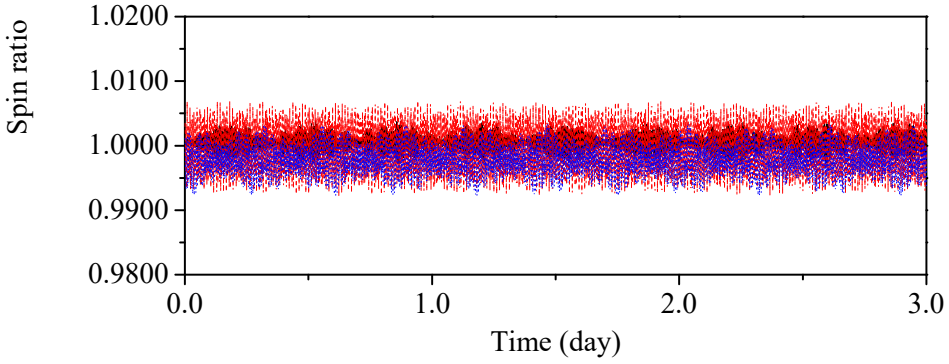

(c) Spin ratio ω/ω_o

Figure 5.9 Dynamic behaviors of E-sail with different initial spin rates.

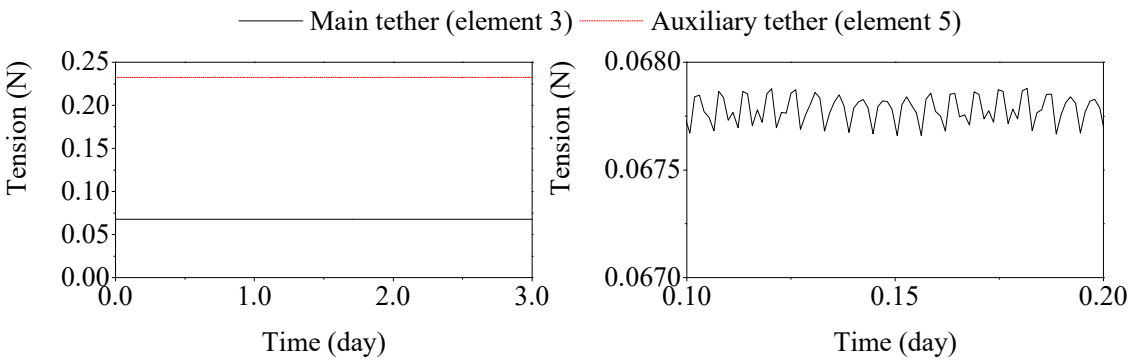

(a) Spin rate ω is 0.12 deg/s

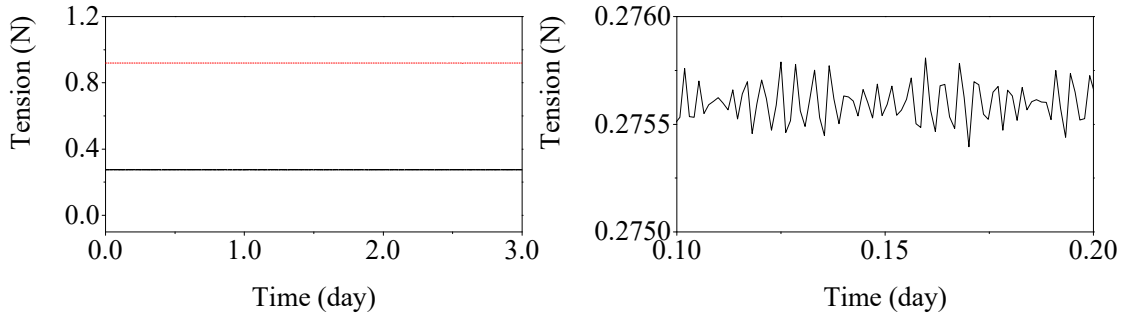

(b) Spin rate ω is 0.24 deg/s

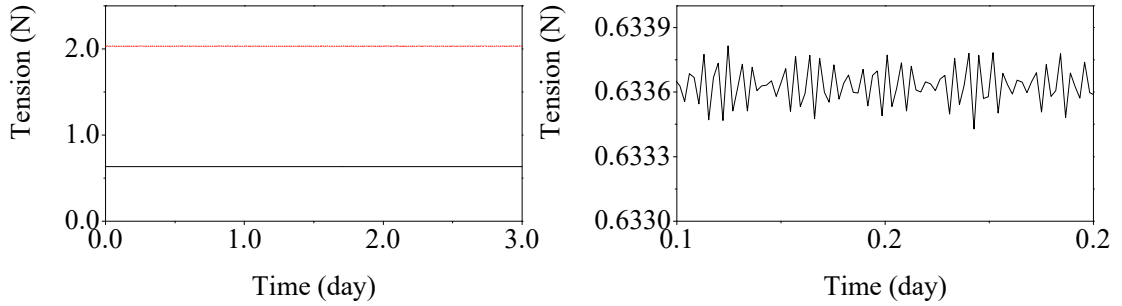

(c) Spin rate ω is 0.36 deg/s

Figure 5.10 Tensions in main and auxiliary tethers with different initial spin rates.

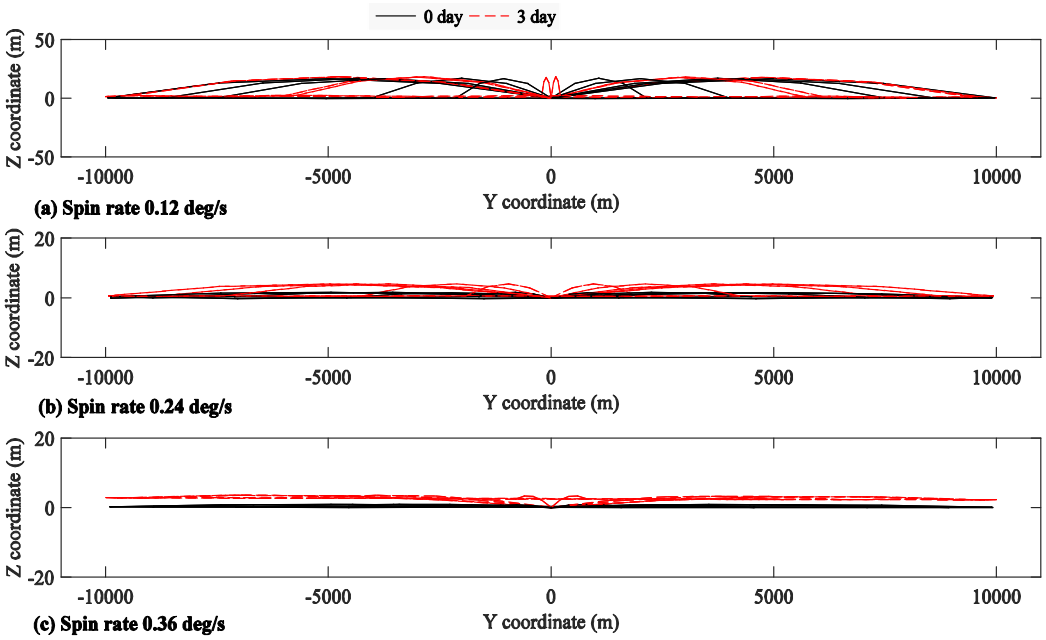

Figure 5.11 Geometrical configuration of E-sail in orbital coordinate system with different initial spin rates.

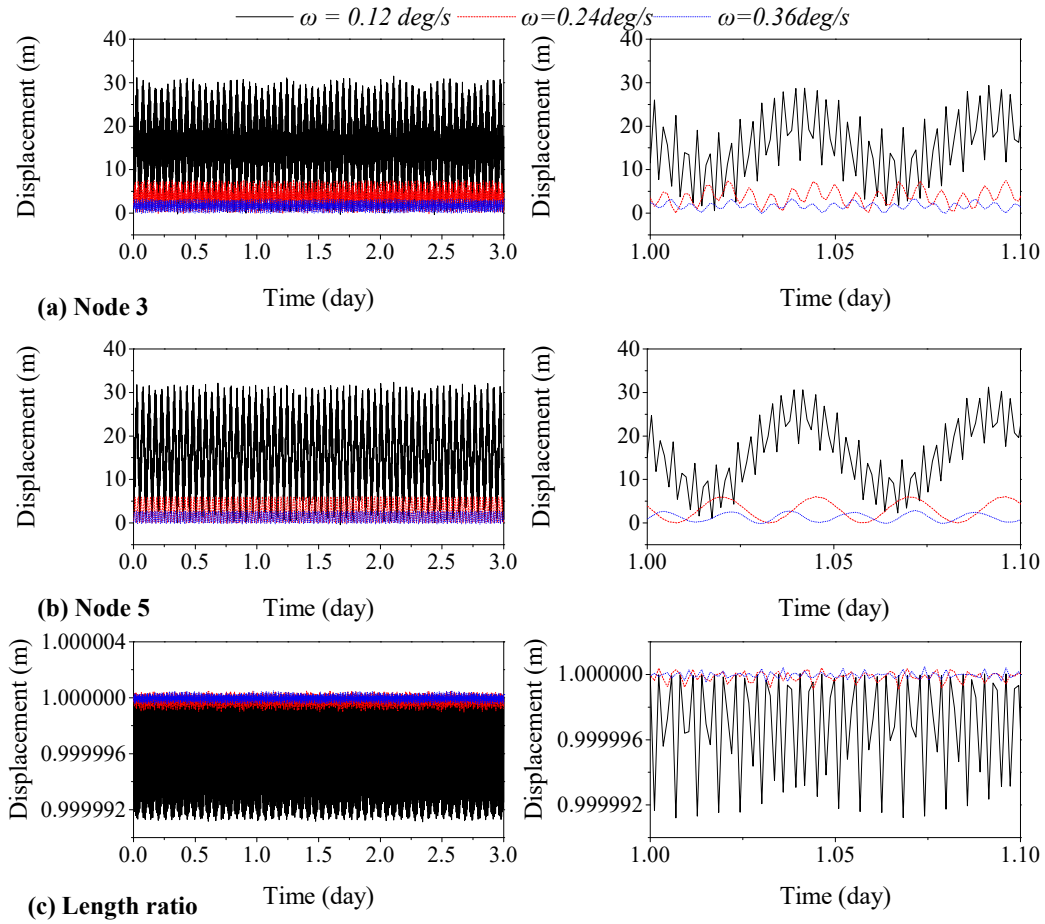

Figure 5.12 Z component of displacement of E-sail (nodes 3 and 5) and variation of length ratio of first main tether (instant length/original length).

Second, the effect of sail angle α_s on the dynamic behavior of E-sail is investigated. Three initial angles (0, 20, –20) deg are selected, while the initial spin rate is 0.24 deg/s. The results are shown in Figs. 5.13 and 5.14. Figure 5.13 shows that the initial sail angle affects the orbital distance and orbital angular velocity significantly, because the thrust strongly depends on the sail angle as shown in the section 5.2.2. The spin rate, however, is not affected very much by the initial sail angles. Thus, the geometrical

configuration of E-sail can be maintained, as shown in Fig. 5.14.

From these results, it can be concluded that the spin rate should be greater than the lower bound value to overcome the perturbed effects. Furthermore, it is noted that the difference in the orbital distance is distinct. This is because a thrust component in the sail plane is generated when the E-sail inclines to the solar wind. Therefore, the overall thrust for E-sail decreases. It indicates a suitable control strategy should be applied to adjust the attitude of E-sail to accomplish thrust vectoring for the orbital transferring.

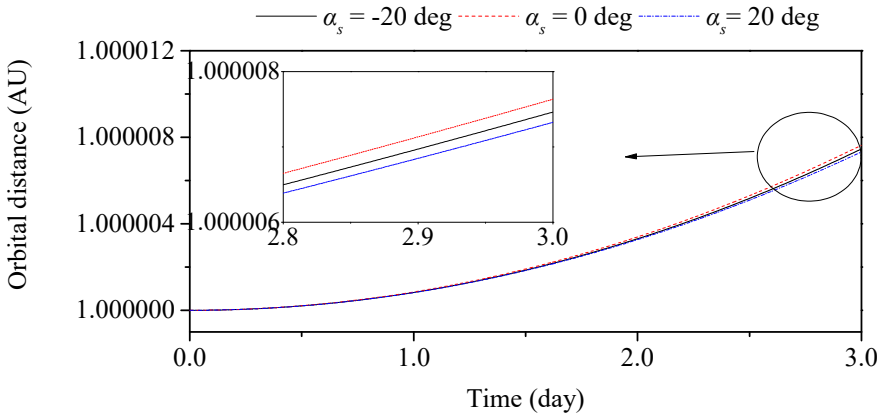

(a) Orbital radius of E-sail

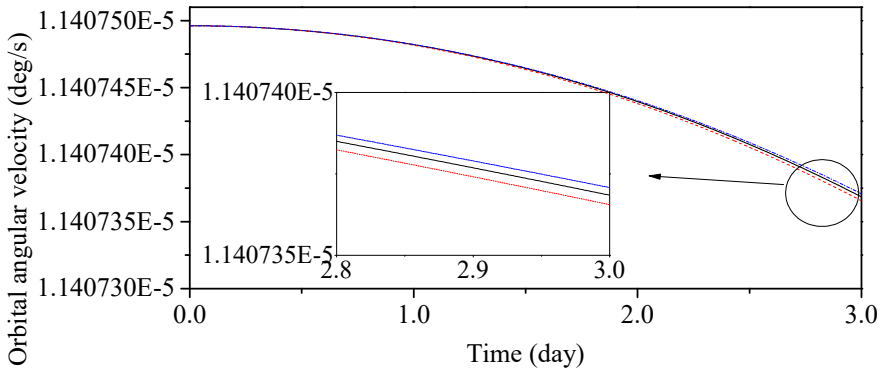

(b) Orbital angular velocity of E-sail

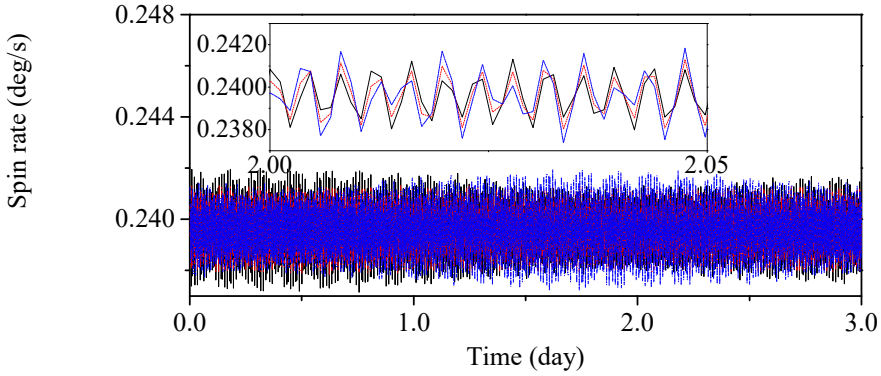

(c) Magnitude of total Spin rate

Figure 5.13 Dynamic behaviors of E-sail with different initial sail angles.

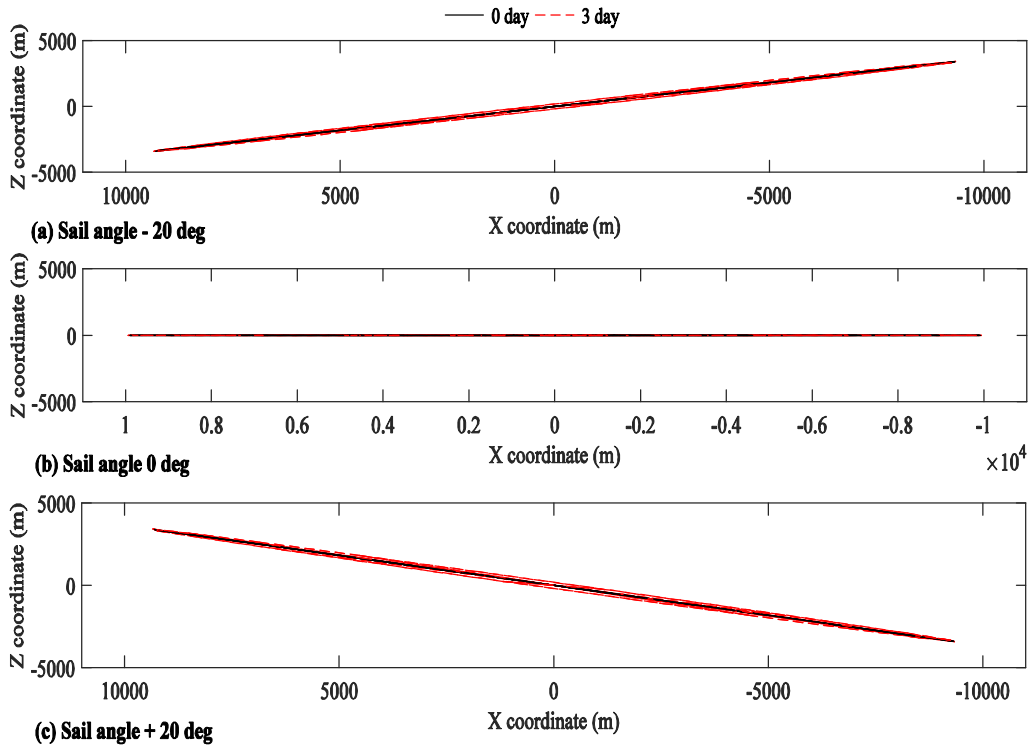

Figure 5.14 Geometrical configuration of E-sail in the orbital coordinate system with different initial sail angles.

5.2.4 Dynamics of E-sail with Attitude Control

Consider a different E-sail with physical parameters listed in Table 5.2 [139]. The parameters of proposed control law are shown in Table 5.3. In this section, the main and auxiliary tethers are modeled with four and one tether element respectively, after the trade-off analysis between the accuracy and computational cost. The time step-size is 0.01s and the simulation time is 691,200s (8 days).

Table 5.2 Physical properties of an E-sail.

Parameters	Values
Mass of main spacecraft (*kg*)	200
Number of main tethers (auxiliary tethers)	18(18)
Base voltage of charging tether(kV)	20
Minimum/Maximum voltage of charging tether(kV)	0/40
Length of main tether (*km*)	10
Material type of main tether (auxiliary tether)	Aluminum (Kapton)
Material density of main tether (kg/m^3)	2,700
Material density of auxiliary tether (*kg/m3*)	1,420
Elastic modulus of main tether ($10^9\ N/m^2$)	100
Elastic modulus of the auxiliary tether ($10^9\ N/m^2$)	2.5
Diameter of the main tether (*m*)	7.38×10^{-5}
Mass of the Remote Unit (*kg*)	1.5
The width of auxiliary tether (*m*)	0.03
The thickness of auxiliary tether (μm)	12.7
The initial orbital radius of E-sail (*AU*)	1.0
Spin rate of E-sail (*deg/s*)	0.24
The target angle expressed in the body fixed system (*deg*)	20.0

Table 5.3 The parameters of proposed controller.

Parameters	Values
The gain of spin plane orientation turning u_1	35.0
The gain of spin rate changing u_2	100.0
The gain of spin plane holding u_3	1.0
The gain of tether collective oscillation damping u_4	3.0
The target relative spin rate r_g	1.0
Lower bound of relative ratio of spin rate c_{min}	-0.5
Upper bound of relative ratio of spin rate c_{max}	0.5

5.2.4.1 Validation of Proposed Method of Orientation of Spin Axis

First, the proposed geometrical evaluation of unit vector of spin axis is verified. As presented in Section 5.1.4, the unit vector of spin axis can be obtained from the geometric perspective by calculating the normal vector of spin plane. To demonstrate the suitability

of this approximation method (called proposed method in this section), four numerical simulations are carried out for maneuvering an E-sail with 18 main tethers in two scenarios, one is the in-plane motion and the other is three-dimensional attitude motion including both the in-plane and out-of-plane motions). For the proposed method, as shown in Fig. 5.15, six candidates of triangles formed by remote units are selected to calculate the unit vector normal to the spin plane. The candidate vectors are sent to determine the attitude angles based on Eq. (5.9). The control gains of the proposed control law are listed in Table 5.3, except for the control gain u_2. Here, u_2 is set zero to observe the natural variation of spin rate in the spin plane maneuvering process. For the first scenario, the desired in-plane and out-of-plane angles (α_{sa}^{t} and β_{sa}^{t}) are set as 20 and 0 degree, respectively. For the second scenario, the α_{sa}^{t} and β_{sa}^{t} are set as 15 and 5 degree, respectively.

The results are compared with the reference method in Ref. [45], in which the spin axis is obtained by solving a differential equation. Figure 5.16 shows the comparison results of the variation of in-plane and out-of-plane angles under two scenarios, and it shows the normal vector of six candidate triangles agrees very well with the spin axis obtained by solving a differential equation of E-sail in the E-sail attitude maneuvering process. Moreover, the differences in the results of attitude angles obtained from the six candidates are extremely small and can be safely ignored. Furthermore, variations of orbital radius, radial thrust, spin rate, and tension under these two scenarios are shown in Figs. 5.17 and 5.18. It can be easily found that the results obtained by the proposed method match very well with that of the reference method. Therefore, we can conclude that the attitude

of spin axis or sail direction of E-sail can be evaluated with sufficient accuracy by simply calculating the normal vector of spin plane, alternative to solving the differential equation as Ref. [45]. For the sake of simplicity, the triangle (formed by 1st, 7th, and 14th remote units) is chosen to calculate the normal vector of spin plane in the following simulation cases in this section.

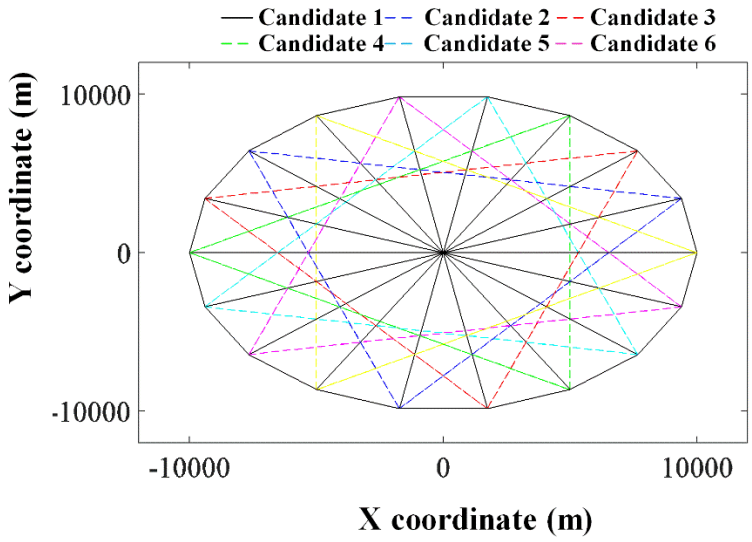

Figure 5.15 Triangle plane candidates represent spin plane of a typical E-sail.

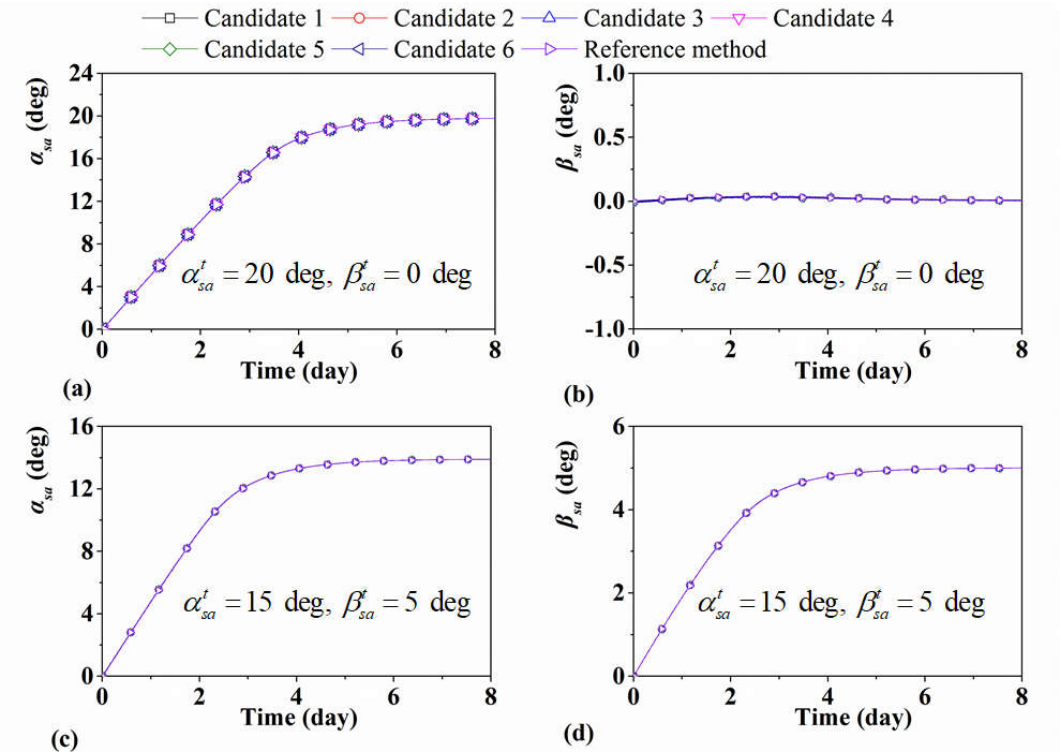

Figure 5.16 Attitude angles by the proposed (six candidate triangles) and reference methods.

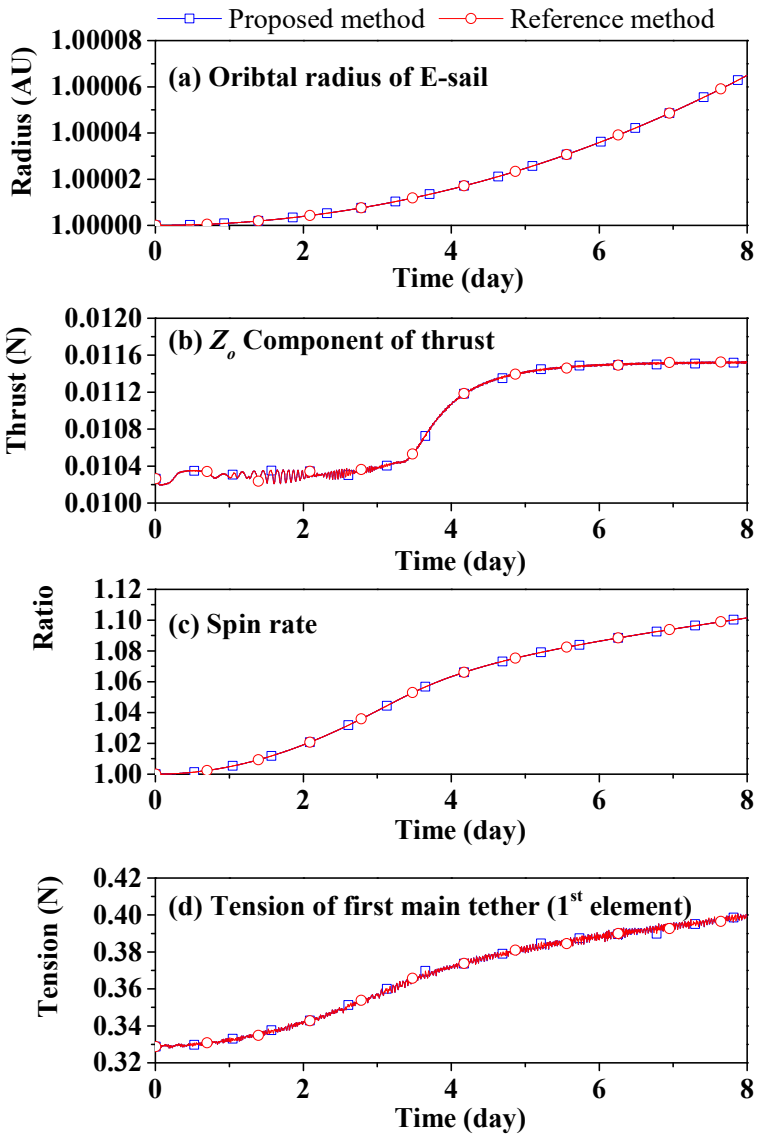

Figure 5.17 Comparison between the proposed and reference methods (α_{sa}^{t} is 20 deg, β_{sa}^{t} is 0 deg).

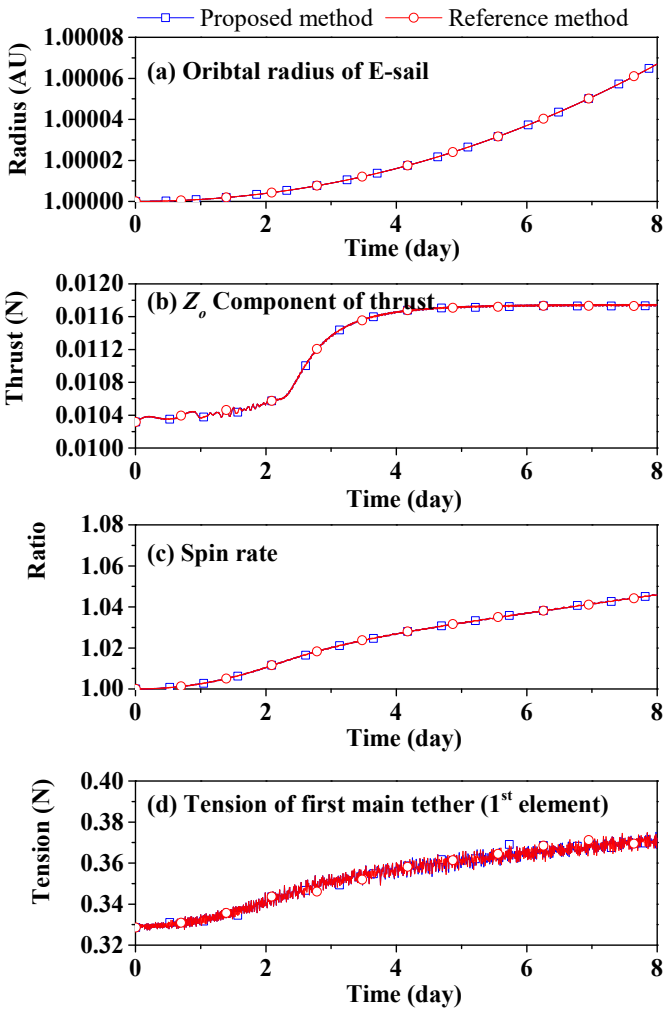

Figure 5.18 Comparison between the proposed and reference methods ((α_{sa}^{t} is 15 deg, β_{sa}^{t} is 5 deg).

5.2.4.2 Parametric Study

In this section, as listed in Table 5.4, a series of numerical simulations are carried out to investigate the influence of physical parameters of an E-sail system on its orbital and attitude dynamics. The parameters considered in this section includes the number of main tethers, the length of each main tether, the initial spin rate, and the mass of remote units,

which are important for the design of an E-sail system.

Table 5.4 Numerical simulations relate to variation of physical parameters.

Name	Main tether No.	Main tether length (*km*)	Spin rate (*rad/s*)	Remote unit mass (*kg*)
Case A	6	10	0.24	1.5
Case B	12	10	0.24	1.5
Case C	18	10	0.24	1.5
Case D	18	15	0.24	1.5
Case E	18	20	0.24	1.5
Case F	18	10	0.12	1.5
Case G	18	10	0.18	1.5
Case H	18	10	0.30	1.5
Case I	18	10	0.24	0.5
Case J	18	10	0.24	3.0

The modified throttling factor algorithm is applied to accomplish the attitude maneuver of E-sail. However, the spin rate control is not activated by setting the gain u_2 to zero to observe the variation trends of spin rate during the attitude maneuvering process. Only the in-plane attitude motion of E-sail is considered, and the α_{sa}^{t} and β_{sa}^{t} are set as 20 deg and 0 degree, respectively. As shown in Fig. 5.16(b), the out-of-plane angle β_{sa} is small and it will be not plotted in the following numerical simulation cases in this section. The influence of system parameters is examined by the following two criteria: (i) attitude maneuver time T_{at}: the time for attitude of E-sail from initial state to target state, and (ii) orbital travel distance D_{at}: the travel distance of CM of E-sail in the period of attitude maneuver.

Effect of Number of Main Tethers

A typical E-sail system may have main tethers up to 100 [139]. The influence of number

of main tethers on its dynamics is investigated in three cases, where the number of main tether changes from 6 to 18 with an increment of 6. The results are shown in Figs. 5.19-5.22 and Table 5.5. Intuitively, the more the main tethers of an E-sail the higher the thrust it generates because the radial thrust is proportional to the number of main tethers. As a result, as listed in Table 5.5, the E-sail travels more distance at a given time. This shows clearly in Fig. 5.19(a-b) in term of the orbital travel distance and radial thrust (Z_o component of thrust). For the attitude motion of E-sail, Figs. 5.20(a) and 5.21 show the variation of in-plane angle α_{sa} and geometrical configuration of E-sail expressing in the orbital frame, respectively. Obviously, there is a significant difference exists. It reveals that the more the number of main tethers, the higher the attitude maneuvering capability. For instance, as listed in Table 5.5, the attitude maneuver time T_{at} reduces from 10.6 days to 6.5 days when the number of main tethers increases from 6 to 18. Figure 5.20(b) shows the spin rate ratio (instance/initial) of E-sail, where the value of instant spin rate is obtained by the average value of angular velocity of remote units. It shows the spin rate ratio increases when the in-plane angle α_{sa} reaches the target angle α_{sa}^{t} [45, 108]. This is because a torque along the spin axis is generated when the modulation of voltage algorithm for the main tethers is used, see Fig. 5.19(e). In addition, the more the number of main tethers, the less the oscillation of tether in the out-of-spin plane direction. This can be obtained by observing the oscillation of tension around the mean value, seen in Fig. 5.20(c). Furthermore, the same phenomenon can be observed from the geometric configuration of E-sail expressed in the body coordinate system, see in Fig. 5.22. Finally, it can be

concluded that a higher number of main tethers is preferred in terms of orbital travel distance and attitude maneuver time.

Table 5.5 The results of parametric study.

Name	Case A	Case B	Case C	
T_{at} (day)	11.6	8.4	6.5	
D_{at} (AU)	2.28×10^{-5}	4.44×10^{-5}	6.49×10^{-5}	
Name	Case C	Case D	Case E	
T_t (day)	6.5	8.2	9.6	
D_{at} (AU)	6.49×10^{-5}	8.95×10^{-5}	11.10×10^{-5}	
Name)	Case F	Case G	Case C	Case H
T_t (day)	3.8	5.8	6.5	9.0
D_{at} (AU)	6.77×10^{-5}	6.62×10^{-5}	6.49×10^{-5}	6.38×10^{-5}
Name	Case I	Case C	Case J	
T_t (day)	5.4	6.5	11.2	
D_{at} (AU)	7.14×10^{-5}	6.49×10^{-5}	5.74×10^{-5}	

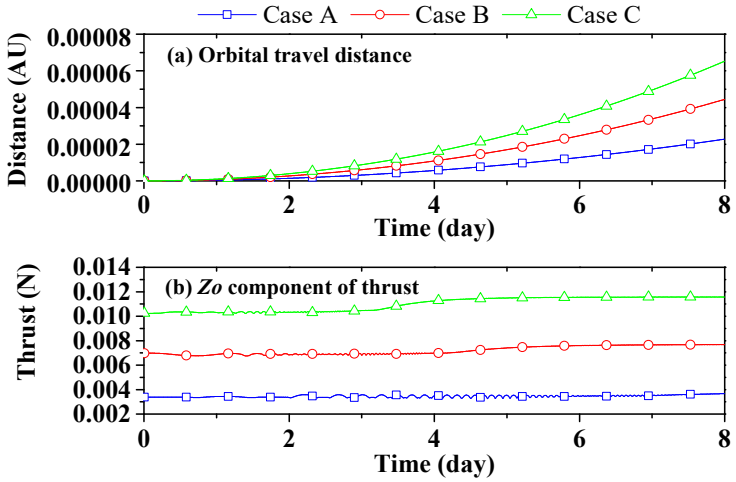

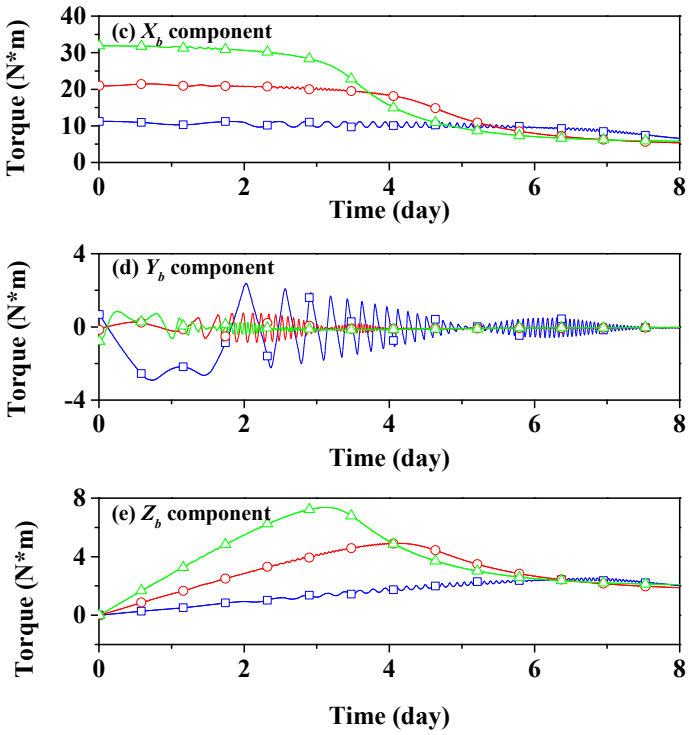

Figure 5.19 Influence of main tether number on travel distance, thrust, and torque.

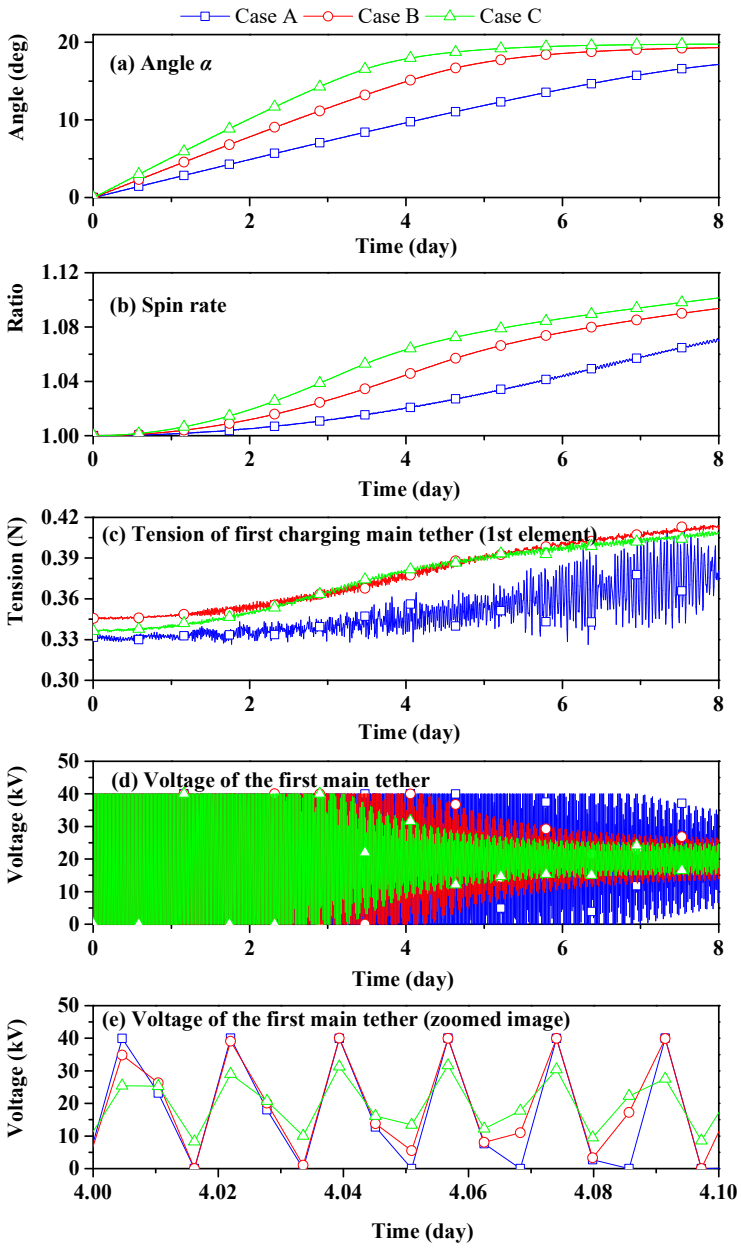

Figure 5.20 Influence of main tether number on dynamic response of E-sail.

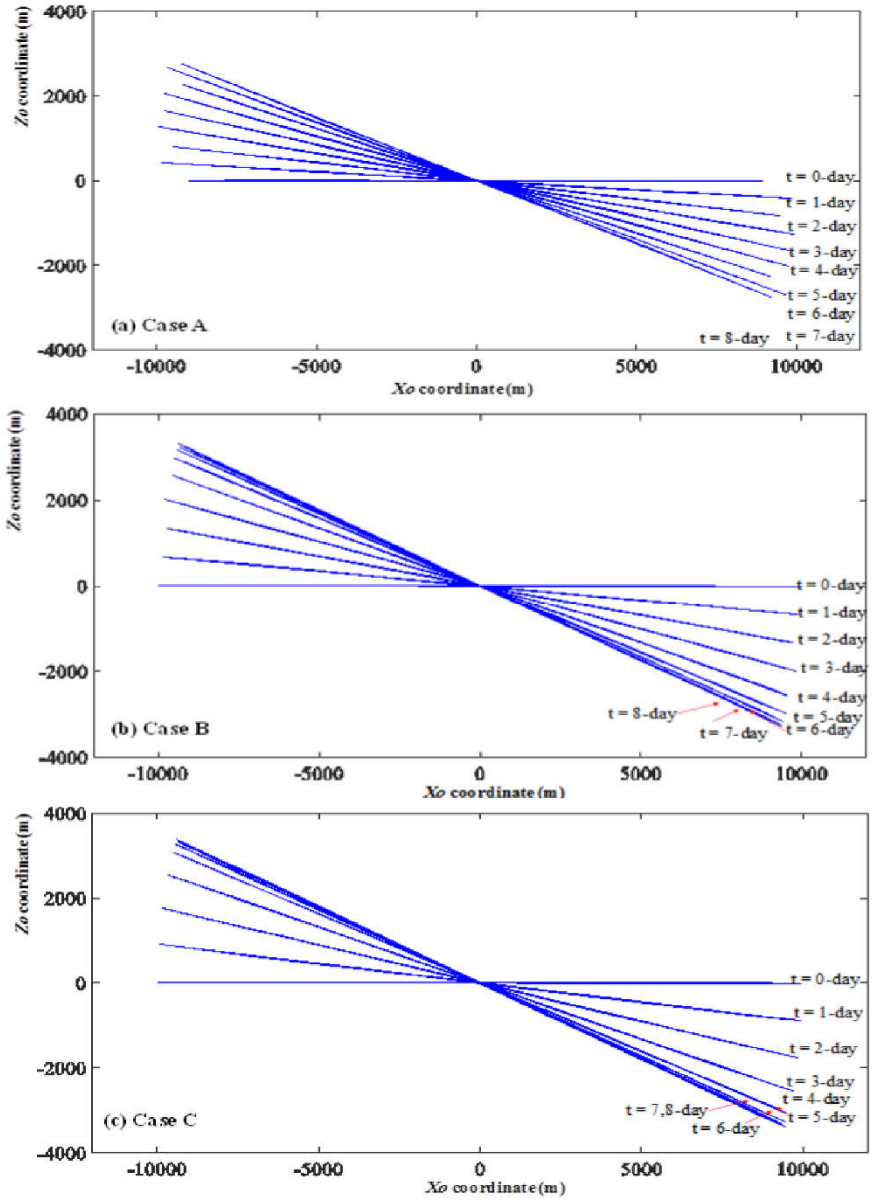

Figure 5.21 Influence of main tether number on attitude motion of E-sail.

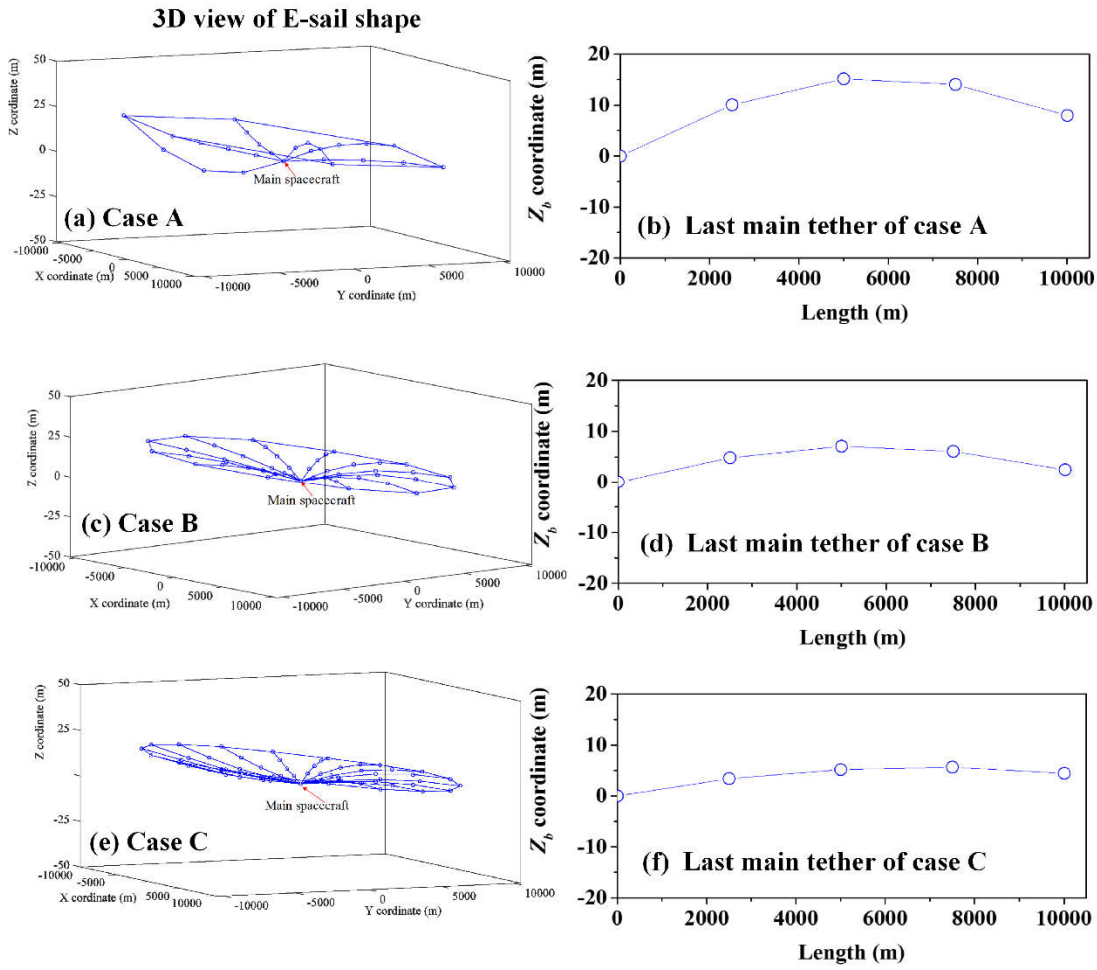

Figure 5.22 Influence of main tether number on geometrical configuration of E-sail expressing in the body coordinate system (4-day).

Effect of Length of Main Tether

Let the length of each main tether vary from 10 km to 20 km with increment of 5 km [45, 139]. The results are shown in Figs. 5.23-5.26 and Table 5.5. As shown in Fig. 5.23(a), it can be easily found that the longer the length of main tether is, the more distance the E-sail travels. This is because the thrust is proportional to the length of main tether, see in Fig. 5.23(b). For the attitude motion of E-sail, as shown in Figs. 5.24(a) and 5.25, the attitude

maneuver time T_{at} increases as the length of main tether increases. For example, T_{at} increases from 5.6 days to 9.6 days when the length of main tether increases from 10km to 20km. Two reasons can be attributed: (i) the inertia of E-sail increases for longer main tethers; (ii) the applied voltage of tether is bounded due to its limited power source of main spacecraft. It shows that the longer the main tether, the less capability of attitude maneuvering the E-sail has when the applied voltage is bounded. In addition, as shown in Fig. 5.24(c), the longer the main tether is, the higher the tether tension it is. As a result, the oscillation of tether still in the same level even when the length of main tether is doubled with the same spin rate, see in Fig. 5.26. The same phenomenon of increase of spin rate ratio (instance value/initial value) can be observed in the attitude maneuver process, see in Fig. 5.24 (b). Therefore, longer main tethers are preferred for a higher level of thrust. However, shorter main tethers are preferred from the attitude-maneuvering viewpoint when the capability of modulation of voltage is limited.

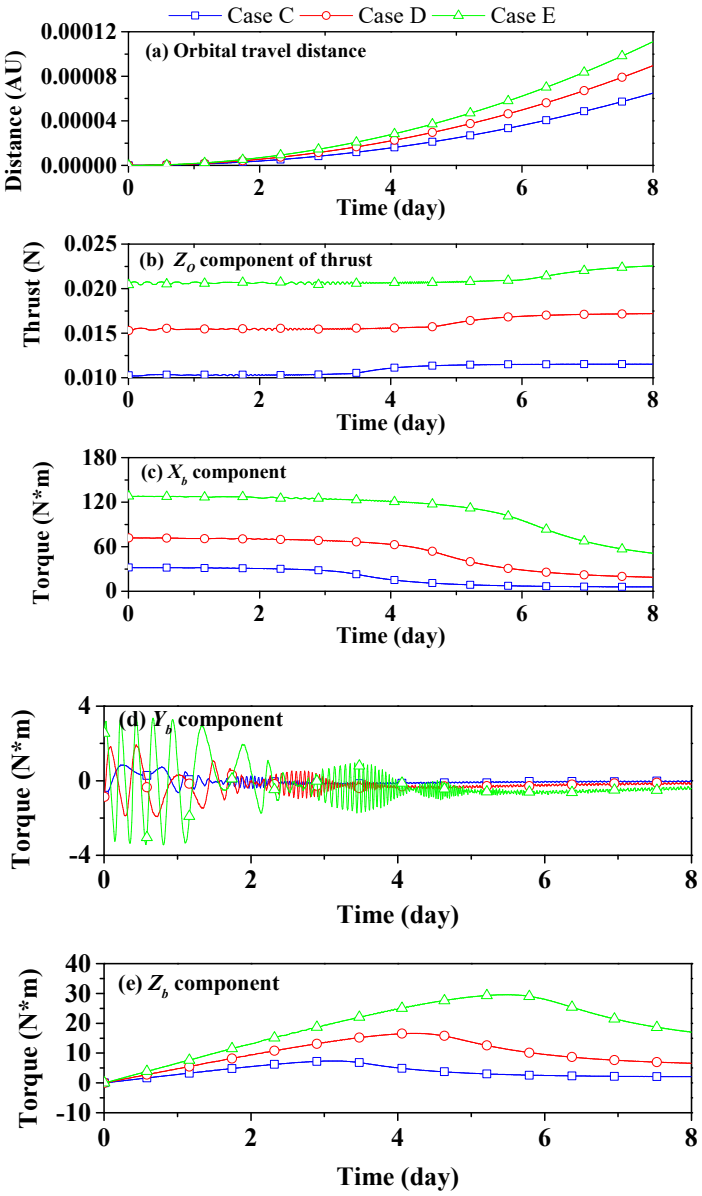

Figure 5.23 Influence of main tether length on travel distance, thrust, and torque.

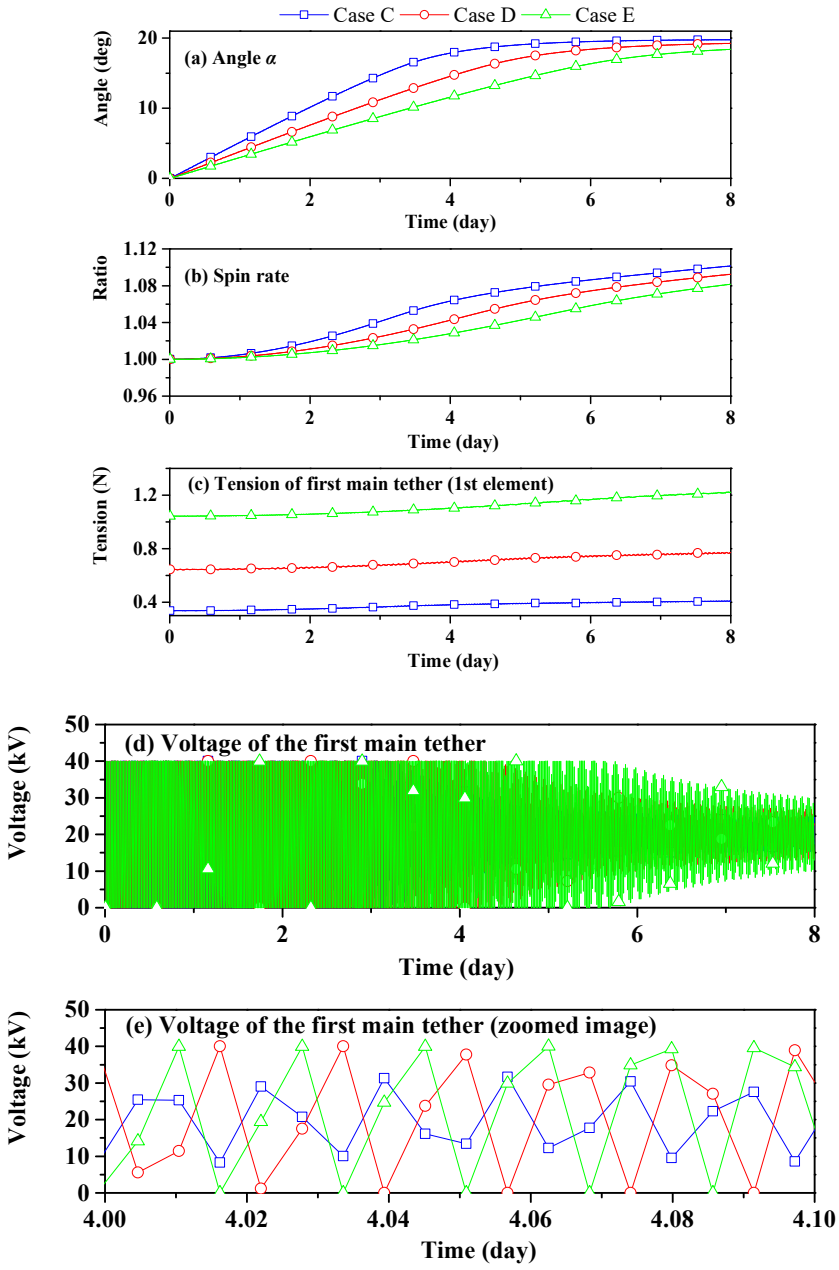

Figure 5.24 Influence of main tether length on dynamic response of E-sail.

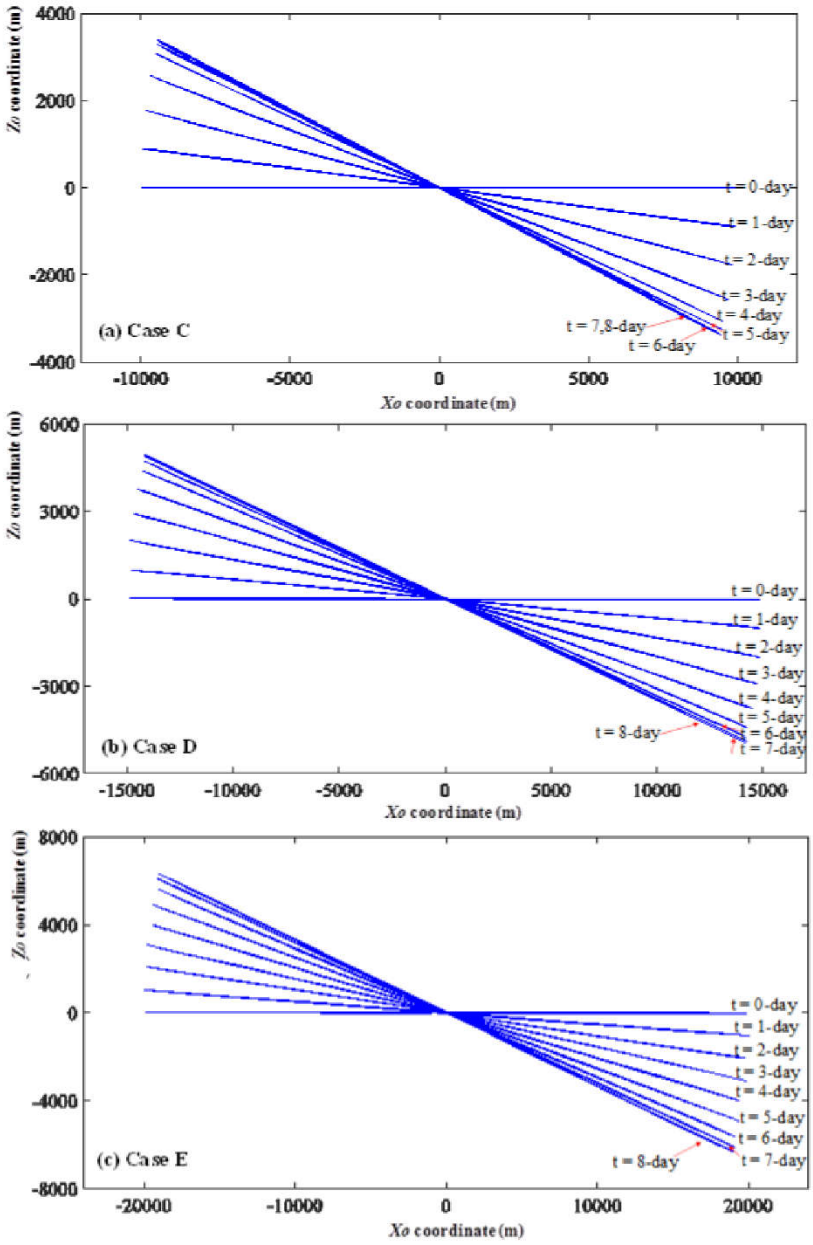

Figure 5.25 Influence of main tether length on attitude motion of E-sail.

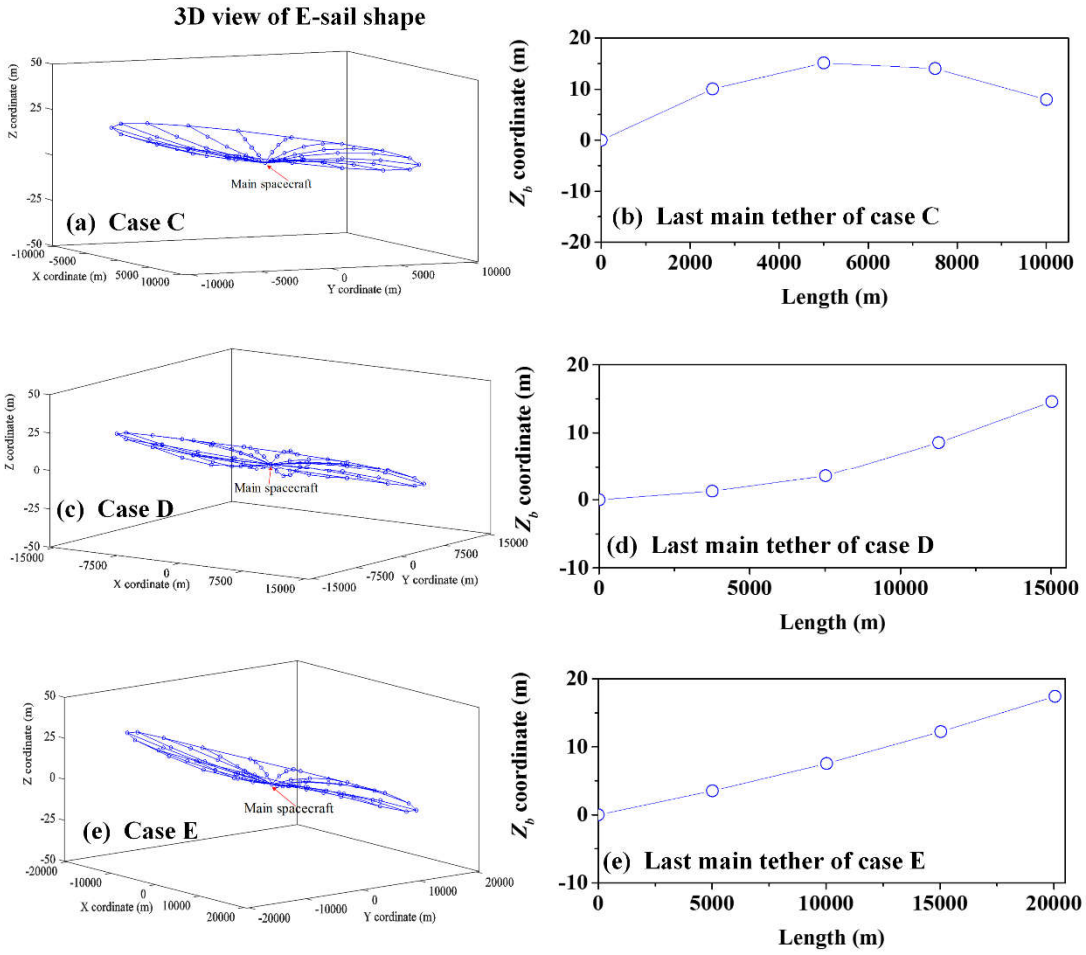

Figure 5.26 Influence of main tether length on geometrical configuration of E-sail expressing in the body coordinate system (4-day).

Effect of Initial Spin Rate

To avoid the tether broken by the centrifugal force, the spin rate of E-sail system is carefully designed not to exceed certain limit [116, 140]. As listed in Table 5.4, four numerical cases are carried out to investigate the initial spin rate influence on its dynamics. As shown in Fig. 5.27(a-b), it is found that the initial spin rate has trivial impact on the orbital travel distance because the thrusts are at the same level for the given spin rates.

However, the initial spin rate has a significant impact on the attitude maneuvering capability, see in Fig. 5.28(a) and Fig. 5.29. It reveals that the higher the spin rate is, the less capable the attitude maneuvering it is. For example, as listed in Table 5.5, the attitude maneuvering time T_{at} of the case *H* is 2.4 times than the results of case *F*. There are two reasons can be attributed, (i) the momentum of E-sail increases as the spin rate increases (ii). the voltage on main tether is limited by the pre-defined bounds. In addition, as shown in Fig. 5.30, it can be found that a high spin rate is beneficial for the suppress of the oscillation of tether in the out-of-spin plane direction. For example, the bending profile of main tether decreases as the spin rate increases, which results in higher tension in tether due the increase of centrifugal force. Therefore, a suitable medium spin rate is preferred.

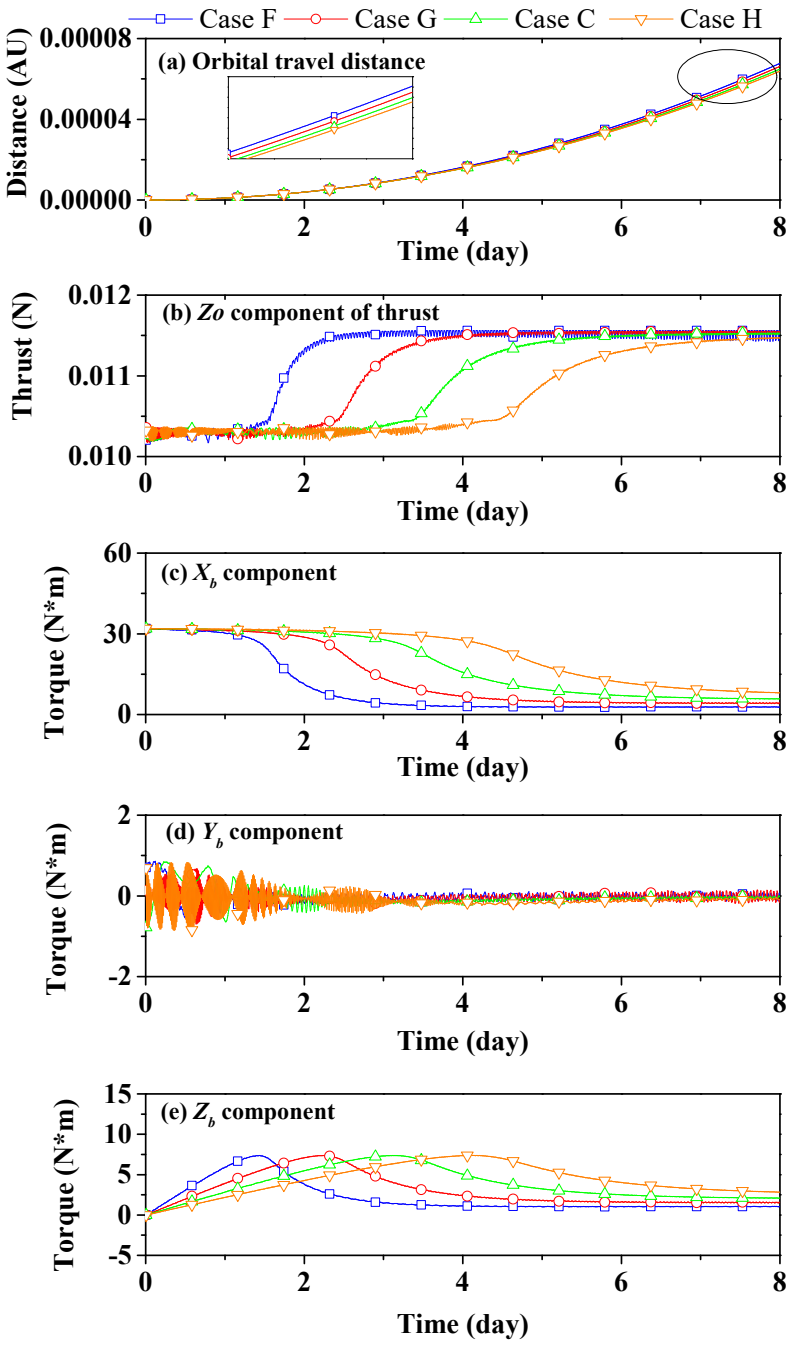

Figure 5.27 Influence of initial spin rate on travel distance, thrust, and torque.

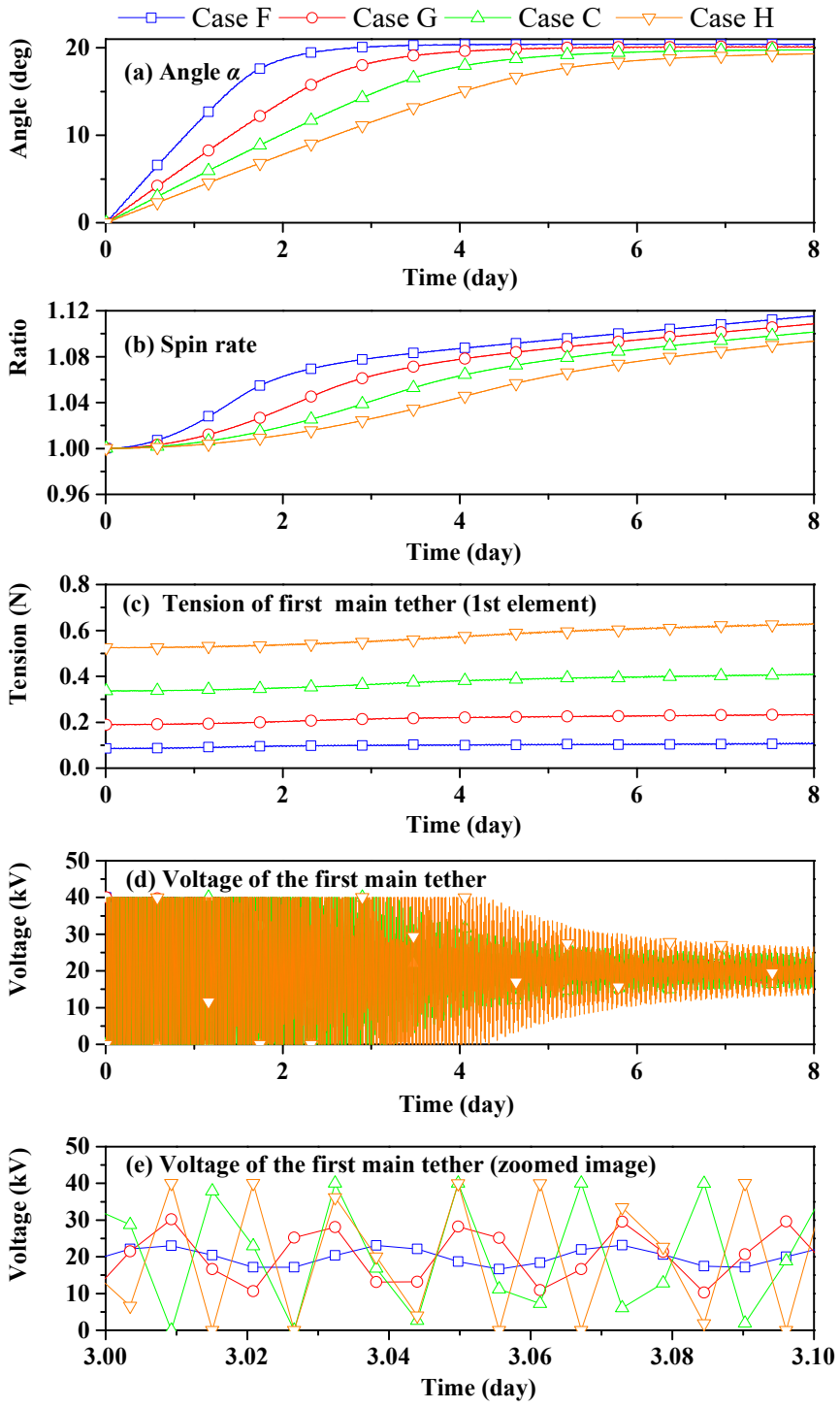

Figure 5.28 Influence of initial spin rate on dynamic response of E-sail.

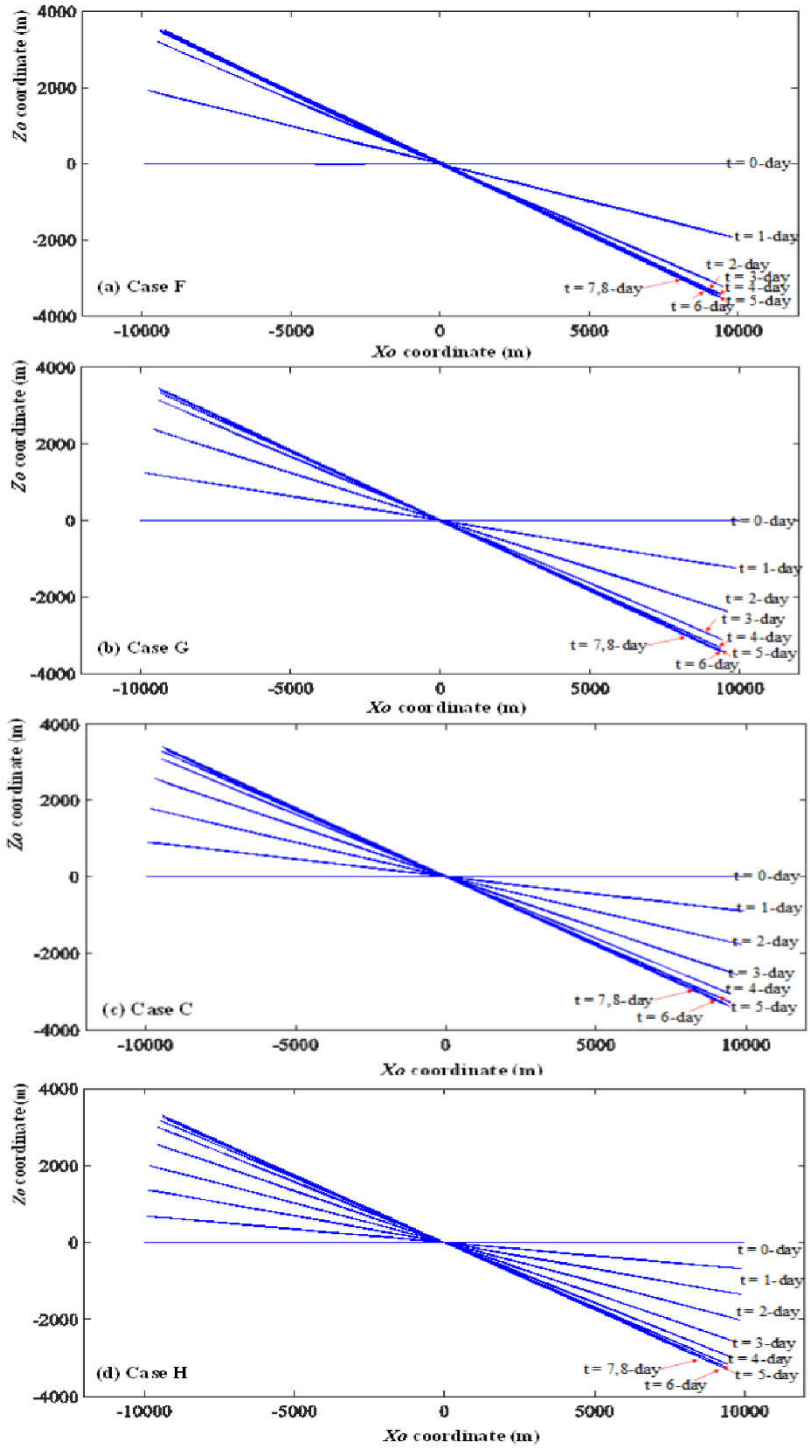

Figure 5.29 Influence of initial spin rate on attitude motion of E-sail.

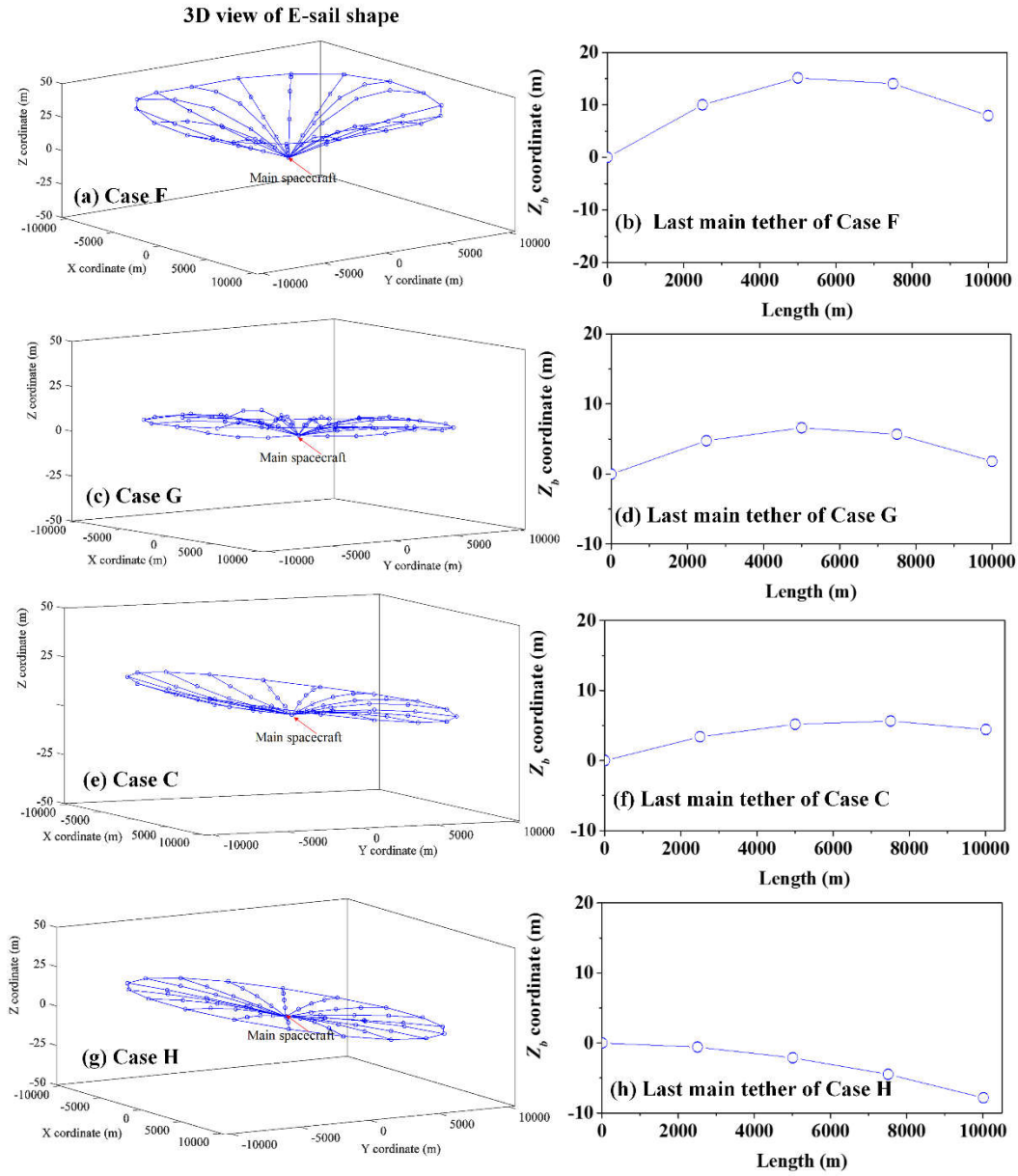

Figure 5.30 Influence of initial spin rate on geometrical configuration of E-sail expressing in the body coordinate system (4-day).

Effect of Mass of Remote Unit

The remote unit is the host platform for the reels and low thrusters for deploying the tether

and controlling the spin rate of tether's rig [139]. As listed in Table 5.4, three numerical cases are carried out to investigate the influence of the mass of remote unit on the dynamics of E-sail. As shown in Fig. 5.31(a), it can be found that there is a slight difference in the orbital travel distance. This is caused by the difference in the total mass of E-sail while the thrusts are in the same level, see Fig. 5.31(b). However, as shown in Figs. 5.32(a) and 5.33, the smaller the mass of remote unit is, the higher the attitude maneuvering capability it is. For example, as listed in Table 5.5, the attitude maneuvering time T_{at} of the case J is 2.1 times than the result of case I. The reasons are two folds, (i) the inertia of E-sail increase with the mass of remote unit (ii) there is an upper bound for the applied voltage due to the system's power supply capacity, see in Figs. 5.32(d)-(e). In addition, as shown in Fig. 5.32(c), the tension increases with the mass of remote unit, which is helpful for suppressing the oscillation of main tether in the out-of-spin plane direction during the E-sail attitude maneuver process. For example, Fig. 5.34 shows the Z_b coordinate of E-sail decreases as the mass of remote unit increases. It reveals a larger mass of remote unit is helpful for holding the spin plane.

Finally, three conclusions can be obtained through this parametric study. First, the attitude maneuvering capability of E-sail is restricted due to the power limitation of main spacecraft. Second, the spin rate increases when the attitude of E-sail maneuvers from initial angle to the target angle. Third, both the maneuvering capability and the orbital travel distance increase significantly as the number of main tethers increases. Conversely, they decrease as the initial spin rate and the mass of remote unit increases. The maneuvering capability decreases while the orbital radius increases when the length of

main tether increases.

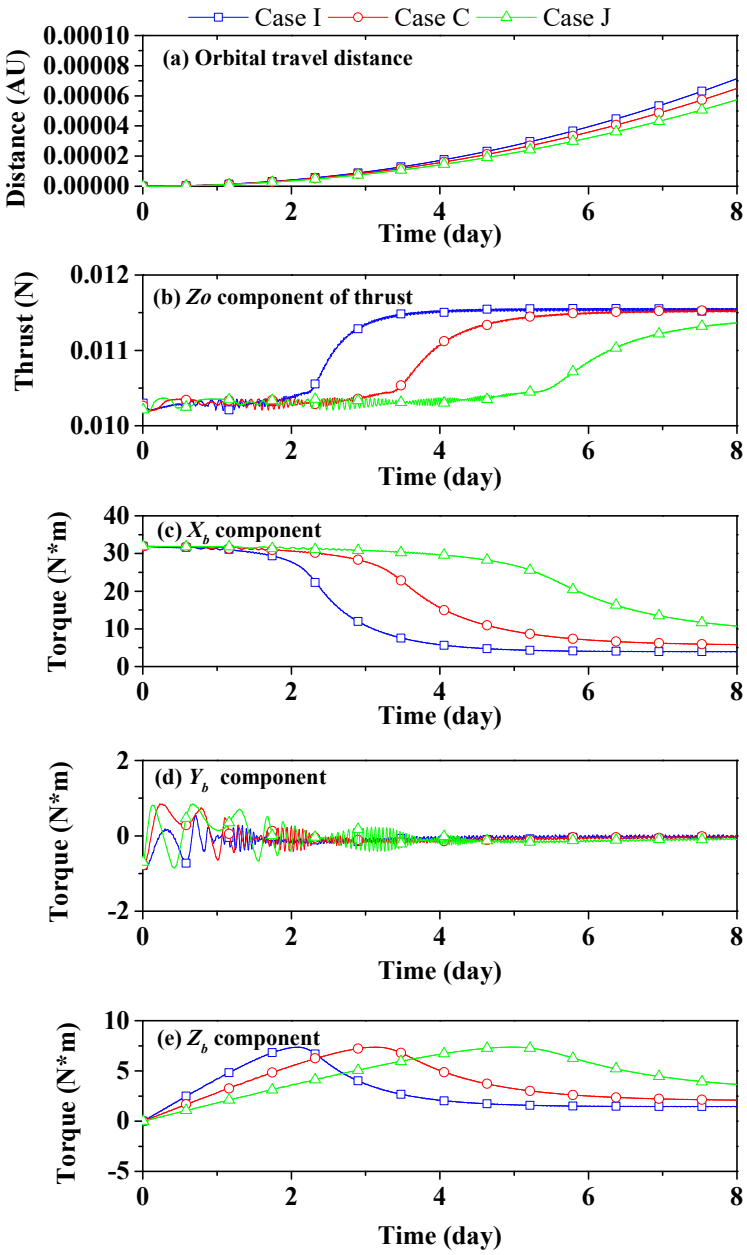

Figure 5.31 Influence of remote unit on movement of E-sail, thrust, and torque.

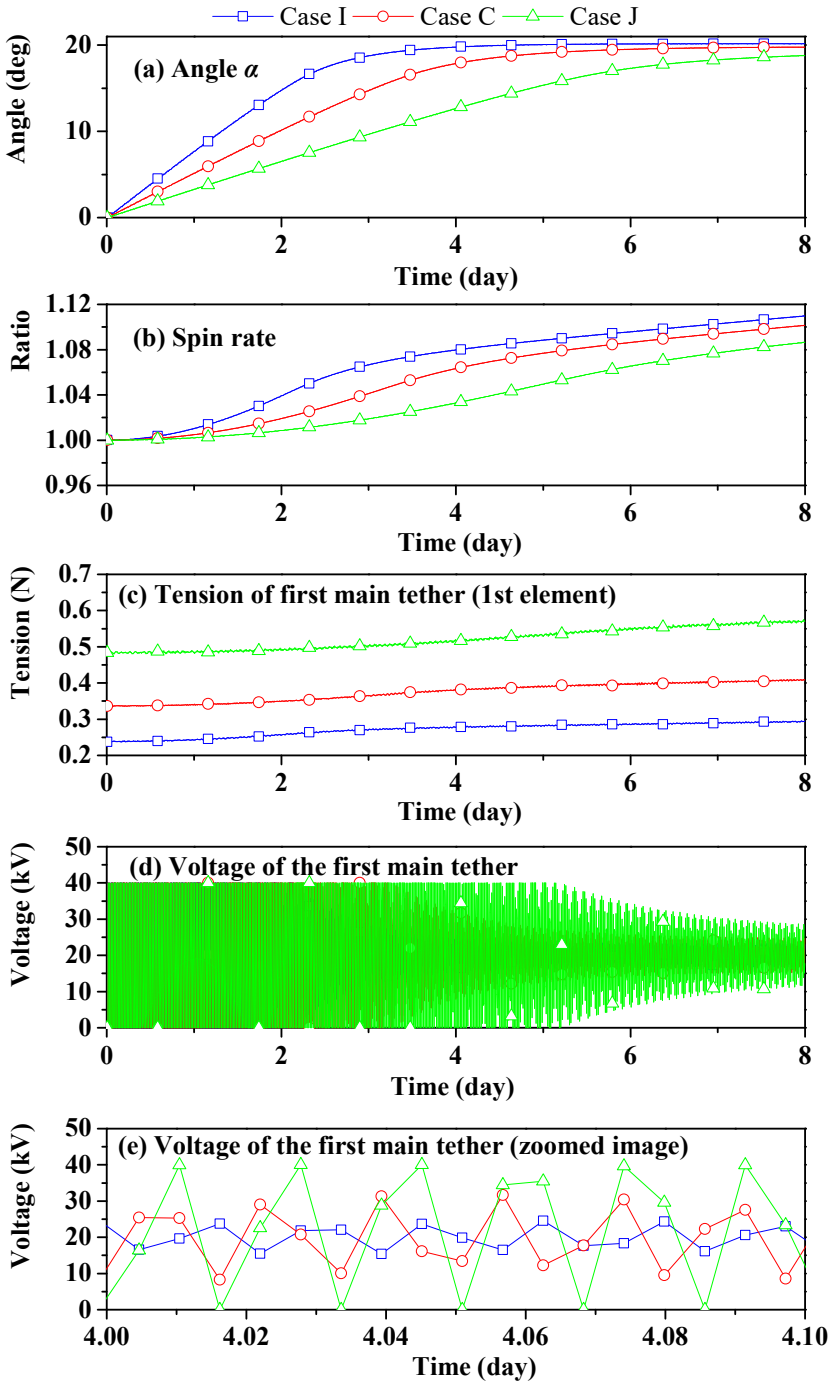

Figure 5.32 Influence of remote unit on dynamic response of E-sail.

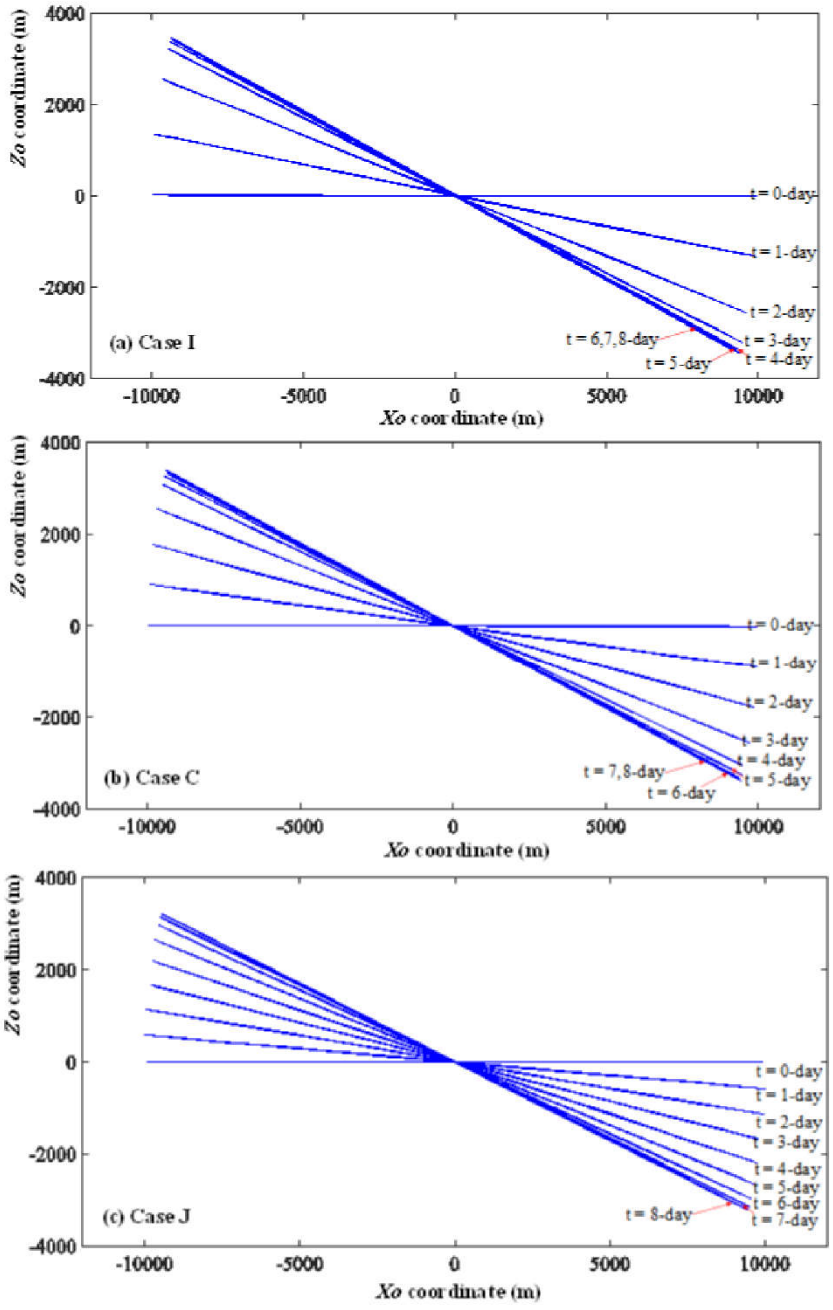

Figure 5.33 Influence of remote unit on attitude motion of E-sail.

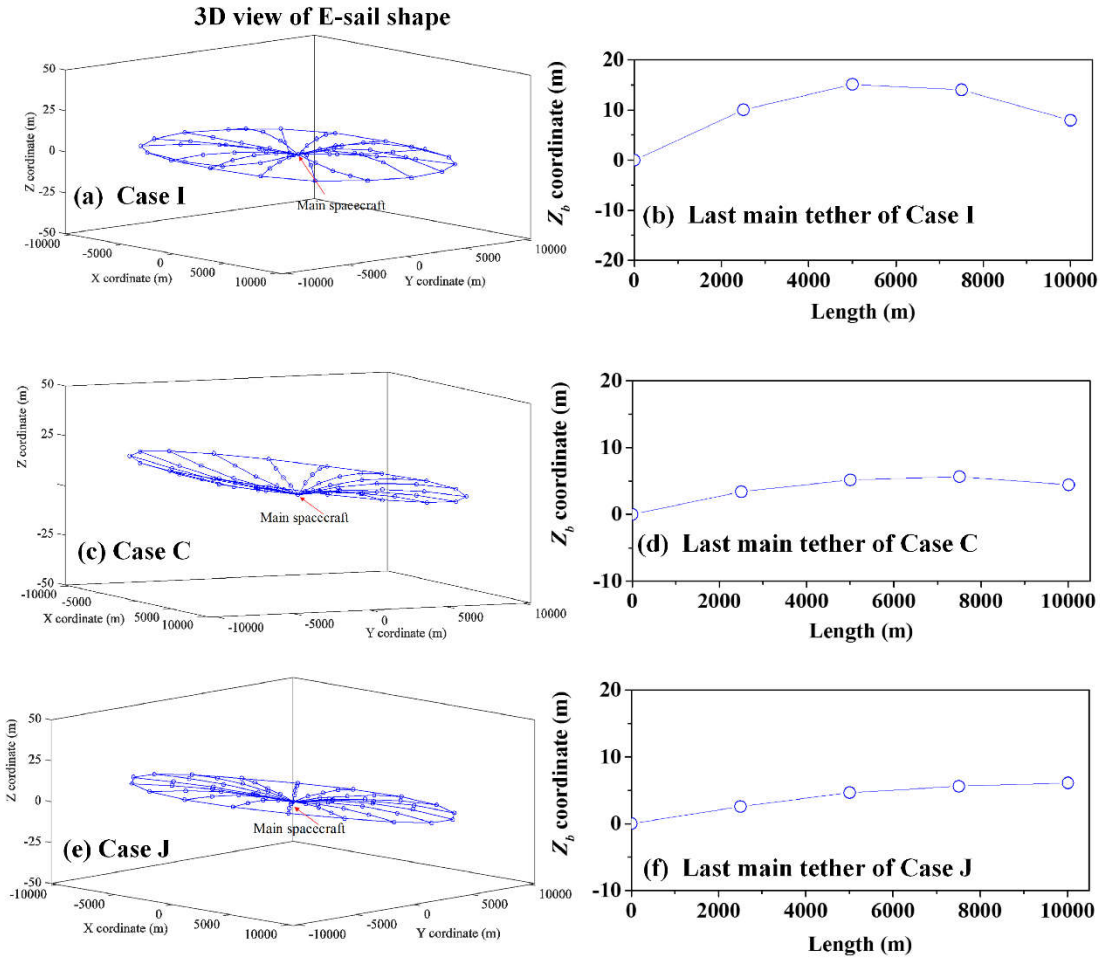

Figure 5.34 Influence of remote unit on geometrical configuration of E-sail expressed in the body coordinate frame (4-day).

5.2.4.3 Relative Velocity and TI Concept Effect

The TI type is defined to explore the suppression of the increase of spin rate caused by the attitude maneuvering, where all tethers are charged, and the main tethers are electrically connected to auxiliary tethers at every two main tethers. This type of E-sail called TI type, the advantage of this type of E-sail is that a component along the spinning plane is generated, and it is used to suppress the increase of spin rate. As listed in Eq. (5.5), the

Coulomb force per unit length depends on the velocity of incoming solar wind velocity. However, the relative velocity between two moving objects should be considered. Moreover, the TI type E-sail has been proposed to suppress the increase of spin rate caused by the E-sail attitude maneuvering. Before activating the spin rate control as listed in Eq. (5.13), the TI type E-sail impacting on the dynamics should be investigated. As listed in Table 5.6, three cases are simulated, and the physical and controller parameters are set the same as the case C. The target in-plane and out-of-plane angles (α_{sa}^{t} and β_{sa}^{t}), are the same as in the section 5.2.4.2.

Table 5.6 Numerical simulations relate to relative velocity and TI concept effects.

Name	Relative Velocity effect	TI effect	Spin rate controller
Case K	Yes	No	No
Case L	No	Yes	No
Case M	Yes	Yes	No
Case N	Yes	Yes	Yes

Table 5.7 The results of relative velocity and TI concept effects.

Name	Attitude maneuvering time T_{at} (day)	Travelling distance D_{at} (AU)
Case C	6.5	6.49×10^{-5}
Case K	6.5	6.43×10^{-5}
Case L	4.4	9.40×10^{-5}
Case M	4.3	9.31×10^{-5}

Effect of Relative Velocity of Solar Wind

Here, the effect of relative velocity of solar wind with respect to the E-sail on the dynamics of E-sail is investigated. As shown in Fig. 5.35 (a-b), the difference is trivial in both orbital

travel distance and in-plane angle due to the slight difference in the thrust force. For example, as listed in Table 5.7, the attitude maneuvering time T_{at} is equal. Thus, it reveals that the relative velocity effect has little influence on the attitude maneuvering capability and orbital motion. As a contrary, a distinct difference in the ratio of spin rate is observed, see Fig. 5.35(c). Correspondingly, the difference in tension of main tether is also distinct. It indicates that the conclusion in Ref. [45] about the variation of spin rate is non-conservative because it didn't consider the effect of relative velocity. For example, as shown in Fig. 5.35(c), the spin rate increases 10% in Ref. [45]. However, it increases 14% after the consideration of this relative velocity effect.

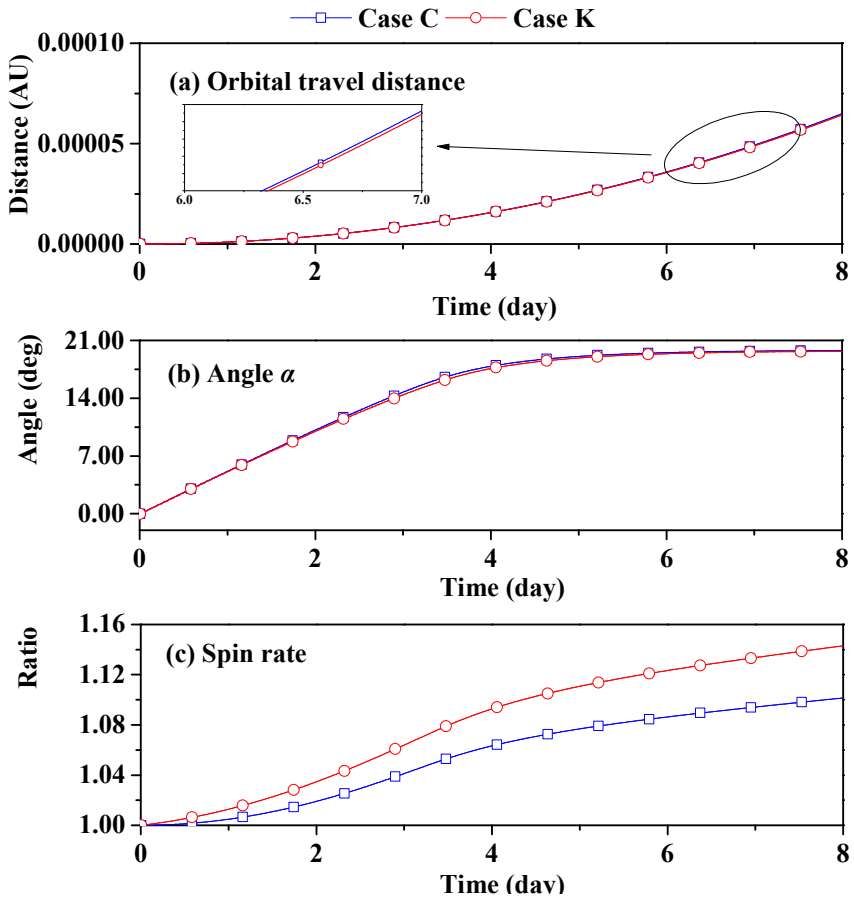

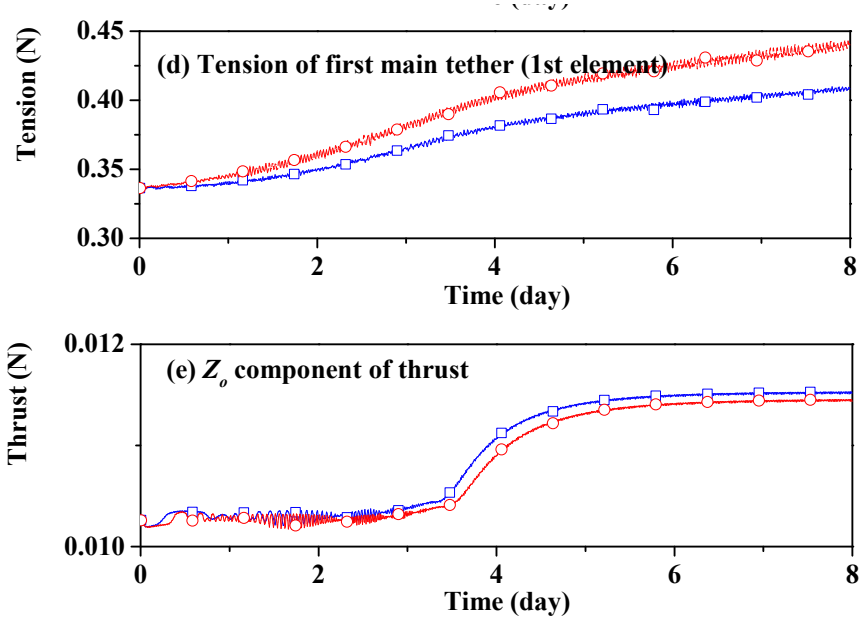

Figure 5.35 Comparison of controlled flight dynamics under relative velocity effect.

Effect of TI Type

The TI type of E-sail is chosen while the effect of relative velocity of solar wind with respect to the E-sail is not considered temporarily. It should keep in mind that all tethers of TI type E-sail are electrically charged. To make the results of two competitors comparable, the properties of auxiliary tethers used in section 5.2.4.2, such as, the cross-section area, elastic module, and material density, are kept the same as the case C except they are electrically conductive. As shown in Figs. 5.36(a) and (d), the TI type E-sail travels more distance because the thrust increases when the non-conductive auxiliary tethers become conductive and generate thrust. Moreover, the TI type E-sail is beneficial to improve the attitude maneuvering capability. For example, as listed in Table 5.7, the attitude maneuvering time T_{at} is 4.4 days compared with the competitor's result 6.5 days. The TI

type E-sail is also helpful for suppressing spin rate increase due to the thrust component in the spin plane, see in Figs. 5.36(d) and (f). For example, the spin rate increases only by 6.2% compared with 10% of case C.

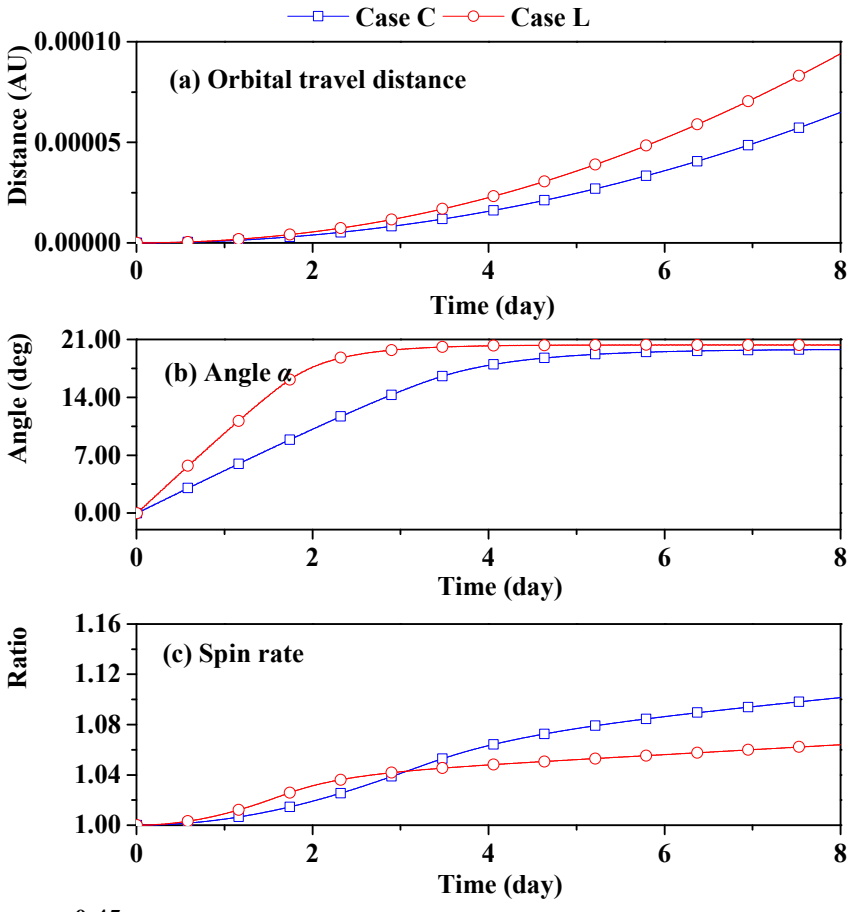

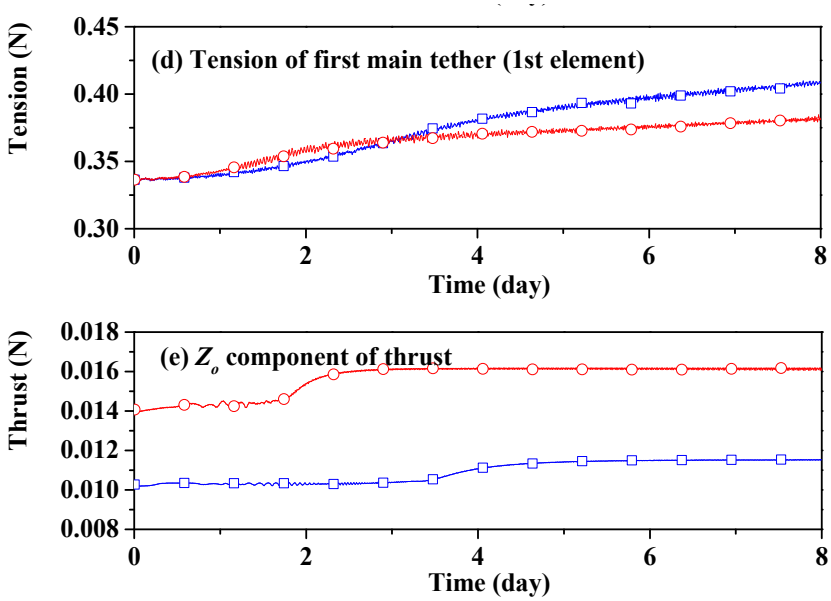

Figure 5.36 Comparison of flight dynamics under TI effect.

Combined Effects

Here, both the effects of solar wind velocity with respect to tether and TI type E-sail are considered. The same properties of auxiliary tethers in the section 5.2.4.2 are used. Regarding to the attitude maneuvering capability in terms of the in-plane angle α_{sa}, the same conclusion is obtained by comparing the results of the case L, see Figs. 5.37(a) and 5.36(a). Moreover, the variation of orbital travel distance of E-sail under the combined effects is the same as the case L. The reason is that the effect of relative velocity of solar wind has negligible effect on the thrust as shown in Fig. 5.35(e). However, the spin rate decreases under the combined effect due to the counterbalance of these two effects. For example, the spin rate increases 8.8 % under for the combined case, which is less than the result of cases L and M.

Based on these analyses, it shows the effect of velocity relative of solar wind to the E-sail has a considerable influence on the variation of spin rate. Moreover, the TI type E-sail is helpful to suppress the increase of spin rate from the system design aspect. Meanwhile, it is also beneficial to the orbital motion due to the increase of thrust of auxiliary tethers. However, the increase of spin rate is still observed. Therefore, the control strategy for suppressing the increase of spin rate is still needed.

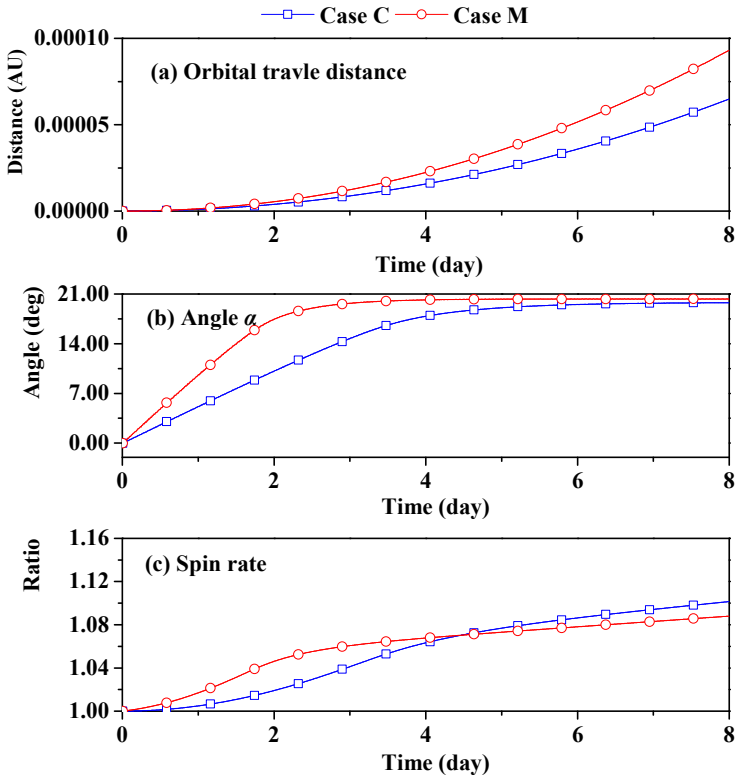

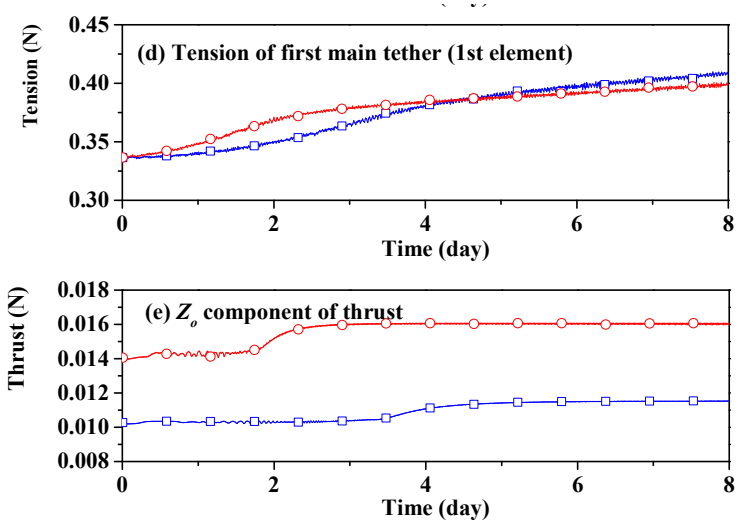

Figure 5.37 Comparison of controlled flight dynamics under the combined effects.

5.2.4.4 Spin Rate Control

As presented in last section, the spin rate increases even for the TI type E-sail. In this section, the proposed spin rate control in Eq. (5.15), is used together with the TI type E-sail. The control gain u_2 for spin rate is 50.

As shown in Fig. 5.38(c), it can be easily found that the proposed spin rate control is working successfully when the TI type E-sail is used. Moreover, it is observed that there is an increasing/decreasing phenomenon for the spin rate. The spin rate increases in the attitude maneuvering phase, and it decreases in the attitude holding phase. Difference form previous results without the spin rate control, the in-plane libration angle α_{sa} has an overshoot when the spin rate control is active in the attitude hold phase. It reveals that the spin rate adjustment and attitude maneuvering parts of the control algorithm slightly compete each other because they both use the same voltage as control actuation. The phenomenon can be observed from the variation of tether voltage in the first main tether,

see Fig. 5.39. In addition, Fig. 5.38(e) shows the proposed spin rate control has a negligible impact on the thrust and orbital travel distance. Finally, it is concluded that the proposed spin rate control works well based on the reduction of orbital thrust.

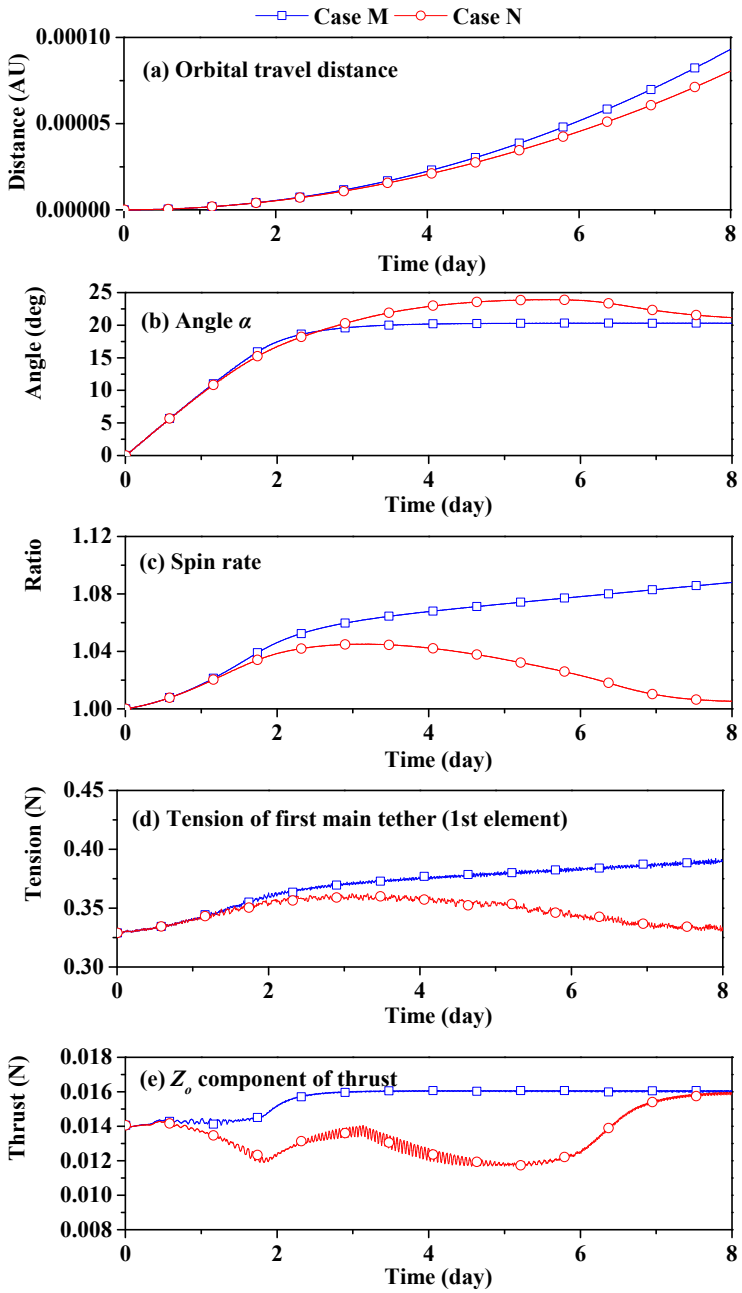

Figure 5.38 Comparison of flight dynamics with/without spin rate control.

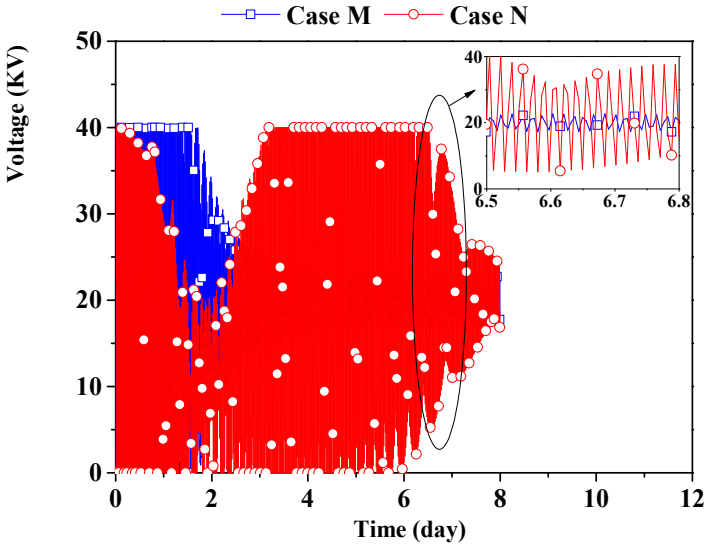

Figure 5.39 Variation of tether voltage of the first charging main tether.

5.3 Conclusion

In this chapter, a high accurate and fidelity model of E-sail is developed to include elastic flexibility of tether, and the attitude of control strategy is employed. First, the thrust (Coulomb force) dependence on the sail and coning angles is investigated. It is found that the thrust strongly depends on the coning angle, even in the small sail angle cases. Second, the dynamic analysis of E-sail system is conducted when the E-sail subjects to the Coulomb and gravitational forces. The results show that the initial spin rate and sail angle have a significant impact on the system dynamic behavior. Third, the attitude motion of E-sail under the control strategy through the modulation of applied tether voltage is analyzed. Then, the influence of physical design parameters on the dynamics of E-sail is conducted by a parametric analysis to better understand the dynamics of E-sail. Finally, the influence

of the effects of relative velocity of solar wind to E-sail and TI type E-sail on the dynamics is studied.

Chapter 6 DYNAMICS OF TETHER TRANSPORTATION SYSTEM

Summary: In this chapter, the TSS model with variable-length tether is used to study the dynamic behavior of tether transportation system with multiple climbers and tether deployment and retrieval at the end spacecrafts.

6.1 Dynamics of Tether Transportation System with Climber(s)

In this section, the dynamic behavior of TTS without tether deployment or retrieval under two situations is analyzed. One is from one climber and the other involves multiple climbers. Chapter 3 shows the out-of-plane libration motion is trivial in TTS and thus, it is not plotted in the following simulation cases inside this section.

6.1.1 One Climber

As presented in Section 3.2.8.1 of chapter 3, it has been shown that the results of NPFEM_ALE match very well with the results of dumbbell mode, if the tether is discretized into two variable-length straight elements. This implies the mode of flexible transverse deformation of tether is not considered. To be more accurate, the tether will be discretized into multiple elements and the process of merging and dividing of element is activated in this chapter, and the detail information can be found in chapter 3. In this section, the effects of tether discretization scheme and velocity of climber influence on the dynamic behavior of TTS is studied.

6.1.1.1 Influence of Tether Discretization Scheme

In this section, the physical parameters of tether are listed in Table 3.2. The effect of tether discretization on the dynamic response of TTS with one climber is investigated by discretizing the tether into two, four, 10 and 20 elements, respectively. For the number of elements greater than two, the merging and dividing elements occurs as the climber across the element boundary. Accordingly, the degree-of-freedom of the TTS model varies. The parameters for dividing and merging elements are given as: $L_s = 3000\ m$, $L_s = 1000\ m$ and $L_s = 500\ m$ for the 4, 10 and 20-element meshes respectively, $L_{max} = 1.65 L_s$, $L_{\min} = 0.49 L_s$, and $\delta_e = 10^{-3}\ m$. Unless noted otherwise, the following parameters of the TTS are used in this section: the TTS is flying in a circular orbit and its altitude of the CM is 6600 km, $m_m = m_s = 1000\ kg$, $m_c = 100\ kg$, $L = 10\ km$, and $V_c = 1\ m/s$. The climber starts at $0.01L$ from the sub-spacecraft upwards and stops at $0.99L$ from the main spacecraft, which means the material coordinate of the climber changes from $100m$ to $9{,}900m$, respectively. A parameter is defined to show the different position of the climber

$$R_{j,k} = \frac{\sqrt{\left(X_{c,k} - X_{c,j}\right)^2 + \left(Y_{c,k} - Y_{c,j}\right)^2 + \left(Z_{c,k} - Z_{c,j}\right)^2}}{\sqrt{X_{c,j}^2 + Y_{c,j}^2 + Z_{c,j}^2}} \times 100\% \quad \text{with} \quad j,k = 2,4,10 \text{ and } 20$$

representing the different discretization schemes.

The analysis results are shown in Figs.6.1-6.3 and Table 6.1. It can be easily observed that the general trends of libration angles of TTS are similar for different discretization schemes, see Fig. 6.1. However, it is noted that the tether transverse oscillation motion becomes obvious with more tether elements. Therefore, it indicates that

more elements should be used to capture the high frequency transverse oscillation of tether. The same phenomenon is found in the variation of tether geometrical configuration, see Fig. 6.3. From Fig. 6.3, it is noticed that the libration angle α_1 experiences a large amplitude motion due to the short length of element where the climber locating as the climber moves close to the end. Furthermore, the analysis also reveals that the constant velocity profile of climber is not realistic and is responsive partially for the high frequency transverse oscillation, especially at the beginning and end of climber's movement. It is noted the difference between the 10 and 20-element discretization schemes is not noticeable compared with the difference between the 4 and 10-element discretization schemes, see in Fig. 6.2 and Table. 6.1. For example, as listed in Table 6.1, the ratio $R_{10,20}$ for 10 and 20 elements is around 0.2%. However, as the tether is discretized into more elements, the computational loads increases significantly. Therefore, after the trade-off between the accuracy and computational load, the 10-element discretization scheme is used in the following analysis.

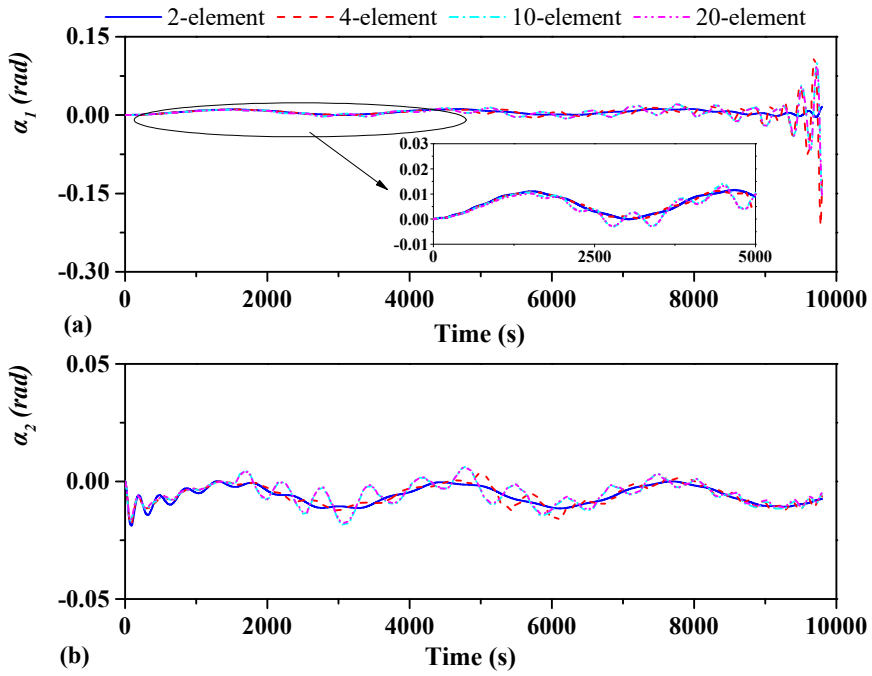

Figure 6.1 Libration motion of climber in upward transfer (a) Libration angle α_1. (b) Libration angle α_2.

Table 6.1 Ratio of position of climber between different discretization schemes.

Time (s)	Ratio $R_{2,4}$ (%)	Ratio $R_{4,10}$ (%)	Ratio $R_{10,20}$ (%)
100	2.71	0.51	0.18
2000	7.78	0.90	0.03
4000	2.93	0.96	0.20
6000	1.12	0.69	0.21
8000	9.18	0.29	0.12
9500	2.87	0.54	0.23

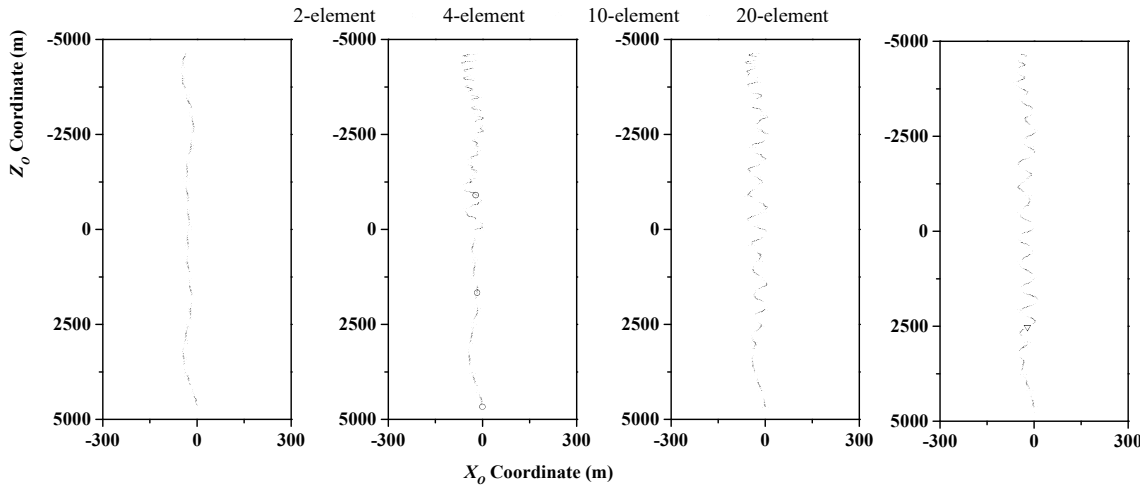

Figure 6.2 Trajectory of climber in the orbital coordinate system.

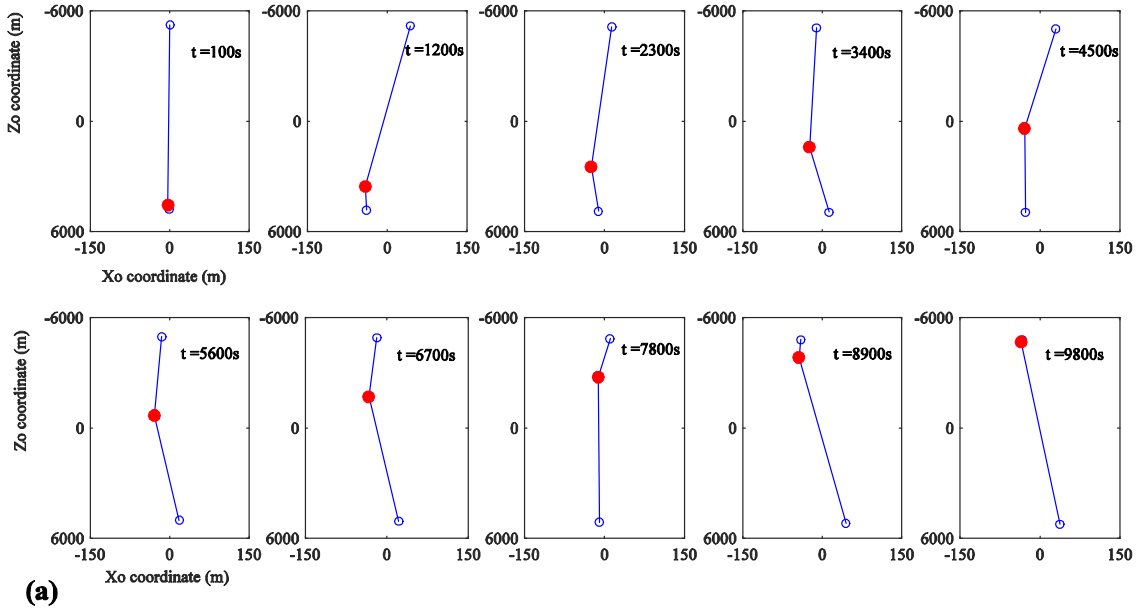

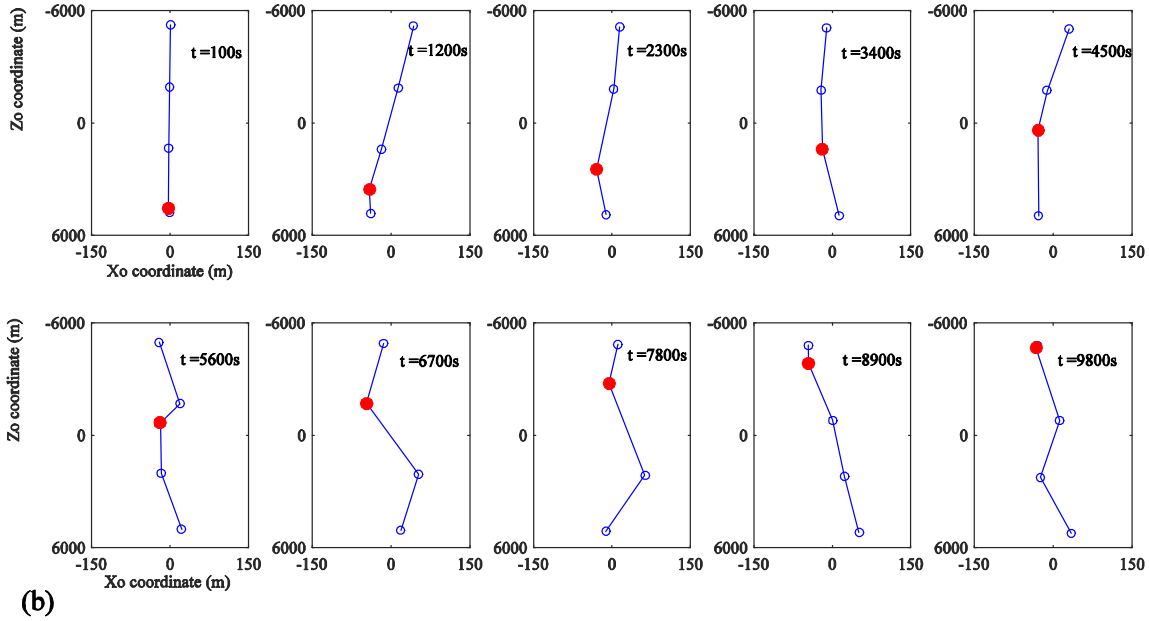
Zo coordinate (m)
Xo coordinate (m)
t =100s
t =1200s
t =2300s
t =3400s
t =4500s
t =5600s
t =6700s
t =7800s
t =8900s
t =9800s
-6000
0
6000
-150
0
150

(b)

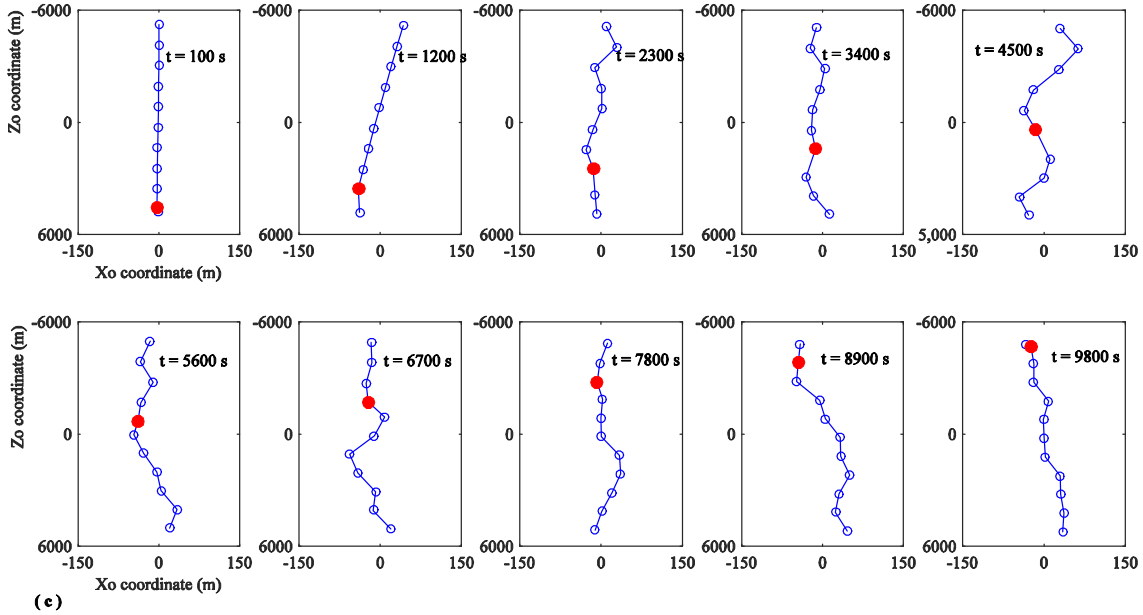
Zo coordinate (m)
Xo coordinate (m)
t = 100 s
t = 1200 s
t = 2300 s
t = 3400 s
t = 4500 s
t = 5600 s
t = 6700 s
t = 7800 s
t = 8900 s
t = 9800 s
-6000
0
6000
5,000
-150
0
150

(c)

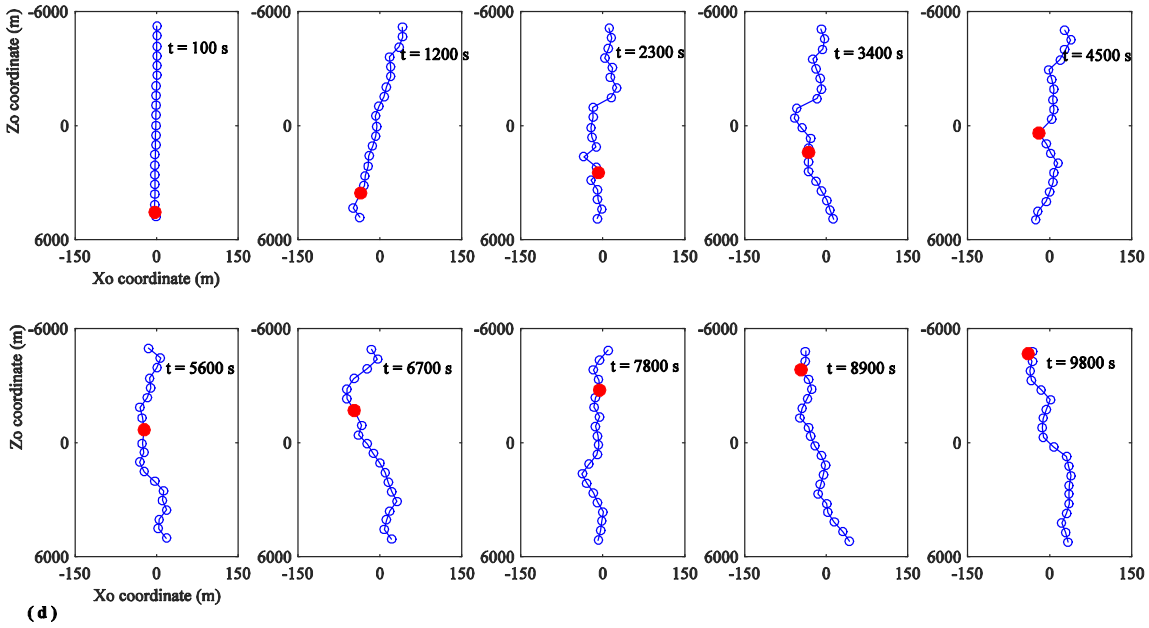

Figure 6.3 Geometrical configuration at instant time 100s: (a) 2-element. (b) 4-element (c) 10-element. (d) 20-element.

6.1.1.2 Influence of Velocity Profile of Climber

In this section, a more realistic start-stop velocity profile of the climber, instead of constant velocity, is considered to investigate the dynamic response of TTS. The motion profile of the climber contains an acceleration phase, a constant velocity cruising phase, and a deceleration phase, as shown in Eq. (6.1). The non-dimensional parameter τ defines the time duration of acceleration to the time duration of cruise Refs. [48, 117]. In the section, the duration of acceleration and deceleration phases are assumed the same.

$$p_{j,\text{desired}} = \begin{cases} -\dfrac{1}{\kappa}\dfrac{L_{eq}}{\pi}\sin\left(\dfrac{1}{\tau}\pi\dfrac{V_{cr}}{L_{eq}}t\right)+\dfrac{V_{cr}}{2}t & t \le t_a \\ V_{cr}t-\dfrac{\tau}{2}L_{eq} & t_a \le t \le t_b \\ \dfrac{1}{\kappa}\dfrac{L_{eq}}{\pi}\sin\left(\dfrac{1}{\tau}\pi\dfrac{V_{cr}}{L_{eq}}\left(t-t_b\right)\right)+\dfrac{V_{cr}}{2}t+\dfrac{1-\tau}{2}L_{eq} & t_b \le t \le t_c \end{cases} \tag{6.1}$$

where L_{eq} and V_{cr} are the equivalent moving distance and cruise velocity respectively, $\kappa = 2/\tau$. $t_a = \tau L_{eq}/V_{cr}$, $t_b = L_{eq}/V_{cr}$, and $t_c = (1+\tau)L_{eq}/V_{cr}$.

First, the effect of the magnitude of cruise velocity on the dynamic response of TTS is investigated. The parameter τ is 0.2, and three cases are conducted with the cruise velocity being 1, 2, and 4 m/s, respectively. The results are shown in Figs. 6.4 and 6.5. Figure 6.4 shows the libration angles of TTS system, where the *x*-axis represents the variation of material coordinate. The amplitude of libration angles increases as the cruise velocity increases. The same phenomenon is observed from the trajectories of main/sub-spacecraft, and the climber, seen Fig. 6.5.

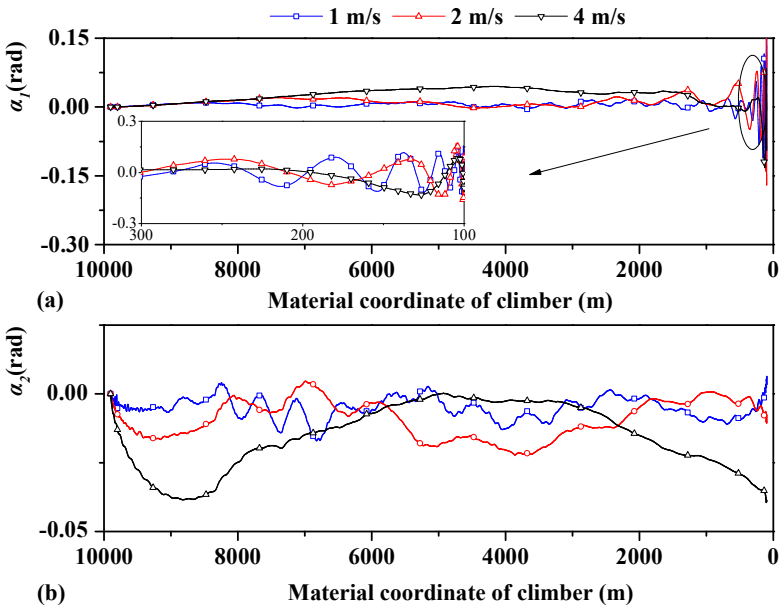

Figure 6.4 Libration angles of the climber with different cruise velocities (a) Libration angle α_1. (b) Libration angle α_2.

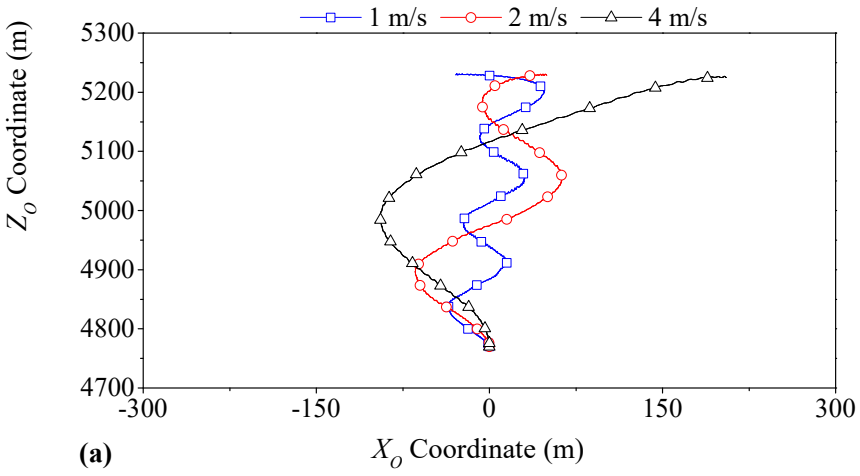

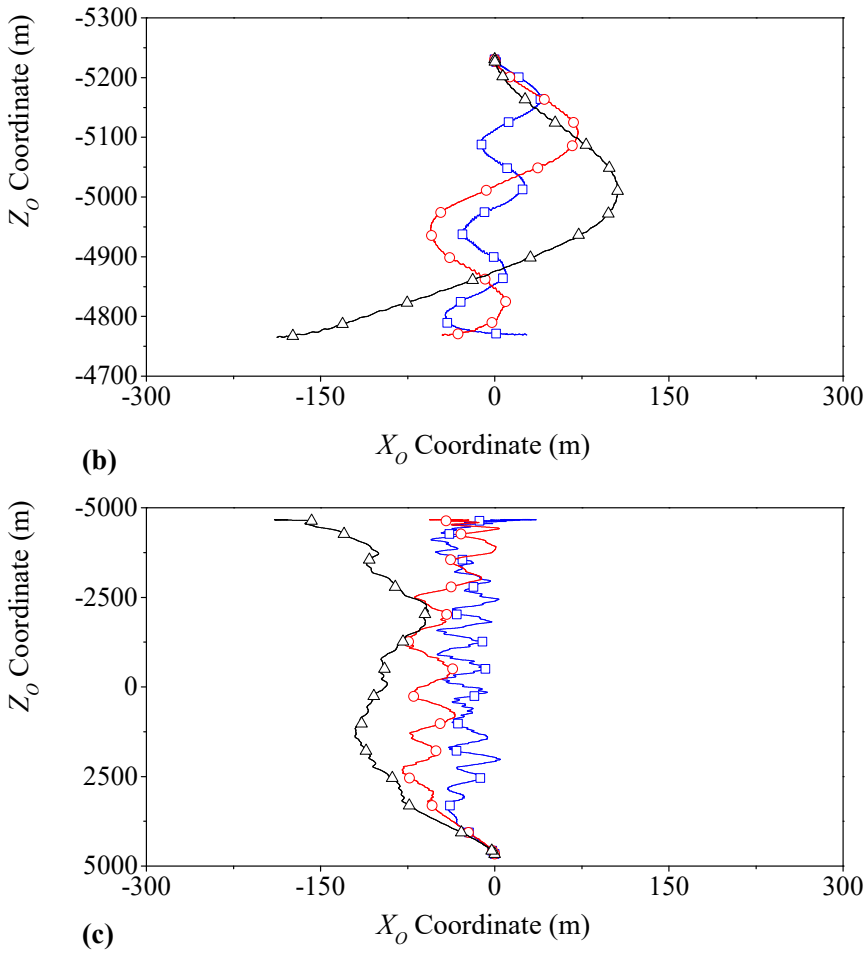

Figure 6.5 Trajectories in the orbital coordinate system: (a) main spacecraft (b) sub spacecraft (c) climber.

Then, the effect of parameter τ on the dynamic response of TTS is investigated, and the cruise velocity V_{cr} is 4 m/s. Four cases are conducted with τ being 0.1, 0.3, 0.6, and 0.9, respectively. As shown in Fig. 6.6, the total time of transient motion varies due to different values of τ. To observe the residual libration of the climber upon climber arrest, the simulation time is extended by 1,000 s. The results are shown in Fig. 6.7. It shows the parameter τ significantly affects the libration angles. The increase of parameter τ represents the decrease of induced Coriolis force by the climber motion. Furthermore, the residual

libration motion is observed, and the amplitude of residual libration decreases as the parameter τ increases. The results indicate that gradual acceleration and deceleration are helpful for the suppression of libration angle of the TTS.

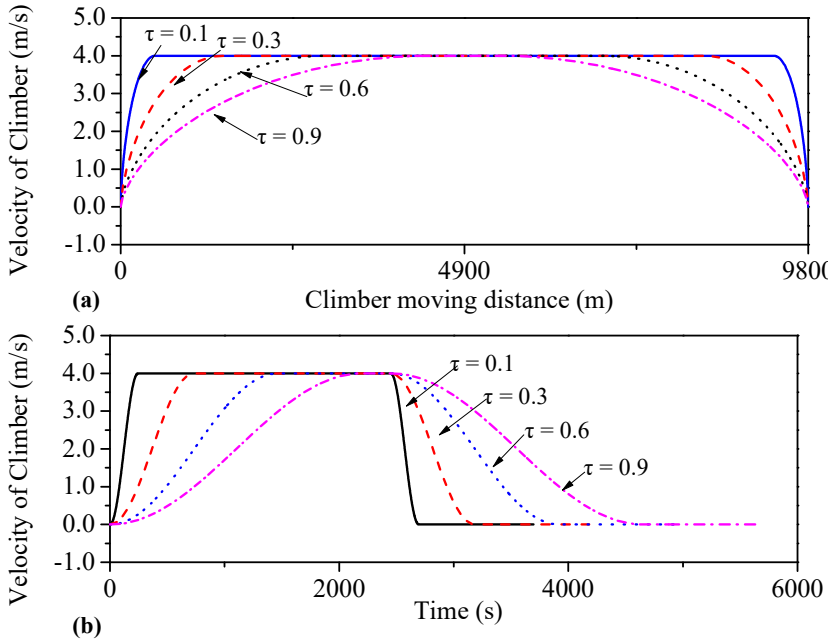

Figure 6.6 Velocity profiles of climber with different time ratios.

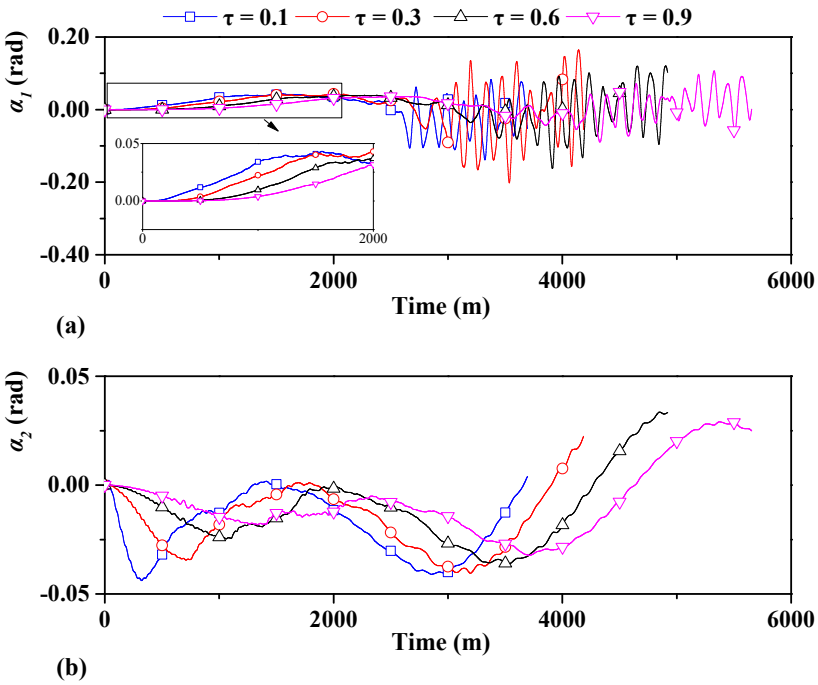

Figure 6.7 Libration angles of the climber with different time ratios (a) Libration angle α_1. (b) Libration angle α_2.

6.1.2 Multiple Climbers

In this section, multiple climbers with proper phase shift have been proposed to suppress the libration to zero [29, 117]. The existing works are mainly done with multi-piece dumbbell model. To demonstrates the superiority of our flexible tether modeling approach in the dynamic analysis of TSSC with multiple climbers, we take three climbers as an example. For simplicity, each climber has the same velocity profile and the same mass (33.333 kg). The climber is launched with a delay of 100s. The velocity profile in Eq. (6.1) is adopted, where the climber's time ratio τ is 0.2, the cruise velocity V_{cr} is 4 m/s and the equivalent moving length L_{eq} is 9866.67m. As shown in Fig. 6.8, both the ascending and descending transfer motions are simulated. The results are shown in Figs. 6.9-6.11.

Figure 6.9 shows the libration angles of climbers where α_2 and α_3 associates the virtual tether segment located between climbers. It is easily seen that the libration angle experiences a high frequency oscillation with large amplitude in the final part, such as α_1, α_2 and α_3. This is because the climbers are located too close, i.e. the length of virtual element is short. Figure 6.10 shows the variation of main and sub spacecraft relative to the CM in the orbital frame. It can be found that both spacecraft have a displacement in the Z-axis of the orbital frame, seen in Figs. 6.10 (a) and 6.10 (c). The reason for this phenomenon is that the CM of TTS changes as the climber moves up/down, and the origin of the orbital frame is located at the CM position. For example, both the main and sub spacecraft move up, and the displacements are 459.37 m and 467.34 m, respectively. Moreover, the bending profile of tether is observed when the climber moves up, see in Fig. 6.11. Therefore, these two values are slightly different from the analytical solution of 463.485 m, which is calculated based on the assumption of a vertical straight tether. In addition, as shown in Figs. 6.9(b) and 6.9(d), the high frequency oscillation of the climber can be found caused by the oscillation of tether.

Finally, we can conclude that our flexible tether model using NPFEM_ALE approach can be easily applied to the TTS with multiple climbers. It should be applied in the detailed mission design.

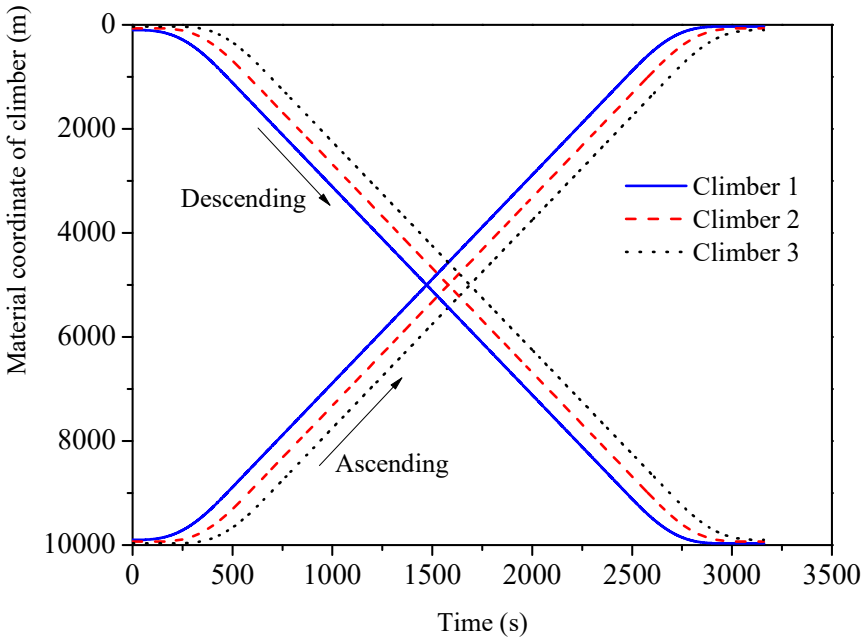

Figure 6.8 Climber movement with phase shift in ascending and descending cases.

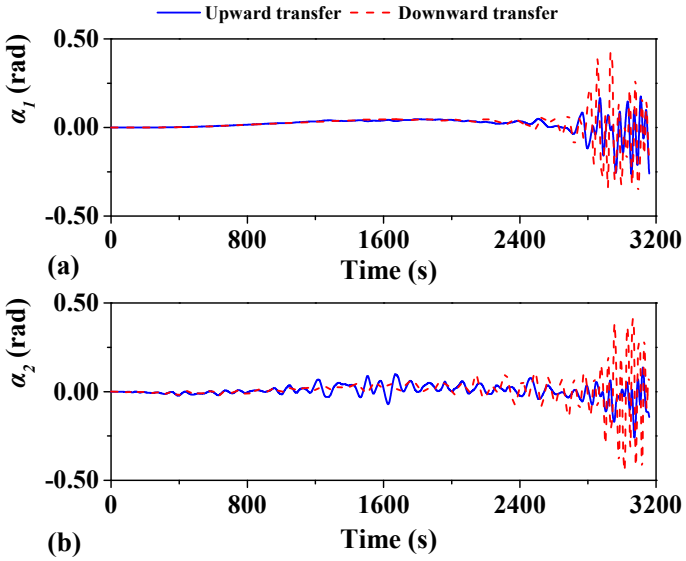

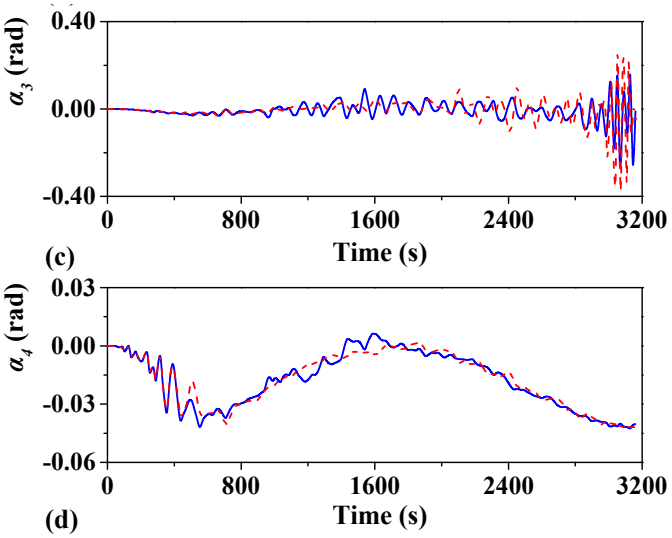

Figure 6.9 Libration angles with 3 climbers in upward and downward transfer cases.

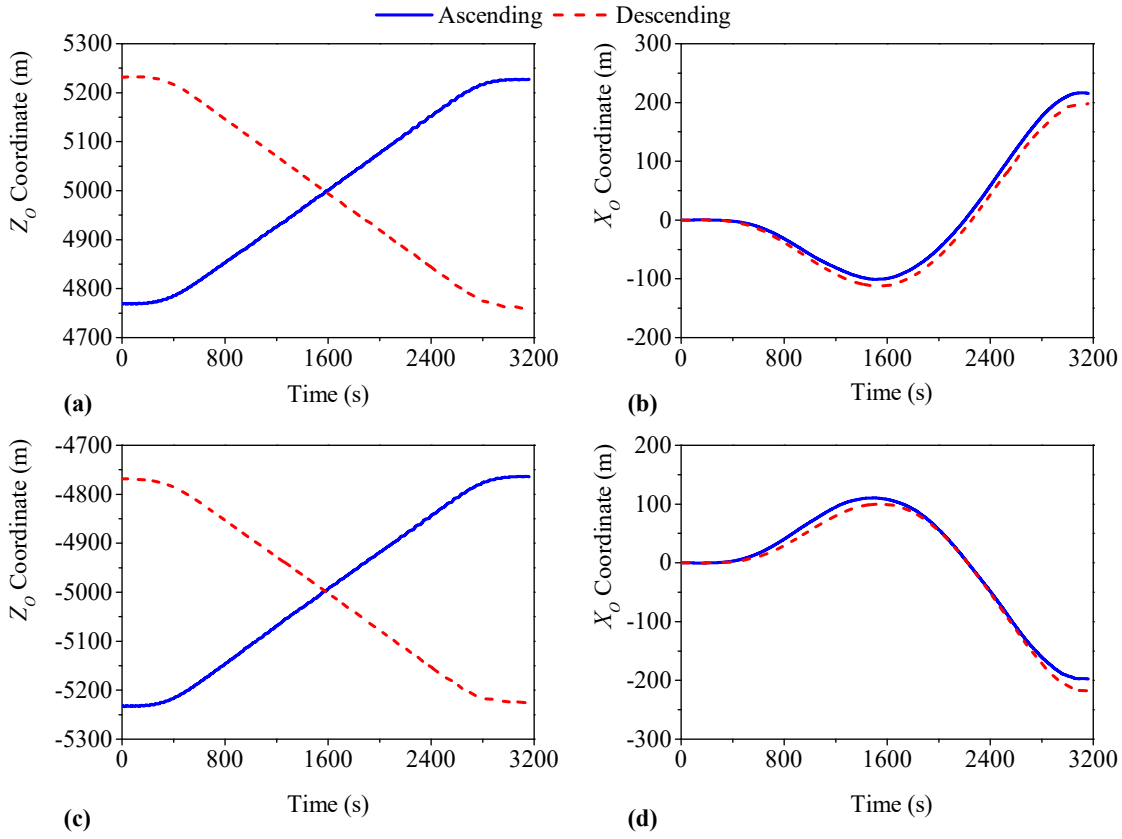

Figure 6.10 Displacements of main and sub spacecraft.

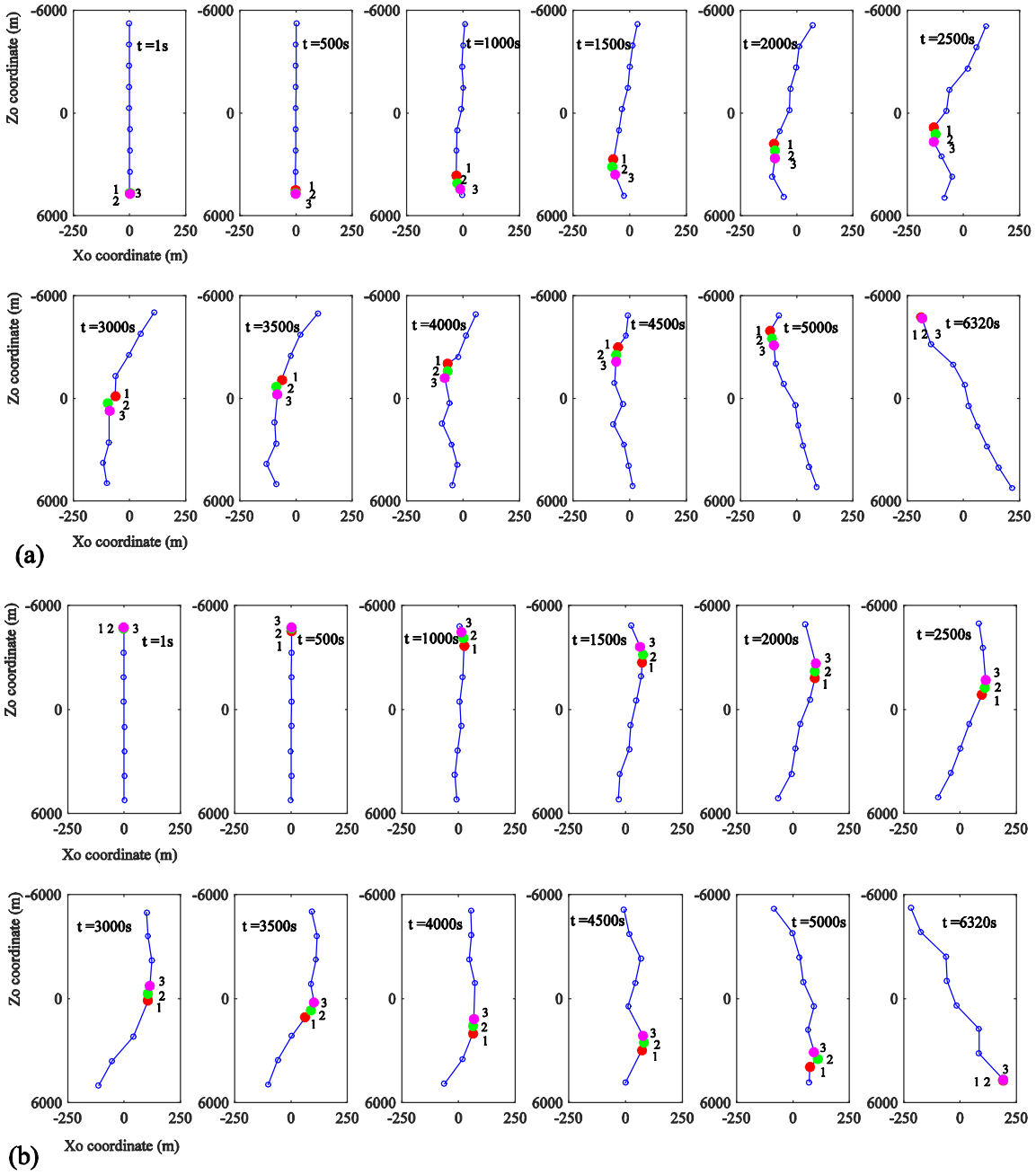

Figure 6.11 Tether geometrical configuration in the orbital coordinate frame (a) upward transfer (b) downward transfer.

6.2 Dynamics of Tether Transportation System with Climber and Tether Deployment or Retrieval

In this section, the dynamic behavior of TTS with tether deployment or retrieval is investigated under two situations. One is that the climber is moving upward while the sub spacecraft is deploying tether. The other is that the climber is moving downward while the sub spacecraft is retrieving tether. The effects of tether discretization scheme and speed of tether deployment or retrieval influence on the dynamics of TTS are investigated.

6.2.1 Influence of Tether Discretization Scheme

The effect of high-order transverse oscillation modes of tether on dynamic behavior of TTS is investigated by discretizing the tether into multiple (>2) elements. Unless specified otherwise, the tether is initially divided into 14 elements, where one element length is 500m and the lengths of other elements are the same (1500 m). To avoid the numerical instability caused by lengths of variable-length elements becoming too long or too short, the function of merging and dividing element is activated and the degrees of freedom of numerical model change accordingly. The following parameters are used in this case: $L_s = 1500\ m$, $L_{\max} = 1.65 L_s$, $L_{\min} = 0.49 L_s$ and $\delta_e = 10^{-3}\ m$. The integration time step size is 0.0001s. As comparison, the TTS is also analyzed by a two-element model with the same velocities of climber and tether deployment in the previous section.

6.2.1.1 Upward Transfer

First, the climber moves upward at a constant speed 4*m/s* while the sub spacecraft deploys

the tether at 2*m/s*. Figure 6.12 shows the geometrical configuration of TTS in the period of first 10*s* after the climber starts to move. It shows clearly that the amplitude of transverse oscillation of tether increases because the moving climber generates a Coriolis force acting on the tether. In addition, the oscillation propagates along the tether upwards like a wave as shown in Fig. 6.13. For example, the wave propagates from the bottom (climber position) to the top (main spacecraft) and then is reflected from the top to the bottom. It shows that the multiple-element model is superior to the two-piece dumbbell model in Refs. [33, 118], which is unable to capture the wave propagation phenomenon.

Next, Figure 6.14 shows the number of elements varies as expected when the climber transfers upward and the sub spacecraft deploys tether. The increase and decrease of variable-length element lengths leads to element merge/divide that corresponds to the zigzag variation in Fig. 6.14. At the same time, the length increases of variable-length element connecting the sub-spacecraft leads to only element divide that corresponds to the increase of element number. It indicates that the procedure of merging and dividing elements works as expected.

Furthermore, as shown in Figs. 6.15 and 6.16, the difference in libration angles and trajectories of the climber and sub spacecraft predicted by the multiple-element and two-element models is small initially. It becomes noticeable after the climber moves up because the transverse oscillation of tether increases and changes the dynamic behavior of TTS. For example, Figure 6.17 shows that the bending of tether in the multiple-element model, but not in the two-element model. In addition, the tether slack-taut phenomenon is predicted by the multiple-element tether model, see Fig. 6.18 where element 4 experiences zero

tension at 2,200*s*. The slack-taut of tether may break the tether and should be avoided in the operation of orbital transfer. This shows the importance of the multiple element model in the dynamic analysis of TTS.

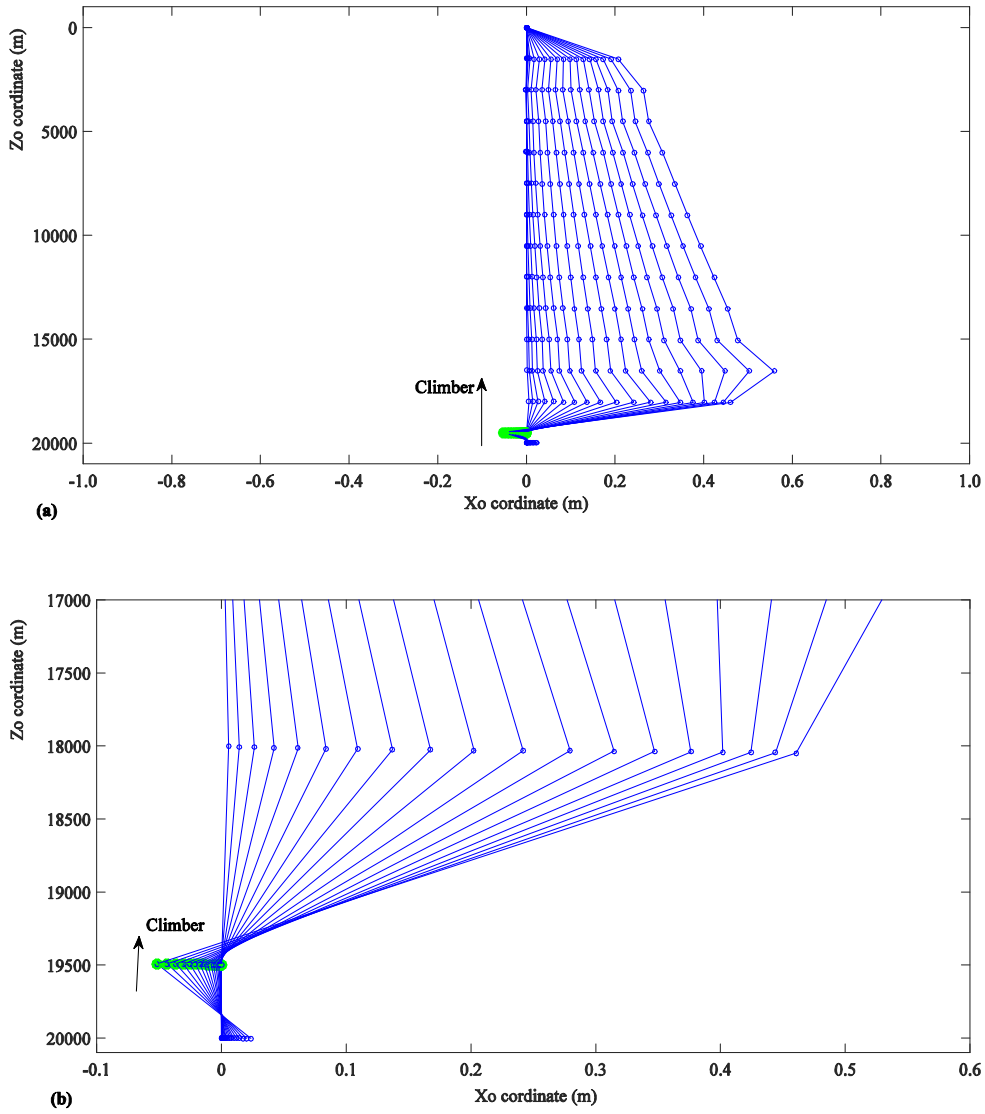

Figure 6.12 In-plane geometrical configuration of tether in upward transfer in first 10s: (a) global and (b) zoomed views.

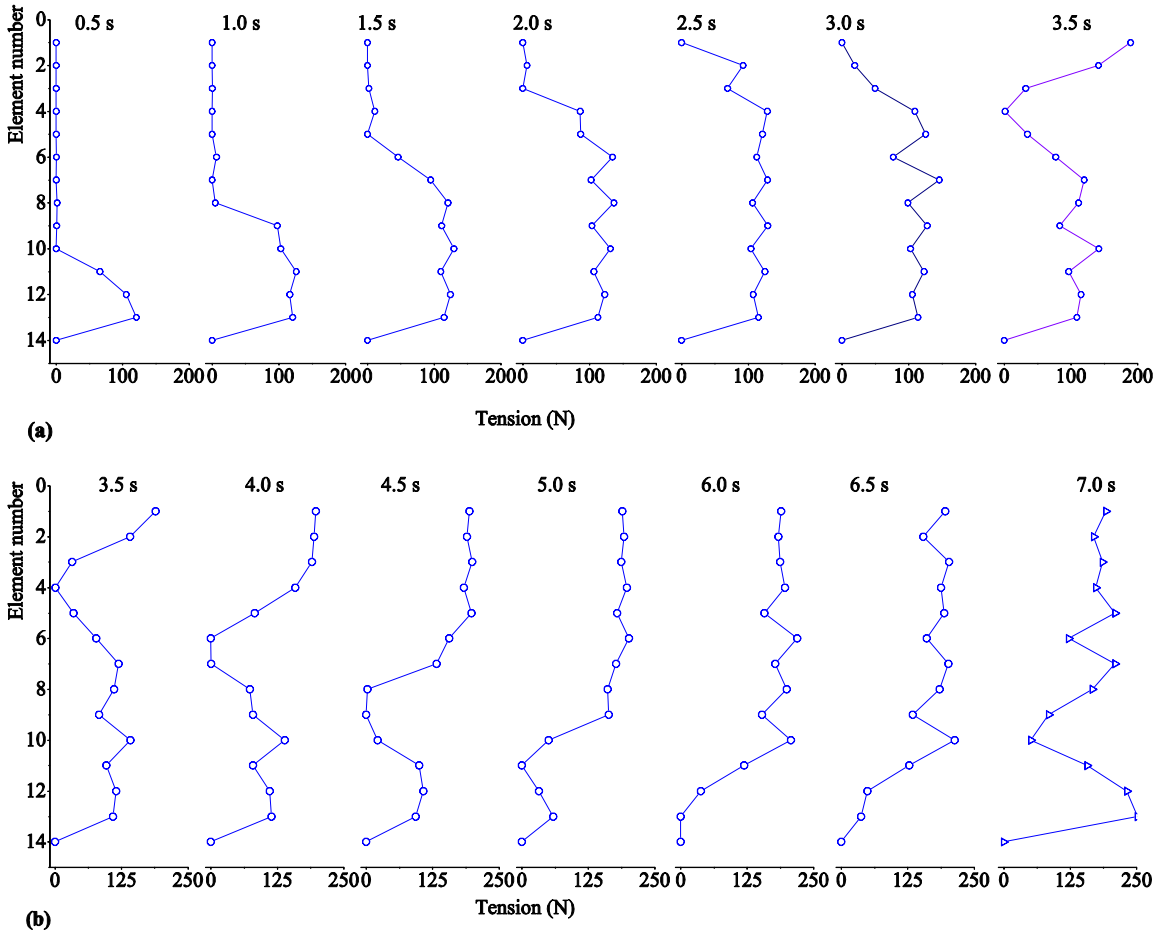

Figure 6.13 Tether tension distribution along tether in upward transfer.

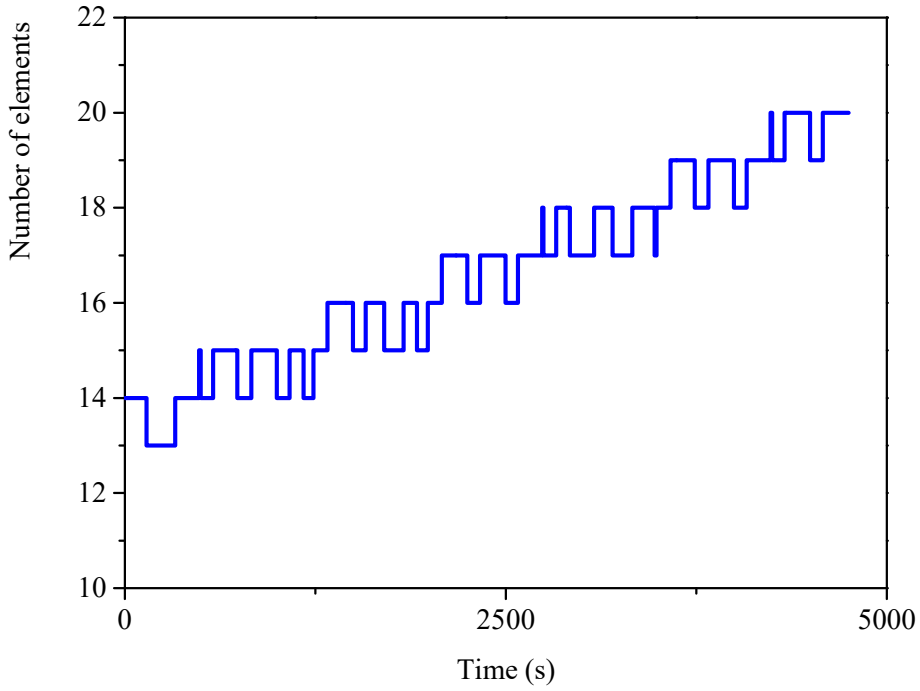

Figure 6.14 Variation of element numbers in upward transfer and tether deployment.

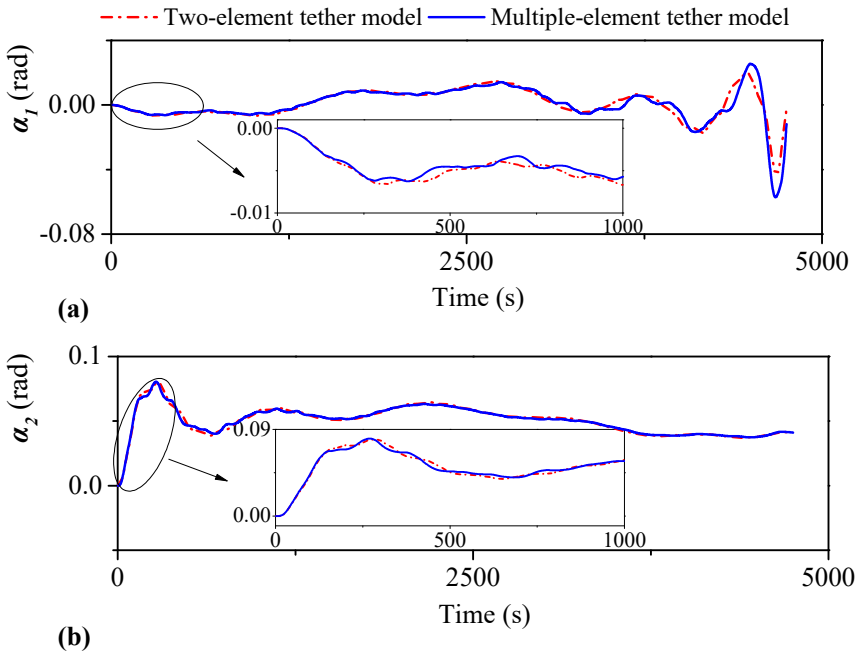

Figure 6.15 Libration angles predicted by two and multiple element models in upward transfer: (a) Libration angle α_1. (b) Libration angle α_2.

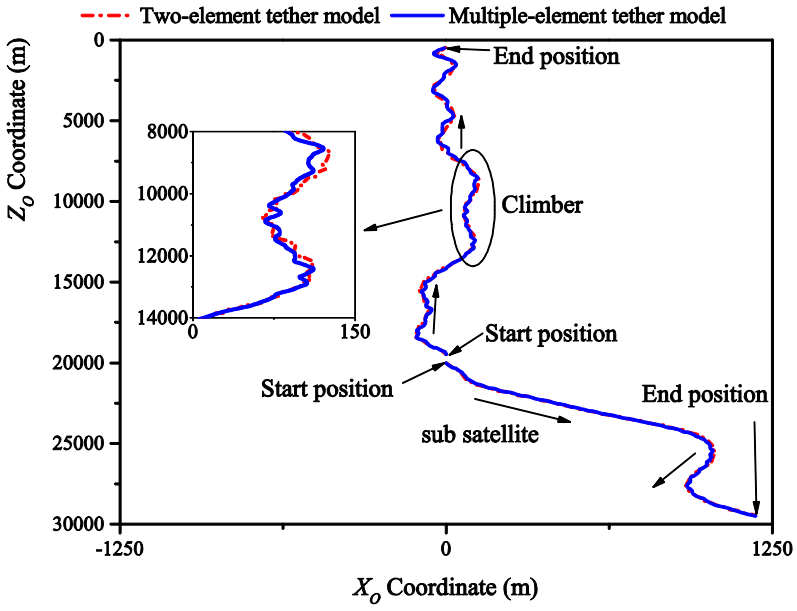

Figure 6.16 In-plane trajectories of climber and sub spacecraft predicted by two and multiple element models in upward transfer.

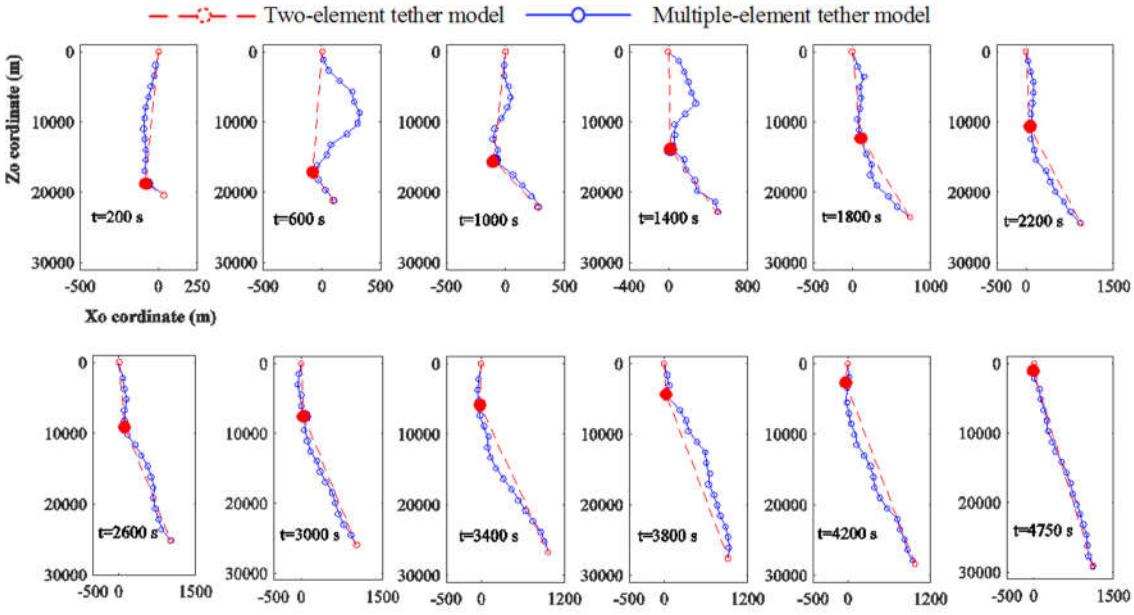

Figure 6.17 In-plane geometrical configuration of TSS predicted by two and multiple element models in upward transfer.

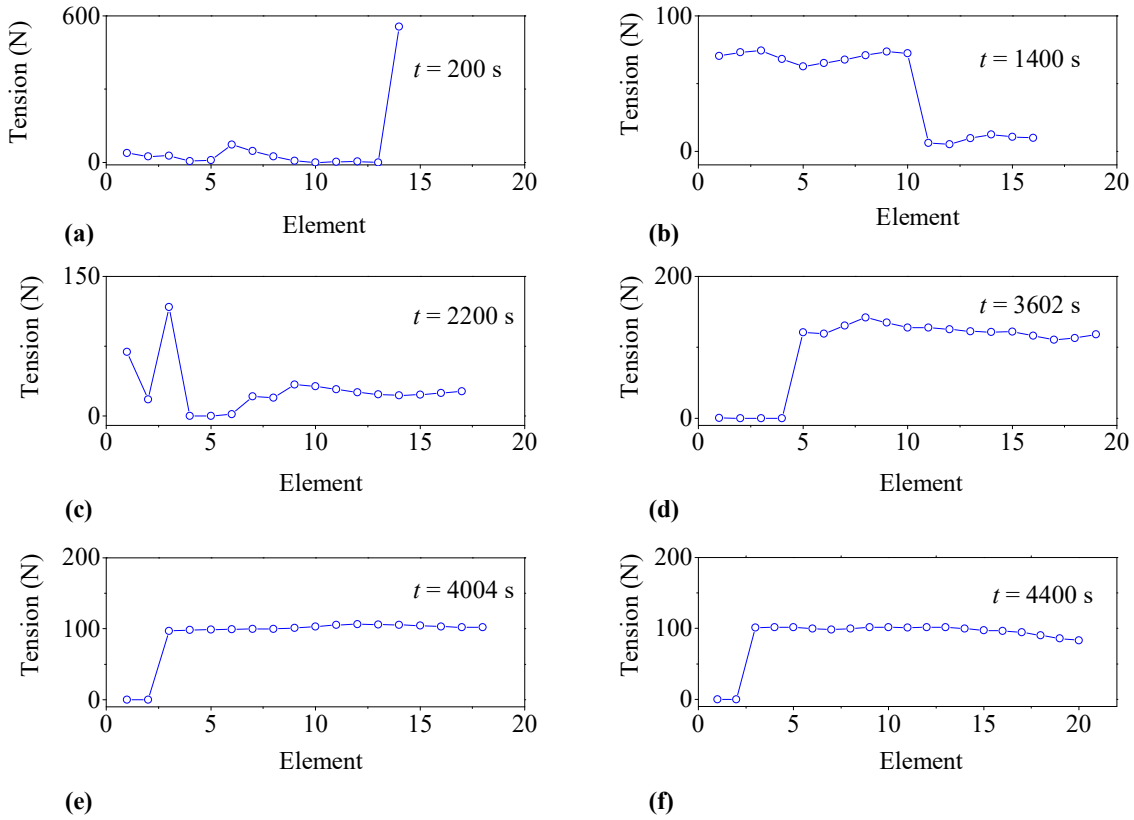

Figure 6.18 Tension variation along tether at different moments in upward transfer.

6.2.1.2 Downward Transfer

The results for downward transfer motion are shown in Figs. 6.19-6.23. As shown in Fig. 6.19, the number of elements decreases that is consistence with our expectation. Different from the last section, the retrieval of tether corresponds to the linear decrease part of curve. As shown in Figs. 6.20 and 6.21, it shows that the difference in libration angles of TTS is noticed as the time increases, which is caused by the transverse motion of tether of TTS. For example, the transverse motion of tether can be clearly observed in the multiple-element tether model, not in the two-element tether model, sees Fig. 6.22. It can be concluded that the effect of high-order transverse oscillation of tether influences the

dynamic behavior of TSS and cannot be ignored. Thus, the multiple-element tether model should be used in the detailed mission analysis. In addition, as shown in Fig. 6.23, it shows that part of tether is possible to experience the slack situation.

In summary, the comparison shows that the high-order transverse oscillation of tether affects the dynamic behavior of TTS noticeably. Thus, the transverse motion of tether should be considered in the detailed engineering analysis of TTS. The working condition of TTS can be extended into low-tension range, and part of tether may experience a slack situation.

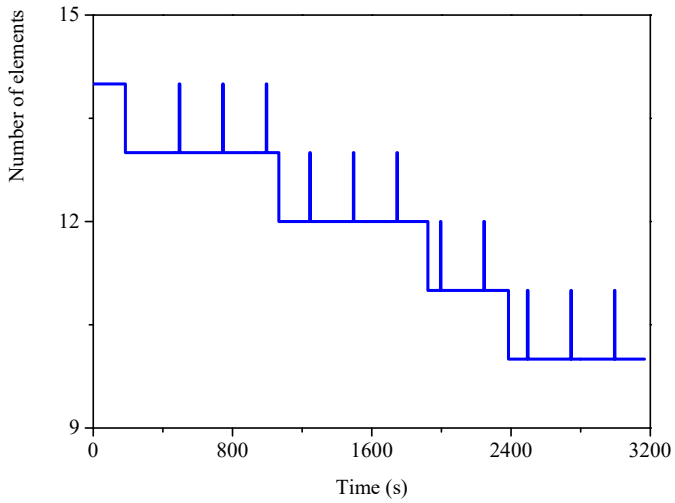

Figure 6.19 Variation of element numbers in climber's downward transfer motion and tether retrieval of sub spacecraft.

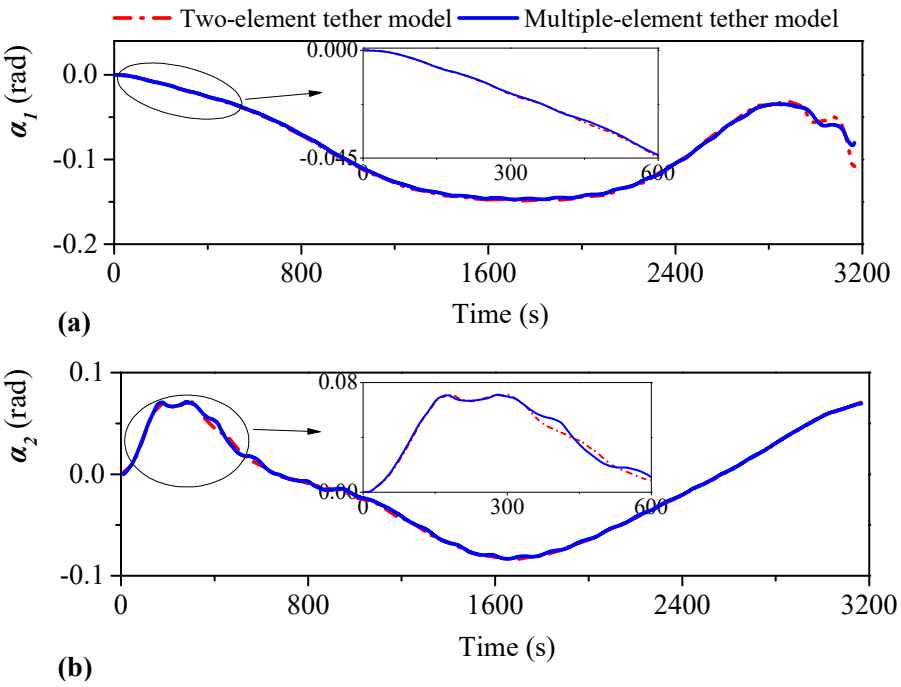

Figure 6.20 Comparison of libration angles in climber's downward transfer and tether retrieval at sub spacecraft. (a) Libration angle α_1. (b) Libration angle α_2.

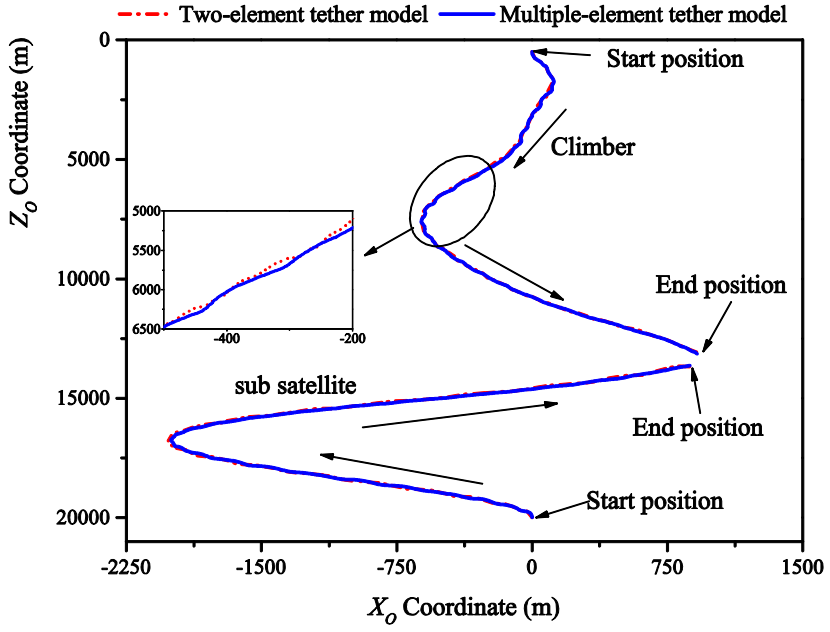

Figure 6.21 In-plane trajectories of climber and sub spacecraft predicted by two and multiple element models in downward transfer.

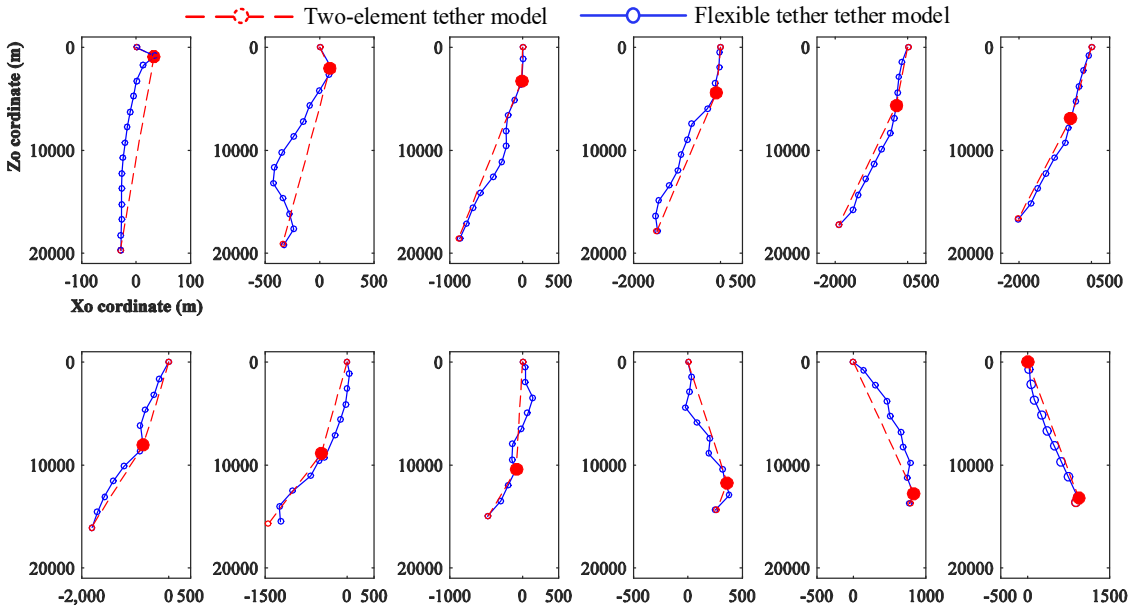

Figure 6.22 In-plane geometrical configuration of TSS in climber's downward transfer and tether retrieval at sub spacecraft.

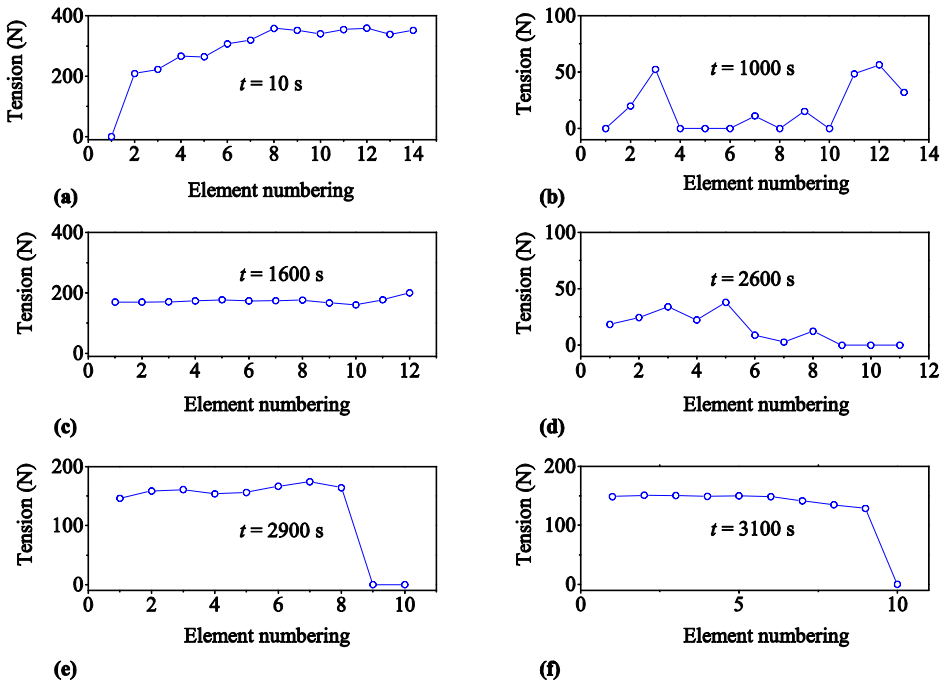

Figure 6.23 Tension variation along tether in climber's downward transfer and tether retrieval at sub spacecraft.

6.2.2 Influence of Deployment and Retrieval Velocity

The influence of deployment or retrieval velocity on the dynamic behavior of TTS is investigated. The discretization scheme of tether and the parameters are the same as those in the section 6.2.1. The integration time step size is 0.0001*s*. The climber moves at a constant velocity upward (-4 *m/s*) or downward (+4 *m/s*). In addition, the tether is deployed (positive velocity) or retrieved (negative velocity) at either main spacecraft or sub spacecraft, respectively. Table 6.2 shows the deployment and retrieval velocity in different cases.

Table 6.2 The deployment or retrieval velocity in different cases

Name	Deployment or retrieval velocity of sub spacecraft (m/s)	Name	Deployment or retrieval velocity of main spacecraft (m/s)
Case A_1	2.0	Case B_1	2.0
Case A_2	1.0	Case B_3	1.0
Case A_3	0.0	Case B_3	0.0
Case A_4	-1.0	Case B_4	-1.0
Case A_5	-2.0	Case B_5	-2.0

First, consider the climber in the upward transfer. Five simulation cases with different deployment or retrieval velocities at the sub spacecraft are conducted. It contains two cases of tether deployment (A_1 and A_2), two cases of tether retrieval (Case A_4 and A_5), and one case of constant tether length (Case A_3). Figure 6.24 shows libration angles of TTS where the *X*-axis represents the material coordinate of climber. Figure 6.25 shows the trajectories of climber with respect to the main spacecraft in the orbital frame. Based on these results, it is found that the variation amplitude of libration angles of TTS decrease in the cases A_1 and A_2, and it increases in the cases A_4 and A_5. It shows the

deployment of tether at the sub spacecraft suppresses the libration of TTS, and the retrieval of tether at the sub spacecraft increases the libration. This is because the deployment of tether at the sub spacecraft generates a Coriolis force acting on the sub spacecraft in the opposite direction of the Coriolis force acting the moving climber. The same phenomenon is observed from the geometrical configuration of TTS, as shown in Fig. 6.26. Thus, in case of the climber's upward transfer, the deployment of tether at the sub spacecraft produces a positive effect in suppressing the libration and the retrieval of tether at the sub spacecraft produces a negative effect. In addition, as shown in Fig. 6.24, the maximum amplitude of libration angles decreases as the tether's deployment velocity increases. It implies that the tethers' deployment velocity should be optimized to maximize the effect of tether's deployment on the libration suppression.

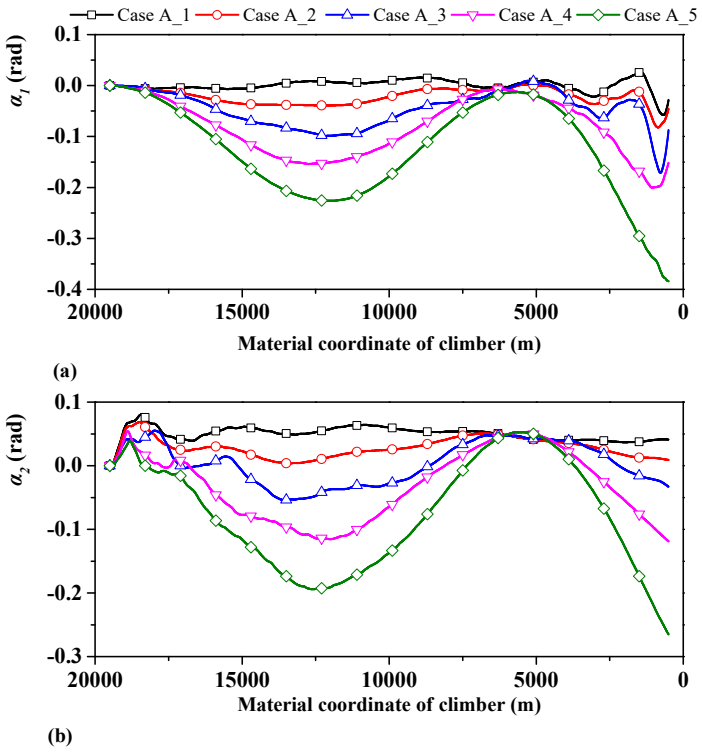

Figure 6.24 Libration angles of TSS in upward transfer with tether deployment or retrieval at sub spacecraft. (a) Libration angle α_1. (b) Libration angle α_2.

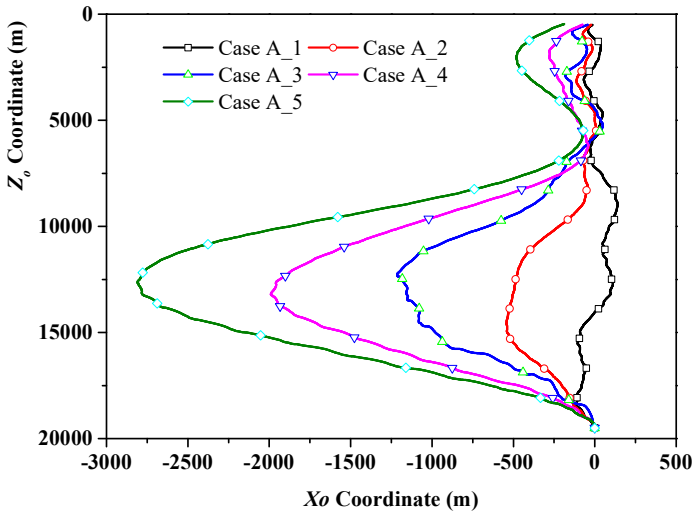

Figure 6.25 In-plane trajectory of climber with respect to main spacecraft in upward transfer with tether deployment or retrieval at sub spacecraft.

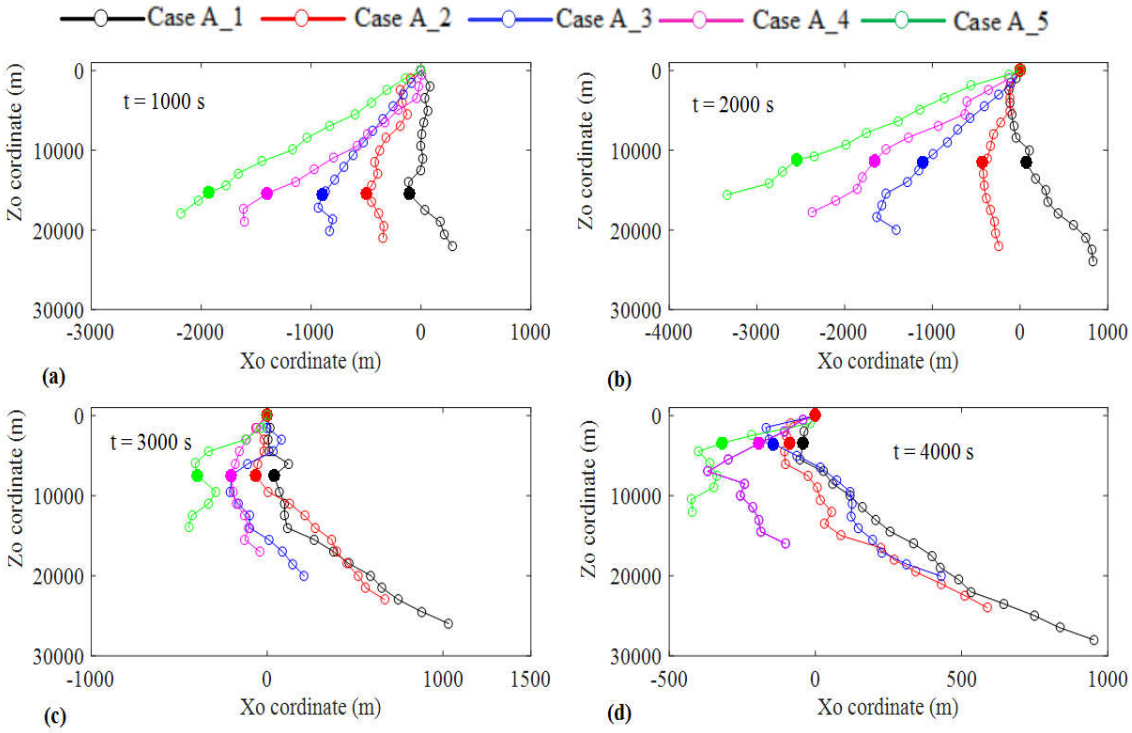

Figure 6.26 In-plane geometrical configuration of TSS in upward transfer with tether

deployment or retrieval at sub spacecraft.

Next, in case of the climber's downward transfer, another five numerical simulations are conducted with different deploying or retrieving velocities at main spacecraft. They are: two cases of tether deployment (Cases B_1 and B_2), two cases of tether retrieval (Cases B_3 and B_4), and one case of constant tether length (Cases B_3). The results are shown in Figs. 6.27-6.29. As shown in Figs. 6.27 and 6.28, it is found that the retrieval of tether at the main spacecraft pulls back the climber and makes the climber oscillating around the local vertical line. However, it excites a large amplitude of oscillation of TTS. For the deployment of tether, as shown in Fig. 6.28, it is helpful to suppress the oscillation motion. However, it is noted that the oscillation is no longer around the initial vertical line. For example, Fig. 6.29 shows that the TTS is inclined to the initial vertical when the main spacecraft deploys the tether. From the viewpoint of libration suppression, the deployment of tether is beneficial. However, the final equilibrium position of TTS deviates away from the initial radial direction significantly. Therefore, for the climber's downward transfer, the optimization of deploying or retrieving velocities at the main spacecraft cannot suppress the libration of TTS around the local vertical direction.

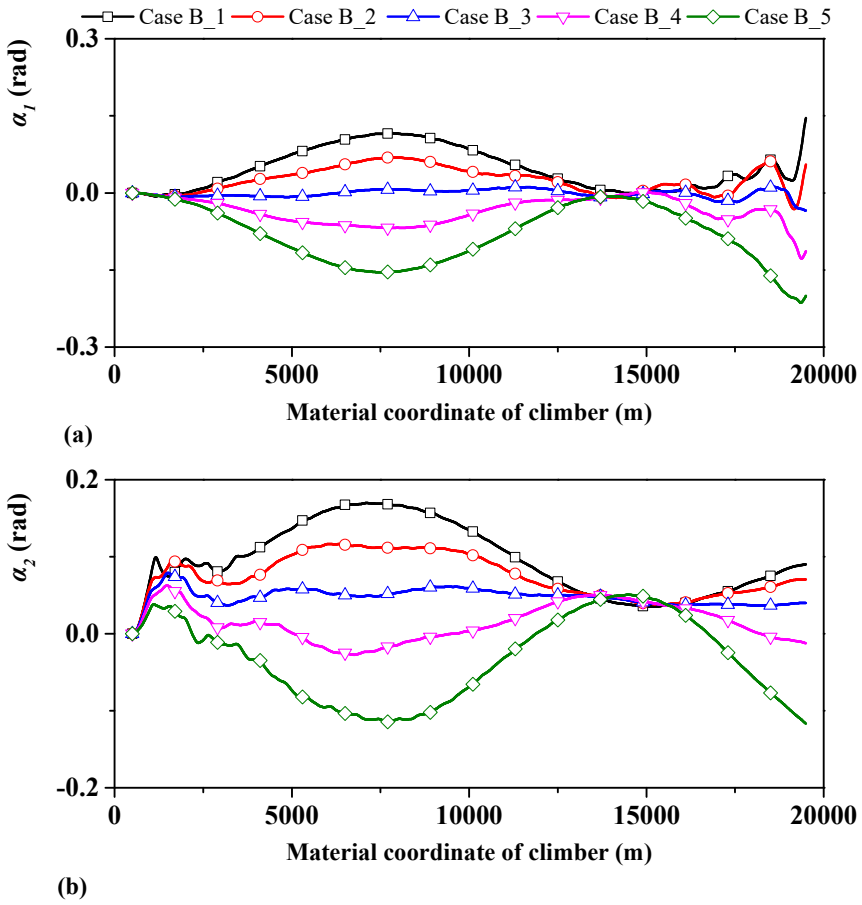

Figure 6.27 Libration angles of TSS in downward transfer with tether deployment or retrieval at main spacecraft. (a) Libration angle α_1. (b) Libration angle α_2.

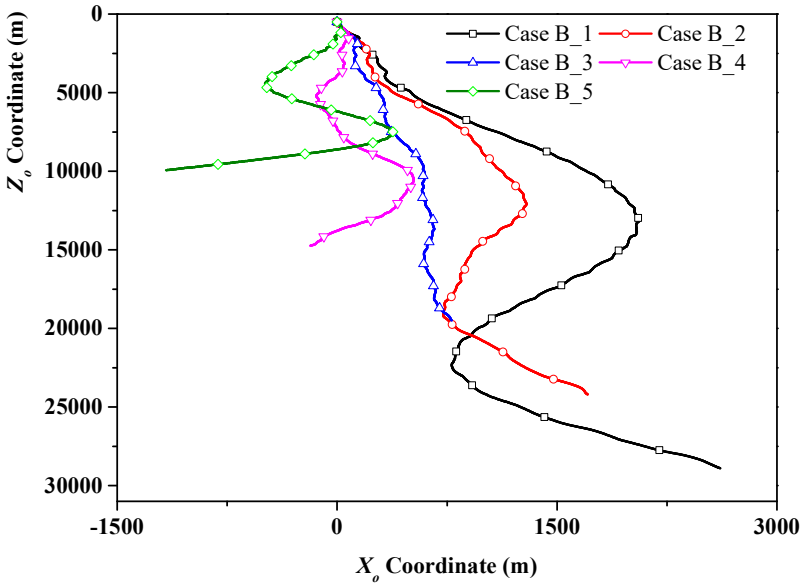

Figure 6.28 In-plane trajectory of climber with respect to main spacecraft in downward transfer with tether deployment or retrieval at main spacecraft.

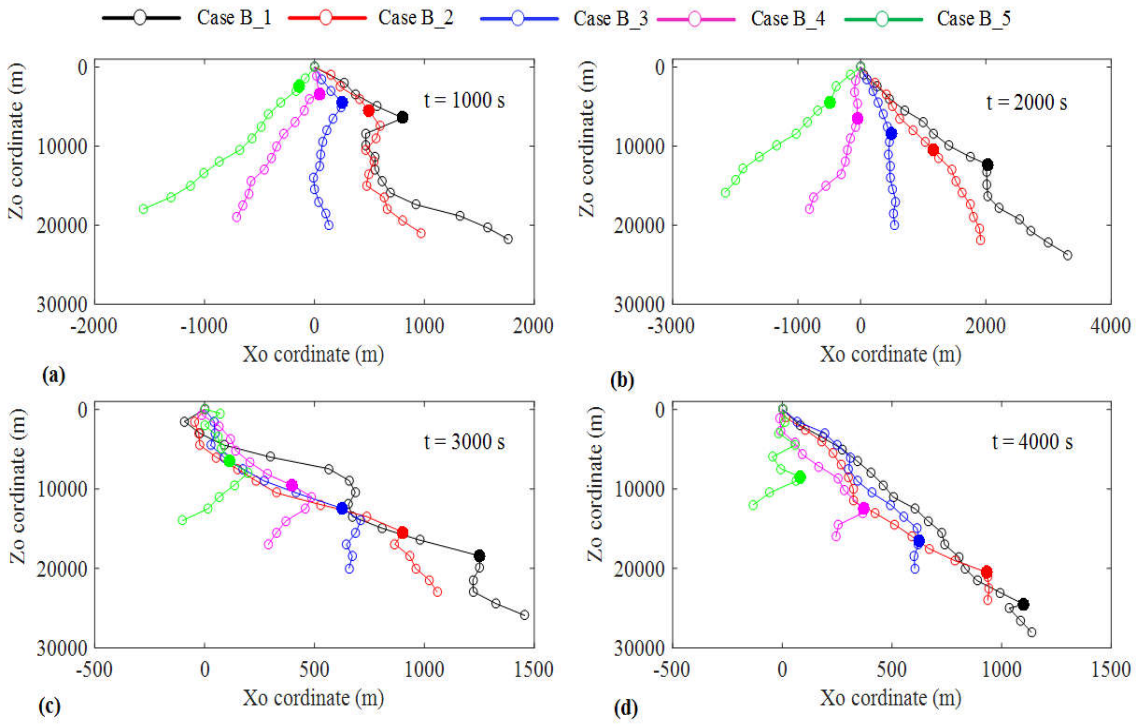

Figure 6.29 In-plane geometrical configuration of TSS in downward transfer with tether deployment or retrieval at main spacecraft.

In summary, for the climber's upward transfer motion, the deployment of tether at the sub spacecraft is helpful to suppress the libration motion, and the deployment speed should be optimized to minimize the libration oscillation. However, for the climber's downward transfer motion, the retrieval of tether at the main spacecraft pulls back the TTS. This makes the system oscillating around the local vertical and aggravates the amplitude of libration angles of TTS.

6.3 Conclusion

In this chapter, the dynamic behavior of TTS with climber is investigated under two situations: one is that the climber is moving along tether without tether deployment or retrieval, the other is that the climber is moving along tether with tether deployment and retrieval. For the first scenario, the results reveal that the orbital transfer by the climber will induce high frequency transverse oscillation of tether, which is not discovered by the existing rigid tether model. The oscillation could lead to the fatigue failure of tether and must be considered. For the second scenario, the deployment or retrieval velocity affects the dynamic behavior of TTS. From the viewpoint of suppressing the libration motion of TTS, the deployment of tether at the sub spacecraft produces positive effect in the climber's upward transfer motion. For the climber's downward transfer motion, the retrieval of tether at the main spacecraft pulls back the TTS. It makes the system oscillating around the local vertical and aggravates the amplitude of libration angles of TTS.

Chapter 7 CONCLUSIONS AND FUTURE WORK

Summary: This chapter summarizes the contributions and future research directions for the continuation of current work.

7.1 Summary of Contributions

This dissertation focuses on the modeling of TSS and the analysis of dynamic behaviors of TSS. The contributions ae summarized as follows.

7.1.1 Mathematical Modeling of Tethered Spacecraft System

(i) For the case of fixed tether length, the existing approach with the consideration of tether elasticity is prone to the numerical instability and error accumulation over long-term numerical integration. This study addresses the challenges by developing a high-fidelity and accurate model of TSS using a globally stable numerical approach that integrates the NPFEM with the implicit, Symplectic, 2-stage and 4th order Gaussian-Legendre Runge-Kutta time integration.

(ii) For the case of variable tether length, the high-fidelity and accurate model of TSS is expanded to model tether transportation system with climbers and tether deployment or retrieval in the framework of Arbitrary Lagrangian Eulerian. The proposed approach reveals the slack-taut phenomenon of tether happens as the climber starts to move, which is not reported by the rigid tether model.

7.1.2 Electrodynamic Tether System

(i) A high-fidelity multiphysics model is developed by coupling the high-fidelity TSS model with orbital motion limited theory for space plasma.

(ii) The proposed approach discretizes the tether dynamics in the spatial and time domain and the orbital motion limited theory in the spatial domain using the same finite element mesh. The resulting system equations consist of nodal positions, velocities, accelerations as well as electric current and potential bias as state variables and are solved in both domains simultaneously.

7.1.3 Electric Solar Wind Sail System

(i) The high-fidelity multiphysics model is used to investigate the coupling effects of orbital and self-spinning motions of E-sail, and the interaction between the axial/transverse elastic motions of tether and the Coulomb force.

(ii) Parametric study is conducted to better understand these coupling effects. The simulation results show that the coupling effects have a significant impact on the dynamic behavior of E-sail and the induced thrust.

(iii) An alternative approach is explored to define the normal vector of spin plane based on the geometrical configuration.

(iv) A modified control throttling algorithm is proposed to control attitude motion of E-sail.

7.1.4 Tether Transportation System with Climbers

(i) The high-fidelity TSS model using NPFEM_ALE is used for tether transportation system with climbers and tether deployment or retrieval.

7.2 Conclusions

For TSS, two detailed mathematical models have been developed to analysis the coupling effects of low Earth orbit environment on TSS. The first model is developed for the TSS with fixed tether length based nodal position finite element method, and a robust time integration with Symplectic property to eliminate the accumulation error due to the long-term integration. The second model is developed for the TSS with variable tether length based on the nodal position finite element in the Arbitrary Lagrangian Eulerian description. The material coordinate is introduced and as the state variables together with the position coordinate. The concept of moving node and variable-length element are brought to handle the tether length variation problem caused by the movement of climber along tether and deployment and retrieval of tether at the end spacecraft.

Then, the first model is applied to study the long-term dynamic behavior of EDT system with updated environmental external perturbative forces. Then, the specific tethered spacecraft model is extended, and a multiphysics coupled finite element model is developed, where the following two coupling effects are considered. First, the coupling effect between tether dynamics and electron collection efficiency, second, the coupling effect between thermal, elasticity, and electrical. Then, they are applied to study the long-term dynamic behavior of electrodynamic tether system in the deorbit process.

Next, the model of TSS with fixed tether length is applied to study the dynamic behavior of a spinning E-sail. Among it, a special subroutine with numerical damping is developed attenuate the initial transient oscillation caused by the unknown tension of an elastic tether. Then, the steady state of a spinning motion of E-sail are sent to couple the orbital motion. To control the attitude motion of a flexible E-sail, a modified and refined control strategy is developed by modulate the applied voltage of each tether. The increase of spin rate caused by the attitude maneuvering is controlled by the proposed spin rate controller based on the TI structure.

Finally, the model of TSS with variable tether length is applied to study the dynamic behavior of TTS. First, the results show the proposed approach can be easily applied to the case of multiple climbers by changing the properties of nodes and elements. Second, the model is applied to the study of tether transportation system with climbers and tether deployment and retrieval, and the tether deployment or retrieval velocity influence on the dynamic behavior of PSE is investigated.

7.3 Suggestions for Future Work

Based on the current study, the following researches are suggested to continue and expand the current work.

(i) The proposed model based on the nodal position finite element method can be applied to EDT for orbital maneuvering (lifting and decay).

(ii) The proposed approach based on the nodal position finite element in the Arbitrary Lagrangian-Eulerian description can be applied the deployment dynamic analysis

of E-sail.

(iii) The development of full dynamic coupling model of climber and tether. It is important to study the dynamic interaction between climber and tether, such as the contact force, and the propulsive force resulting from the thruster of climber.

(iv) The nodal position finite element method can be applied to study the deployment dynamics of bare tape tether that is stored in a folded form instead of winding on a drum.

(v) The proposed method can be applied to study the capture dynamics of tether capture system with the varying length.

Bibliography

[1] J.C. Liou, N.L. Johnson, Risks in Space from Orbiting Debris, Science, 311 (2006) 340.

[2] J.M. Fernandez, L. Visagie, M. Schenk, O.R. Stohlman, G.S. Aglietti, V.J. Lappas, S. Erb, Design and development of a gossamer sail system for deorbiting in low earth orbit, Acta Astronautica, 103 (2014) 204-225.

[3] C. Lücking, C. Colombo, C.R. McInnes, Solar Radiation Pressure-Augmented Deorbiting: Passive End-of-Life Disposal from High-Altitude Orbits, Journal of Spacecraft and Rockets, 50 (2013) 1256-1267.

[4] S.W. Ziegler, M.P. Cartmell, Using Motorized Tethers for Payload Orbital Transfer, Journal of Spacecraft and Rockets, 38 (2001) 904-913.

[5] J.R. Sanmartin, M. Martinez-Sanchez, E. Ahedo, Bare wire anodes for electrodynamic tethers, Journal of Propulsion and Power, 9 (1993) 353-360.

[6] D. Zanutto, E.C. Lorenzini, R. Mantellato, G. Colombatti, A. Sánchez Torres, Orbital debris mitigation through deorbiting with passive electrodynamic drag, (2012).

[7] C. Bombardelli, J. Pelaez, Ion Beam Shepherd for Contactless Space Debris Removal, Journal of Guidance, Control, and Dynamics, 34 (2011) 916-920.

[8] J.R. Sanmartin, E.C. Lorenzini, M. Martinez-Sanchez, Electrodynamic Tether Applications and Constraints, Journal of Spacecraft and Rockets, 47 (2010) 442-456.

[9] E.L.M. Lanoix, A.K. Misra, V.J. Modi, G. Tyc, Effect of Electromagnetic Forces on the Orbital Dynamics of Tethered Satellites, Journal of Guidance, Control, and Dynamics, 28 (2005) 1309-1315.

[10] L. Johnson, J. Ballance, B. Gilchrist, R. Estes, E. Lorenzini, Propulsive small expendable deployer system (ProSEDS) space experiment, in: 34th AIAA/ASME/SAE/ASEE Joint Propulsion Conference and Exhibit, 1998, pp. 4035.

[11] R. Hoyt, J. Slostad, I. Barnes, N. Voronka, M. Lewis, Cost-effective end-of-mission disposal of LEO microsatellites: The Terminator Tape, (2010).

[12] P. Janhunen, Electric Sail for Spacecraft Propulsion, Journal of Propulsion and Power, 20 (2004) 763-764.

[13] G. Mengali, A.A. Quarta, P. Janhunen, Electric Sail Performance Analysis, Journal of Spacecraft and Rockets, 45 (2008) 122-129.

[14] P. Toivanen, P. Janhunen, Electric Solar Wind Sail: Deployment, Long-Term Dynamics, and Control Hardware Requirements, in: M. Macdonald (Ed.) Advances in Solar Sailing, Springer Berlin Heidelberg, Berlin, Heidelberg, 2014, pp. 977-987.

[15] P. Janhunen, A. Sandroos, Simulation study of solar wind push on a charged wire: basis of solar wind electric sail propulsion, Annales Geophysicae, 25 (2007) 755-767.

[16] C. Liu, Q. Tian, D. Yan, H. Hu, Dynamic analysis of membrane systems undergoing overall motions, large deformations and wrinkles via thin shell elements of ANCF, Computer Methods in Applied Mechanics and Engineering, 258 (2013) 81-95.

[17] J. Zhao, Q. Tian, H.-Y. Hu, Deployment dynamics of a simplified spinning IKAROS solar sail via absolute coordinate based method, Acta Mechanica Sinica, 29 (2013) 132-142.

[18] X. Hu, S. Gong, Flexibility influence on passive stability of a spinning solar sail, Aerospace Science and Technology, 58 (2016) 60-70.

[19] R.M. Zubrin, D.G. Andrews, Magnetic sails and interplanetary travel, Journal of Spacecraft and Rockets, 28 (1991) 197-203.

[20] R.H. Frisbee, Advanced Space Propulsion for the 21st Century, Journal of Propulsion and Power, 19 (2003) 1129-1154.

[21] P. Toivanen, P. Janhunen, J. Envall, Electric sail control mode for amplified transverse thrust, Acta Astronautica, 106 (2015) 111-119.

[22] P. Janhunen, J.-P. Lebreton, S. Merikallio, M. Paton, G. Mengali, A.A. Quarta, Fast E-sail Uranus entry probe mission, Planetary and Space Science, 104 (2014) 141-146.

[23] A.A. Quarta, G. Mengali, P. Janhunen, Electric sail option for cometary rendezvous, Acta Astronautica, 127 (2016) 684-692.

[24] M. Huo, G. Mengali, A.A. Quarta, Optimal planetary rendezvous with an electric sail, Aircraft Engineering and Aerospace Technology, 88 (2016) 515-522.

[25] G. Mengali, A.A. Quarta, Non-Keplerian orbits for electric sails, Celestial Mechanics and Dynamical Astronomy, 105 (2009) 179-195.

[26] M. Huo, H. Liao, Y. Liu, N. Qi, The Coupled Orbit-Attitude Dynamics and Control of Electric Sail in Displaced Solar Orbits, International Journal of Aerospace Engineering, 2017 (2017) 12.

[27] A.A. Quarta, G. Mengali, Electric Sail Mission Analysis for Outer Solar System Exploration, Journal of Guidance, Control, and Dynamics, 33 (2010) 740-755.

[28] P. Woo, A.K. Misra, Energy considerations in the partial space elevator, Acta Astronautica, 99 (2014) 78-84.

[29] P. Woo, A.K. Misra, Dynamics of a partial space elevator with multiple climbers, Acta Astronautica, 67 (2010) 753-763.

[30] U. Kirchgraber, U. Manz, D. Stoffer, Rigorous Proof of Chaotic Behaviour in a Dumbbell Satellite Model, Journal of Mathematical Analysis and Applications, 251 (2000) 897-911.

[31] J.R. Ellis, C.D. Hall, Model Development and Code Verification for Simulation of Electrodynamic Tether System, Journal of Guidance, Control, and Dynamics, 32 (2009) 1713-1722.

[32] D.P. Jin, H. Wen, H. Chen, Nonlinear resonance of a subsatellite on a short constant tether, Nonlinear Dynamics, 71 (2013) 479-488.

[33] W. Jung, A.P. Mazzoleni, J. Chung, Nonlinear dynamic analysis of a three-body tethered satellite system with deployment/retrieval, Nonlinear Dynamics, 82 (2015) 1127-1144.

[34] X. Dafu, K. Xianren, L. Jun, Y. Zhengxian, W. Feng, Dynamic modeling and simulation of electrodynamic tether system in stationkeeping phase, Journal of Mechanical Science and Technology, 25 (2011) 97-102.

[35] M. Krupa, W. Poth, M. Schagerl, A. Steindl, W. Steiner, H. Troger, G. Wiedermann, Modelling, Dynamics and Control of Tethered Satellite Systems, Nonlinear Dynamics, 43 (2006) 73-96.

[36] K.U. Kristiansen, P. Palmer, M. Roberts, A Unification of Models of Tethered Satellites, SIAM Journal on Applied Dynamical Systems, 10 (2011) 1042-1069.

[37] T. Lee, M. Leok, N. Harris McClamroch, High-fidelity numerical simulation of complex dynamics of tethered spacecraft, Acta Astronautica, 99 (2014) 215-230.

[38] J. Peláez, M. Sanjurjo, Generator Regime of Self-Balanced Electrodynamic Bare Tethers, Journal of Spacecraft and Rockets, 43 (2006) 1359-1369.

[39] o. Jes, s. Pel-Uuml, ez, M. Ruiz, O. L-igrave, R. pez, E.C. Lorenzini, M.L. Cosmo, Two-Bar Model for the Dynamics and Stability of Electrodynamic Tethers, Journal of Guidance, Control, and Dynamics, 25 (2002) 1125-1135.

[40] R. Zhong, Z.H. Zhu, Libration dynamics and stability of electrodynamic tethers in satellite deorbit, Celestial Mechanics and Dynamical Astronomy, 116 (2013) 279-298.

[41] J. Zhang, Z.H. Zhu, Z.W. Sun, Reduction of Libration Angle in Electrodynamic Tether Deployment by Lorentz Force, Journal of Guidance, Control, and Dynamics, 40 (2016) 164-169.

[42] G. Li, Z.H. Zhu, Multiphysics Finite Element Modeling of Current Generation of Bare Flexible Electrodynamic Tether, Journal of Propulsion and Power, 33 (2016) 408-419.

[43] G. Li, Z.H. Zhu, J. Cain, F. Newland, A. Czekanski, Libration Control of Bare Electrodynamic Tethers Considering Elastic–Thermal–Electrical Coupling, Journal of Guidance, Control, and Dynamics, 39 (2015) 642-654.

[44] S. Kawamoto, T. Makida, F. Sasaki, Y. Okawa, S.-i. Nishida, Precise numerical simulations of electrodynamic tethers for an active debris removal system, Acta Astronautica, 59 (2006) 139-148.

[45] P. Janhunen, P. Toivanen, TI tether rig for solving secular spinrate change problem of electric sail, arXiv preprint arXiv:1603.05563, (2016).

[46] K. Tao, Y. Yamagiwa, K. Otsuka, Y. Ishikawa, Study about the simultaneous deployment performance of the cables from GEO station at the space elevator construction, Acta Astronautica, 138 (2017) 590-595.

[47] Y. Ishikawa, K. Otsuka, Y. Yamagiwa, H. Doi, Effects of ascending and descending climbers on space elevator cable dynamics, Acta Astronautica, 145 (2018) 165-173.

[48] X. Sun, M. Xu, R. Zhong, Dynamic analysis of the tether transportation system using absolute nodal coordinate formulation, Acta Astronautica, 139 (2017) 266-277.

[49] W. Jung, A.P. Mazzoleni, J. Chung, Dynamic analysis of a tethered satellite system with a moving mass, Nonlinear Dynamics, 75 (2014) 267-281.

[50] K.D. Kumar, Review on Dynamics and Control of Nonelectrodynamic Tethered Satellite Systems, Journal of Spacecraft and Rockets, 43 (2006) 705-720.

[51] P. Williams, P. Trivailo, Dynamics of Circularly Towed Aerial Cable Systems, Part I: Optimal Configurations and Their Stability, Journal of Guidance, Control, and Dynamics, 30 (2007) 753-765.

[52] H.A. Fujii, T. Watanabe, T. Kusagaya, D. Sato, M. Ohta, Dynamics of a Flexible Space Tether Equipped with a Crawler Mass, Journal of Guidance, Control, and Dynamics, 31 (2008) 436-440.

[53] H.I. Park, D.Y. Kwon, D.H. Jung, A Numerical Analysis For the Dynamic Behavior of ROV Launcher And Umbilical Cable Under Combined Excitations, in: The Fifteenth International Offshore and Polar Engineering Conference, International Society of Offshore and Polar Engineers, Seoul, Korea, 2005, pp. 6.

[54] C. Gatti-Bono, N.C. Perkins, PHYSICAL AND NUMERICAL MODELLING OF THE DYNAMIC BEHAVIOR OF A FLY LINE, Journal of Sound and Vibration, 255 (2002) 555-577.

[55] J.C. Simo, N. Tarnow, The discrete energy-momentum method. Conserving algorithms for nonlinear elastodynamics, Zeitschrift für angewandte Mathematik und Physik ZAMP, 43 (1992) 757-792.

[56] J.C. Simo, N. Tarnow, M. Doblare, Non-linear dynamics of three-dimensional rods: Exact energy and momentum conserving algorithms, International Journal for Numerical Methods in Engineering, 38 (1995) 1431-1473.

[57] A.M. Jablonski, R. Scott, Deorbiting of low earth orbit (LEO) microsatellites, Canadian Aeronautics and Space Journal, 55 (2009) 55-67.

[58] C.T. Howell, Investigation of the dynamics of low-tension cables, in, Woods Hole Oceanographic Institution MA, 1992.

[59] B. Buckham, F.R. Driscoll, M. Nahon, Development of a Finite Element Cable Model for Use in Low-Tension Dynamics Simulation, Journal of Applied Mechanics, 71 (2004) 476-485.

[60] Z.H. Zhu, S.A. Meguid, Elastodynamic Analysis of Aerial Refueling Hose Using Curved Beam Element, AIAA Journal, 44 (2006) 1317-1324.

[61] K.U. Kristiansen, P.L. Palmer, R.M. Roberts, Numerical modelling of elastic space tethers, Celestial Mechanics and Dynamical Astronomy, 113 (2012) 235-254.

[62] Z. Zhu, S. Meguid, L. Ong, -Dynamic multiscale simulation of towed cable and body, in: Computational Fluid and Solid Mechanics 2003, Elsevier, 2003, pp. 800-803.

[63] Z.H. Zhu, Dynamic modeling of cable system using a new nodal position finite element method, International Journal for Numerical Methods in Biomedical Engineering, 26 (2010) 692-704.

[64] F. Wang, G.-l. Huang, D.-h. Deng, Dynamic response analysis of towed cable during deployment/retrieval, Journal of Shanghai Jiaotong University (Science), 13 (2008) 245.

[65] Z.H. Zhu, S.A. Meguid, Modeling and simulation of aerial refueling by finite element method, International Journal of Solids and Structures, 44 (2007) 8057-8073.

[66] H.G. James, K.G. Balmain, Guided electromagnetic waves observed on a conducting ionospheric tether, Radio Science, 36 (2001) 1631-1644.

[67] G.Q. Li, Z.H. Zhu, Long-term dynamic modeling of tethered spacecraft using nodal position finite element method and symplectic integration, Celestial Mechanics and Dynamical Astronomy, 123 (2015) 363-386.

[68] P. Williams, Dynamic multibody modeling for tethered space elevators, Acta Astronautica, 65 (2009) 399-422.

[69] V.S. Aslanov, A.S. Ledkov, A.K. Misra, A.D. Guerman, Dynamics of Space Elevator After Tether Rupture, Journal of Guidance, Control, and Dynamics, 36 (2013) 986-992.

[70] S.S. Cohen, A.K. Misra, Elastic Oscillations of the Space Elevator Ribbon, Journal of Guidance, Control, and Dynamics, 30 (2007) 1711-1717.

[71] V.S. Aslanov, A.S. Ledkov, Dynamics of Reusable Tether System with Sliding Bead Capsule for Deorbiting Small Payloads, Journal of Spacecraft and Rockets, (2018) 1-9.

[72] H. Wen, Z.H. Zhu, D. Jin, H. Hu, Space Tether Deployment Control with Explicit Tension Constraint and Saturation Function, Journal of Guidance, Control, and Dynamics, 39 (2015) 916-921.

[73] H. Kojima, Y. Sugimoto, Y. Furukawa, Experimental study on dynamics and control of tethered satellite systems with climber, Acta Astronautica, 69 (2011) 96-108.

[74] B.S. Yu, P.B. Dai, D.P. Jin, Modeling and dynamics of a bare tape-shaped tethered satellite system, Aerospace Science and Technology, 79 (2018) 288-296.

[75] F.J. Sun, Z.H. Zhu, M. LaRosa, Dynamic modeling of cable towed body using nodal position finite element method, Ocean Engineering, 38 (2011) 529-540.

[76] G. Li, Z.H. Zhu, S. Ruel, S.A. Meguid, Multiphysics elastodynamic finite element analysis of space debris deorbit stability and efficiency by electrodynamic tethers, Acta Astronautica, 137 (2017) 320-333.

[77] G. Li, Z.H. Zhu, Precise Analysis of Deorbiting by Electrodynamic Tethers Using Coupled Multiphysics Finite Elements, Journal of Guidance, Control, and Dynamics, 40 (2017) 3348-3357.

[78] J.M. Aristoff, J.T. Horwood, A.B. Poore, Orbit and uncertainty propagation: a comparison of Gauss–Legendre-, Dormand–Prince-, and Chebyshev–Picard-based approaches, Celestial Mechanics and Dynamical Astronomy, 118 (2014) 13-28.

[79] J.M. Aristoff, J.T. Horwood, A.B. Poore, Implicit-Runge–Kutta-based methods for fast, precise, and scalable uncertainty propagation, Celestial Mechanics and Dynamical Astronomy, 122 (2015) 169-182.

[80] C. Pardini, T. Hanada, P.H. Krisko, Benefits and risks of using electrodynamic tethers to de-orbit spacecraft, Acta Astronautica, 64 (2009) 571-588.

[81] J. Pelaez, M. Ruiz, O. Lopez-Rebollal, E.C. Lorenzini, M.L. Cosmo, Two-bar model for the dynamics and stability of electrodynamic tethers, Journal of Guidance Control and Dynamics, 25 (2002) 1125-1135.

[82] R. Zhong, Z.H. Zhu, Optimal Control of Nanosatellite Fast Deorbit Using Electrodynamic Tether, Journal of Guidance, Control, and Dynamics, 37 (2014) 1182-1194.

[83] D. Zanutto, E.C. Lorenzini, R. Mantellato, G. Colombatti, A. Sánchez Torres, Orbital debris mitigation through deorbiting with passive electrodynamic drag, 63th International Astronautical Congress, (2012).

[84] P. Williams, S. Yeo, C. Blanksby, Heating and Modeling Effects in Tethered Aerocapture Missions, Journal of Guidance, Control, and Dynamics, 26 (2003) 643-654.

[85] J. Pelaez, E.C. Lorenzini, O. Lopez-Rebollal, M. Ruiz, A new kind of dynamic instability in electrodynamic tethers, J. Astronaut. Sci., 48 (2000) 449-476.

[86] L. Somenzi, L. Iess, J. Pelaez, Linear Stability Analysis of Electrodynamic Tethers, Journal of Guidance, Control, and Dynamics, 28 (2005) 843-849.

[87] H. Kojima, T. Sugimoto, Stability analysis of in-plane and out-of-plane periodic motions of electrodynamic tether system in inclined elliptic orbit, Acta Astronautica, 65 (2009) 477-488.

[88] Y. Yamaigiwa, E. Hiragi, T. Kishimoto, Dynamic behavior of electrodynamic tether deorbit system on elliptical orbit and its control by Lorentz force, Aerospace Science and Technology, 9 (2005) 366-373.

[89] B.S. Yu, D.P. Jin, Deployment and retrieval of tethered satellite system under J2 perturbation and heating effect, Acta Astronautica, 67 (2010) 845-853.

[90] R. Mantellato, M. Pertile, G. Colombatti, A. Valmorbida, E.C. Lorenzini, Two-bar model for free vibrations damping of space tethers by means of spring-dashpot devices, CEAS Space J, 6 (2014) 133-143.

[91] P. Williams, T. Watanabe, C. Blanksby, P. Trivailo, H.A. Fujii, Libration Control of Flexible Tethers Using Electromagnetic Forces and Movable Attachment, Journal of Guidance, Control, and Dynamics, 27 (2004) 882-897.

[92] P. Williams, Energy Rate Feedback for Libration Control of Electrodynamic Tethers, Journal of Guidance, Control, and Dynamics, 29 (2006) 221-223.

[93] J. Corsi, L. Iess, Stability and control of electrodynamic tethers for de-orbiting applications, Acta Astronautica, 48 (2001) 491-501.

[94] N. Takeichi, Practical Operation Strategy for Deorbit of an Electrodynamic Tethered System, Journal of Spacecraft and Rockets, 43 (2006) 1283-1288.

[95] S.G. Tragesser, H. San, Orbital Maneuvering with Electrodynamic Tethers, Journal of Guidance, Control, and Dynamics, 26 (2003) 805-810.

[96] N.J. Sabey, S. Tragesser, General Perturbations Guidance Scheme for Electrodynamic Orbital Maneuvers with Libration Effects, Journal of Guidance, Control, and Dynamics, (2015) 1-8.

[97] P. Tortora, L. Somenzi, L. Iess, R. Licata, Small Mission Design for Testing In-Orbit an Electrodynamic Tether Deorbiting System, Journal of Spacecraft and Rockets, 43 (2006) 883-892.

[98] M. Iñarrea, V. Lanchares, A.I. Pascual, J.P. Salas, Attitude stabilization of electrodynamic tethers in elliptic orbits by time-delay feedback control, Acta Astronautica, 96 (2014) 280-295.

[99] P. Williams, Libration Control of Electrodynamic Tethers Using Predictive Control with Time-Delayed Feedback, Journal of Guidance, Control, and Dynamics, 32 (2009) 1254-1268.

[100] E. Ahedo, J.R. Sanmart-egrave, Analysis of Bare-Tether Systems for Deorbiting Low-Earth-Orbit Satellites, Journal of Spacecraft and Rockets, 39 (2002) 198-205.

[101] G. Sánchez-Arriaga, C. Bombardelli, X. Chen, Impact of Nonideal Effects on Bare Electrodynamic Tether Performance, Journal of Propulsion and Power, 31 (2015) 951-955.

[102] M. Sanjurjo-Rivo, G. Sánchez-Arriaga, J. Peláez, Efficient Computation of Current Collection in Bare Electrodynamic Tethers in and beyond OML Regime, Journal of Aerospace Engineering, 28 (2015) 04014144.

[103] D.M. Blash, J.D. Williams, Determination of hollow cathode plasma contactor system requirements using an electrodynamic tether system simulation tool, in: 13th Spacecraft Charging and Technology Conference, Pasadena, CA, 2014.

[104] J.R. Sanmartin, M. Charro, E.C. Lorenzini, H.B. Garrett, C. Bombardelli, C. Bramanti, Electrodynamic Tether at Jupiter—I: Capture Operation and Constraints, IEEE Transactions on Plasma Science, 36 (2008) 2450-2458.

[105] C. Bombardelli, D. Zanutto, E. Lorenzini, Deorbiting Performance of Bare Electrodynamic Tethers in Inclined Orbits, Journal of Guidance, Control, and Dynamics, 36 (2013) 1550-1556.

[106] A. Rocchi, M. Lavagna, Versatile electro-dynamic tethers dynamics simulator for debris mitigation tools design, in: Proceedings of the 13th Symposium on Advanced Space Technologies in Robotics and Automation, European Space Agency Noordwijk, The Netherlands, 2015.

[107] G. Li, Z.H. Zhu, Multiphysics Finite Element Modeling of Current Generation of Bare Flexible Electrodynamic Tether, JOURNAL OFPROPULSION ANDPOWER, 33 (2017) 408-419.

[108] P.K. Toivanen, P. Janhunen, Spin Plane Control and Thrust Vectoring of Electric Solar Wind Sail, Journal of Propulsion and Power, 29 (2012) 178-185.

[109] M. Huo, J. Zhao, S. Xie, N. Qi, Coupled Attitude-Orbit Dynamics and Control for an Electric Sail in a Heliocentric Transfer Mission, PLOS ONE, 10 (2015) e0125901.

[110] M. Huo, G. Mengali, A.A. Quarta, Electric Sail Thrust Model from a Geometrical Perspective, Journal of Guidance, Control, and Dynamics, 41 (2017) 735-741.

[111] P. Toivanen, P. Janhunen, Thrust vectoring of an electric solar wind sail with a realistic sail shape, Acta Astronautica, 131 (2017) 145-151.

[112] M. Bassetto, G. Mengali, A.A. Quarta, Thrust and torque vector characteristics of axially-symmetric E-sail, Acta Astronautica, 146 (2018) 134-143.

[113] P. Janhunen, P. Toivanen, An intrinsic way to control E-sail spin, arXiv preprint arXiv:1406.6847, (2014).

[114] P. Toivanen, P. Janhunen, J. Envall, S. Merikallio, Electric solar wind sail control and navigation, Advances in the Astronautical Sciences, 145 (2012) 275-285.

[115] P. Janhunen, Photonic spin control for solar wind electric sail, Acta Astronautica, 83 (2013) 85-90.

[116] P. Janhunen, P. Toivanen, J. Polkko, S. Merikallio, P. Salminen, E. Haeggström, H. Seppänen, R. Kurppa, J. Ukkonen, S. Kiprich, Electric Solar Wind Sail In-Space Propulsion Status Report, in: Space Propulsion, 2010, San Sebastian, Spain, May 3-6, 2010, 2010.

[117] S.S. Cohen, A.K. Misra, The effect of climber transit on the space elevator dynamics, Acta Astronautica, 64 (2009) 538-553.

[118] G. Shi, Z. Zhu, Z.H. Zhu, Libration suppression of tethered space system with a moving climber in circular orbit, Nonlinear Dynamics, 91 (2018) 923-937.

[119] G. Shi, Z. Zhu, Z.H. Zhu, Stable orbital transfer of partial space elevator by tether deployment and retrieval, Acta Astronautica, 152 (2018) 624-629.

[120] A.K. Misra, Z. Amier, V.J. Modi, Attitude dynamics of three-body tethered systems, Acta Astronautica, 17 (1988) 1059-1068.

[121] D.A. Vallado, Fundamentals of astrodynamics and applications, Springer Science & Business Media, 2001.

[122] E. Hairer, C. Lubich, G. Wanner, Geometric numerical integration: structure-preserving algorithms for ordinary differential equations, Springer Science & Business Media, 2006.

[123] X. Wu, K. Liu, W. Shi, Structure-preserving algorithms for oscillatory differential equations II, Springer, 2015.

[124] D. Hong, G. Ren, A modeling of sliding joint on one-dimensional flexible medium, Multibody System Dynamics, 26 (2011) 91-106.

[125] J.L. Tang, G.X. Ren, W.D. Zhu, H. Ren, Dynamics of variable-length tethers with application to tethered satellite deployment, Communications in Nonlinear Science and Numerical Simulation, 16 (2011) 3411-3424.

[126] D. Hong, J. Tang, G. Ren, Dynamic modeling of mass-flowing linear medium with large amplitude displacement and rotation, Journal of Fluids and Structures, 27 (2011) 1137-1148.

[127] G. Li, Z.H. Zhu, S.A. Meguid, Libration and transverse dynamic stability control of flexible bare electrodynamic tether systems in satellite deorbit, Aerospace Science and Technology, 49 (2016) 112-129.

[128] R. Zhong, Z.H. Zhu, Dynamics of Nanosatellite Deorbit by Bare Electrodynamic Tether in Low Earth Orbit, Journal of Spacecraft and Rockets, 50 (2013) 691-700.

[129] R. Zhong, Z.H. Zhu, Long-Term Libration Dynamics and Stability Analysis of Electrodynamic Tethers in Spacecraft Deorbit, Journal of Aerospace Engineering, 27 (2014) 04014020.

[130] C.C. Finlay, S. Maus, C.D. Beggan, T.N. Bondar, A. Chambodut, etc, International Geomagnetic Reference Field: the eleventh generation, Geophysical Journal International, 183 (2010) 1216-1230.

[131] V. Anguero, R. Adamo, Space applications of spindt cathode field emission arrays, in: 6th Spacecraft Charging Technology, 1998, pp. 347-352.

[132] J.R. Sanmartín, R.D. Estes, The orbital-motion-limited regime of cylindrical Langmuir probes, Physics of Plasmas, 6 (1999) 395-405.

[133] D. Bilitza, L.-A. McKinnell, B. Reinisch, T. Fuller-Rowell, The international reference ionosphere today and in the future, Journal of Geodesy, 85 (2011) 909-920.

[134] Z. Zhu, R. Zhong, Deorbiting dynamics of electrodynamic tether, International Journal of Aerospace and Lightweight Structures (IJALS), 1 (2011).

[135] K. Fuhrhop, D. Morris, B. Gilchrist, Electron emission for electrodynamic tether systems in space, in: 40th AIAA/ASME/SAE/ASEE Joint Propulsion Conference and Exhibit, pp. 3495.

[136] J. Cain, F. Newland, AIM Microsatellite Platform: A Canadian Multi-Mission Satellite Bus Solution, in: 30th AIAA International Communications Satellite System Conference (ICSSC), American Institute of Aeronautics and Astronautics, 2012.

[137] P. Janhunen, A. Sandroos, Simulation study of solar wind push on a charged wire: basis of solar wind electric sail propulsion, Ann. Geophys., 25 (2007) 755-767.

[138] A. Sanchez-Torres, Propulsive Force in an Electric Solar Sail, Contributions to Plasma Physics, 54 (2014) 314-319.

[139] P. Janhunen, A.A. Quarta, G. Mengali, Electric solar wind sail mass budget model, Geosci. Instrum. Method. Data Syst., 2 (2013) 85-95.

[140] F. Liu, Q. Hu, J. Zhang, K. Yang, Y. Li, Dynamics of Single Charged Wire for Solar Wind Electric Sail.

Appendices

APPENDIX A Extended Mass Matrix

The mass matrices in Eq. (3.35)are defined as,

$$\boldsymbol{M}_{12} = \left(\frac{p_{k+1} - p_k}{2}\right)\int_{-1}^{1} \rho_k A_k \boldsymbol{N}_{a,k}^T \frac{\partial \boldsymbol{N}_{a,k}}{\partial p_k} d\xi \boldsymbol{X}_{a,k}$$
$$= -\frac{1}{6}\rho_k A_k \begin{bmatrix} -2 & 0 & 0 & 2 & 0 & 0 \\ 0 & -2 & 0 & 0 & 2 & 0 \\ 0 & 0 & -2 & 0 & 0 & 2 \\ -1 & 0 & 0 & 1 & 0 & 0 \\ 0 & -1 & 0 & 0 & 1 & 0 \\ 0 & 0 & -1 & 0 & 0 & 1 \end{bmatrix} \boldsymbol{X}_{a,k} \tag{A.1}$$

$$\boldsymbol{M}_{13} = \left(\frac{p_{k+1} - p_k}{2}\right)\int_{-1}^{1} \rho_k A_k \boldsymbol{N}_{a,k}^T \frac{\partial \boldsymbol{N}_{a,k}}{\partial p_{k+1}} d\xi \boldsymbol{X}_{a,k}$$
$$= -\frac{1}{6}\rho_k A_k \begin{bmatrix} -1 & 0 & 0 & 1 & 0 & 0 \\ 0 & -1 & 0 & 0 & 1 & 0 \\ 0 & 0 & -1 & 0 & 0 & 1 \\ -2 & 0 & 0 & 2 & 0 & 0 \\ 0 & -2 & 0 & 0 & 2 & 0 \\ 0 & 0 & -2 & 0 & 0 & 2 \end{bmatrix} \boldsymbol{X}_{a,k} \tag{A.2}$$

$$\boldsymbol{M}_{22} = \boldsymbol{X}_{a,k}^{T}\left(\frac{p_{k+1}-p_k}{2}\right)\int_{-1}^{1}\rho_k A_k\left(\frac{\partial \boldsymbol{N}_{a,k}}{\partial p_k}\right)^{T}\frac{\partial \boldsymbol{N}_{a,k}}{\partial p_k}d\xi \boldsymbol{X}_{a,k}$$

$$= \frac{1}{3}\frac{\rho_k A_k}{p_{k+1}-p_k}\boldsymbol{X}_{a,k}^{T}\begin{bmatrix} 1 & 0 & 0 & -1 & 0 & 0 \\ 0 & 1 & 0 & 0 & -1 & 0 \\ 0 & 0 & 1 & 0 & 0 & -1 \\ -1 & 0 & 0 & 1 & 0 & 0 \\ 0 & -1 & 0 & 0 & 1 & 0 \\ 0 & 0 & -1 & 0 & 0 & 1 \end{bmatrix}\boldsymbol{X}_{a,k} \tag{A.3}$$

$$\boldsymbol{M}_{23} = \boldsymbol{X}_{a,k}^{T}\left(\frac{p_{k+1}-p_k}{2}\right)\int_{-1}^{1}\rho_k A_k\left(\frac{\partial \boldsymbol{N}_{a,k}}{\partial p_k}\right)^{T}\frac{\partial \boldsymbol{N}_{a,k}}{\partial p_{k+1}}d\xi \boldsymbol{X}_{a,k}$$

$$= \frac{1}{6}\frac{\rho_k A_k}{p_{k+1}-p_k}\boldsymbol{X}_{a,k}^{T}\begin{bmatrix} 1 & 0 & 0 & -1 & 0 & 0 \\ 0 & 1 & 0 & 0 & -1 & 0 \\ 0 & 0 & 1 & 0 & 0 & -1 \\ -1 & 0 & 0 & 1 & 0 & 0 \\ 0 & -1 & 0 & 0 & 1 & 0 \\ 0 & 0 & -1 & 0 & 0 & 1 \end{bmatrix}\boldsymbol{X}_{a,k} \tag{A.4}$$

$$\boldsymbol{M}_{33} = \boldsymbol{X}_{a,k}^{T}\left(\frac{p_{k+1}-p_k}{2}\right)\int_{-1}^{1}\rho_k A_k\left(\frac{\partial \boldsymbol{N}_{a,k}}{\partial p_{k+1}}\right)^{T}\frac{\partial \boldsymbol{N}_{a,k}}{\partial p_{k+1}}d\xi \boldsymbol{X}_{a,k}$$

$$= \frac{1}{3}\frac{\rho_k A_k}{p_{k+1}-p_k}\boldsymbol{X}_{a,k}^{T}\begin{bmatrix} 1 & 0 & 0 & -1 & 0 & 0 \\ 0 & 1 & 0 & 0 & -1 & 0 \\ 0 & 0 & 1 & 0 & 0 & -1 \\ -1 & 0 & 0 & 1 & 0 & 0 \\ 0 & -1 & 0 & 0 & 1 & 0 \\ 0 & 0 & -1 & 0 & 0 & 1 \end{bmatrix}\boldsymbol{X}_{a,k} \tag{A.5}$$

APPENDIX B Additional Inertial Term

The detailed expressions of the additional term $\boldsymbol{Q}_{p,k}$ due to the mass flow are obtained as,

$$\boldsymbol{Q}_{p,k} = \sum_{j=1}^{5} \boldsymbol{Q}_{p,k}^{j} \tag{B.1}$$

$$\boldsymbol{Q}_{p,k}^{1} = \begin{bmatrix} \boldsymbol{Q}_{p,k}^{1,1} & \boldsymbol{Q}_{p,k}^{1,2} & \boldsymbol{Q}_{p,k}^{1,3} \end{bmatrix} \tag{B.2}$$

$$\begin{aligned} \boldsymbol{Q}_{p,k}^{1,1} &= \rho_k A_k \left(p_{k+1} - p_k \right) \dot{p}_k \int_{-1}^{1} \boldsymbol{N}_{a,k}^{T} \frac{\partial \boldsymbol{N}_{a,k}}{\partial p_k} d\xi \dot{\boldsymbol{X}}_{a,k} \\ &= -\frac{1}{3} \rho A \dot{p}_k \begin{bmatrix} -2 & 0 & 0 & 2 & 0 & 0 \\ 0 & -2 & 0 & 0 & 2 & 0 \\ 0 & 0 & -2 & 0 & 0 & 2 \\ -1 & 0 & 0 & 1 & 0 & 0 \\ 0 & -1 & 0 & 0 & 1 & 0 \\ 0 & 0 & -1 & 0 & 0 & 1 \end{bmatrix} \dot{\boldsymbol{X}}_{a,k} \end{aligned} \tag{B.3}$$

$$\begin{aligned} \boldsymbol{Q}_{p,k}^{1,2} &= \rho_k A_k \left(p_{k+1} - p_k \right) \dot{p}_k \boldsymbol{X}_{a,k}^{T} \int_{-1}^{1} \left(\frac{\partial \boldsymbol{N}_{a,k}}{\partial p_k} \right)^{T} \frac{\partial \boldsymbol{N}_{a,k}}{\partial p_k} d\xi \dot{\boldsymbol{X}}_{a,k} \\ &= \frac{2}{3} \frac{\rho_k A_k \dot{p}_k}{p_{k+1} - p_k} \boldsymbol{X}_{a,k}^{T} \begin{bmatrix} 1 & 0 & 0 & -1 & 0 & 0 \\ 0 & 1 & 0 & 0 & -1 & 0 \\ 0 & 0 & 1 & 0 & 0 & -1 \\ -1 & 0 & 0 & 1 & 0 & 0 \\ 0 & -1 & 0 & 0 & 1 & 0 \\ 0 & 0 & -1 & 0 & 0 & 1 \end{bmatrix} \dot{\boldsymbol{X}}_{a,k} \end{aligned} \tag{B.4}$$

$$\boldsymbol{Q}_{p,k}^{1,3} = \rho_k A_k \left(p_{k+1} - p_k \right) \dot{p}_k \boldsymbol{X}_{a,k}^T \int_{-1}^{1} \left(\frac{\partial \boldsymbol{N}_{a,k}}{\partial p_{k+1}} \right)^T \frac{\partial \boldsymbol{N}_a}{\partial p_k} d\xi \dot{\boldsymbol{X}}_{a,k}$$

$$= \frac{1}{3} \frac{\rho_k A_k \dot{p}_k}{p_{k+1} - p_k} \boldsymbol{X}_{a,k}^T \begin{bmatrix} 1 & 0 & 0 & -1 & 0 & 0 \\ 0 & 1 & 0 & 0 & -1 & 0 \\ 0 & 0 & 1 & 0 & 0 & -1 \\ -1 & 0 & 0 & 1 & 0 & 0 \\ 0 & -1 & 0 & 0 & 1 & 0 \\ 0 & 0 & -1 & 0 & 0 & 1 \end{bmatrix} \dot{\boldsymbol{X}}_{a,k} \tag{B.5}$$

$$\boldsymbol{Q}_{p,k}^{2} = \begin{bmatrix} \boldsymbol{Q}_{p,k}^{2,1} & \boldsymbol{Q}_{p,k}^{2,2} & \boldsymbol{Q}_{p,k}^{2,3} \end{bmatrix} \tag{B.6}$$

$$\boldsymbol{Q}_{p,k}^{2,1} = \rho_k A_k \left(p_{k+1} - p_k \right) \dot{p}_{k+1} \int_{-1}^{1} \boldsymbol{N}_{a,k}^T \frac{\partial \boldsymbol{N}_{a,k}}{\partial p_{k+1}} d\xi \dot{\boldsymbol{X}}_{a,k}$$

$$= -\frac{1}{3} \rho A \dot{p}_{k+1} \begin{bmatrix} -2 & 0 & 0 & 2 & 0 & 0 \\ 0 & -2 & 0 & 0 & 2 & 0 \\ 0 & 0 & -2 & 0 & 0 & 2 \\ -1 & 0 & 0 & 1 & 0 & 0 \\ 0 & -1 & 0 & 0 & 1 & 0 \\ 0 & 0 & -1 & 0 & 0 & 1 \end{bmatrix} \dot{\boldsymbol{X}}_{a,k} \tag{B.7}$$

$$\boldsymbol{Q}_{p,k}^{2,2} = \rho_k A_k \left(p_{k+1} - p_k \right) \dot{p}_{k+1} \boldsymbol{X}_{a,k}^T \int_{-1}^{1} \left(\frac{\partial \boldsymbol{N}_{a,k}}{\partial p_k} \right)^T \frac{\partial \boldsymbol{N}_{a,k}}{\partial p_{k+1}} d\xi \dot{\boldsymbol{X}}_{a,k}$$

$$= \frac{1}{3} \frac{\rho_k A_k \dot{p}_{k+1}}{p_{k+1} - p_k} \boldsymbol{X}_{a,k}^T \begin{bmatrix} 1 & 0 & 0 & -1 & 0 & 0 \\ 0 & 1 & 0 & 0 & -1 & 0 \\ 0 & 0 & 1 & 0 & 0 & -1 \\ -1 & 0 & 0 & 1 & 0 & 0 \\ 0 & -1 & 0 & 0 & 1 & 0 \\ 0 & 0 & -1 & 0 & 0 & 1 \end{bmatrix} \dot{\boldsymbol{X}}_{a,k} \tag{B.8}$$

$$\boldsymbol{Q}_{p,k}^{2,3} = \rho_k A_k \left(p_{k+1} - p_k \right) \dot{p}_{k+1} \boldsymbol{X}_{a,k}^T \int_{-1}^{1} \left(\frac{\partial \boldsymbol{N}_{a,k}}{\partial p_{k+1}} \right)^T \frac{\partial \boldsymbol{N}_a}{\partial p_{k+1}} d\xi \dot{\boldsymbol{X}}_{a,k}$$

$$= \frac{2}{3} \frac{\rho_k A_k \dot{p}_{k+1}}{p_{k+1} - p_k} \boldsymbol{X}_{a,k}^T \begin{bmatrix} 1 & 0 & 0 & -1 & 0 & 0 \\ 0 & 1 & 0 & 0 & -1 & 0 \\ 0 & 0 & 1 & 0 & 0 & -1 \\ -1 & 0 & 0 & 1 & 0 & 0 \\ 0 & -1 & 0 & 0 & 1 & 0 \\ 0 & 0 & -1 & 0 & 0 & 1 \end{bmatrix} \dot{\boldsymbol{X}}_{a,k} \tag{B.9}$$

$$\boldsymbol{Q}_{p,k}^{3} = \begin{bmatrix} \boldsymbol{Q}_{p,k}^{3,1} & \boldsymbol{Q}_{p,k}^{3,2} & \boldsymbol{Q}_{p,k}^{3,3} \end{bmatrix} \tag{B.10}$$

$$\boldsymbol{Q}_{p,k}^{3,1} = \rho_k A_k \left(\frac{p_{k+1} - p_k}{2} \right) \dot{p}_k^2 \int_{-1}^{1} \boldsymbol{N}_{a,k}^T \frac{\partial^2 \boldsymbol{N}_{a,k}}{\partial p_k^2} d\xi \boldsymbol{X}_{a,k}$$

$$= -\frac{1}{3} \frac{\rho_k A_k \dot{p}_k^2}{p_{k+1} - p_k} \begin{bmatrix} -2 & 0 & 0 & 2 & 0 & 0 \\ 0 & -2 & 0 & 0 & 2 & 0 \\ 0 & 0 & -2 & 0 & 0 & 2 \\ -1 & 0 & 0 & 1 & 0 & 0 \\ 0 & -1 & 0 & 0 & 1 & 0 \\ 0 & 0 & -1 & 0 & 0 & 1 \end{bmatrix} \boldsymbol{X}_{a,k} \tag{B.11}$$

$$\boldsymbol{Q}_{p,k}^{3,2} = \rho_k A_k \left(\frac{p_{k+1} - p_k}{2} \right) \dot{p}_k^2 \boldsymbol{X}_{a,k}^T \int_{-1}^{1} \left(\frac{\partial \boldsymbol{N}_{a,k}}{\partial p_k} \right)^T \frac{\partial^2 \boldsymbol{N}_{a,k}}{\partial p_k^2} d\xi \boldsymbol{X}_{a,k}$$

$$= \frac{2}{3} \frac{\rho_k A_k \dot{p}_k^2}{\left(p_{k+1} - p_k \right)^2} \boldsymbol{X}_{a,k}^T \begin{bmatrix} 1 & 0 & 0 & -1 & 0 & 0 \\ 0 & 1 & 0 & 0 & -1 & 0 \\ 0 & 0 & 1 & 0 & 0 & -1 \\ -1 & 0 & 0 & 1 & 0 & 0 \\ 0 & -1 & 0 & 0 & 1 & 0 \\ 0 & 0 & -1 & 0 & 0 & 1 \end{bmatrix} \boldsymbol{X}_{a,k} \tag{B.12}$$

$$\boldsymbol{Q}_{p,k}^{3,3} = \rho_k A_k \left(\frac{p_{k+1} - p_k}{2} \right) \dot{p}_k^2 \boldsymbol{X}_{a,k}^T \int_{-1}^{1} \left(\frac{\partial \boldsymbol{N}_{a,k}}{\partial p_{k+1}} \right)^T \frac{\partial^2 \boldsymbol{N}_{a,k}}{\partial p_k^2} d\xi \boldsymbol{X}_{a,k}$$

$$= \frac{1}{3} \frac{\rho_k A_k \dot{p}_1^2}{\left(p_{k+1} - p_k \right)^2} \boldsymbol{X}_{a,k}^T \begin{bmatrix} 1 & 0 & 0 & -1 & 0 & 0 \\ 0 & 1 & 0 & 0 & -1 & 0 \\ 0 & 0 & 1 & 0 & 0 & -1 \\ -1 & 0 & 0 & 1 & 0 & 0 \\ 0 & -1 & 0 & 0 & 1 & 0 \\ 0 & 0 & -1 & 0 & 0 & 1 \end{bmatrix} \boldsymbol{X}_{a,k} \tag{B.13}$$

$$\boldsymbol{Q}_{p,k}^{4} = \begin{bmatrix} \boldsymbol{Q}_{p,k}^{4,1} & \boldsymbol{Q}_{p,k}^{4,2} & \boldsymbol{Q}_{p,k}^{4,3} \end{bmatrix} \tag{B.14}$$

$$\boldsymbol{Q}_{p,k}^{4,1} = \rho_k A_k \left(\frac{p_{k+1} - p_k}{2} \right) \dot{p}_{k+1}^2 \int_{-1}^{1} \boldsymbol{N}_{a,k}^T \frac{\partial^2 \boldsymbol{N}_{a,k}}{\partial p_{k+1}^2} d\xi \boldsymbol{X}_{a,k}$$

$$= \frac{1}{3} \frac{\rho_k A_k \dot{p}_{k+1}^2}{\left(p_{k+1} - p_k \right)} \begin{bmatrix} -1 & 0 & 0 & 1 & 0 & 0 \\ 0 & -1 & 0 & 0 & 1 & 0 \\ 0 & 0 & -1 & 0 & 0 & 1 \\ -2 & 0 & 0 & 2 & 0 & 0 \\ 0 & -2 & 0 & 0 & 2 & 0 \\ 0 & 0 & -2 & 0 & 0 & 2 \end{bmatrix} \boldsymbol{X}_{a,k} \tag{B.15}$$

$$\boldsymbol{Q}_{p,k}^{4,2} = \rho_k A_k \left(\frac{p_{k+1} - p_k}{2} \right) \dot{p}_{k+1}^2 \boldsymbol{X}_{a,k}^T \int_{-1}^{1} \left(\frac{\partial \boldsymbol{N}_{a,k}}{\partial p_k} \right)^T \frac{\partial^2 \boldsymbol{N}_{a,k}}{\partial p_{k+1}^2} d\xi \boldsymbol{X}_{a,k}$$

$$= -\frac{1}{3} \frac{\rho_k A_k \dot{p}_{k+1}^2}{\left(p_{k+1} - p_k \right)^2} \boldsymbol{X}_{a,k}^T \begin{bmatrix} 1 & 0 & 0 & -1 & 0 & 0 \\ 0 & 1 & 0 & 0 & -1 & 0 \\ 0 & 0 & 1 & 0 & 0 & -1 \\ -1 & 0 & 0 & 1 & 0 & 0 \\ 0 & -1 & 0 & 0 & 1 & 0 \\ 0 & 0 & -1 & 0 & 0 & 1 \end{bmatrix} \boldsymbol{X}_{a,k} \tag{B.16}$$

$$\boldsymbol{Q}_{p,k}^{4,3} = \rho_k A_k \left(\frac{p_{k+1} - p_k}{2} \right) \dot{p}_{k+1}^2 \boldsymbol{X}_{a,k}^T \int_{-1}^{1} \left(\frac{\partial \boldsymbol{N}_{a,k}}{\partial p_{k+1}} \right)^T \frac{\partial^2 \boldsymbol{N}_{a,k}}{\partial p_{k+1}^2} d\xi \boldsymbol{X}_{a,k}$$

$$= -\frac{2}{3} \frac{\rho_k A_k \dot{p}_{k+1}^2}{\left(p_{k+1} - p_k \right)^2} \boldsymbol{X}_{a,k}^T \begin{bmatrix} 1 & 0 & 0 & -1 & 0 & 0 \\ 0 & 1 & 0 & 0 & -1 & 0 \\ 0 & 0 & 1 & 0 & 0 & -1 \\ -1 & 0 & 0 & 1 & 0 & 0 \\ 0 & -1 & 0 & 0 & 1 & 0 \\ 0 & 0 & -1 & 0 & 0 & 1 \end{bmatrix} \boldsymbol{X}_{a,k} \tag{B.17}$$

$$\boldsymbol{Q}_{p,k}^{5} = \begin{bmatrix} \boldsymbol{Q}_{p,k}^{5,1} & \boldsymbol{Q}_{p,k}^{5,2} & \boldsymbol{Q}_{p,k}^{5,3} \end{bmatrix} \tag{B.18}$$

$$\boldsymbol{Q}_{p,k}^{5,1} = \rho_k A_k \left(\frac{p_{k+1} - p_k}{2} \right) \dot{p}_k \dot{p}_{k+1} \int_{-1}^{1} \boldsymbol{N}_{a,k}^T \frac{\partial^2 \boldsymbol{N}_{a,k}}{\partial p_k \partial p_{k+1}} d\xi \boldsymbol{X}_{a,k}$$

$$= \frac{1}{3} \frac{\rho_k A_k}{\left(p_{k+1} - p_k \right)} \dot{p}_k \dot{p}_{k+1} \begin{bmatrix} 1 & 0 & 0 & -1 & 0 & 0 \\ 0 & 1 & 0 & 0 & -1 & 0 \\ 0 & 0 & 1 & 0 & 0 & -1 \\ -1 & 0 & 0 & 1 & 0 & 0 \\ 0 & -1 & 0 & 0 & 1 & 0 \\ 0 & 0 & -1 & 0 & 0 & 1 \end{bmatrix} \boldsymbol{X}_{a,k} \tag{B.19}$$

$$\boldsymbol{Q}_{p,k}^{5,2} = \rho_k A_k \left(\frac{p_{k+1} - p_k}{2} \right) \dot{p}_k \dot{p}_{k+1} \boldsymbol{X}_{a,k}^T \int_{-1}^{1} \left(\frac{\partial \boldsymbol{N}_{a,k}}{\partial p_k} \right)^T \frac{\partial^2 \boldsymbol{N}_{a,k}}{\partial p_k \partial p_{k+1}} d\xi \boldsymbol{X}_{a,k}$$

$$= \frac{1}{3} \frac{\rho_k A_k \dot{p}_k \dot{p}_{k+1}}{\left(p_{k+1} - p_k \right)^2} \boldsymbol{X}_{a,k}^T \begin{bmatrix} 1 & 0 & 0 & -1 & 0 & 0 \\ 0 & 1 & 0 & 0 & -1 & 0 \\ 0 & 0 & 1 & 0 & 0 & -1 \\ -1 & 0 & 0 & 1 & 0 & 0 \\ 0 & -1 & 0 & 0 & 1 & 0 \\ 0 & 0 & -1 & 0 & 0 & 1 \end{bmatrix} \boldsymbol{X}_{a,k} \tag{B.20}$$

$$\boldsymbol{Q}_{p,k}^{5,3} = \rho_k A_k \left(\frac{p_{k+1} - p_k}{2} \right) \dot{p}_k \dot{p}_{k+1} \boldsymbol{X}_{a,k}^T \int_{-1}^{1} \left(\frac{\partial \boldsymbol{N}_{a,k}}{\partial p_{k+1}} \right)^T \frac{\partial^2 \boldsymbol{N}_{a,k}}{\partial p_k \partial p_{k+1}} d\xi \boldsymbol{X}_{a,k}$$

$$= -\frac{1}{3} \frac{\rho_k A_k}{\left(p_{k+1} - p_k \right)^2} \dot{p}_k \dot{p}_{k+1} \boldsymbol{X}_{a,k}^T \begin{bmatrix} 1 & 0 & 0 & -1 & 0 & 0 \\ 0 & 1 & 0 & 0 & -1 & 0 \\ 0 & 0 & 1 & 0 & 0 & -1 \\ -1 & 0 & 0 & 1 & 0 & 0 \\ 0 & -1 & 0 & 0 & 1 & 0 \\ 0 & 0 & -1 & 0 & 0 & 1 \end{bmatrix} \boldsymbol{X}_{a,k} \tag{B.21}$$

where $\bar{\varepsilon}_{0,k}$ is the average value of strain in the *k-th* element.

APPENDIX C Elastic Force

The detailed expressions of elastic force $\boldsymbol{Q}_{e,k} = \left(\boldsymbol{Q}_{e,k}^{1}, \boldsymbol{Q}_{e,k}^{2}, \boldsymbol{Q}_{e,k}^{3}\right)^{T}$ are as,

$$\begin{aligned}\boldsymbol{Q}_{e,k}^{1} &= -\left(\frac{2}{p_{k+1}-p_k}\right)\left(\bar{\varepsilon}_{0,k}+c\dot{\bar{\varepsilon}}_{0,k}\right)E_kA_k\int_{-1}^{1}\left(\frac{\partial \boldsymbol{N}_{a,k}}{\partial\xi}\right)^{T}\left(\frac{\partial \boldsymbol{N}_{a,k}}{\partial\xi}\right)d\xi\boldsymbol{X}_{a,k}\\ &= -\frac{1}{p_{k+1}-p_k}\left(\bar{\varepsilon}_{0,k}+c\dot{\bar{\varepsilon}}_{0,k}\right)E_kA_k\begin{bmatrix}1&0&0&-1&0&0\\0&1&0&0&-1&0\\0&0&1&0&0&-1\\-1&0&0&1&0&0\\0&-1&0&0&1&0\\0&0&-1&0&0&1\end{bmatrix}\boldsymbol{X}_{a,k}\end{aligned} \tag{C.1}$$

$$\begin{aligned}\boldsymbol{Q}_{e,k}^{2} &= \frac{1}{\left(p_{k+1}-p_k\right)^2}\left(\bar{\varepsilon}_{0,k}+c\dot{\bar{\varepsilon}}_{0,k}\right)E_kA_k\boldsymbol{X}_{a,k}^{T}\int_{-1}^{1}\left(\frac{\partial \boldsymbol{N}_{a,k}}{\partial\xi}\right)^{T}\left(\frac{\partial \boldsymbol{N}_{a,k}}{\partial\xi}\right)d\xi\boldsymbol{X}_{a,k}\\ &= +\frac{-1}{2\left(p_{k+1}-p_k\right)^2}\left(\bar{\varepsilon}_{0,k}+c\dot{\bar{\varepsilon}}_{0,k}\right)E_kA_k\boldsymbol{X}_{a,k}^{T}\begin{bmatrix}1&0&0&-1&0&0\\0&1&0&0&-1&0\\0&0&1&0&0&-1\\-1&0&0&1&0&0\\0&-1&0&0&1&0\\0&0&-1&0&0&1\end{bmatrix}\boldsymbol{X}_{a,k}\end{aligned} \tag{C.2}$$

$$\begin{aligned}\boldsymbol{Q}_{e,k}^{3} &= -\frac{1}{\left(p_{k+1}-p_k\right)^2}\left(\bar{\varepsilon}_{0,k}+c\dot{\bar{\varepsilon}}_{0,k}\right)E_kA_k\boldsymbol{X}_{a,k}^{T}\int_{-1}^{1}\left(\frac{\partial \boldsymbol{N}_{a,k}}{\partial\xi}\right)^{T}\left(\frac{\partial \boldsymbol{N}_{a,k}}{\partial\xi}\right)d\xi\boldsymbol{X}_{a,k}\\ &= -\frac{1}{2\left(p_{k+1}-p_k\right)^2}\left(\bar{\varepsilon}_{0,k}+c\dot{\bar{\varepsilon}}_{0,k}\right)E_kA_k\boldsymbol{X}_{a,k}^{T}\begin{bmatrix}1&0&0&-1&0&0\\0&1&0&0&-1&0\\0&0&1&0&0&-1\\-1&0&0&1&0&0\\0&-1&0&0&1&0\\0&0&-1&0&0&1\end{bmatrix}\boldsymbol{X}_{a,k}\end{aligned} \tag{C.3}$$

where $\bar{\varepsilon}_{0,k}$ and $\dot{\bar{\varepsilon}}_{0,k}$ are the average value of strain and its rate in the *k-th* element.

APPENDIX D Gravitational Force

The detailed expressions of the gravitational force term $\boldsymbol{Q}_{g,k} = \left(\boldsymbol{Q}^1_{g,k}, \boldsymbol{Q}^2_{g,k}, \boldsymbol{Q}^3_{g,k}\right)^T$ are,

$$\begin{aligned}\boldsymbol{Q}^1_{g,k} &= \left(\frac{p_{k+1}-p_k}{2}\right)\int_{-1}^{1} \boldsymbol{N}^T_{a,k}\boldsymbol{f}_{g,k}d\xi \\ &= \frac{p_{k+1}-p_k}{2}\begin{bmatrix}1&0&0\\0&1&0\\0&0&1\\1&0&0\\0&1&0\\0&0&1\end{bmatrix}\boldsymbol{f}_{g,k}\end{aligned} \tag{D.1}$$

$$\begin{aligned}\boldsymbol{Q}^2_{g,k} &= \boldsymbol{X}^T_{a,k}\left(\frac{p_{k+1}-p_k}{2}\right)\int_{-1}^{1}\left(\frac{\partial \boldsymbol{N}_{a,k}}{\partial p_k}\right)^T d\xi \boldsymbol{f}_{g,k} \\ &= -\frac{1}{2}\boldsymbol{X}^T_{a,k}\begin{bmatrix}-1&0&0\\0&-1&0\\0&0&-1\\1&0&0\\0&1&0\\0&0&1\end{bmatrix}\boldsymbol{f}_{g,k}\end{aligned} \tag{D.2}$$

$$\begin{aligned}\boldsymbol{Q}^3_{g,k} &= \boldsymbol{X}^T_{a,k}\left(\frac{p_{k+1}-p_k}{2}\right)\int_{-1}^{1}\left(\frac{\partial \boldsymbol{N}_{a,k}}{\partial p_{k+1}}\right)^T d\xi \boldsymbol{f}_{g,k} \\ &= -\frac{1}{2}\boldsymbol{X}^T_{a,k}\begin{bmatrix}-1&0&0\\0&-1&0\\0&0&-1\\1&0&0\\0&1&0\\0&0&1\end{bmatrix}\boldsymbol{f}_{g,k}\end{aligned} \tag{D.3}$$